# Diaminodicyanoquinodimethanes: Bioimaging Applications and Mechanically Responsive Molecular Hopper Crystals

# A Thesis Submitted for the Degree of **DOCTOR OF PHILOSOPHY**

by

# N. SENTHILNATHAN



School of Chemistry University of Hyderabad Hyderabad 500 046 INDIA

December 2020

# Dedicated to My Teachers

# **CONTENTS**

		Page No.			
Declaratio	n	i			
Certificate	<b>?</b>	ii			
Acknowled	Acknowledgements				
Common Abbreviations					
Chapter 1	Introduction				
	1.1. Molecular materials	2			
	1.2. Fluorescent materials	13			
	1.3. Fluorescence probes	22			
	1.4. Actuators	31			
	1.5. Layout of the thesis	38			
	References	41			
Chapter 2	Efficient Bioimaging with Diaminodicyanoquinodimethanes: Selective Imaging of Epidermal and Stomatal Cells and Insigh into the Molecular level Interactions	t			
	2.1. Introduction	55			
	2.2. Synthesis and characterization	58			
	2.3. Stomatal cells imaging	59			
	2.4. Molecular level interactions	66			
	2.5. General utility of DADQs	74			
	2.6. Autofluorescence analysis	75			
	2.7. Stability and cytotoxicity	76			
	2.8. Summary	77			
	References	79			

Chapter 3	Zwitterionic Small Molecule based Fluorophores for Efficient and Selective Imaging of Bacterial Endospores				
	3.1. Introduction	83			
	3.2. Synthesis and characterization	86			
	3.3. Characteristic features of BT <sub>2</sub> and BHADQ	87			
	3.4. Endospore preparation	91			
	3.5. Imaging of bacterial cells and its endospore using BT <sub>2</sub>	93			
	3.6. Imaging of endospores using different DADQs; selective imaging with BHADQ	95			
	3.7. Molecular level interactions of BT <sub>2</sub> and BHADQ with components of the endospore cell wall	99			
	3.8. Molecular level interaction of BHADQ with components of the endospore core	103			
	3.9. Plausible staining mechanism	109			
	3.10. Effect of staining on endospores	110			
	3.11. General utility of BHADQ	114			
	3.12. Supporting experiments	116			
	3.13. Summary	118			
	References	119			
Chapter 4	Molecular Hopper Crystals and Electron Beam-Triggered Reversible Actuation				
	4.1. Introduction	121			
	4.2. Synthesis and characterization	124			
	4.3. Characteristics of BCPADQ	125			
	4.4. Hopper microcrystals	130			
	4.5. Actuation of microcrystals	139			
	4.6. An empirical model for the actuation	145			
	4.7. Summary	161			
	Reference	162			

Chapter 5	Overview of the present work and Future Prospects		
	5.1. Overview of the present work	165	
	5.2. Future directions	168	
	References	170	
Appendix		171	
Publication	ns and Presentations	175	

# DECLARATION

I hereby declare that the matter embodied in the thesis entitled "Diaminodicyanoquinodimethanes: Bioimaging Applications and Mechanically Responsive Molecular Hopper Crystals" is the result of investigations carried out by me in the School of Chemistry, University of Hyderabad, India under the supervision of Prof. T. P. Radhakrishnan.

I also confirm that this thesis is free from plagiarism. In keeping with the general practice of reporting scientific investigations, acknowledgements have been made wherever the work described is based on the finding of other investigators.

N. Senthilnathan

remod



This is to certify that the thesis entitled "Diaminodicyanoquinodimethanes: Bioimaging Applications and Mechanically Responsive Molecular Hopper Crystals" submitted by N. Senthilnathan bearing registration number 14CHPH25 in partial fulfillment of the requirements for the award of Doctor of Philosophy (Ph.D.) in the School of Chemistry is a bonafide work carried out by him under my supervision and guidance.

This thesis is free from plagiarism and has not been submitted previously in part or full to this or any other University/Institution for any degree or diploma.

#### Parts of this thesis have been:

#### A. Published as the following articles/book chapter:

- 1. N. Senthilnathan, Ch. G. Chandaluri, T. P. Radhakrishnan, Sci. Rep., 2017, 7, 10583 (1-11). (Chapter 2)
- 2. N. Senthilnathan, Kumar Gaurav, Ch. Venkata Ramana, T. P. Radhakrishnan, *J. Mater. Chem. B*, 2020, **8**, 4601-4608. *(Chapter 3)*
- 3. N. Senthilnathan, T. P. Radhakrishnan, Chem. Mater., 2020, 32, 8567-8575. (Chapter 4)
- 4. N. Senthilnathan, T. P. Radhakrishnan, In *Handbook of Aggregation-Induced Emission, Vol. 2: Typical AIEgens Design*, Eds., B. Z. Tang and Y. Tang, Wiley and Sons. *(In press)*

#### B. Presented in the following conferences:

- 1. National Conference on Fluorescence and Raman Spectroscopy (FCS 2017), IIT Guwahati, Assam. December 17-21, 2017.
- 2. International Conference on Recent Trends in Materials Science and Technology, Vikram Sarabhai Space Centre (ICMST 2018), Thiruvananthapuram, Kerala. October 10-13, 2018.
- 3. National Symposium on Convergence of Chemistry and Materials (CCM 2019), BITS-Pilani, Hyderabad campus, Telangana. December 17-18, 2019.

Further, the student has passed the following courses towards the fulfillment of coursework requirement for Ph.D.:

Sl. No.	<b>Course Code</b>	Title	Credits	Pass/Fail
1.	CY-801	Research Proposal	3	Pass
2.	CY-805	Instrumental Methods-A	3	Pass
3.	CY-806	Instrumental Methods-B	3	Pass
4.	CY-504	Chemistry of Materials	3	Pass

Prof. T. P. Radhakrishnan Prof. T.P. Radhakrishnan (Thesis Supervisor School of Chemistry

University of Hyderabad Hyderabad-500 046, India Dean 21.12.2020

School of Chemistry

Dean
SCHOOL OF CHEMISTRY
University of Hyderabad
Hyderabad-500 046

## **ACKNOWLEDGEMENTS**

I would like to express my heartfelt gratitude to **Prof. T. P. Radhakrishnan**, my research supervisor for his constant guidance, encouragement, inspiration and motivation. The never ending care and support he has shown despite his busy schedules gives a true strength and spirit to carry out work. His sincerity, discipline, patience and commitment to the work are highly admirable and worthy of emulation. I feel honored for being associated with him.

I thank my doctoral committee members, Prof. M. J. Swamy and Prof. M. Ghanashyam krishna for their support and concern. I thank present and former deans, School of Chemistry, University of Hyderabad and all the faculty members of school of chemistry for their help and support in various occasions. I would like also thank Prof. Ch. Venkata Ramana (School of Life Science), Hendrix Demers (Universite de Sherbrooke, Quebec, Canada) and Dr. N. Sri Ram Gopal (School of Physics) for their support and help in my research.

I thank UGC, New Delhi, for providing the fellowship and DST for financial support during the Ph.D tenure. I would like to acknowledge Mr. Prasad (CLSM, CIL), Ms. Nalini (CLSM, CFN), Mr. Dasharath (CLSM, School of Life Science), Mr. Durgaprasad (FESEM and FLIM, School of Chemistry), Mr. Sunil (FESEM, School of chemistry), Mr Anand (FTIR), Mr. A. V. Ramanakumar (SCXRD) and Mr. Rathod Mahesh Shrichand (SCXRD) for their assistance in work with instruments. I would like also thank all non-teaching members of school of chemistry for their cooperation.

I thank all the seniors from our laboratory and especially Dr. Ch. Chadaluri Gupta and Dr. U. Divya Madhuri for their contributions to the area I have worked and constant guidance. I extend my thanks to Dr. Dhanasekaran, Sasikanth, Ritesh and Anu for their cooperation in the lab. I am very thankful to the cooperation and coordination of my labmates while carrying out the research work. I would also like to thank all the project students who worked with me, Srijan Mondal, Biplab Patra, Amal Ajay and Roja. I also thank all research scholars of school of chemistry for support and help at various instances.

Its great pleasure to thank Mr. Kumar Gourav (School of Life Science), Mr. Vinod and Dr. Nabil (School of Physics) for their contribution in my research. I thank my friends, Dr. Dhamodharan, Dr. Sathya and Dr. Rajkumar for their help.

I would like to specially thank Tamilarasan and Narasimhulu for being with me during tough times. I thank Rajesh, Venket, Ankit, Saddam, Apurba, Arun, Ramesh, Manzoor, Tanmay, Tasnim and Sneha for making my stay pleasant and memorable. I would like to extend my thanks to Dr. Shankar, and Dr. C. Sudheer Kumar for their help. It's a great pleasure to thank my seniors and well-wishers, Dr. Ramkumar, Dr. Naveen, Dr. Ponsathish kumar, Dr. Ramesh, Dr. Manikandan, Dr. Rangarajan, Dr. Santhana Prabhu and Dr. Annadhasan for their care, support and guidance. I would also like to thank to all my friends for every positive impact given to me.

I am deeply indebted to all my teachers right from my school to the University for the excellent training I received throughout my academics. I would like to thank my teachers, Dr. M. Dhandapani, Dr. A. Muthusamy, Dr. A. Chandramohan, Dr. E. Selvakumar and Dr. Gopalswamy for their advice to reach my goal.

Finally, I would like to express my deep sense of gratitude to my beloved grandma. I could overcome every hurdle in my path only because of her love and affection. Her support and encouragement has led me to this position.

N. Senthilnathan

### **COMMON ABBREVIATIONS**

AFM atomic force microscope

AIE aggregation induced emission

br broad

CLSM confocal laser scanning microscope

d doublet

dec. decomposition

EDXS energy dispersive X-ray spectroscopy

FESEM field emission scanning electron microscope

FTIR fourier transform infra-red

h hour

ITC isothermal titration calorimetry

IC<sub>50</sub> half maximal inhibitory concentration

kV kilovolt
m multiplet

µm micrometer

µg microgram

µl microliter

min minute

m.p. melting point
nm nanometer
nmols nanomoles
ns nanosecond

Na<sub>2</sub>DPA sodium dipicolinate PGN peptidoglycan

PGA polygalacturonic acid

q quartet

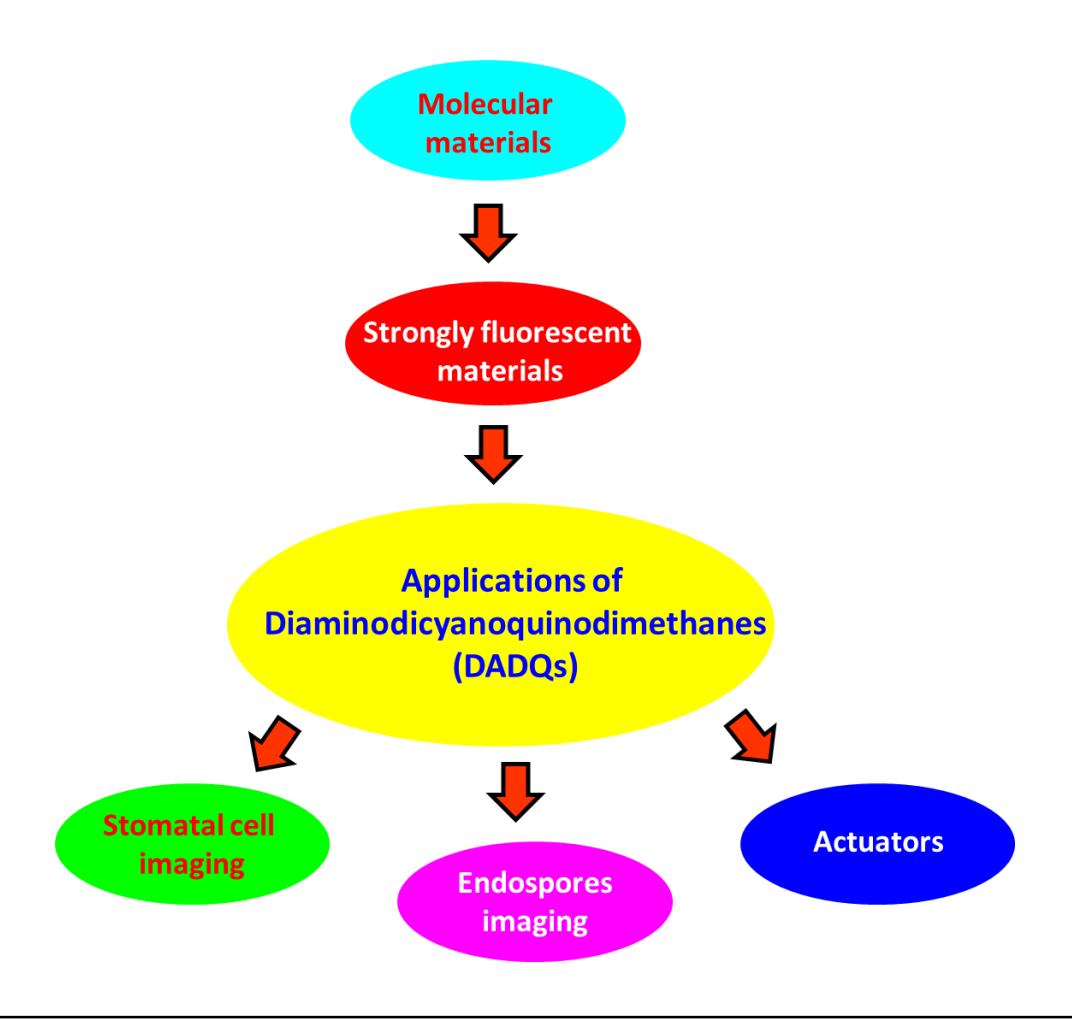
rpm rotations per minute

t triplet

2.5 D 2.5 dimension

# **CHAPTER 1**

# Introduction



A brief introduction to molecular materials, their different forms with prominent properties, and strongly fluorescent materials along with their application in the areas of bioimaging and actuators are discussed.

# Scope

Over the past several decades, molecular materials have emerged as extremely interesting systems, primarily because of their unique electronic, optical and magnetic attributes, and relatively less explored mechanical properties. Among the optical properties, strongly fluorescent materials have attracted special attention, as fluorescence emission in aggregates and solids is often adversely effected by self-quenching. Selected classes of molecular crystals that exhibit enhanced fluorescence emission have emerged as ideal candidates for a wide range of applications in technological to biological fields. Among the various kinds of fluorescent molecular materials, small molecule-based ones are especially alluring due to their facile structural tailorability, widely tunable emission, and high quantum yields that can be realised. Diaminodicyanoquinodimethanes (DADQs) is one such class of small molecules. The primary objective of this thesis is to explore novel applications of DADQs in areas of bioimaging and actuators; the latter has emerged as a new domain in the field of mechanically responsive molecular materials. The structural tailorability of DADQs enabled us to develop simple staining protocols and successfully implement them to selectively stain primary targets such as cell walls along with different organelles in plant cells, bacteria and bacterial endospores. The selection of the fluorophore for bioimaging is based on suitable functionalities for binding with the biological components, and characteristics such as hydrophobicity and enhanced quantum efficiency in the rigid and aggregated states. A very different direction that we have explored is the development of unique organic hopper crystals and their electron beam triggered actuation. Here again, the unique structural, electronic and organizational aspects of DADQs leading to highly unsymmetrical morphology and polar crystal lattices is exploited. Detailed experimental investigations and simulation studies led to an empirical model for the mechanical responses.

This chapter provides a general introduction to molecular materials and specific topics of interest in the development of the work presented in the thesis. A brief review of molecular materials, their types and some of the prominent properties they display are provided in Sec. 1.1. Sec. 1.2 provides salient details of fluorescent materials, fundamental concepts and some relevant applications. Basic aspects of fluorescence probes, their different classes, labeling approaches, and bioimaging of various cell lines including plant cells and microorganisms, are described in Sec.1.3. Fundamental aspects of actuators and micromachines, fabrication procedures, different types and their applications are presented in Sec. 1.4. Layout of the whole thesis is outlined in Sec. 1.5 along with the critical highlights of each chapter.

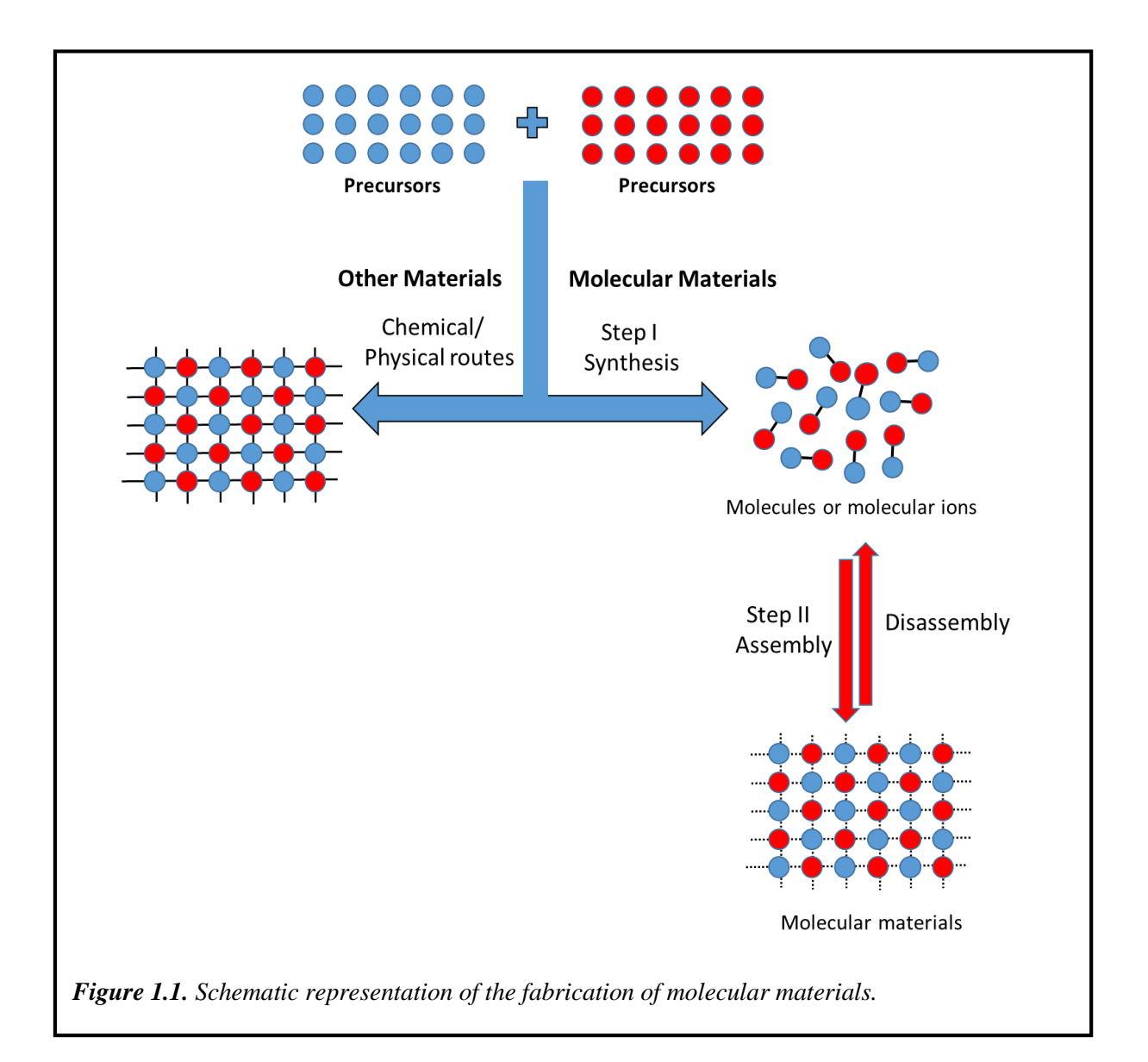
#### 1.1. Molecular materials

Materials play a pivotal role in our day to day life due to their critical applications in various fields such as technology, agriculture, and medicine. Many improvements and innovations in the strategy of fabrication and utilization of materials have taken place through the evolution of human civilization. The era of prehistory was named after the materials that were primarily utilized, as ages of stone, copper, bronze, and iron; this clearly illustrates the significance and impact of materials on the growth of civilization. Latter half of the 20<sup>th</sup> century was named the 'silicon age' or 'digital age'. The same period also witnessed the emergence of a new family of materials called molecular materials.<sup>1,2</sup> Fabrication of molecular materials involves essentially two stages (Figure 1.1). Molecules or molecular ions of the material of interest (building blocks) are synthesized from suitable precursors exploiting covalent interactions. In the subsequent stage, these building blocks are assembled using various fabrication methods like crystallization,<sup>3</sup> host-guest complexation,<sup>4</sup> Langmuir-Blodgett technique,<sup>5</sup> intercalation,<sup>6</sup> organic molecular beam deposition<sup>7</sup> and sol-gel technique;8 various noncovalent interactions that includes electrostatic, hydrogen bonding,  $\pi$ - $\pi$  stacking, and van der Waals<sup>9</sup> are utilized in this process. Most notably, molecular materials, display properties close to that of the individual building blocks with subtle perturbations that can be very crucial. In the case of extended solids based on ionic, covalent and metallic bonding, the properties often differ vastly from that of their constituents. Various sorts of molecular materials like conducting, superconducting, optical and magnetic materials have been designed and developed with a wide range of applications. 10-12 A brief discussion on the different classes follows.

# **1.1.1.** Types of molecular materials

### 1.1.1.1. Crystals and amorphous solids

In view of the arrangements of the building blocks, solids can be broadly divided into two categories, (i) crystalline and (ii) amorphous. The translationally ordered three-dimensional arrangement of atoms, molecules, or ions is characteristic of crystals or crystalline solids; depending on the spatial extent of the order, they could be single, micro or nanocrystals. Lack of order in some directions can provide liquid crystalline materials. Amorphous solids show no order in the arrangement of the constituents, spatially or orientationally. The reversible transition between crystalline and amorphous states is of great



interest in terms of applications as well as to gain basic insight into crystallization process. In some specific electronic and optoelectronic devices (organic light-emitting devices, solar cells, etc.) single crystals could be more effective than amorphous films. In field-effect transistors, organic crystals have been employed as the active layer and for transport of charge carriers.<sup>13</sup> Indeed, many of the traditional laser crystals (Nd:YAG, Nd:Ce:YAG, Er:YAG, Nd:YVO<sub>4</sub>, etc.) are typically single crystals doped with transition metal ions.<sup>14</sup> like Bridgman-Stockbarger method, 15 Czochralski method<sup>16</sup> Techniques Sankaranarayanan-Ramasamy method<sup>17</sup> are followed in the fabrication of the large single crystals. However, it is extremely difficult and expensive to employ single crystals in large

scale applications. In those cases, polycrystalline solids are often employed because of their advantages in terms of large area fabrication, facility to tune dopant levels, etc.

Amorphous solids are also useful in different fields like optoelectronics, memory devices and pharmaceuticals. In the pharmaceutical industry, amorphous materials are favoured over crystalline solids because of their appreciable bioactivity and solubility. 18 Amorphous forms of organic compounds, including tris(oligoaryl)amines, triarylboranes, 1,3,5-triphenylbenzene, core molecules of triphenylamine and capped triarylamines of thiophenes and oligothiophenes are employed as transport layers for charge carriers in optoelectronic devices. 19,20 The common fabrication techniques followed for the fabrication of amorphous solids include grinding, melt-quench, ball-milling, lyophilization, reprecipitation, and spray drying. Polymers generally possess coexisting crystalline and amorphous regions; the degree of crystallinity is tunable in many systems.<sup>21</sup> Materials that undergo reversible transformations between different phases such as solid and liquid or amorphous and crystalline, upon external stimuli are called phase change materials (PCM). Various organic and inorganic PCMs have been developed for different applications such as latent heat thermal energy storage, optical information storage, etc; the latter is used in phase change random access memory devices. Our research group has developed functional PCMs based on alkoxyalkyl chain substituted DADQs; fluorescence emission energy and intensity switching in these thin films were studied. <sup>22, 23</sup>

#### 1.1.1.2. Nanocrystals

Nanomaterials have gained significant interest because of their wide range of applications in fields such as electronics, sensors, biotechnology and engineering. A Materials with at least one dimension in the range of 1-100 nm can be categorized as nanomaterials and synthesized using either the 'top-down' or 'bottom-up' method. Size-dependence of properties is the important signature of nanomaterials. The novel and unique property of 'quantum size effects' has fuelled extensive development of metal or semiconductor NCs. Quantum dots are semiconductor nanocrystals of the size of a few nanometers in all directions, that are highly useful in several applications such as light-emitting diodes (LEDs), photovoltaic cells, and biosensors. Molecular nanoparticles developed using organic molecules and polymers like phthalocyanine, perylene and polydiacetylene have been synthesized and investigated. Like inorganic NCs, organic NCs often exhibit size-

dependent optical properties. However, organic NCs are more fragile and thermally unstable than inorganic NCs. Several approaches to fabricate new classes of nanomaterials, such as hybrids of organic and inorganic nanomaterials, have been attempted to overcome this problem.

#### 1.1.1.3. **Colloids**

Colloids or colloidal solutions are the heterogeneous mixtures in which micro or nano particles of a substance are dispersed in a solvent medium. Size of the colloidal particles can vary from a few nm to µm. Colloids play an essential role in our everyday lives. They are utilized as thickening agents in industrial products such as lotions, toothpaste, lubricants, paints and inks. Colloidal gold and calcium solutions are used in the biomedical field. Other examples of colloids used in medication are hetastarch, albumin, and dextran. <sup>30</sup> Based on the functionalization of the colloidal particles, they can be broadly classified into two types (i) isotropic and (ii) anisotropic, when unsymmetric with two different faces, they are known as Janus particles.

Janus particles possess fascinating properties due to their asymmetric geometry. The charge and polarity on the surface, chemical composition, optical and magnetic properties, etc. show asymmetric characteristics. The Janus particles are generally divided into three categories (i) inorganic-inorganic, (ii) organic-inorganic, (iii) polymer-polymer hybrid particles. In 1985, Lee et al. reported the first Janus particles of anisotropic PS (polystyrene)/ PMMA (poly (methyl methacrylate)) latex, fabricated using a seeded emulsion polymerization technique.<sup>31</sup> Light, magnetic and electric field, ultrasound, and chemical energy driven Janus particles (TiO2-Fe, TiO2-Au, TiO2-Cu, Polystyrene-Au) based micro/nanomotors have been developed. 32,33 In addition, Janus particles have been employed for drug delivery, molecular imaging, and biomolecular labeling applications. <sup>34,35</sup>

#### 1.1.1.4. Monolayer film

A single, continuous layer or film with the thickness of an atom or molecule is known as a monolayer or ultrathin films. Langmuir-Blodgett technique is one of the elegant methods employed in the fabrication of ultrathin films. In 1917, Irving Langmuir reported the experimental and theoretical concept of monolayer thin films formed at the air-water interfaces.<sup>36</sup> Later, Katherine Blodgett developed a method for transferring floating monolayer to a substrate; the transferred films are generally referred to as Langmuir-Blodgett (LB) films.<sup>37</sup> The LB films can be considered as two-dimensional solids. LB films are used in various fields like sensors<sup>38</sup> and biomedicine<sup>39,40</sup> due to the well-defined optical and electronic properties of the layered structure and minimal defect density. LB films have been utilized to mimic the function of biological membranes to study their interactions with molecules, ions, and drugs in biological functions.<sup>41</sup> Several nonlinear optical materials have been developed using LB films in our laboratory.<sup>42,43</sup>

# 1.1.2. Prominent functions and properties

# 1.1.2.1. Liquid crystals

Liquid crystal is a state of matter that exists between three dimensionally ordered crystalline solids and isotropic liquid. Liquid crystals are broadly classified into thermotropic, lyotropic, and metallotropic phases. Based on the molecular orientational ordering, liquid crystals are further divided into several mesophases such as smectic, nematic, calamitic and discotic. Liquid crystals exhibit various properties like birefringence due to their anisotropic nature. Orthogonal polarization components of light beams passing through these materials experience different refractive indices. High birefringence nematic liquid crystals such as biphenyl derivatives are of interest in display applications. Orientations of molecules in twisted nematics can be tuned by external electric fields making them useful in liquid crystal displays. Lyotropic liquid crystals are of interest in the field of biomimetic chemistry. Interestingly, several biological organelles exist in the form of liquid crystals. Due to the various optical and electrical properties, liquid crystals have been exploited in diverse applications such as solar cells, optical imaging, medicine and thermal mapping.

#### 1.1.2.2. Magnetic materials

Magnetic materials are broadly classified into diamagnetic and paramagnetic systems. Depending on the nature of spin interactions, they can be ferromagnetic, antiferromagnetic or ferrimagnetic; several other magnetic orderings are also known. Metals such as Fe, Co, Ni, Gd), metal oxides (CrO<sub>2</sub>, Fe<sub>3</sub>O<sub>4</sub>, Ce<sub>3</sub>O<sub>4</sub>) and alloys (SmCo<sub>5</sub>, Nd<sub>2</sub>Fe<sub>14</sub>B) are well known magnetic materials and their magnetic properties arise from electrons in valence *d* and *f* orbitals.<sup>47</sup> The magnetic materials are generally fabricated by using high-temperature

metallurgical processes.<sup>48</sup> Because of their interesting characteristics, such as plasticity, flexibility, solubility, and biocompatibility, organic ferromagnetic materials are gaining more attention, but the stability issues and relevant magnetic characteristics like Curie temperature, limit their development and applications. The first report of a purely organic ferromagnetic material is that of p-4-nitrophenylnitronyl nitroxide (p-NPNN) with ferromagnetic order below 0.6 K.<sup>49</sup> A few organic-based magnetic materials have been reported with an ordering temperatures exceeding room temperature; however they suffer from chemical stability issues. Transition metal-based ferromagnetic molecular materials with magnetic order and a wide range of ordering temperatures have been fabricated by forming coordination complexes of transition metal ions and tetracyanoethylene (TCNE) or (TCNQ).50 tetracyanoquinodimethane Several organic radical based on nitroxides/nitronylnitroxides and thia/selena-azolyls and TCNE has been developed.<sup>51</sup> Single-molecule magnets (SMMs) are another fascinating class of magnetic materials that have been developed with potential applications in display devices and information storage.<sup>52</sup>

#### 1.1.2.3. **Optical materials**

Luminescence is one of the most popular and important optical properties of molecular materials, making them useful in various fields like chemical sensors, medicine, fluorescent labeling, dyes, biological detectors, and electro-optic devices. Various external stimuli such as light, electric field and chemical reaction are applied to excite the molecules electronically leading to the light emission. Based on the source of excitation, light, mechanical, emission electrical, chemical and phenomena are classified as photoluminescence, electroluminescence, chemiluminescence, and mechanoluminescence respectively. Photoluminescence can be fluorescence or phosphorescence, depending on where emission is from singlet or triplet excited state energy levels respectively. Applications of light emitting organic molecules, metal complexes, nanoparticles, nanoclusters, and polymers are found in sensors, 53 display devices, 54 bio-imaging, 55 optical waveguides, <sup>56</sup> and field-effect transistors. <sup>57</sup> Nonlinear optical (NLO) properties of materials arise when the polarization responds nonlinearly to the electric field of incident light, especially with high-intensity light. The beginning was marked by the observation of secondharmonic generation in quartz by Franken et al; the frequency of light passing through the material is doubled. Later, other nonlinear optical phenomena such as third, and higher harmonic generation, optical parametric oscillation, Kerr effect, cross-phase modulation, multi-photon absorption, etc. were discovered.<sup>58</sup> These properties enhance the importance of the nonlinear optical materials in various applications like short-pulsed lasers, ultrafast switches, optical computers, sensors, and laser amplifiers. Several organic molecular materials have been developed with permanent NLO characteristics. A famous example is N-(4-nitrophenyl)-(L)-prolinol (NPP)<sup>59</sup> which exhibits efficient second harmonic generation. Many conjugated polymers show strong third order optical NLO effects. 60 Nonlinear optical responses of simple zwitterionic diaminodicyanoquinodimethanes (DADQs) have been reported from our laboratory.<sup>2,61</sup>

#### 1.1.2.4. Semiconductors and organic metals

Semiconductors typically possess electrical conductivity between that of metals and insulators. A small energy gap (~1 eV) between the filled valence band and the empty conduction band, is the crucial characteristics of semiconductors (Figure 1.2). Elements such as silicon (Si) and germanium (Ge) and their compounds such as gallium arsenide (GaAs), mercury indium telluride (HgIn<sub>2</sub>Te<sub>4</sub>) and aluminum gallium arsenide (Al<sub>x</sub>Ga<sub>1-x</sub>As) are classic examples of semiconductors. They are broadly classified into two groups, intrinsic and extrinsic. Intrinsic semiconductors are chemically pure and, consisting of a single material whereas extrinsic semiconductors contain dopant impurities. Based on the type of impurities added, extrinsic semiconductors are divided into p-type and n-type. Examples of n and ptype semiconductors are tetravalent materials (Si or Ge) doped with trivalent (B, Al, In) and pentavalent (P, As, Sb, Bi) atoms respectively. Interface between the two semiconductor materials, known as the p-n junction allowing electrical current flow in only one direction, is useful in electronic and optoelectronic devices. Perylene-bromine complex is the first molecular materials reported, exhibiting semiconducting properties; it showed an electrical resistivity  $\sim 1~\Omega$  cm at 90 K.<sup>62</sup> Subsequently several organic semiconductors were developed; many of them were based on charge transfer complexes of tetracyanoquinodimethane (TCNQ).63

External energy like light and electric field, can trigger the transfer of electrons from valence band to the conduction band in the optoelectronic devices, thus creating a hole in the valence band. The excited electron in the conduction band can release its energy and fall back into the valence band; the electron-hole recombination process can be accompanied

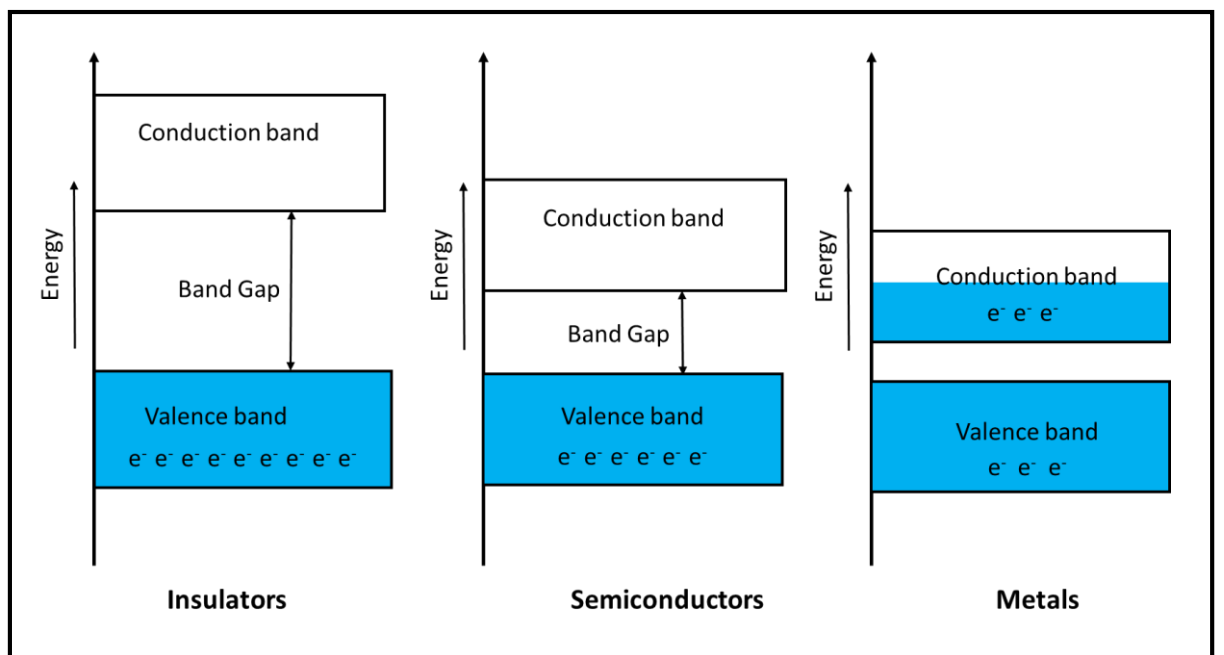


Figure 1.2. Schematic illustration of energy band structure of insulators, semiconductors, and metals.

by bright emission. Indium gallium nitride (InGaN) and aluminium gallium indium phosphide (AlGaInP) have been employed in the light-emitting devices as the emissive layer. 64,65 Tris-(8-hydroxyquinolinato)aluminum (AlO<sub>3</sub>) is the first molecular material reported, showing well defined electroluminescence (EL).<sup>66</sup> Poly(*p*-phenylenevinylene) (PPV), <sup>67</sup> a conjugated polymers, and its derivatives are extremely useful in EL applications. <sup>68</sup> Due to their advantages such as low cost, small and tunable energy gaps and controlled electrical conductivity, semiconductors are utilized in a wide range of applications in lasers, solar cells, transistors, diodes, integrated chips, photosensors, and light emitting devices.<sup>69</sup> Metallic conduction in molecular materials was realized for the first time in the donoracceptor complex of tetrathiafulvalene (TTF) and TCNQ. Organic conductors were wide range of donors including TTF. developed using a alkylphenazines, tetramethyltetrathiafulvalene (TMTTF) etc. and acceptors such as TCNQ, N,N'dicyanoquinone diimines (DCNQI) etc.<sup>70</sup>

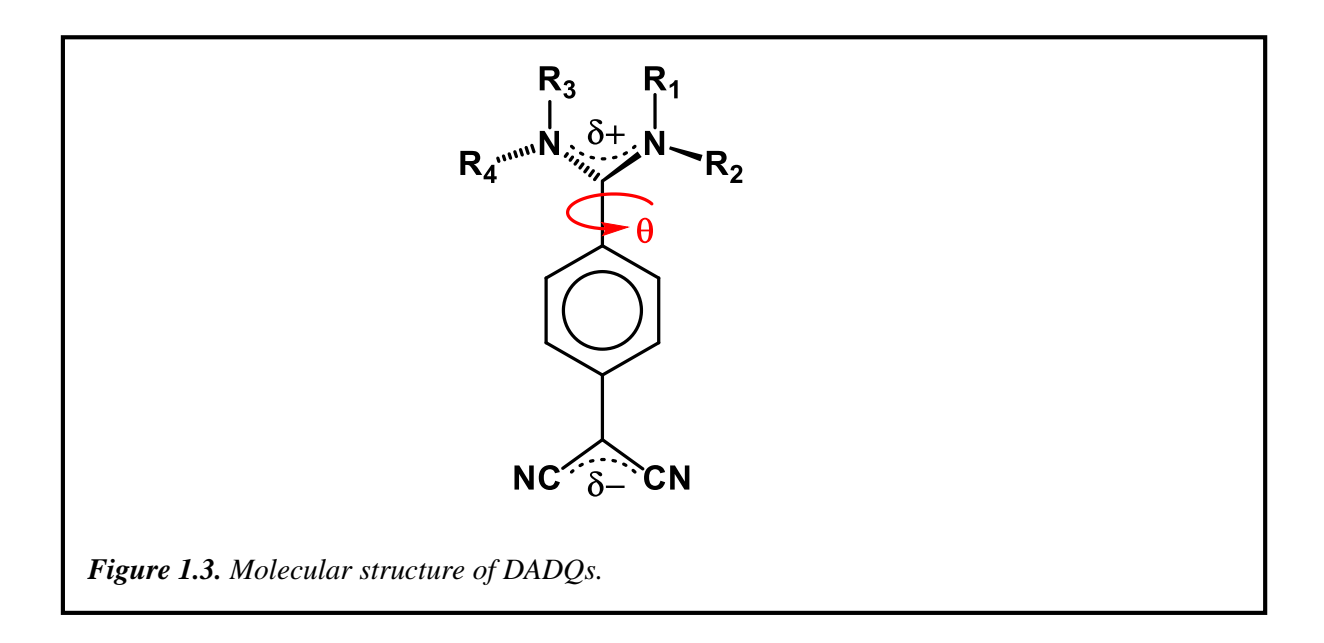
#### 1.1.2.5. **Superconductors**

Superconductivity is one of the fascinating properties of materials, in which electrical resistance disappears completely at low temperatures. The magnetic flux is expelled during

the transformation of the material into the superconducting state; this phenomenon is known as the Meissner effect. The superconductivity disappears when the temperature is raised above the critical value ( $T_c$ ) or the magnetic field, beyond the critical magnetic field ( $H_c$ ). Superconductivity was discovered by Kamerlingh Onnes in mercury in 1911 ( $T_c$ = 4.8 K).<sup>71</sup> Several alloys including Nb<sub>3</sub>Ge were shown to be superconducting with the highest  $T_c$  of 23.2 K. The discovery by Bednorz and Muller in 1986, led to oxide superconductors with  $T_c$  even above that of liquid  $N_2$  temperature. Organic molecular superconductors were discovered in 1980 by Bechgaard.<sup>72</sup> They were based on the TMTSF salts. BEDT-TTF salts were shown to have higher  $T_c$ .<sup>73</sup>

# 1.1.3. Diaminodicyanoquinodimethanes (DADQs)

DADQs are an important group of TCNQ derivatives, of central interest in this thesis work. The first synthesis of DADQs was reported by a du Pont group in 1962;<sup>74</sup> The synthesis is very simple and a wide range of derivatives, including primary and secondary, alkyl, alicyclic, and heterocyclic amines can be prepared, with appreciable yield. The uniqueness of DADQs arises from a number of molecular structural features, as well as the potential assembly patterns. DADQs with two amino groups and two cyano groups attached at either end of the p-quinodimethane moiety can possess formally quinonoid or benzenoid structures; experimental evidence for most DADQ derivatives indicate that the structure is largely benzenoid. The prominent negative solvatochromism of the optical absorption (blue shift with increasing solvent polarity)<sup>75</sup> indicates the strongly zwitterionic nature of the molecule in solution. Bond lengths in the benzenoid ring as well as the exocyclic part, observed in a large number of crystal structures support this picture in the solid-state. The dipole moment of a DADQ derivative determined through a charge density study of the crystal is > 40 D.<sup>76</sup> A consequence of the strongly zwitterionic ground-state structure is that the bond between the aromatic benzenoid ring and the diaminomethylene moiety is nearly single. This allows the steric repulsion between the *ortho* H atoms on the benzenoid ring and the substituents on the nitrogen atoms of the diaminomethylene group to be relieved through a dihedral twist  $(\theta)$  between the planes of the two moieties (Fig. 1.3). Depending on the substituents on the diaminomethylene groups, this twist angle could be as high as 50° or more.<sup>77,78</sup> This twisted molecular structure is a fundamentally important and characteristic signature of the DADQs.



The strong electrostatic interactions between the highly dipolar molecules lead to the unique thermal stability in DADQ based materials. The strongly dipolar structure together with the large dipole moment change  $(\Delta \mu)$  on electronic excitation can provide high hyperpolarizability (β) values in DADQs. Computational studies bear this out; they also reveal interesting correlations between the hyperpolarizability of DADQs and their structural features like the dihedral twist angle,  $\theta$ . In order to generate well-defined crystalline materials capable of SHG, chiral derivatives, 1 - 5 (Figure 1.4) were synthesized in our laboratory. The first case of SHG active DADQ crystals were reported from our laboratory;<sup>79</sup> the crystals belong to the noncentrosymmetric space group, P2<sub>1</sub>, and Kurtz-Perry measurements showed SHG ~ 3 U (1 U is the saturation value of the SHG from microcrystalline urea at larger particle sizes). Subsequently, we showed that crystals of 4 and 5 also have noncentrosymmetric structures and exhibit SHG; 5 shows the strongest response of ~ 27.5 U in this group.80

Some derivatives of DADQs, were found to show enhanced fluorescence emission in viscous media and aggregates structures.<sup>81</sup> A systematic study of a series of DADQs showed that remote functionalised systems can show significant fluorescence enhancement from the solution to the crystalline state and doped polymers. <sup>75,82</sup> The ease of synthetic tailorability of DADOs allows the preparation of different derivatives showing fluorescence emission that spans a wide range of colors.<sup>83</sup> Figure. 1.5 shows a typical collection of derivatives with emission colors ranging from red (6) to blue (8). Rigidification of the environment of the

$$H_3COH_2C$$
 $CH_2OCH_3$ 
 $NC^*\delta^+$ 
 $CN$ 
 $NC^*\delta^ CN$ 
 $NC^*\delta^ CN$ 
 $NC^*\delta^ CN$ 
 $NC^*\delta^ CN$ 
 $NC^*\delta^ CN$ 
 $NC^*\delta^ NC^*\delta^ NC^*\delta^-$ 

Figure 1.4. Molecular structure of various DADQ derivatives developed for SHG applications.

fluorophore and the consequent enhancement in the fluorescence emission intensity can also be realized by complexation with a polymer, as shown with 7,7-bis(piperazinium)-8,8dicyanoquinodimethane bis(p-toluene sulfonate) (BT<sub>2</sub>) and the sodium salt of poly(styrene sulfonate); this can also result in the formation of colloidal and nanocrystalline structures with strong fluorescence emission.<sup>84</sup> Fluorescence emission switching with enhancement accompanying amorphous to crystalline transformation of 7,7-(bis(2-(4-bromophenyl) ethylamino)-8,8-dicyanoquinodimethane (BBPEDQ) microparticles fixed in a thin film<sup>22</sup> and fluorescence tuning of 7-pyrrolidino-7-benzylamino-8,8-dicyanoquinodimethane (PBEDQ) nanoparticles with respect to their extent of crystallinity have been studied. 85 Phase change materials with fluorescence switching have also been developed with DADQs. Various DADO derivatives have been utilized in information storage applications,<sup>23</sup> chemical sensing, 86 construction of photo electrochemical electrode, 87 and organic resistive switching memory devices.<sup>88</sup> In this thesis, we have also demonstrated bioimaging<sup>89,90</sup> and actuator<sup>91</sup> applications. Basic concepts related to the areas in which this thesis work has focused are presented in the following sections.

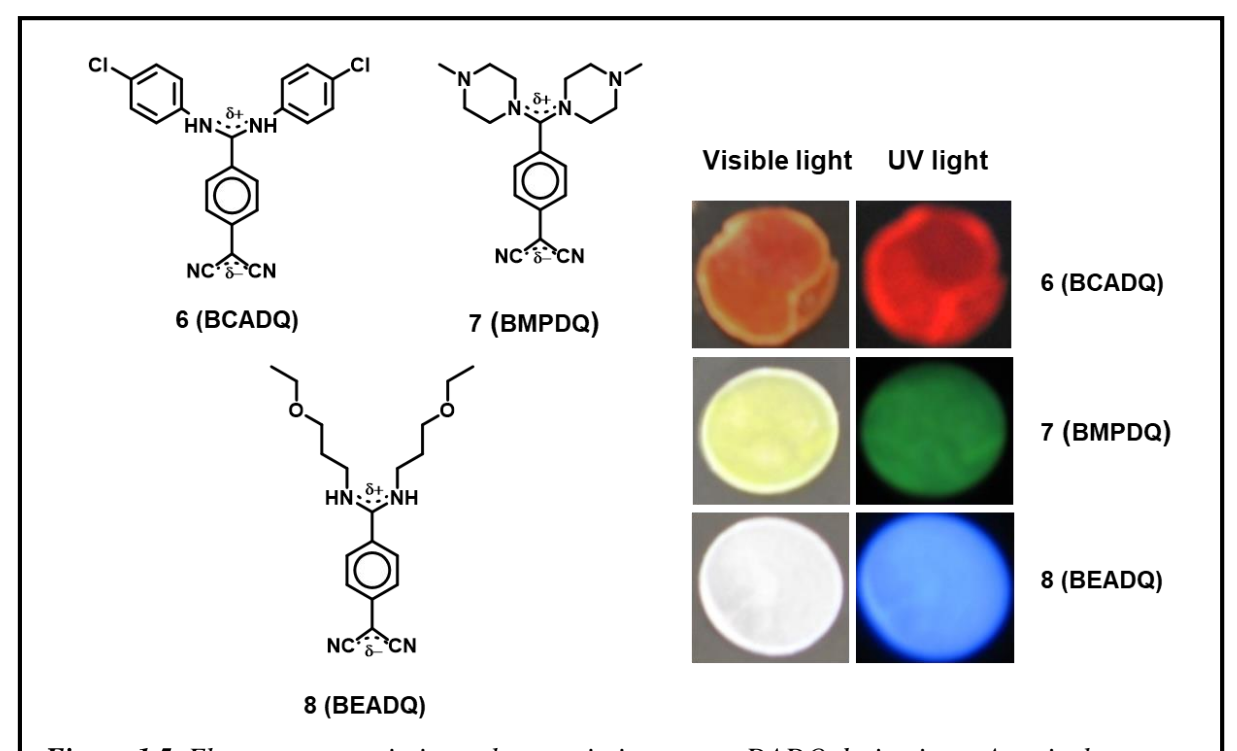


Figure 1.5. Fluorescence emission colour variation across DADQ derivatives. A typical selection of structures 6-8 are shown along with the photograph of red, green and blue emitting solid pellets.

#### 1.2. Fluorescent materials

#### 1.2.1. Fluorescence: A brief overview

Light emission from a material as a result of the absorption of light (usually of slightly higher energy) is called photoluminescence; when this occurs in a very short time scale, from an excited singlet state, it is known as fluorescence. The phenomenon was first observed by Herschel in 1845 in the quinine solution in presence of sunlight.<sup>92</sup> Through the absorption of radiation, molecules get electronically excited from their ground state to excited state, and they fall back into the ground state via radiative and nonradiative pathways. Radiative relaxation occurs through light emission. In non-radiative pathways, the excited state energy is channeled into molecular vibration, internal rotation etc; in some cases, photochemical processes are induced. Ground and excited states of the molecules and their various photophysical transitions are illustrated in the Jablonski diagram (Figure 1.6). Frank-Condon principle is used to determine the intensities of the vibronic transitions. Fluorescent molecules are utilized in various fields, including biomedical, biological, toxicological, and environmental studies. 93,94 Fluorescence intensity based sensing and imaging are discussed in Sec. 1.2.5.

The quantum yield and fluorescence lifetime are important photophysical properties of the fluorophores that play a significant role in their applications. Quantum yield or quantum efficiency is the ratio of the number of emitted photons to absorbed photons. The life span of the fluorescent molecules in the excited state is expressed in terms of the fluorescence lifetime; it is the time constant for the exponential decay of the fluorescence intensity. In organic fluorophores, the excited state lifetimes are in the range of picoseconds to nanoseconds. The fluorescence lifetime is independent of the static quenching, inner filter effects, fluorescence intensity, and concentration. Due to this uniqueness, the lifetime is utilized to characterize the fluorescence species in biophysical analysis. In the last few decades, several sensors and assays have been developed based on the fluorescence lifetime. Fluorescence Lifetime Imaging Microscopy (FLIM) introduced in the late 80's, provide images that map the excited state lifetime of the fluorophores rather than the fluorescence intensity, and are useful in imaging various biological specimens, such as tissue surfaces, cells, and even photodynamic processes. 16

#### 1.2.2. Fluorescence quenching

Fluorescence quenching refers to any process that diminishes the intensity of the light emission from the fluorophore. In solution state, the fluorescence of molecules can be quenched by different processes including nonradiative decay, molecular rearrangement, and static and dynamic quenching processes (Figure 1.7). In the static quenching process complexation of fluorophores with quenchers before excitation, leads to non-fluorescent

species; molecular oxygen, acrylamide, purine, pyrimidines, and halide ions can act as quenchers. 93,97 On the other hand, in the dynamic quenching process, the fluorescent molecules interact with quenchers in the excited state, leading to the relaxation of the fluorophore from the excited state to the ground state without light emission. Quenching is described by the Stern-Volmer equation (1.1).

$$\frac{F_0}{F} = 1 + K_D[Q] \tag{1.1}$$

where the  $F_o$  and F are the intensity of the fluorophore in the absence and presence of the quencher respectively. [Q] is the concentration of the quencher. K<sub>D</sub> is the Stern-Volmer quenching constant.

In the aggregated solid or crystalline materials, the role of intramolecular motion and molecular collisions in the fluorescence quenching are negligible. Therefore, in principle, they should exhibit enhanced fluorescence. However, most of the aggregates or crystals undergo fluorescence quenching; this arises due to various factors such as intermolecular energy transfer (Forster resonance energy transfer (FRET) and Dexter energy transfer) processes, excimer and exciplex generation of molecules, and intermolecular  $\pi$ - $\pi$  stacking and interactions. This phenomenon is sometimes described as 'aggregation caused quenching' (ACQ).98 FRET is the energy transfer process in which excited state of a fluorescent molecules (donor) transfers its energy to another (acceptor), through dipole-dipole interactions. Dexter energy transfer occurs through direct orbital overlap interactions between molecules, and hence across very short distances.

# 1.2.3. Enhanced fluorescence in the aggregated/solid-state

#### 1.2.3.1. **Molecular aggregation**

Molecular aggregation can be driven by various intermolecular interactions ranging from the weak van der Waals to strong electrostatic forces. Aggregation of chromophores can be broadly of two types, H and J.99 H-type aggregates are formed by stacking of the molecules in a parallel, face-to-face fashion; whereas J-type aggregates have a head-to-tail or tail-to-tail orientation (Figure 1.8). Aggregation of the type H and J can shift the electronic absorption of the molecules towards shorter (hypsochromic shift) and longer (bathochromic

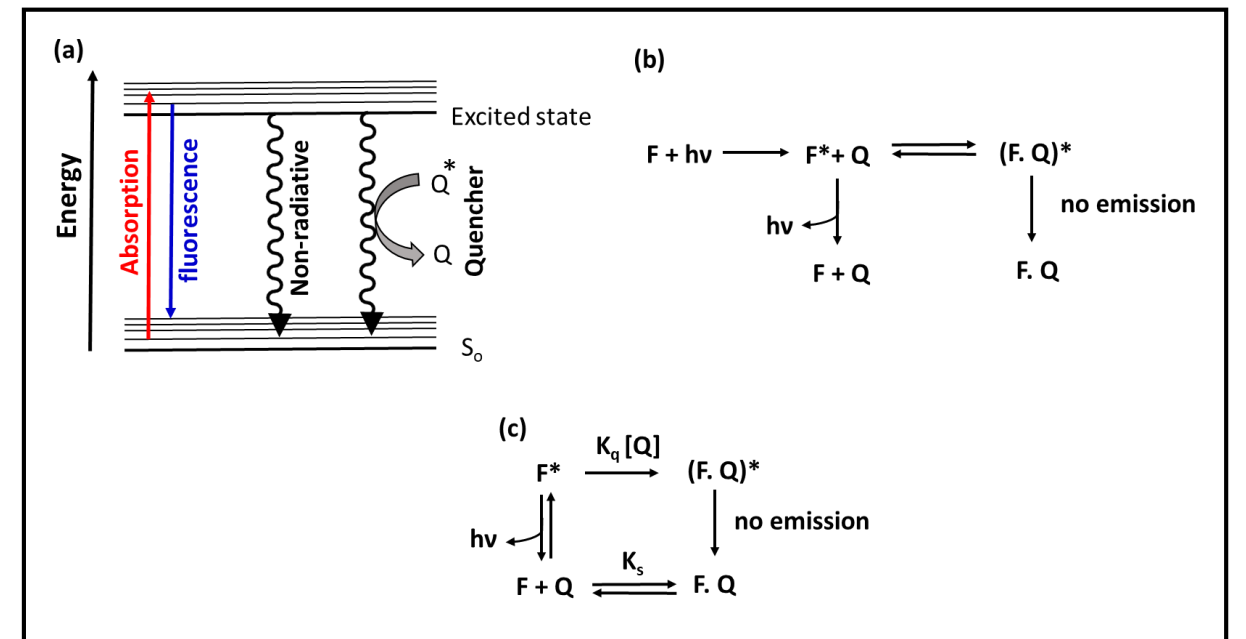
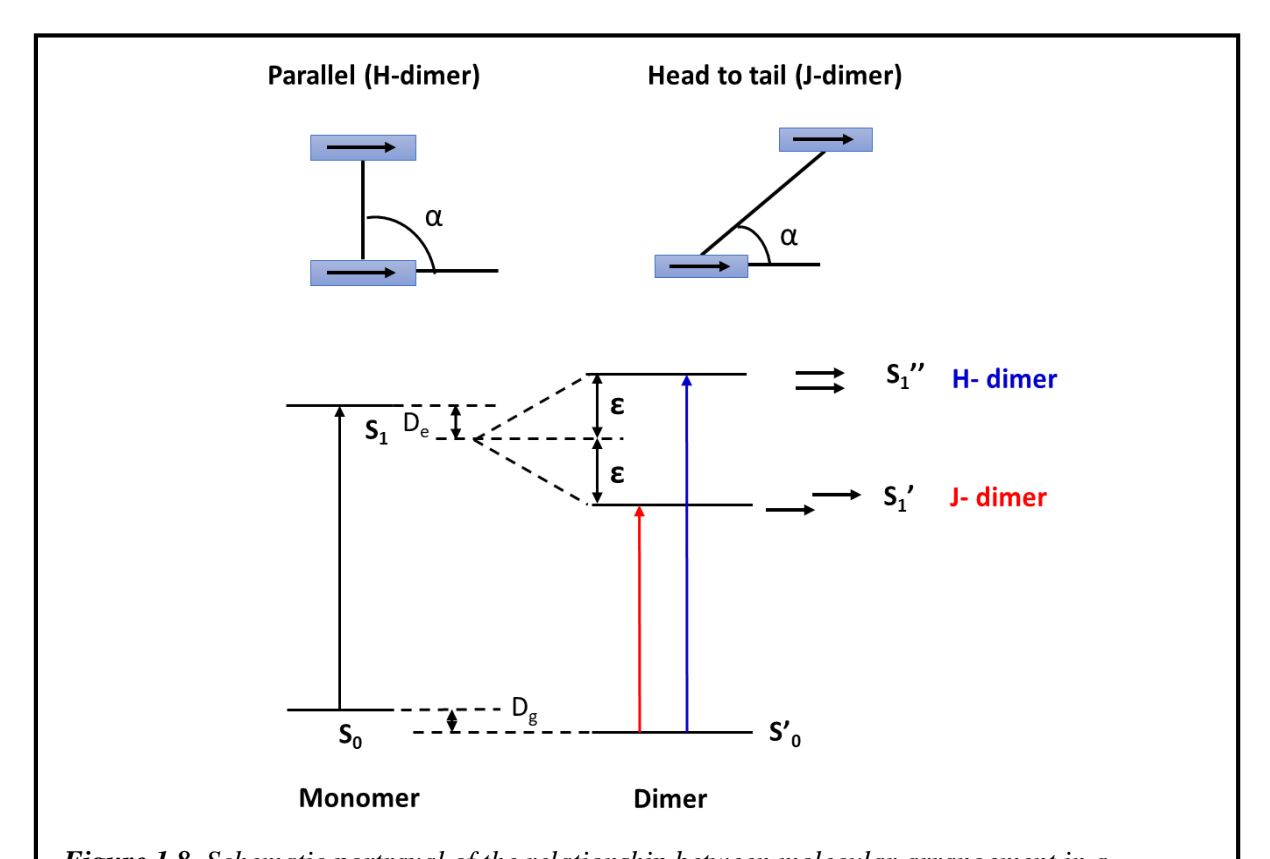


Figure 1.7. (a) Collisional quenching, (b) static quenching and (c) combination of collisional and static quenching.

shift) wavelengths, respectively. Molecular exciton coupling theory provides a mechanistic understanding of the spectral shifts<sup>100</sup> as schematically depicted in Figure 1.8. S<sub>0</sub> and S<sub>1</sub> are the energy levels of the isolated molecules. When molecules are close enough to each other, the transition dipoles interact, causing split of their singlet excited energy level into multiple states. The splitting depends on the distance and angle between the interacting transition dipole moments of the molecules and the number of molecules involved. For a simple dimer, transition energies are given by equation 1.2.

$$\Delta E_{dimer} = \Delta E_{monomer} + \Delta D \pm \varepsilon \tag{1.2}$$

where  $\Delta E$  is the transition energy of the monomer or dimer from the ground to excited state,  $\Delta D$  =  $D_g$  -  $D_e$  is the van der Waals dispersion energy difference and  $\epsilon$  is the interaction energy. J and H type aggregation impacts upon the fluorescence energy as well, due to the excitation energy changes. H aggregates generally exhibit frail fluorescence emission due to the existence of more nonradiative channels for dissipation of the excitation energy, whereas in the J aggregates, fluorescence intensities are generally enhanced.



# Figure 1.8. Schematic portrayal of the relationship between molecular arrangement in a chromophore dimer and spectral shift based on the molecular exciton theory.

#### 1.2.3.2. Fluorescence enhancement

Molecular aggregation mostly causes fluorescence quenching as discussed above. However, selected molecules were found to show enhanced emission in the solid-state. In the latter half of the last century, Oelkrug et al. reported the fluorescence enhancement of oligophenylenevinylenes in nanoparticle suspensions and thin films, due to the rigid environments present. 101,102 Tang et al. have reported enhanced fluorescence emission of 1methyl-1,2,3,4,5-pentaphenylsilole upon aggregation in ethanol-water mixture. <sup>103</sup> They have described the phenomenon as 'aggregation induced emission' (AIE). 104 Understanding the enhanced emission is essential for further development in terms of design and synthesis. In 2003, Chen et al. reported that intramolecular rotations of the fluorophores cause the fluorescence quenching through nonradiative channels in the solution state. 105 Such intramolecular fluorophore rotations are halted upon aggregation, which leads to the relaxation of excited molecules through radiative channels; the phenomenon is called 'restricted internal rotation' (RIR). Propeller shaped molecules like tetraphenylethylene show fluorescence enhancement consistent with the RIR mechanism. But fluorescence quenching

was not properly explained in some other molecules like 10,10',11,11'- tetrahydro-5,5'idibenzo[a,d] [7] annulenylidene (THBDBA) and 5,5'-bidibenzo[a,d] [7] annulenylidene (BDBA) using the RIR mechanism. <sup>106</sup> It clearly shows that other factors are also involved in the fluorescence quenching of the molecules in the solid-state.

Another relaxation pathway for the nonradiative decay is intramolecular vibrations of the fluorophore molecules. It has been reported that aggregation can hinder the vibrational motion of the molecules too and block the nonradiative decay channel; this is the 'restricted internal vibration' (RIV) mechanism. RIV and RIR mechanisms are together called 'restricted internal motion' (RIM) to explain the fluorescence enhancement. Even though RIM should apply to most fluorophores to some extent, many still show fluorescence quenching in the aggregated and solid-states. The critical role of intermolecular energy transfer pathways has been demonstrated through studies reported from our laboratory. 107 It is concluded that the concomitant impact of intermolecular and intermolecular effects lead to the fluorescence enhancement. Enhanced fluorescent emission can be quantified using the Fluorescent Efficiency Enhancement (FEE) factor that can be defined as the ratio of the quantum yield of fluorescence emission of the material in the aggregated or solid-state to that of the isolated or solution state (FEE=  $\varphi_{\text{solid}}/\varphi_{\text{solution}}$ ). Examples of the solid-state fluorescent materials are cruciform, 108 tetraphenylethylenes, 109 hexaphenylsilole, 110 diphenylbutadienes 111 and diaminodicyanoquinodimethanes (DADQs). 75,112 Various applications of the solid-state fluorescence materials are discussed in the following section.

## 1.2.4. Strongly fluorescent materials

Based on the structural features, examples of solid-state fluorescence materials can be classified into - (i) organic, (ii) organometallics, (iii) polymeric and (iv) supramolecular.

#### 1.2.4.1. **Organic molecules**

Many of the organic molecules that exhibit strong fluorescence in the solid-state are either hydrocarbons or heterocyclic based derivatives. Hydrocarbon systems are simple and can assist as basic models to reveal the relationship between structure and fluorescence enhancements. Tetraphenylethylene based supramolecular structures are highly useful in light-emitting devices due to their high fluorescence quantum yield, almost reaching unity in some cases. 113 However, hydrocarbon-based materials often emit blue or green colour, which limits their high-tech applications. In order to overcome this problem, a new class of molecules has been developed, which contains heteroatoms with a broad range of emissions. Cyclic siloles are the first molecules reported in this group, and extensively studied for their electronic properties and structural tailorability. Silole based semiconductors such as spirosilole, tetraarylsilole, and fused silole have been applied in the optoelectronic display devices.<sup>114</sup> A large number of materials containing cyano groups have been developed for optical applications. Detailed explorations of the fluorescence enhancement of DADQs in different states, including crystals,<sup>75</sup> nanocrystals,<sup>115</sup> ultra-thin films,<sup>116</sup> and amorphous particles<sup>22</sup> have been reported from our laboratory; the potential utility of DADQs as sensors for NH<sub>3</sub> was reported recently. 86 In this thesis, the application of DADQs in bioimaging and actuators is explored.89-91

#### 1.2.4.2. Organometallic molecules

Organometallic luminogens are specially known for the emission of light from the triplet energy excited state. Phosphorescent materials are also potential candidates in various applications. [Au<sub>3</sub>(CH<sub>3</sub>N=COCH<sub>3</sub>)<sub>3</sub>] is one of the first organometallic complexes of Au, reported with enhanced phosphorescence in the aggregated state. Solid-state phosphorescence emission of different transition metal complexes (of Ir, Pt, Zn, Cu and Pd) have been studied. 118 Various iridium complexes such as [Ir(ppy)<sub>2</sub>(m-Cl)]<sub>2</sub> and [Ir(F<sub>2</sub>ppy)<sub>2</sub>(m-Cl)<sub>2</sub>] have been developed for mitochondrial tracking and MTT assay. 119 Ruthenium based rRNA imaging probe has been employed in the selective imaging of the nucleus in the HeLa cells. 120 Another fascinating property of the organometallic materials is the tunability of the emissive light by changing the counter anions.

#### 1.2.4.3. Metal nanoclusters

The physical and chemical properties of metal nanoclusters (NCs) depend on their size, shape, and composition. Metal nanoclusters are highly useful in various applications, including bioimaging, photosensitizers, optical sensors, and light-emitting devices due to their unique optical properties, such as large Stokes shift, large two-photon absorption crosssection, excellent biocompatibility, and photostability. Fluorescent metal NCs are synthesized using two main strategies. (i) Template assisted fabrication, where

#### 1.2.4.4. Other systems

A wide range of conjugated polymers have been developed with strong fluorescence emission in the aggregated state in thin films. Trimethylamine and tetraphenyl butadiene based polymers have been employed in tumor cell imaging and the detection of nitroaromatic explosives, respectively. <sup>127,128</sup> Electro-luminescent thin films of poly (phenylene vinylene) (PPV) and its derivatives are employed in light emitting devices as emissive layers. <sup>67</sup> Another interesting class of materials is chromophore conjugated metal nanoparticles (MNPs). The fluorescence emission enhancement of MNPs upon aggregation is due to the plasmon coupling. Applications of MNPs have been shown in various domains, including sensors and biomedical fields. <sup>129</sup>

#### 1.2.5. Applications

Solid-state fluorescent materials find extensive applications in various fields including sensors, optoelectronics, and bioimaging.

#### (a) Sensors

The sensitive changes in the fluorescence response of materials upon external stimuli make them potential candidates for various sensor applications. Based on the nature of the analytes, sensors can be broadly divided into two types. (i) biosensors (for proteins, amino acids, glucose and intercellular pH) and (ii) chemical sensors (for explosives, ions, gases, hazardous species etc.). Tunable emissive properties of a material as a function of pH make them useful in pH sensors. (4,4'-(hydrazine-1,2-diylidene *bis*(methanylylidene)) *bis*(3-hydroxybenzoic acid) (HDBB) is a well-known example; it emits orange fluorescence at low

pH (<4); increasing pH changes it gradually to green. When HDBB is treated with a mixture of cancer and normal cells, the acidic lysosomes of the former are stained causing emission of a distinct fluorescence; the normal cells do not show this response, illustrating the potential application of HDBB in the diagnosis of cancer cells. 130 Tetraphenylethylene derivatives have been applied to track the folding and unfolding state of the BSA proteins as a selective bio-probe. 131 Selective sensing of HF<sub>2</sub>- anion, Al<sup>3+</sup>cation, and nitro explosives have been reported using hydrazide based probes. 132

### (b) Optoelectronics

Solid-state fluorescent materials are ideal candidates for optoelectronic devices such as light-emitting diodes (OLEDs), 133 electro-fluorochromic devices, 134 circularly polarised luminescence systems, <sup>135</sup> and luminescent solar concentrators. <sup>136</sup> Appreciable quantum yield in the thin film (solid) state and excellent thermal properties of the fluorophores make them ideal for constructing OLEDs. Silole, tetraphenylethylene (TPE), tetraphenylpyrazine, and their derivatives are classic examples utilized in the OLEDs as the emitting layer. Adduct of carbazole with multiple TPE units exhibits the highest solid-state fluorescence quantum yield ( $\varphi \sim 100\%$ ). Using the TPE as building blocks, a significant number of blue-emitting OLEDs have been fabricated. 138 Hole or electron-transporting properties as well as bipolar carrier mobility along with enhanced fluorescence emission make them very useful in the fabrication of OLEDs, with performances comparable to those of multilayer devices with additional hole/electron transport layer.

Circularly Polarised Luminescence (CPL) is one of the fascinating properties of chiral materials; it involves differential emission intensities with right and left circularly polarized light, utilizing the excited state features of chiral molecules. It has been employed in various areas, including optoelectronics, display and information storage. 139-141 Luminescence dissymmetry factor ( $g_{em}$ ) and luminescence efficiency ( $\varphi_f$ ) are the parameters that denote the efficiency of the CPL devices. Adduct of two chiral sugar moieties with silole core is a classic example of a CPL material; the g<sub>em</sub> value in the aggregated state (~ 0.32) is higher by many order of magnitude than in the solution state ( $\sim 10^{-5}$  to  $10^{-2}$ ). <sup>142</sup>

#### (c) Bioprobes

Solid-state fluorescence materials with considerable photobleaching resistance, high emission efficiency, and biocompatibility are used as bio-probes to monitor biological processes and to image various cells. Bio-probes must possess suitable functional groups like -COOH, -NH<sub>2</sub>, -OH, -SO<sub>3</sub>H, etc. for efficient interactions with the chemical components of the biological specimen. Materials with near-infrared (NIR) emission are particularly useful for *in vivo* imaging because of the deep tissue penetration ability of NIR. 6,7-diphenyl-[1,2,5]thiadiazolo[3,4-g]quinoxaline derivatives with emission in the range of 800-1200 nm have been applied in the *in vivo* imaging of H22 tumor bearing mouse. Materials with large two-photon absorption cross-sections like triphenylamine derivatives have been employed in cancer cell imaging. Moreover, solid-state fluorescence materials have great potential for imaging-guided photodynamic therapy. Materials

# 1.3. Fluorescence probes

Fluorescence probes are fluorescent materials with suitable functional groups that interact chemically with the analyte samples (often biological specimens) to envision their morphology or functions without any significant physical interference. <sup>146</sup> They are employed in various applications including biosensing, bioimaging, and theranostics. The essential parameters for an ideal fluorescence probe include large absorption coefficient, fluorescence lifetime, and quantum yield as well as large Stokes shift, absence of cytotoxicity and stability to light, heat, and different pH. Probe molecules exhibiting enhanced fluorescence emission in their aggregated state, are of great interest in bioimaging applications. Recent developments, such as two-photon and super-resolution fluorescence microscopy, energy transfer microscopy, fluorescence resonance (FRET) and fluorescence recovery/redistribution after photobleaching (FRAP), make bioimaging more effective and efficient. Through these techniques, a broad range of parameters can be determined, such as cell counts, distribution of the fluorophores within cells or cellular components, rate of protein synthesis and gene expressions, amount and sequence of RNA, DNA, etc. and cell viability. Bioimaging can be carried out in two ways, in vitro and in vivo. In vitro imaging is a non-invasive approach, wherein the isolated part of the organism is treated with fluorophores outside their natural biological surroundings. In in vivo imaging, part of the organism is treated with fluorophores with or within the organism. Fluorescence probes with

suitable functional groups have been reported for selective imaging of various biological species, including viruses, bacteria, fungi, cancer cells, plant parts and animal models like mice.

#### **1.3.1.** Types of fluorescence probes

#### 1.3.1.1. **Small molecule-based fluorophores**

Most of the fluorescence probes are based on small organic molecules composed of a few tens of atoms. Structural tailorability that rationally tunes the chemical and photophysical properties of the fluorophores makes them potential candidates for imaging and sensing applications in multidisciplinary areas such as molecular biology, biochemistry, and material science. Small fluorescent molecules have greater accessibility to targets, and pose limited interference in the local functions of the target. Quinoline, coumarin, xanthone, napthalimide, fluorescein, rhodamine, BODIPY and cyanine derivatives are classic examples of small molecules based fluorophores. 147-150 Recently, several two-photon absorption, nearinfrared I (700-900 nm) and near-infrared II (1000-1700 nm) fluorophores have been employed for bioimaging. 151,152

#### 1.3.1.2. **Quantum dots**

Semiconductor nanocrystals, also called quantum dots, are employed for bioimaging applications because of their high quantum yield, long fluorescence lifetime, size-tunable light emission and negligible photobleaching. However, the toxicity of the QDs limits their applications. Various features of the QDs, such as their elemental composition and size, coating ligands, charge, oxidative ability, and mechanical stability can lead to cytotoxic effects. 153 Another critical factor that causes cytotoxicity is the leaching of the heavy metal from the core of QDs through oxidation and photolysis processes. Aqueous stability is another setback of these systems in biological research. Major types of QDs are based on the combination of elements (several being toxic) from different groups in the periodic table, such as the II-VI (CdTe, CdSe, CdS), III-V (InP, InAs), I-III-VI<sub>2</sub> (CuInS<sub>2</sub>,AgInS<sub>2</sub>), and IV-VI (PbSe, PbS) systems. Low cytotoxicity ones like silicon QDs and conjugated polymer dots have been developed and successfully employed in biological applications. 154

#### **1.3.1.3.** Biological fluorophores

Biological fluorophores are simply proteins with auto fluorescence used as biomarkers to track various physiological activities, identify protein localization, and assess transgenic expression. These systems are gaining greater attention in biological research due to their appreciable quantum yield, high selectivity, and negligible toxic effects. Fluorescence of proteins arises from their amino acids, particularly phenylalanine (Phe), tyrosine (Tyr), tryptophan (Trp), and their specific conformational arrangements. Green fluorescent protein (GFP) is the first fluorescent protein isolated from the jellyfish Aequorea Victoria, and it consists of 238 amino acid residues that emit green light. Blue (BFP), yellow (YFP), cyan (CFP), and red (RFP) fluorescent proteins are the mutation forms of the GFP, used to express in cells, tissues, and various organisms. Green fluorescent proteins and their derivatives like phycoerythrocyanin, phycobilproteins, allophococyanin, phycoerythrin etc. are the common fluorophores used in bioimaging applications. High cost, light and heatsensitivity, possibility to interfere with the biological function of the target, time-consuming staining protocols etc. are significant drawbacks of these probes.

# 1.3.2. Labeling approach

Fluorescence labeling or staining is the process of docking between the fluorophores and biomolecules. For efficient fluorescence imaging, a suitable labeling technique has to be adopted based on the nature of the target and the fluorophores. Among the various imaging methods, fluorescence labeling is attractive and useful as it is easy to perform, highly sensitive and non-destructive. Various fluorescence labeling techniques are briefly outlined below.

#### 1.3.2.1. Chemical labeling

Amino, thiol, azide, and tetrazine labeling are the most commonly followed chemical labeling methods in the fluorescence imaging process. Fluorophores with suitable functional groups that can easily dock with these functionalities of the target biomolecules through covalent and noncovalent binding are ideal choices for the labeling techniques. Chemical labeling has numerous benefits over the other techniques, such as ease of handling, low cost, and availability of a wide range of functionalities. Chemical labeling is more appropriate for

in vitro than in vivo imaging studies. Amino labeling is probably the most popular, due to the common existence of NH<sub>2</sub> functionalities in the bio species.<sup>157</sup> Amino labeling is carried out mostly through acetylation and alkylation reactions<sup>158</sup> (Figure 1.9) and often employed to sense proteins. Azide<sup>159</sup> and tetrazine<sup>160</sup> groups do not exist directly in the proteins. Initially, azide groups are incorporated into the biomolecules and then labeled using appropriate fluorescence probes.

#### 1.3.2.2. **Enzymatic labeling**

Enzymatic labeling is a fast and highly sensitive technique. Two different enzymatic types of labeling are known. In the first type, enzymes (transglutaminase, sortase) act as catalysts in the labeling of the target molecules using a chemical probe (fluorophores). <sup>161</sup> In the second case, the enzymes (cutinase and intein) employed undergo self-modifications before labeling of target molecules. 162 Mechanistically, the enzyme is initially coupled with the target and then binds with the chemical probes (fluorophores). The advantages of these techniques include high target selectivity and better penetration across the cell membrane. Larger size and possible interference in the natural functions of the target molecules make enzyme labeling less desirable.

#### 1.3.2.3. Tag labeling

Tag labeling is the most powerful and attractive technique for protein labeling due to its simple protocol, site-specificity, improved selectivity and high efficiency. Protein or peptide staining can be accomplished without disruption to its folding and functions by adding a small fluorescent tag. This technique involves transition metal linkage with specific residues in a fluorescent tag. Tetracysteine/biarsenical, 163 histidine, 164 and FLAG165 are commonly used tags for protein labeling.

#### 1.3.3. Bioimaging

#### 1.3.3.1. **Plant cells**

There is a necessity to understand the complex interactions of plants with the environment at the molecular, cellular, and organismal levels. Fluorescence-based cell imaging is one of the best techniques that helps to study their structure, dynamics, and

functions under different conditions. The autofluorescence emission from the cells and their background is a major concern for efficient fluorescence based bioimaging. Imaging of the plant cells and their organelle like mitochondria, lysosome, nuclei, membranes, cell walls, etc. using small fluorescent molecules is discussed here.

## (a) Mitochondria

Mitochondria, also known as the powerhouse of the cell, generates energy through the production of ATP from sugar molecules in the eukaryotic cell. The functions of mitochondria includes cellular signaling, reactive oxygen species (ROS) and ketone bodies generation, Ca<sup>2+</sup> buffering, and hormone synthesis. 166 Dynamics and viability of mitochondria has been determined by tracking its membrane potential using cationic fluorescent labels like tetramethylrhodamine methyl (or ethyl) ester, rhodamine 123, and carbocyanine iodide derivatives. 167 Commercial mitochondrial trackers like mitotracker

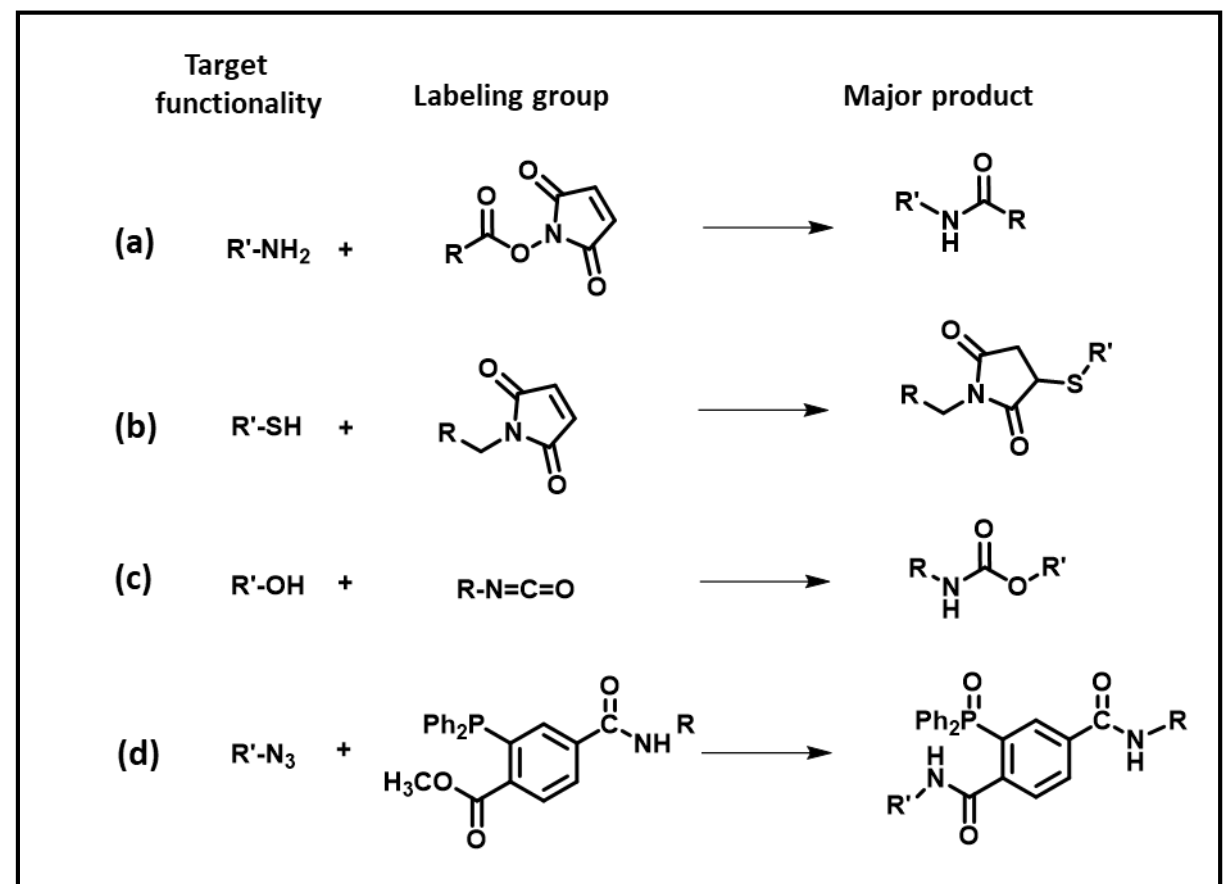


Figure 1.9. Schematic illustration of chemical labeling of target functialities, (a) amine, (b) hydroxy, (c) thiol and (d) azide.

green, orange, and deep red, stain the mitochondria by binding with thiol groups of the mitochondria. 168 Recently developed naphthalimide and BODIPY derivatives have been applied to monitor the morphological changes in different conditions. 169 However, most of these commercial dyes exhibit weak fluorescence emission in the solid or aggregate state. Recently, new solid-state emissive tetraphenylethylene derivatives have been exploited for efficient mitochondrial imaging. 170,171

## (b) Nucleus

Nucleus is a membrane organelle composed of phospholipid bilayer, nucleoplasm, nucleolus, and chromatin. Controlling and copying genetic information at the time of cell division is the primary function of the nucleus. The traditional nucleic acid stains such as 4,6-diamidino-2-phenylindole (DAPI), and propidium iodide (PI) are used to visualize the nucleus. 172 Based on the ability of the fluorophores to cross the membranes, nucleus stains are classified into (i) cell-permeant and (ii) cell impermeant stains. By crossing the phospholipid bilayer, cell-permeant dyes stain both live and dead cells; Hoechst and SYTO stains are such commercial stains. 173 On the other hand, cell impermeant dyes such as DAPI, PI, TO-PRO3, and SYTOX (Figure 1.10) have been applied in the cell viability assay as it stains only dead cells.<sup>174</sup> Several amino-modified derivatives of tetraphenylethylene have recently been shown to image the nucleus.<sup>175</sup>

## (c) Cell wall and membrane

The structural complexity of the cell wall is raised by interlinking between various polysaccharides such as cellulose, hemicellulose, lignin, and pectin. Versatile fluorescent probes, such as calcofluor white, congo red, aniline blue, and ruthenium red have been employed to image plant cell walls and their complex structure. <sup>176</sup> In general, the cell wall selective fluorophores are not specific to one particular polysaccharide of the cell wall. Due to their non-selectivity, revealing the distribution of the polysaccharides across the cell wall is difficult. In recent times, the development of highly selective fluorescence probes for the individual polysaccharides of the cell wall is gaining interest. Pontamine fast scarlet 4B has been reported as a specific fluorophore for cellulose in the higher cell wall. 177 COS 488 and PI fluorescent dyes have been shown to label pectin selectively. 178

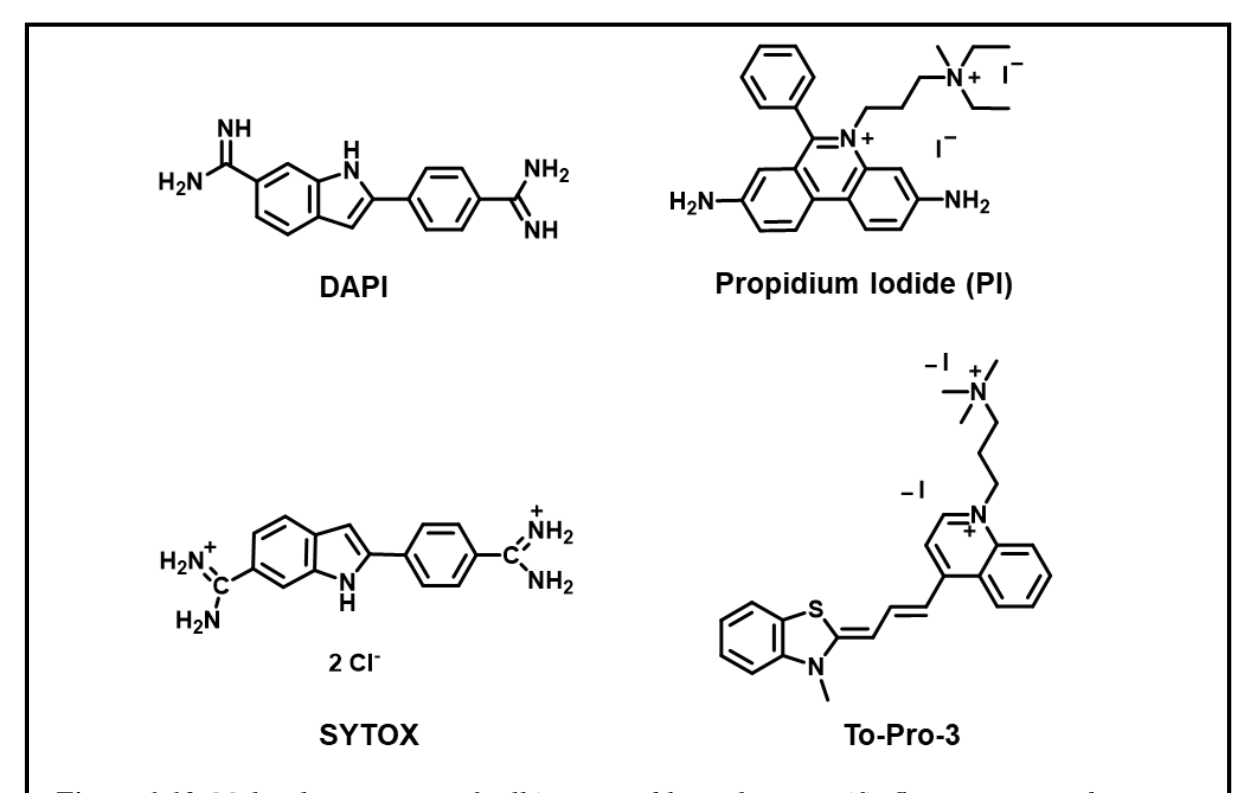


Figure 1.10. Molecular structure of cell impermeable nucleus-specific fluorescence probes.

Plasma membrane of the cell consists of a phospholipid bilayer that regulates the transport of the materials into and out of the cell. Several dyes have been developed to investigate the morphology, function, and dynamics of the cell membrane. Existing fluorescence probes for membrane imaging include, anilinonapthalenesulfonates, anthroyloxystearates, diphenylhexatrienepropionate, and 6-lauryl-2-dimethylamino naphthalene. 179 New solid-state fluorescent naphthalimide derivatives have been reported for cell membrane tracking. 180

## (d) Stomatal cells

Stomata are modified special cell structures in plant leaves that consist of a pair of bean-shaped guard cells. Key functions of the guard cells are controlling the gaseous exchange and water loss in the photosynthesis and transpiration process, respectively. Like normal cells, guard cells also have various organelles such as microtubules, endoplasmic reticulum, lysosomes, nuclei and mitochondria. Influence of several factors such as light, humidity, temperature, CO<sub>2</sub>, K<sup>+</sup> ions, and hormones, on the dynamics and functions of the guard cells and their organelle are critical. 181 Fluorescence based bioimaging is one of the

best techniques for these studies, as it is non-destructive, easy to use, and sensitive. Propidium iodide, safranin, aniline blue, calcofluor white, acridine orange, etc. (Figure 1.11) are the popular choices for imaging the guard cells and their organelles. 182-187 We have developed DADQ based fluorescence probes for the selective imaging of the cell wall of the guard cells and epidermis layer, and analysed the interactions between the fluorescence probes and the biological components as discussed in Chapter 2.

#### 1.3.3.2. Microorganisms

Detection and visualization of microorganisms and their functions, using fluorescence probes have found extensive utility in several fields like antibiotics development, agriculture, food science and industry. Microorganisms are classified into several classes - bacteria, viruses, fungi, algae, archaea, protozoa, and multicellular animal parasites. Among them, bacteria and fungi have a significant role in the nutrient recycle and decay of organic bodies. A brief discussion of the fluorescence imaging of microorganisms is presented here.

## (a) Fungi

Fungi are a type of eukaryotes that play an important role in the economy and ecology of the world. Some of them can be directly utilized as food. However, in several cases, fungal infection is a potential threat to the medical and food industry, and hence the need to develop effective techniques for detecting them. Small molecule fluorescence probes for fungi, include fluorescein diacetate, 5-chloromethyl fluorescein diacetate, carboxyfluorescein diacetate, and calcofluor white. They droxy-9H-(1,3-dichloro-9,9-dimethylacridin-2-one) and triphenylamine derivatives with solid-state fluorescence emission have been applied in the visualization of fungi. 189, 190

## (b) Bacterial cells

Bacteria, the single-cell microorganisms without nucleus, play a central role in the ecosystem balancing. Bacterial infections and their antibody resistivity are posing great challenges in the medical field. Gram staining is a well-known technique for bacterial imaging; drawbacks of the protocol include, the lengthy steps involved, potential cell damage, absence of fluorescence, and various side effects. Imaging the bacterial cells using fluorescence probes is of great importance for understanding the heterogeneity of their morphology and functions, including infections, resistance, and viability under different conditions. Commercial fluorophores such as SYTO 9 and PI are used in bacterial cell viability assay. Different classes of solid-state emissive fluorophores such as tetraphenylethylene derivatives, is nanoparticles conjugated with *N,N*-dimethyl-*N*-octadecylbetaine derivatives, is nanoparticles conjugated with *N,N*-dimethyl-*N*-octadecylbetaine derivatives, is nanoparticles derivative (PPV-NMe<sub>3</sub><sup>+</sup>) and cationic conjugated polymers such as poly(phenylene vinylene) derivative (PPV-NMe<sub>3</sub><sup>+</sup>) have been developed for the selective imaging of bacterial cells.

## (c) Bacterial spores

Spores are non-reproductive structures which are produced from the bacterial cells under unfavorable or starvation conditions. Spores are broadly classified into two types, (i) exospores and (ii) endospores. Endospores form within the bacterial cell and are released in the cell division, while exospores form outside the fungi, algae, and bacterial cells and are released as buds. Spores are the dormant form of bacterial cells that can survive under

debilitating conditions like dehydration, radiation, chemicals, and heat, due to their robust protective coating.

Spores are a potential threat to the food, health and medicine industry; therefore there is an urgent need to develop efficient methods and probes for their detection. Traditional imaging methods like Gram-stain, Ziehl-Neelsen, Dorner, and Schaeffer-Fulton are not efficient due to the lengthy protocols, extended heating required in many cases and the involvement of acids or acidified alcohol used for decolorisation. 196,197 Commercial dyes for spores imaging such as acridine orange, DAPI, Hoechst 34580 and SYTO 9 have crucial limitations; DAPI is useful only for imaging dead endospores as it is not cell-permeable and, the others ineffective in differentiating endospores from bacteria, as they stain both. 198-200 To overcome these limitations, we have developed a DADQ derivative with appropriate functional groups for selective imaging of bacterial spores; the results are presented in Chapter 3.

#### 1.4. **Actuators and micromachines**

Actuators are devices that induce controlled mechanical motions in response to various stimuli such as light, heat, electric and magnetic field, electron beams, humidity, chemical energy etc. In the case of molecular and macromolecular actuators, the mechanical motion is stimulated at the micro or nanoscopic level. Micromotors or micromachines (engines) are also of interest in terms of controlled mechanical motion; they find applications in areas such as biomedical, drug delivery, biosensors, environmental, and microsurgery. Several well-known motility mechanisms like photothermal, photo-isomerization, osmotic propulsion, self-diffusiophoresis and bubble propulsion are involved in the movement of the particles. Various self-propelled micromotors have been developed, with their autonomous propulsion powered by surface tension gradients bubble propulsion in a chemical reaction, self-electrodiffusiophoresis or self-diffusiophoresis. In 2004, Paxton et al. demonstrated the autonomous (self-diffusiophoresis) movement of synthetic Pt/Au micro-rods in an aqueous solution of hydrogen peroxide.<sup>201</sup> Electrically<sup>202</sup> and magnetically<sup>203</sup> driven micromotors were also developed and utilized in various applications. Photocatalytic (TiO2) or photothermally active (Pt, Au, and C) materials based micromotors have been developed, and their light-induced mechanical motion studied.<sup>34</sup> In 2012, an ultrasound energy-driven

AuRu micro rod was reported. 204 Paxton et al. have discussed the various designs of micro and nanoscale objects and their locomotions powered by chemical and light energy.<sup>205</sup>

## 1.4.1. Fabrication

The specific fabrication technique used is a key factor that determines the performance of actuators and micromachines. The objective of the fabrication is to develop suitable systems for a desired application in a simple and efficient way. Various techniques, including electrochemical deposition, lithography, sputtering, physical vapour deposition, strain engineering and materials self-assembly are used to fabricate different types of nanowires, thin films etc. of interest in actuators and micromachines.

#### 1.4.1.1. **Electrochemical deposition**

Electric current is used to deposit materials of interest ranging from different metals to polymers. Membranes with different pore sizes were employed as the template to fabricate rod, wire, and tube-shaped nano/micro actuators and micromachines composed of metal, polymers, and semiconductors. Membranes are ideal templates to fabricate similar nanostructures due to the monodisperse diameters and the large density of pores. Alumina and etched polycarbonate membranes are prime examples of the commonly used membranes for fabricating nanostructures. The nanostructures formed depend on the nature of the pore walls of the membranes and the deposited materials. 2 µm long Au-Pt nanowires have been fabricated electrochemically using anopore alumina membrane, and their autonomous motion studied in 2-3% hydrogen peroxide.<sup>201</sup> Apart from porous membranes, several specially designed templates such as etched silver wire<sup>206</sup> and DC<sub>8</sub>, <sub>9</sub>PC liquid tubules<sup>207</sup> have been employed in the fabrication of nanostructures.

#### 1.4.1.2. Physical vapour deposition

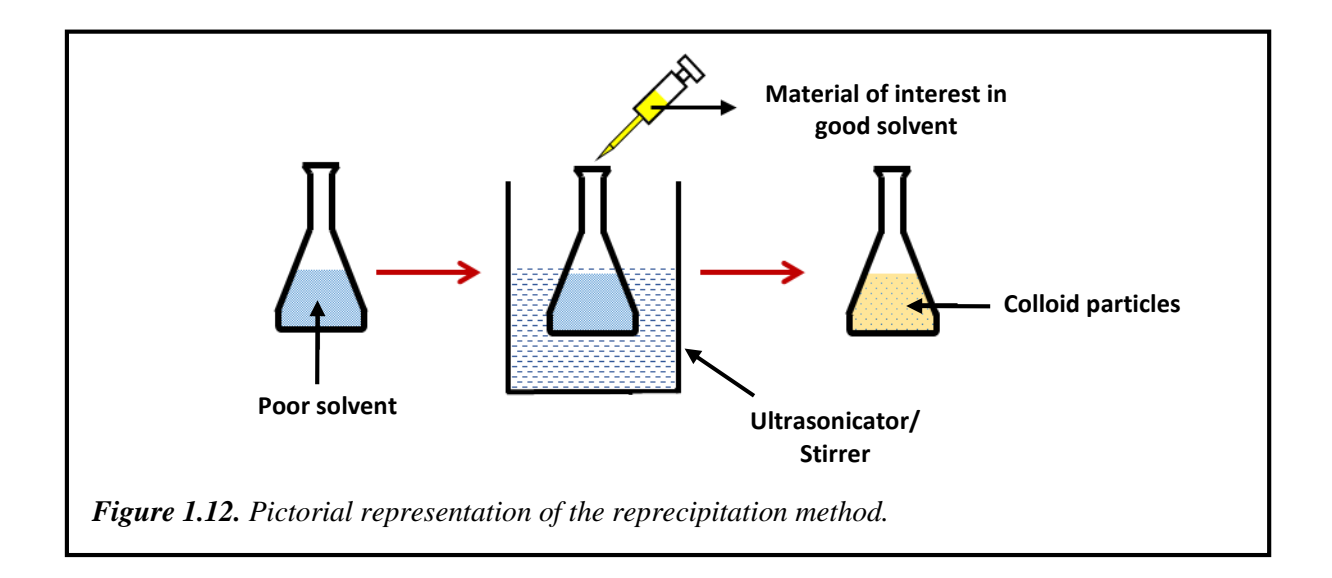
Physical vapour deposition (PVD) is a thin-film coating technique wherein the vapourised materials of interest are condensed on the substrate as a thin-film. The most popular PVD techniques include electron beam evaporation and sputtering. Electron beam evaporation is a technique that creates vapours of the material by exposure to an electron beam, whereas sputtering relies on the gaseous plasma and accelerated ions, mostly argon, to vapourise the material into gaseous state. PVD is an effective technique for incorporating magnetic and photocatalytic materials at appropriate regions of the nanostructures. It is the widely used fabrication technique to break the symmetry of the nanostructures by covering one side alone, leading to the formation of Janus particles, 208,209 of great interest in locomotion.

#### 1.4.1.3. **Self-assembly**

Spontaneous organization of building blocks into ordered structures or patterns is known as self-assembly. Building blocks may be atoms, molecules, or nanostructures of various material compositions. Building blocks are assembled through weak or noncovalent interactions (and in some cases covalent bonds), forming monolayers that are useful to develop micromotors or micromachines. The self-assembled structures can be divided into different types, (i) self-assembled monolayers (SAMs) (ii) layer-by-layer assembled films and (iii) encapsulation/incorporation of micro or nanoparticles. SAMs are formed by the assembly of functionalized long chain molecules on suitable substrate surface; the most popular example is that of n-alkyl thiols on Au (III) surfaces. Alternate deposition of oppositely charged monolayers forms a multilayer structure in the layer-by-layer assembly technique.<sup>210</sup> In vet another approach, fabrication of three dimensional structures of micro/nanoparticles or nanocomposites with suitable properties for specific applications is achieved through self-assembly of materials via encapsulation or incorporation process.<sup>211</sup> Dong et al. have fabricated nanoparticles of gold, iron oxide, and platinum incorporated into a single polymer crystal, and investigated their autonomous motion.<sup>212</sup>

#### 1.4.1.4. Reprecipitation technique

Reprecipitation method was developed by Nakanishi et al. in the past decade. 213,214 It is a simple and convenient technique for the synthesis of nano/microstructures. Reprecipitation is a solvent exchange process in which a homogeneous solution of the material of interest is treated with a poor solvent with or without external stimuli, leading to precipitation (Figure 1.12). The size and morphology of the nanostructures are controlled by various experimental conditions such as temperature, the solvent combination, concentration of the materials, size of the container, and aging period of the colloids. In certain cases, the nanostructures can be affected by external forces such as the stirring speed and ultrasonic



frequency. The crystallization process in the reprecipitation method involves four stages. <sup>215</sup> (i) addition of homogenous solution of material into a stirred poor solvent allows formation of liquid droplets; (ii) entry of the poor solvent into the liquid droplets, which changes the microenvironment of the molecules, and cluster formation; (iii) nucleation due to thermal collision of these clusters; and (iv) crystal growth. Kastrup et al. have developed porous CaCO<sub>3</sub> micromotors using a controlled precipitation method and studied their medical applications. <sup>216</sup> We have applied this technique to fabricate a new class of asymmetric hopper microcrystals; the details are presented in Chapter 4.

Several other techniques such as rolled-up technology, <sup>217</sup> self-scrolling, <sup>218</sup> and threedimensional laser or electron beam writing<sup>219</sup> have been utilized to reorganize nanomembranes into desired shapes of three-dimensional nanostructures such as wrinkles, helices, tubes etc.

## 1.4.2. Morphology

The morphology of actuators and micromachines influences their mechanical motion. It can determine dynamic modes of actuators and micromachines such as translation, rotation, spin etc. Many of well-known actuators and micromachines are based on micro/nanorods, wires, tubes, helices, sheets and spherical Janus particles; their fabrication was briefly discussed in Sec. 1.4.1. Actuators and micromachines with highly asymmetric morphology have not been explored extensively. In this thesis, we have established the fabrication of new asymmetric hopper organic microcrystals with an unusual morphology and analysed their growth pattern. In hopper crystals, enhanced deposition of atoms or molecules at the edges and corners than at the centers of the crystal faces leads to unusual morphology under supersaturation conditions. Mostly hopper morphology exists in inorganic salt crystals, and the mechanism involved in the formation of hopper crystals has been extensively studied with NaCl. 220 The only example from organic systems was reported by Cao et al. who developed hopper crystals of tetrakis[methylene-3-(3-5-ditert-butyl-4-hydroxyphenyl) propionyloxy] methane.<sup>221</sup> We have developed a series of DADQ based hopper crystals by simple reprecipitation from DMSO-toluene mixture; details of the fabrication and morphology and their actuation under electron beam are presented in Chapter 4.

## 1.4.3. Types of actuators and micromachines

Various kinds of actuators and micromachines based on the nature of stimuli that drive them, are discussed below.

#### 1.4.3.1. Light

Various organic photochromic systems such as azobenzene, salicylideneaniline, fulgides and diarylethenes exhibit photomechanical effects that arise from reversible conformational and unit cell volume changes under light irradiation. UV irradiation causes trans-4-dimethylaminoazobenzene crystals to transform into the cis isomer; the crystal bends up to 90°. It reverses back into the trans isomer at ambient temperature bringing the crystal back to its initial position. This reversible transformation can be repeated more than 100 times, and their response and recovery times are 0.2 and 3.8 s, respectively.<sup>222</sup> Similarly, trans 4-aminoazobenzene microcrystals exhibit reversible cycles of bending followed by straightening upon alternate irradiation of UV and visible light.<sup>223</sup> The photoresponsive actuation of salicylideneaniline microcrystals is explained as a result of reversible keto-enol tautomerism upon alternate exposure of UV and visible light.<sup>224</sup> The narrow plate-like crystals of fulgides bend towards UV light and unbend to initial position under visible light due to unit cell length elongation and contraction, respectively.<sup>225</sup> Several coordination complexes undergo mechanical movement in presence of light due to their valence tautomerism, charge transfer reaction and linkage isomerism. Light has been used to induce photocatalytic or thermophoretic activity of Janus particles in propulsion media. Recently,

Wang *et al.* developed the light-driven Ag/AgCl Janus micromotors with high mobility of 100 µm per second.<sup>226</sup>

### 1.4.3.2. Heat

Thermally driven actuators and micromachines are uncommon and least studied because of stability related challenges. Reversible phase transitions and anisotropic variations of the unit cell volume could be the driving force in thermoresponsive actuators and micromachines. Crystals undergo phase transition upon heating that leads them to jump; the phenomenon is termed as thermosalient effect. The effect has been reported for the first time in phenylazophenyl palladium hexafluoracetylactonate crystals. <sup>227</sup> Over the past two decades, more examples of thermosalient or jumping crystals have been developed. Taniguchi *et al.* reported walking and rolling of *N*-[[4-*p*-dimethylaminohenylazo]benzoyl]-1-phenylethylamine crystals under heating and cooling around the phase transition temperature. <sup>228</sup>

## 1.4.3.3. Electric field

The electric field guided unidirectional motion of micromotors arise from the electrokinetic effect of the material in the medium, through self-electrophoresis, bubble propulsion, electroosmotic and bioelectrochemical propulsion. Electrostatic attraction drives charged particles towards the oppositely charged electrodes in a uniform DC field. Dielectric particles also exhibit controlled motion in a non-uniform AC field because of dielectrophoretic forces. Linear propulsion of 1 mm sized stainless steel metal particle under 1.6 kV/m electric field has been demonstrated in dilute solutions of H<sub>2</sub>SO<sub>4</sub>. Electric field powered rotational motion of polycarbonate bipolar rotors in HCl medium occurs at 0.5 kV/m electric field.<sup>229</sup> Conjugated polymers, particularly films of polypyrrole derivatives are the classic example of electrically driven actuators and have found application in the biomedical field as artificial muscles.<sup>230,231</sup>

## 1.4.3.4. Magnetic field

Magnetically induced motion is another attractive propulsion strategy based on the magnetophorosis effect. Nelson *et al.* illustrated the magnetically triggered movement of

artificial flagella with helical tails. 232,233 Ishiyama et al. fabricated synthetic NdFeB magnetic micromachines, and their movement under the magnetic torque was demonstrated.<sup>203</sup> Gao et al. illustrated the mechanical response of Au/Ag/Ni nanowire under the influence of magnetic field. Ni and Au sections of the nanowire rotate at different speeds to create device asymmetry that induce propulsion with a velocity of 3 µm/s at optimized magnetic field strength.<sup>234</sup>

#### 1.4.3.5. **Electron beam**

Interaction between high energy electron beams and specimen are well known and widely examined, especially in electron microscopy studies. However, electron beam induced, controlled mechanical movements are very rare and need to be explored. Bending and bundling of gold-coated GaAs nanowires under an optimum voltage electron beam have been reported, and an electrodynamic model developed to understand the mechanical movement. 235-237 Jiang et al. employed electron beams to fold gold nanoparticles ligated dodecanethiol nanomembranes into tubes, and simulations have been used to elucidate the role of the ligated membrane and electron beams in the mechanical response.<sup>238</sup> It has been shown that under the electron beam, light deformed stacking layers of the perylenediimide microribbons are restored to their original morphology.<sup>239</sup> As mentioned earlier, we present the controlled and reversible actuation of molecular hopper crystals under electron beam irradiation, in Chapter 4.

## 1.4.4. Applications

Micromotors with suitable functional groups are useful in various biomedical applications such as microsurgery, bioimaging, bioassay drug delivery and environmental remediation. 240-242 Electrically driven conjugated polymer based actuators and magnetically driven motors are useful in various medical treatments such as kidney stone destruction, eye treatments and cardiovascular surgery; their biocompatibility, and biodegradability are particularly relevant. Electron beam trigged motion of gold-coated epoxy nano post has been employed in efficient patterning.<sup>235</sup>

#### 1.5. Layout of the thesis

In this thesis, we have explored diaminodicyanoquinodimethane (DADQ) derivatives including some newly synthesized ones, and their novel applications as fluorescent labels in bioimaging and electron beam induced actuation. We have selected DADQ derivatives with appropriate functional groups to bind with the major chemical components present in the cell walls of stomatal cells and spores of bacterial cells for efficient staining. The molecular level interactions that enable staining were explored through calorimetry, spectroscopy, and microscopic investigations. In a different avenue, we have fabricated asymmetric organic hopper microcrystals of DADQs and examined their reversible mechanical bending followed by straightening under exposure to electron beams. Factors that influence the growth and mechanical response of the hopper microcrystals were addressed; insight into the actuation process was developed using a simple empirical model based on the experimental observations, crystal characterizations, and simulation studies. The detailed research work is presented in three chapters, followed by the final chapter with summary of the work and overview of future directions for exploration.

Chapter 2 - Efficient Bioimaging with Diaminodicyanoquinodimethanes: Selective Imaging of Epidermal and Stomatal Cells and Insight into the Molecular level Interactions

In this chapter, a simple and efficient protocol for staining the cell walls of stomata using select DADQ derivatives is presented. The imaging of epidermal and stomatal cells reveals the efficient and selective staining with DADQs. Major advantages of the protocols developed include the very small quantities of the fluorophore required, choice of DADQs soluble in water and organic solvents, and quick staining of the specimen in buffer-free state and in buffer medium. The molecular-level interactions that enable staining are unraveled through isothermal calorimetry, infrared spectroscopy and microscopy with energydispersive X-ray spectroscopy analysis. We propose that the efficient staining occurs by DADQs with the piperazinium (BT<sub>2</sub>) or piperazine (DPZDQ) functionalities binding to the polygalacturonic acid moieties in the cell wall of stomata and epidermal layer; the former can also bind to nucleic acid polyanions. The emission enhancement that enables efficient imaging is explained through various fluorescence experiments that point to DADQs in their rigid or aggregated states. We explored also, the general utility of DADQs as bio-imaging

dyes by carrying out preliminary experiments on various cell lines including human prostate and cyanobacteria cell lines.

# Chapter 3 - Zwitterionic Small Molecule based Fluorophores for Efficient and Selective *Imaging of Bacterial Endospores*

This chapter describes the selective imaging of bacterial endospores using the hexylamine substituted DADQ derivative (BHADQ) and the exploration of the underlying molecular-level interactions. The derivatives with ionic moieties (BT<sub>2</sub>) and optimally long alkyl chains (BHADQ) are shown to be excellent fluorescence probes for endospores. BT<sub>2</sub> stains bacterial cells and endospores, whereas BHADQ stains endospores selectively. To the best of our knowledge, this is the first example of selective fluorescence imaging of endospores in their dormant state. Spectroscopy, microscopy, and calorimetry studies provide insight into the molecular level interactions that enable efficient staining and bright images. In the BT<sub>2</sub> staining, clear evidence is found for H bonding between the peptidoglycan and BT<sub>2</sub>; there are also electrostatic interactions between them. In the case of BHADQ, the hexyl groups possibly interact with the supramolecular architecture of the peptidoglycan. Detailed staining experiments suggest that BT<sub>2</sub> stains bacteria efficiently, whereas BHADQ gets washed away and hence does not stain them. Fluorescence titration and lifetime studies indicate that BHADQ enters into the core of the spores and selectively stains it, whereas BT<sub>2</sub> is stopped at the outer layers of the bacterial cells and their endospores.

## Chapter 4 - Molecular Hopper Crystals and Electron Beam-Triggered Reversible Actuation

This chapter establishes the fabrication of a new class of molecular hopper crystals. Microcrystals of cyclopentyl functionalised DADQ (BCPADQ) with an unusual hopper morphology are fabricated through a simple reprecipitation-growth method. The approach is established with other DADQ derivatives as well. Formation of the hopper crystal of BCPADQ in the DMSO-toluene solvent mixtures is monitored by its characteristic fluorescence enhancement. X-ray diffraction, microscopy, and surface potential mapping analysis provide insight into the development of the unique morphology. Under optimized conditions of electron beam irradiation in a scanning electron microscope, the BCPADQ microcrystal is found to exhibit smooth, prominent, and reversible actuation. The unique observation of electron beam triggered actuation with the small molecule-based organic

hopper microcrystals, is analyzed by a detailed examination of the crystal lattice structure and asymmetric dipole distribution, together with simulations of the electron beam interactions. An empirical model is developed for the responses in the local electrostatic field providing a mechanistic understanding of the actuation process.

## Chapter 5 - Overview of the present work and future prospects

We present a summary of the work described in the previous chapters, on the synthesis of various DADQ derivatives with suitable functional groups and the exploration of their applications as fluorescence probes and actuators. Salient features of the work presented in this thesis include (i) the development of novel DADQ derivatives with suitable functionalities for the selective staining of stomatal cells and bacterial endospores, (ii) optimization of a simple and efficient staining protocol, (iii) selective fluorescence imaging of bacterial endospores in their dormant state, a first report of its kind, (iv) detailed exploration of the interaction between the DADQ molecules and the biological components providing new directions for the design of effective fluorophores to visualize other biological systems, (v) development of a strategy for the fabrication of molecular hopper crystals using the simple reprecipitation-growth method, and (vi) demonstration of controlled and reversible actuation of the hopper crystal under optimal conditions of electron beam irradiation. Further developments of these investigations that can open up new avenues of research and potential applications in various fields are also discussed.

## References

- J. Simon and P. Bassoul, Designs of Molecular Materials: Supramolecular 1. Engineering, Wiley, New York, 2000.
- 2. T. P. Radhakrishnan, Acc. Chem. Res., 2008, 41, 367-376.
- J. Hulliger, J. Angew. Chem. Int. Ed., 1994, 33, 143-162. 3.
- S. J. Dalgarno, S. A. Tucker, D. B. Bassil and J. L. Atwood, Science, 2005, 309, 2037-4. 2039.
- 5. M.C. Petty, Langmuir-Blodgett Films: an Introduction, Cambridge University Press, New York, 1996.
- New Trends in Intercalation Compounds for Energy Storage, Eds. C. Julien, J. P. 6. Ramos and A. Momchilov, Springer, Berlin, 2002.
- S. R. Forrest, Chem. Rev., 1997, 97, 1793-1896. 7.
- 8. A. Kumar, N. Yadav, M. Bhatt, N. K. Mishra, P. Chaudhary and R. Singh, Res. J. Chem. Sci., 2015, 5, 1-6.
- 9. E. Gomar-Nadal, J. Puigmarti-Luis and D. B. Ambilino, Chem. Soc. Rev., 2008, 37, 490-504.
- D. Holten, D. F. Bocian and J. S. Lindsey, Acc. Chem, Res., 2002, 35, 57-69. 10.
- A. R. Rocha, V. M. Garcia Suarez, S. W. Bailey, C. J. Lambert, J. Ferrer and S. 11. Sanvito, Nat. Mater., 2005, 4, 335-339.
- T. M. Swager, Acc. Chem. Res., 1998, 31, 201-207. 12.
- C. Reese and Z. Bao, *Mater. Today*, 2007, **10**, 20-27. 13.
- W. Koechner and M. Bass, Properties of Solid-State Laser Materials- Solid State Lasers, Springer, Herndon, USA, pp. 44-77, 2003.
- 15. P. Salunke, M. Joshi, V. Chaswal, G. Zhang, L. A. Rosenbaum, K. Dowling, P. Decker and V. Shanov, Rev. Sci. Instrum., 2016, 87, 105126 (1-20).
- 16. E. Talik and M. Oboz, Acta. Phys. Pol. A., 2013, 124, 340-343.
- 17. K. Sankaranarayana and P. Ramasamy, J. Cryst. Growth, 2005, 280, 467-473.
- H. W. Starkweather, G. E. Moore, J. E. Hansen, T. M. Roder and R. E. Brooks, J. 18. Polym. Sci., 1956, 21, 189-204.
- 19. Y. Shirota and H. Kageyama, Chem. Rev., 2007, 107, 953-1010.
- 20. Y. Shirota, J. Mater. Chem., 2000, 10, 1-25.

- 21. D. G. M. Wright, R. Dunk, D. Bouvart and M. Autran, *Polymer*, 1988, **29**, 793-796.
- 22. C. G. Chanduluri and T. P. Radhakrishnan, *Angew. Chem. Int. Ed.*, 2012, **51**, 11849-11852.
- 23. P. Srujana and T. P. Radhakrishnan, *Angew. Chem. Int. Ed.*, 2015, **54**, 7270-7274.
- 24. J. Jeevanandam, A. Barhoum, Y. S. Chan, A. Dufresne and M. K. Danquah, *Beilstein J. Nanotechnol.*, 2018, **9**, 1050-074.
- 25. V. B. Sandomirskii, Sov. Phys. JETP, 1967, 25, 101-106.
- 26. N. Heydari, S. M. B. Ghorashi, W. Han and H. H. Park, *Quantum Dot-based Light Emitting Diodes (QDLEDs): New Progress*, Eds. M. S. Ghamsari, Intech Open, Croatia, pp. 25-45, **2017**.
- 27. H. Kasai, H. Kamatani, S. Okada, H. Oikawa, H. Matsuda and H. Nakanishi, *Jpn. J. Appl. Phys.*, 1996, **35**, 221-223.
- 28. H. Katagi, H. Kasai, S. Okada, H. Oikawa, K. Komatsu, Z. Liu and H. Nakanishi, *Jpn. J. Appl. Phys.*, 1996, **35**, 1364-366.
- 29. T. Yanagawa, Y. Urokawa, H. Kasai and H. Nakanishi, *Opt. Commun.*, 1997, **137**, 103-106.
- 30. L. Smith, Nursing Times (online), 2007, 113, 20-23.
- 31. I. Cho and K. W. Lee, *J. Appl. Polym. Sci.*, 1985, **30**, 903-1926.
- 32. S. C. Chan and M. A. Barteau, *Langmuir*, 2005, **21**, 5588-5595.
- 33. R. Dong, Q. Zhang, W. Gao, A. Pei and B. Ren, ACS Nano, 2016, 10, 839-844.
- 34. H. Su, C. A. Hurd Price, L. Jing, Q. Tian, J. Liu and K. Qian, *Mater. Today Bio*, 2019, **4**, 1000330 (1-19).
- 35. Y. Yi, L. Sanchez, Y. Gao and Y. Yu, *Analyst*, 2016, **141**, 3526-3539.
- 36. I. Langmuir, J. Am. Chem. Soc., 1917, **39**, 1848-1906.
- 37. K. B. Blodgett, J. Am. Chem. Soc., 1934, **56**, 495.
- 38. S. Malik and C. C. Tripathi, *J. Surf. Eng. Mater. Adv. Technol.*, 2013, **3**, 235-241.
- 39. N. S. Abadeer and C. J. Murphy, *J. Phys. Chem. C*, 2016, **120**, 4691-4716.
- 40. S. S. Lucky, K. C. Soo and Y. Zhang, *Chem. Rev.*, 2015, **115**, 1990-2042.
- 41. T. M. Nobre, F. J. Pavinatto, L. Caseli, A. B. Timmons, P. D. Latka and O. N. Oliveira Jr, *Thin Solid Films*, 2015, **593**, 158-188.
- 42. K. Rajesh, B. Balaswamy, K. Yamamoto, H. Yamaki, J. Kawamata and T. P. Radhakrishnan, *Langmuir*, 2011, **27**, 1064-1069.

- M. Sharath Chandra, Y. Ogata, J. Kawamata and T. P. Radhakrishnan, Langmuir, 2003, **19**, 10124-10127.
- S. Ishihara and M. Mizusaki, J. Soc. Inf. Display, 2020, 28, 44-74. 44.
- 45. J. F. De Souza, K. D. S. Pontes, T. F. R. Alves, V. A. Amaral, M. D. A. Rebelo, M. A. Hausen and M. V. Chaud, *Molecules*, 2017, 22, 419 (1-15).
- G. H. Brown, J. Electron. Mater., 1973, 2, 403-430. 46.
- C. Benelli and D. Gatteschi, *Introduction to Molecular Magnetism*, Wiley, New York, 47. 2015.
- 48. W. H. D. Luna, S. D. Bittencourts, M. M. Dias, P. M. Aquim, R. M. Martins and L. Schaeffer, J. Electr. Syst., 2017, 13, 767-778.
- M. Takahashi, P. Turek, Y. Nakazawa, M. Tamura, K. Nozawa, D. Shiomi, M. 49. Ishikawa and M. Kinoshita, Phys. Rev. Lett., 1991, 67, 746-748.
- 50. S. Chittipeddi, K. R. Cromack, J. S. Miller and A. J. Epstein, *Phys. Rev. Let.*, 1987, **58**, 2695-2698.
- (a) J. S. Miller, *Chem. Soc. Rev.*, 2011, **40**, 3266-3296. (b) J. S. Miller, *Mater. Today*, 51. 2014, **17**, 224-235.
- D. N. Woodruff, R. E. P. Winpenny and R. A. Layfield, Chem. Rev., 2013, 113, 5110-52. 5148.
- 53. M. S. J. Hashmi, Introduction to Sensor Materials, Technologies and Applications, Elsevier, Netherlands, 2014.
- Z. Li, Organic Light-Emitting Materials and Devices, CRC Press, Boca Raton, 2007. 54.
- M. J. Schnermann, *Nature*, 2017, **551**, 166-167. 55.
- C. Zhang, Y. S. Zhao and J. Yao, Phys. Chem. Chem. Phys., 2011, 13, 9060-9073. 56.
- 57. C. Wang, H. Dong, W. Hu, Y. Liu and D. Zhu, *Chem. Rev.*, 2012, **112**, 2208-2267.
- 58. R. W. Boyd, Nonlinear Optics, Academic Press, USA, 2008.
- J. Zyss, J. F. Nicoud and M. Coquillay, J. Chem. Phys., 1984, 81, 4160-4167. 59.
- H. Kishida, K. Hirota, H. Okamoto, H. Kokubo and T. Yamamoto, Appl. Phys. Lett., 60. 2008, **92**, 033309 (1-3).
- A. Patra, N. Venkatram, D. N. Rao, T. P. Radhakrishnan, J. Phys. Chem. C, 208, 112, 61. 16269-16274.
- H. Akamatu, H. Inokuchi and Y. Matsunaga, *Nature*, 1954, **173**, 168-169. 62.

- 63. L. R. Melby, R. J. Harder, W. R. Hertler, W. Mahler, R. E. Benson and W. E. Mochel, *J. Am. Chem. Soc.*, 1962, **84**, 3374-3387.
- 64. H. M. Kim, Y. H. Cho, H. Lee, S. Ii Kim, S. R. Ryu, D. Y. Kim, T. W. Kang and K. S. Chung, *Nano Lett.*, 2004, **4**, 1059-1062.
- 65. Th. Gessmann and E. F. Schubert, *Int. J. Appl. Phys.*, 2004, **95**, 2203-2216.
- 66. C. W. Tang and S. A. Vanslyke, *Appl. Phys. Lett.*, 1987, **51**, 913-915.
- 67. J. H. Burroughes, D. D.C. Bradley, A. R. Brown, R. N. Marks, K. Mackay, R. H. Friend, P. L. Burns and A. B. Holmes, *Nature*, 1990, **347**, 539-541.
- 68. L. Dai, B. Winkler, L. Dong, L. Tong and A. W. H. Mau, *Adv. Mater.*, 2001, **13**, 915-925.
- 69. J. M. Fiore, Semiconductor Devises, Suny Open Textbooks, New York, 2019.
- 70. S. Hunig and E. Herberth, *Chem. Rev.*, 2004, **104**, 5535-5563.
- 71. J. Clay and H. Kamerlingh Onnes, *Proc. K. Ned. Acad. Wet.*, 1907, **10 I**, 207-215.
- 72. D. Jerome, A. Mazaud, M. Ribault and K. Bechgaard, *J. Phys. Lett.*, 1980, **41**, 95-98.
- 73. S. Rashid, S. S. Turner, P. Day, J. A. K. Howard, P. Guionneau, E. J. L. Mcinnes, F. K. Mabbs, R. J. H. Clark, S. Firth and T. Biggs, *J. Mater. Chem.*, 2001, **11**, 2095-2101.
- 74. W. R. Hertler, H. D. Hartzler, D. S. Acker and R. E. Benson, *J. Am. Chem. Soc.*, 1962, **84**, 3387-3393.
- 75. S. Jayanty, T. P. Radhakrishnan, *Chem. Eur. J.*, 2004, **10**, 791-797.
- 76. R. S. Gopalan, G. U. Kulkarni, M. Ravi, C. N. R. Rao, *New J. Chem.*, 2001, **25**, 1108-1110.
- 77. S. Jayanty and T. P. Radhakrishnan, *Chem. Mater.*, 2001, **13**, 2460-2462.
- 78. P. Srujana, T. Gera and T. P. Radhakrishnan, *J. Mater. Chem. C*, 2016, **4**, 6510-6516.
- 79. M. Ravi, D. N. Rao, S. Cohen, I. Agranat and T. P. Radhakrishnan, *Curr. Sci.*, 1995, **68**, 1119-1121.
- 80. M. Ravi, D. N. Rao, S. Cohen, I. Agranat and T. P. Radhakrishnan, *J. Mater. Chem.*, 1996, **6**, 1119-1122.
- 81. D. Bloor, Y. Kagawa, M. Szablewski, M. Ravi, S. J. Clark, G. H. Cross, L. O. Pålsson, A. Beeby, C. Parmer and G. Rumbles, *J. Mater. Chem.*, 2001, **11**, 3053 3062.
- 82. S. Jayanty, P. Gangopadhyay and T.P. Radhakrishnan, *J. Mater. Chem.*, 2002, **12**, 2792-2797.

- C. G. Chandaluri and T. P. Radhakrishnan, Opt. Mater., 2011, 34, 119-125.
- 84. C. G. Chandaluri, A. Patra and T. P. Radhakrishnan, Chem. Eur. J., 2010, 16, 8699-8706.
- 85. C. G. Chandaluri and T. P. Radhakrishnan, J. Mater. Chem. C. 2013, 1, 4464-4471.
- 86. P. Sudhakar and T. P. Radhakrishnan, *Chem. Asian J.*, 2019, **14**, 4754-4759.
- 87. T. S. Metzger, C. G. Chandaluri, R. T. Vered, R. Shenhar and I. Willner, Adv. Funct. Mater., 2016, 26, 7148-7155.
- SD. Anwarhussaini, H. Battlua, P. V. Boppidi, S. Kundu, C. Chakraborty and S. 88. Jayanty, Org. Electron., 2020, 76, 105457 (1-11).
- 89. N. Senthilnathan, Ch. G. Chandaluri and T. P. Radhakrishnan, Sci. Rep., 2017, 7, 10583 (1-11).
- N. Senthilnathan, K. Gaurav, Ch. Venkata Ramana and T. P. Radhakrishnan, J. 90. Mater. Chem. B, 2020, 8, 4601-4608.
- 91. N. Senthilnathan, and T. P. Radhakrishnan, Chem. Mater., 2020, DOI. 10.1021/acs.chemmater.0c02892.
- 92. J. F. W. Herschel, *Phil. Trans. R. Soc. Lond.*, 1845, **135**, 143-145.
- 93. J. R. Lackowicz, Principles of Fluorescence Spectroscopy, Springer, New York, 2006.
- 94. E. L. Wehry, *Modern Fluorescence Spectroscopy*, Plenum Press, New York, **1976**.
- 95. M. Y. Berezin and S. Achilefu, Chem. Rev., 2010, 110, 2641-2684.
- 96. W. Becker, J. Microsc., 2012, 247, 119-136.
- 97. D. R. Kearns, *Chem. Rev.*, 1971, **71**, 395-427.
- W. F. Watson, Nature, 1948, 162, 452-453. 98.
- 99. A. Mishra, R. K. Behera, P. K. Behera, B. K. Mishra and G. B. Behera, Chem. Rev., 2000, **10**, 1973-2012.
- 100. M. Kasha, Rev. Mod. Phys., 1959, **31**, 162-169.
- 101. D. Oelkrug, A. Tompert, H. J. Egelhaaf, M. Hanack, E. Steinhuber, M. Hohloch, H. Meier and U. Stalmach, Synth. Met., 1996, 83, 231-237.
- 102. D. Oelkrug, A. Tompert, J. Gierschner, H. J. Egelhaaf, M. Hanack, M. Hohloch and E. Steinhuber, J. Phys. Chem. B, 1998, 102, 1902-1907.
- 103. J. Luo, Z. Xie, J. W. Y. Lam, L. Cheng, H. Chen, C. Qiu, H. S. Kwok, X. Zhan, Y. Liu, D. Zhuc and B. Z. Tang, Chem. Commun., 2001, 1740-1741.

- 104. A. Qin and B.Z. Tang, Aggregation Induced Emission: Fundamentals, Wiley, Chichester, UK, 2014.
- 105. J. Chen, C.C.W. Law, W. Y. Lam, Y. Dong, S. M. F. Lo, I. D. Williams, D. Zhu and B. Z. Tang, Chem. Mater., 2003, 15, 1535-1546.
- 106. E. R. Jimenez and H. Rodriguz, J. Mater. Sci., 2020, **55**, 1366-1387.
- 107. P. Srujana and T. P. Radhakrishnan, *Chem. Eur. J.*, 2018, **24**, 1784-1788.
- 108. J. N. Wilson, M. D. Smith, V. Enkelmann and U. H. F. Bunz, Chem. Commum., 2004, 1700-1701.
- 109. Z. Zhao, J. W. Y. Lam and B. Z. Tang, J. Mater. Chem., 2012, 22, 23726-23740.
- 110. Y. Hong, J. W. Y. Lam and B. Z. Tang, Chem. Commun,, 2009, 4332-4353.
- 111. R. Davis, N. S. S. Kumar, S. Abraham, C. H. Suresh, N. P. Rath, N. Tamaoki and S. Das, J. Phys. Chem. C, 2008, 112, 2137-2146.
- 112. P. Srujana, P. Sudhakar and T. P. Radhakrishnan, J. Mater. Chem. C, 2018, 6, 9314-9329.
- 113. Z. Zhao, C. Y. K. Chan, S. Chen, C. Deng, J. W. Y. Lam, C. K. W. Jim, Y. Hing, P. Lu, Z. Chang, X. Chen, P. Lu, H. S. Kwok, H. Qiu and B. Z. Tang, J. Mater. Chem., 2012, **22**, 4527-4534.
- 114. Y. Cai, A. Qin and B. Z. Tang, J. Mater. Chem. C, 2017, 5, 7375-7389.
- 115. A. Patra, N. Hebalkar, B. Sreedhar, M. Sarkar, A. Samanta and T. P. Radhakrishnan, Small, 2006, 2, 650-659.
- 116. B. Balasamy, L. Maganti, S. Sharma and T. P. Radhakrishnan, Langmuir, 2012, 28, 17313-17321.
- 117. T. Shu, J. Wang, L. Su and X. Zhang, Crit. Rev. Anal. Chem., 2018, 48, 330-36.
- 118. P. Alam, C. Climent, P. Alemany and I. R. Laskar. J. Photochem. Photobiol. C, 2019, **41**, 100317 (1-41).
- 119. P. Alam, S. Dash, C. Climent, G. Kaur, A. R. Choudhury, D. Casanova, P. Alemany, R. Chowdhury and I. R. Lascar, *RSC Adv.*, 2017, **7**, 5642-5648.
- 120. S. K. Sheet, B. Sen, S. K. Patra, M. Rabha, K. Aguan and S. Khatua, ACS Appl. Mater. Interfaces, 2018, 10, 14356-14366.
- 121. J. Xie, Y. Zheng and J. Y. Ying, J. Am. Chem. Soc., 2009, **131**, 88-889.
- 122. J. Zheng, C. Zhang and R. M. Dickson, *Phys. Rev. Lett.*, 2004, **93**, 77402 (1-4).
- 123. L. Shang and S. Dong, Chem. Commun., 2008, 1088-1090.

- 124. M. Zhu, C. M. Aikens, F. J. Hollander, G. C. Schatz and R. Jin, J. Am. Chem. Soc., 2008, **130**, 5883-5885.
- 125. X. Yuan, Z. Luo, Q. Zhang, X. Zhang, Y. Zheng, J. Y. Lee and J. Xie, ACS Nano, 2011, **5**, 8800-8808.
- 126. J. Li, J. J. Zhu and K. Xu, Trends Anal. Chem., 2014, 58, 90-98.
- 127. D. Sengottuvelu, V. Kachwal, P. Raichure, T. Raghav and I. R. Laskar, ACS Appl. Mater. Interfaces, 2020, 12, 31875-31886.
- 128. S. Dineshkumar, A. Raj, A. Srivastava, S. Mukherjee, S. S. Pasha, V. Kachwal, L. Fageria, R. Chowdhury and I. R. Laskar, ACS Appl. Mater. Interfaces, 2019, 11, 31270-31282.
- 129. S. Li, J. He and Q. H. Xu, ACS Omega, 2020, 5, 41-48.
- 130. N. Lin, X. Chen, S. Yan, H. Wang, Z. Lu, X. Xia, M. Liang, Y. L. Wu, L. Zheng, Q. Cao and Z. Ding, RSC Adv., 2016, 6, 25416-5419. S. Li, J. He and Q. H. Xu, ACS Omega, 2020, 5, 41-48.
- 131. J. Tong, T. Hu, A. Qin, J. Z. Sun and B. Z. Tang, Faraday Discuss., 2017, 196, 285-
- 132. S. Dey, R. Purkait, K. Pal, K. Jana and C. Sinha, ACS Omega, 2019, 4, 8451-8464.
- 133. S. J. Zou, Y. Shen, F. M. Xie, J. E. Chen, Y. Q. Li and J. X. Tang, Mater. Chem. Front., 2020, 4, 788-820.
- 134. H. T. Lin, J. T. Wu, M. H. Chen and G. S. Liou, J. Mater. Chem. C, 2020, DOI. 10.1039/D0TC03008B.
- 135. F. Song, Z. Zhao, Z. Liu, J. W. Y. Lam and B. Z. Tang, J. Mater. Chem. C., 2020, 8, 3284-3301.
- 136. F. D. Nisi, R. Francischello, A. Battisti, A. Panniello, E. Fanizza, M. Striccoli, X. Gu, N. L. C. Leung, B. Z. Tang and A. Pucci, *Mater. Chem. Front.*, 2017, 1, 1406-1412.
- 137. Z. Zhao, J. W. Y. Lam and B. Z. Tang, *J. Mater. Chem.*, 2012, **22**, 23726-23740.
- 138. J. Hunag, Y. Jiang, J. Yang, R. Tang, N. Xie, Q. Li, H. S. Kwok, B. Z. Tang and Z. Li, J. Mater. Chem. C, 2014, 2, 2028-2036.
- 139. S. H. Chen, D. Katsis, A. W. Schmid, J. C. Mastrangelo, T. Tsutsuik and T. N. Blanton, Nature, 1999, 397, 506-508.
- 140. A. Montali, C. Bastiaansen, P. Smith and C. Weder, *Nature*, 1998, **392**, 261-264.
- 141. E. Peeters, M. P. T. Christiaans, R. A. J. Janssen, H. F. M. Schoo, H. P. J. M. Dekkers and E. W. Meijer, J. Am. Chem. Soc., 1997, 119, 9909-9910.

- 142. J. Liu, H. Su, L. Meng, Y. Zhao, C. Deng, J. C. Y. Ng, P. Lu, M. Faisal, J. W. Y. Lam, X. Huang, H. Wu, K. S. Wong and B. Z. Tang, Chem. Sci., 2012, 3, 2737-2747.
- 143. S. Li, C. Yin, R. Wang, Q. Fan, W. Wu and X. Jiang, ACS Appl. Mater. Interfaces, 2020, **12**, 20281-20286.
- 144. J. Yang, H. T. D. Li, T. Jiang, Y. Gao, B. Li, X. Qu and J. Hua, RSC Adv., 2016, 6, 58434-58442.
- 145. Z. Yang, W. Yin, S. Zhang, I. Shah, B. Zhang, S. Zhang, Z. Li, Z. Lei and H. Ma, ACS Appl. Bio Mater., 2020, 3, 1187-1196.
- 146. G. P. C. Drummen, *Molecules*, 2012, **17**, 14067-4090.
- 147. H. Liu, Y. Dong, B. Zhang, F. Liu, C. Tan, Y. Tan and Y. Jiang, Sen. Actuators B, 2016, **34**, 16-624.
- 148. Y. Jung, J. Jung, Y. Huh and D. Kim, J. Anal. Methods. Chem., 2018, 5249765 (1-11).
- 149. M. Cao, H. Chen, D. Chen, Z. Xu, S. H. Liu, X. Chen and J. Yin, Chem. Commun., 2016, **52**, 721-724.
- 150. S. Lim, Md. M. Haque, D. Su, S. Kim, J. S. Lee, Y. T. Chang and Y. K. Kim, Chem. Commun., 2017, **53**, 1607-1610.
- 151. X. Zhang, S, Bloch, W. Akers and S. Achilefu, Curr. Protoc. Cytom., 2012, 12, 27 (1-28).
- 152. F. Ding, Y. Zhan, X. Lu and Y. Sun, *Chem. Sci.*, 2018, **9**, 4370-4380.
- 153. K. M. Tsoi, Q. Dai, B. A. Alman and W. C. W. Chan, Acc. Chem. Res., 2013, 46, 662-671.
- 154. S. Jin, Y. Hu, Z. Gu, L. Liu and H. C. Wu, J. Nanomater., 2011, 834139 (1-13).
- 155. S. J. Remington, *Protein Sci.*, 2011, **20**, 1509-1519.
- 156. R. N. Day and M. W. Davidson, *Chem. Soc. Rev.*, 2009, **38**, 2887-2921.
- 157. H. Sahoo, RSC. Adv., 2012, 2, 7017-7029.
- 158. G. Hermanson, *Bioconjugate Techniques*, Academic Press, USA, 2008.
- 159. P. M. E. Gramlich, C T. Wirges, A. Manetto and T. Carell, Angew. Chem. Int. Ed., 2008, 47, 8350-8358.
- 160. H. S. Han, N. K. Devaraj, J. Lee, S. A. Hilderbrand, R. Weissleder and M. G. Bawendi, J. Am. Chem. Soc., 2010, 132, 7838-7839.
- 161. M. Griffin, R. Casadio and C. M. Bergamini, *Biochem. J.*, 2002, **368**, 377-396.

- 162. M. L. M. Mannesse, R. C. Cox, B. C. Koops, H. M. Verheij, G. H. De Haas, M. R. Egmond, H. T. W. M. Vander Hijden and J. D. Vlieg, Biochemistry, 1995, 34, 6400-6407.
- 163. B. A. Griffin, S. R. Adms and R. Y. Tsien, *Science*, 1998, **281**, 269-271.
- 164. A. N. Kapanidis, Y. W. Ebright and R. H. Ebright, J. Am. Chem. Soc., 2001, 123, 12123-12125.
- 165. A. Ojida, K. Honda, D. Shinmi, S. Kiyonaka, Y. Mori and I. Hamachi, J. Am. Chem. Soc., 2006, **128**, 10452-10459.
- 166. E. B. Gokerkucuk, M. Tramier and G. Bertolin, *Genes*, 2020, **11**, 125 (1-24).
- 167. S. W. Perry, J. P. Norman, J. Barbieri, E. B. Brown and H. A. Gelbard, *Biotechniques*, 2011, **50**, 98-115.
- 168. B. Chazotte, *Cold Spring Harb Protoc.*, 2011, 990-992.
- 169. L. Zhang, F. Su, X. Kong, F. Lee, S. Sher, K. Day, Y. Tian and D. R. Meldrum, chembiochem., 216, 17, 1719-1724.
- 170. C. W. T. Leung, Y. Hong, S. Chen, E. Zhao, J. W. Y. Lam and B. Z. Tang, J. Am. Chem. Soc., 2013, 135, 62-65.
- 171. J. Li, N. Kwon, Y. Jeong, S. Lee, G. Kim and J. Yoon, ACS Appl. Mater. Interfaces, 2018, **10**, 12150-12154.
- 172. J. Kapuscinski, *Biotech. Histochem.*, 1995, **70**, 220-233.
- 173. V. Boyd, O. M. Cholewa and K. K. Papas, Curr. Trends. Biotechnol. Pharm., 2008, **2**, 66-84.
- 174. F. C. Mortimer, D. J. Mason and V. A. Gant, Antimicrob. Agents Chemother., 2000, **44**, 676-81.
- 175. L. Xu, Z. Zhu, D. Wei, X. Zhou, J. Qin and C. Yang, ACS Appl. Mater. Interfaces, 2014, **6**, 18344-18351.
- 176. M. M. Smith and M. E. Mccull, *Stain Technol.*, 1978, **53**, 79-85.
- 177. J. Liesche, I. Ziomkiewicz and A. Schulz, *BMC Plant Biol.*, 2013, **13**, 226 (1-8).
- 178. C. Voiniciuc, M. Pauly and B, Usadel, *Plant Physiol.*, 2018, **176**, 2590-2600.
- 179. J. M. Kwiatek, D. M. Owen, A. A. Siniyeh, P. Yan, L. M. Loew and K. Gaus, Plos One, 2013, 8, E52960 (1-7).
- 180. Y. Li, Y. Wu, J. Chang, M. Chen, R. Liu and F. Li, *Chem. Commun.*, 2013, 49, 11335-11337

- 181. J. Negi, M. H. Sugimoto, K. Kusumi and K. Iba, Plant Cell Hysiol. 2014, 55, 241-250.
- 182. R. Chitrakar and M. Melotto, J. Vis. Exp., 2010, 44, 2-5.
- 183. M. G. Ajuru and B. E. Okoli, *Int. J. Mod. Botany*, 2012, **2**, 115-119.
- 184. P. Apostolakos, P. Livanos, T. L. Nikolakopoulou and B. Galatis, Ann. Bot., 2009, **104**, 1373-1387.
- 185. M. R. Puli and A. S. Raghavendra, *J. Exp. Bot.*, 2012, **63**, 1349-1356.
- 186. O. Keech, E. Pesquet, A. Ahad, A. Askne, D. Nordvall, S. M. Vodnala, H. Tuominen, V. Hurry, P. Dizengremel and P. Gardestrom, *Plant Cell Environ.*, 2007, 30, 1523-1534.
- 187. Z. Chen and D. Liu, Computer and Computing Technologies in Agriculture II, Eds. C. Zhao, D. Li, Springer, pp. 2119–2124, USA, 2009.
- 188. S. D. Card, B. A. Tapper, C. L. West and K. M. Wright, *Mycologia*, 2013, **105**, 221-229.
- 189. Z. Tian, Q. Yan, L. Feng, S. Deng, C. Wang, J. Cui, C. Wang, Z. Zhang, T. D. James and X. Ma, Chem. Commun., 2019, 55, 3951-3954.
- 190. X. Ge, M. Gao, B. Situ, W. Feng, B. He, X. He, S. Li, Z. Ou, Y. Zhong, Y. Lin, X. Ye, X. Hu, B. Z. Tang and L. Zheng, *Mater. Chem. Front.*, 2020, **4**, 957-964.
- 191. P. Stiefel, S. S. Emrich, K. M. Weber and Q. Ren, BMC Microbiology, 2015, 15, 36 (1-9).
- 192. E. Hao, Y. Chen, S. Chen, H. Deng, C. Gui, C. W. T. Leung, Y. Hong, J. W. Y. Lam and B. Z. Tang, Adv. Mater., 2015, 27, 4931-4937.
- 193. X. Zhang, X. Chen, J. Yang, H. R. Jia, Y. H. Li, Z. Chen and F. G. Wu, Adv. Funct. Mater., 2016, 26, 5958-5970.
- 194. W. M. Leevy, J. R. Johnson, C. Lakshmi, J. Morris, M. Marquez and B. D. Smith, Chem. Commun., 2006, 1595-1597.
- 195. H. Yuan, Z. Liu, L. Liu, F. Lv, Y. Wang and S. Wang, Adv. Mater., 2014, 26, 4333-4338.
- 196. W. Dorner, Le Lait, 1926, 6, 8-12.
- 197. R. D. Lillie and H. J. Conn, H. J. Conn's Biological Stains: A Handbook on the Nature and Uses of the Dyes Employed in the Biological Laboratory, Williams & Wilikins, Baltimore, 1969.
- 198. D. Schichnes, J. A. Nemson and S. E. Ruzin, *Microscope*, 206, **54**, 91-93.
- 199. P. Dincecco, L. Ong, S. Gras and L. Pellegrino, *Micron*, 2018, **110**, 1-9.

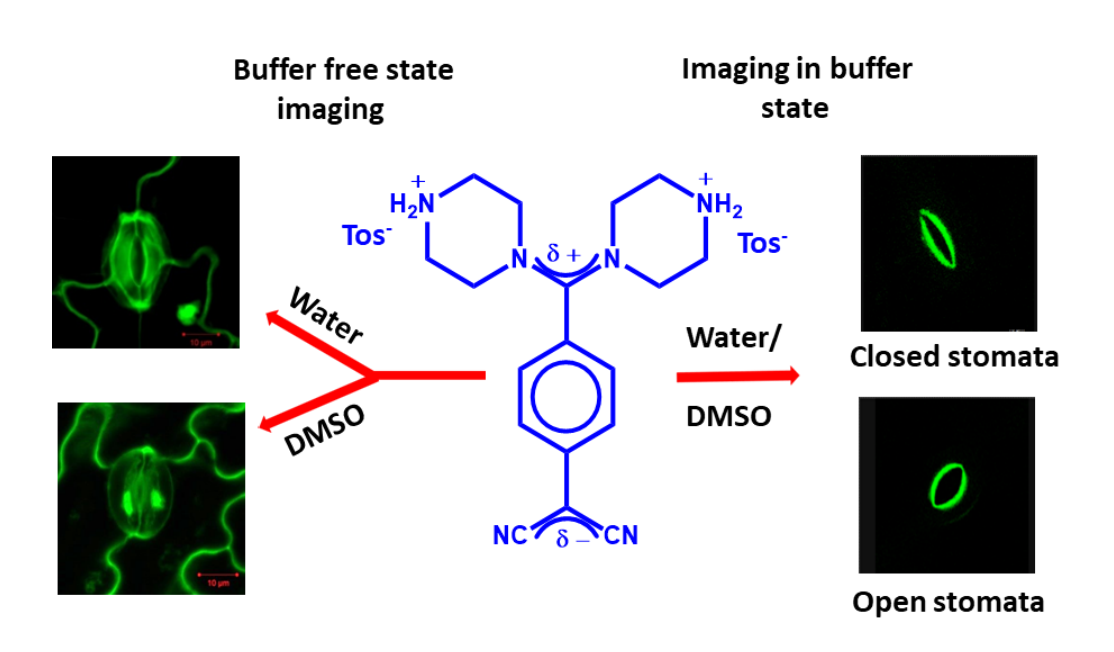
- 200. C. Laflamme, S. Lavigne, J. Ho and C. Duchaine, J. Appl. Microbiol., 2004, 96, 684-692.
- 201. W. F. Paxton, K. C. Kistler, C. C. Olmeda, A. Sen, S. K. St. Angelo, Y. Cao, T. E. Mallouk, P. E. Lammert and V. H. Crespi, J. Am. Chem. Soc., 2004, 126, 13424-13431.
- 202. D. L. Fan, F. Q. Zhu, R. C. Cammarata and C. L. Chien, Appl. Phys. Lett., 2004, 85, 4175-4177.
- 203. K. Ishiyama, M. Sendoh, A. Yamazaki and K. I. Arai, Sens. Actuator A Phys., 2001, **91**, 141-144.
- 204. W. Wang, L. A. Castro, M. Hoyos and T. E. Mallouk, ACS Nano, 2012, 6, 6122-6132.
- 205. W. F. Paxon, S. Sundararajan, T. E. Mallouk and A. Sen, Angew. Chem. Int. Ed., 2006, **45**, 5420-5429.
- 206. K. M. Manesh, M. Cardona, R. Yuan, M. Clark, D. Kagan, S. Balasubramanian and J. Wang, ACS Nano, 2010, 4, 1799-1804.
- 207. Y. Wang, J. Wang and J. Chen, *Mater. Sci. Eng.*, 2018, **322**, 042016 (1-5).
- 208. U. Choudhury, L. Soler, J. Gibbs, S. Sanchez and P. Fischer, Chem. Commun., 2015, **51**, 8660-8663.
- 209. K. B. Sheard, D. A. Christie, C. L. Sosa, C. B. Arnold and R. D. Priestley, *Appl. Phys. Lett.*, 2015, **6**, 093104 (1-5).
- 210. Z. Wu, Y. Wu, W. He, X. Lin, J. Sun and Q. He, Angew. Chem. Int. Ed., 2013, 52, 7000-7003.
- 211. L. S. Zahr, M. D. Villiers and M. V. Pishko, *Langmuir*, 2005, **21**, 403-410.
- 212. B. Dong, T. Zhou, H. Zhang and C. Y. Li, ACS Nano, 2013, 7, 5192-5198.
- 213. H. Kasai, H. S. Nalwa, H. Oikawa, S. Okada, H. Matsuda, N. Minami, A. Kakuta, K. Ono, A. Mukoh and H. Nakanishi, J. Appl. Phys., 1992, 31, 1132-1134.
- 214. K. Baba, H. Kasai, S. Okada, H. Oikawa and H. Nakanishi, Opt. Mater., 2002, 21, 591-594.
- 215. H. Kasai, H. Oikawa and H. Nakanishi, In Organic Mesoscopic Chemistry, Eds. H. Masuhara, F. C. De Schryver, Blackwell Science: Oxford, UK, 1999.
- 216. J. R. Baylis, J. H. Yeon, M. H. Thomson, A. Kazerooni, X. Wang, A. E. St. John, E. B. Lim, D. Chien, A. Lee, J. Q. Zhang, J. M. Piret, L. S. Machan, T. F. Burke, N. J. White and C. J. Kastrup, *Sci. Adv.*, 2015, **1**, e1500379 (1-8).
- 217. Y. Mei, G. Huang, A. A. Solovey, E. B. Urena, I. Monch, F. Ding, T. Reindl, R. K. Y. Fu, P. K. Chu and O. G. Schmidt, *Adv. Mater.*, 2008, **20**, 4085-4090.

- 218. D. J. Bell, S. Leutenegger, K. M. Hammar, L. X. Dong and B. J. Nelson, *Proc. IEEE* Int. Conf. Rob. Autom., 2007, 1128-1133.
- 219. M. Thiel and M. Hermatschweiler, *Photonics*, 2011, **6**, 36-39.
- 220. J. Desarnaud, H. Derluyn, J. Carmeliet, D. Bonn and N. Shahidzadeh, J. Phys. Chem. Lett., 2018, 9, 2961-2966.
- 221. Y. Cao, S. Wang, H. Mou, H. Xu and C. Wu, J. Cryst. Growth, 2010, 312, 1747-1750.
- 222. H. Koshima, N. Ojima and H. Uchimoto, J. Am. Chem. Soc., 2009, 131, 6890-6891.
- 223. H. Koshima and N. Ojima, *Dyes Pigm.*, 2012, **92**, 798-801.
- 224. H. Koshima, K. Takechi, H. Uchimoto, M. Shiro and D. Hashizume, Chem. Commun., 2011, 47, 11423-11425.
- 225. H. Koshima, H. Nakaya, H. Uchimoto and N. Ojima, *Chem. Lett.*, 2012, **41**, 107-109.
- 226. X. Wang, L. Baraban, A. Nguyen, J. Ge, V. R. Misko, J. Tempere, F. Nori, P. Formanek, T. Huang, G. Cuniberti, J. Fassbender and D. Makarov, Small, 2018, 1803613 (1-11).
- 227. M. C. Etter and E. R. Siedle, J. Am. Chem. Soc., 1983, 105, 641-643.
- 228. T. Taniguchi, H. Sugiyama, H. Uekusa, M. Shiro, T. Asahi and H. Koshima, Nat. Commun., 2008, 9, 538 (1-9).
- 229. G. Loget and A. Kuhn, *Nat. Commun.*, 2011, **2**, 535 (1-6).
- 230. E. Smela, Adv. Mater., 2003, 15, 481-494.
- 231. D. Melling, J. G. Martinez and E. W. H. Jager, Adv. Mater., 2019, 31, 1808210 (1-
- 232. L. Zhang, J. J. Abbott, L. Dong, B. E. Kratochvil, D. Bell and B. J. Nelson, *Appl.* Phys. Let., 2009, 94, 094107 (1-4).
- 233. A. Ghosh and P. Fischer, *Nano Lett.*, 2009, **9**, 2243-2245.
- 234. W. Gao, S. Sattayasamitsathit, K. M. Manesh, D. Weihs and J. Wang, J. Am. Chem. Soc., 2010, **132**, 14403-14405.
- 235. A. Seminara, B. Pokroy, S. H. Hang, M. P. Brenner and J. Aienberg, *Phys. Rev. B*: Condens. Matter Mater. Rev., 2011, 83, 235438 (1-6).
- 236. S. Carapezzi, G. Priante, V. Rillo, L. Montes, S. Rubini and A. Cavallini, ACS Nano, 2014, 8, 8932-8941.
- 237. L. A. Bitzer, C. Speich, D. Schafer, D. Erni, W. Prost, F. J. Tegude, N. Benson and R. Schmechel, J. Appl. Phys., 2016, 119, 145101 (1-6).

- 238. Z. Jiang, J. He, S. A. Deshmukh, P. Kanjanaboos, G. Kamath, Y. Wang, S. K. R. S. Sankaranarayanan, J. Wing, H. Jaeger and X. M. Lin, Nat. Mater., 2015, 14, 912-918.
- 239. Y. Zhang, C. Peng, Z. Zhou, R. Duan, H. Ji, Y. Che and J. Zhao, Adv. Mater., 2015, **27**, 320-325.
- 240. W. Xi, A. A. Solovev, A. N. Ananth, D. H. Gracias, S. Sanchez and O. G. Schmidt, Nanoscale, 2013, **5**, 1294-1297.
- 241. M. Guix, J. Orozco, M. Garcia, W. Gao, S. Sattayasamitsathit, A. Merkoci, A. Escarpa and J. Wang, ACS Nano, 2012, 6, 4445-4451.
- 242. E. S. Olson, J. Orozco, Z. Wu, C. D. Malone, B. Yi, W. Gao, M. Eghtedari, J. Wang and R. F. Mattrey, Biomaterials, 2013, 34, 8918-8924.

## **CHAPTER 2**

# Selective Imaging of Epidermal and Stomatal Cells and Insight into the Molecular Level Interactions



Bright, selective and high contrast bioimaging using diaminodicyanoquinodimethane molecules which exhibit enhanced fluorescence emission in the aggregated state, is demonstrated using epidermal and stomatal cell staining; the molecular basis for the efficient staining is unraveled through spectroscopy, calorimetry, microscopy and EDX analysis.

## **Synopsis**

The enhanced fluorescence emission of diaminodicyanoquinodimethanes (DADQs) in rigid and aggregated states holds great promise for bioimaging applications. In this chapter, we demonstrate it through the efficient application in epidermal and stomatal imaging with selective staining of cell walls and nuclei. Stomata are pores on the surfaces of leaves with a pair of guard cells that regulate air and water exchange in photosynthesis and transpiration processes of plants respectively. We demonstrate the major advantages of DADQs in the imaging applications, in terms of the small quantities (a few nmols) of the fluorophore required, choice of DADQs soluble in water and organic solvents, and quick staining of the specimen in buffer-free state and buffer medium. In addition, the molecular level interactions that enable staining are unraveled through various calorimetry, spectroscopy and microscopy analysis and control imaging experiments with a range of DADQs. It is proposed that DADQs with ionic or H-bonding functionalities bind to the polygalacturonic acid moieties in the epidermal layer; the former with their charges can bind also to nucleic acid polyanions. Fluorescence experiments explain the emission enhancement that enables efficient imaging. The work presented here shows that DADQs are easy to synthesize, non-cytotoxic, and thermally, chemically and photo-stable, requiring no special storage conditions. Preliminary experiments also point to their potential utility in imaging different classes of cells. In brief, this Chapter provides a guide to design new classes of efficient fluorophores for bioimaging applications, and unravel possible interactions between the fluorophores and the bio components of the stomatal cell walls.

#### 2.1. Introduction

Fluorescence based imaging is a prominent tool for the investigation of the structure and function of biological systems. 1 Issues related to cytotoxicity, photo-stability and emission quenching have limited the number of fluorophores that can be deployed in practical and efficient imaging applications. Fluorescent protein based probes are mostly expensive, and often suffer from low molar absorptivity, instability during sample fixation that may involve denaturants, potential interference with cell functions, and undesirable sensitivity to environmental factors like temperature and pH.<sup>2-5</sup> Even though quantum dots are highly photo-stable and emissive, they are generally plagued by toxicity issues; <sup>6</sup> nanoparticles based on small organic molecules and macromolecules are emerging as viable alternatives. Small molecule based fluorophores are relatively easy to synthesize and characterize, and afford the

flexibility to incorporate desired functionalities and interactions with the biological systems; however most are susceptible to aggregation-induced self-quenching of fluorescence emission. The limited classes of molecules that exhibit strong fluorescence in the aggregated/solid states (often called aggregation-induced emission enhancement) include tetraphenylethylene,<sup>8</sup> diphenylbutadienes,<sup>9</sup> hexaphenylsilole<sup>10</sup> and diaminodicyano quinodimethanes (DADQs) as discussed in Sec. 1.2.3.2. The fluorescence enhancement of DADQs in crystals,<sup>11</sup> nanocrystals,<sup>12</sup> amorphous particles,<sup>13</sup> and thin films,<sup>14</sup> and the critical role of specifically oriented aggregation in the fluorescence enhancement<sup>15</sup> have been reported from our laboratory earlier, as discussed in Sec. 1.1.3.

An important and illustrative case that we have considered in this thesis work is the imaging of stomata in dicotyledon plant leaves; the stomatal apparatus and epidermal cells, as well as organelles like mitochondria and nuclei are relevant targets (Figure 2.1) and a brief introduction has been provided in Sec. 1.3.3.1. Stomatal imaging is critical for morphological and epidermal studies of plant species, understanding the stimuli responsive dynamics of inner/outer guard cell walls and related signal transduction pathways,16 and stomatal development issues like deposition pattern of callose in the guard cell wall.<sup>17</sup> Small molecule based fluorophores such as propidium iodide, safranin, aniline blue, DAF-2DA, BCECF-AM, H2DCF-DA, calcofluor white and acridine orange have served as popular choices for imaging epidermal constituents (Figure 1.10). 18-23 Shortcomings of many of these probes include high cost and specialized storage conditions like low temperature and protection from light, 24,25 the need to use non-aqueous, toxic solvents like DMSO, 26 carcinogenicity and mutagenicity;<sup>27</sup> aggregation-induced quenching of fluorescence due to factors such as selfabsorption, excimer/exciplex formation and energy transfer is a problem in most of them. In addition to low cost and easy storage, the critical attributes of an ideal dye for fluorescence imaging of stomata include hydrophilicity to minimise the binding to membranes, functionalities like ionic groups to selectively interact or bind with the cell wall, nucleus etc. and aqueous solubility to enable simple staining protocols.

DADQs are very relevant in this context (Sec. 1.1.3). First reported in the 1960s,<sup>28</sup> they can be directly synthesized from commonly available precursors; the simple molecular structure and design flexibility including hydrophilic/water soluble derivatives<sup>11</sup> imply low cost of preparation and usage. The high thermal and photochemical stability are important from an application point of view. The enhancement of fluorescence from solution to

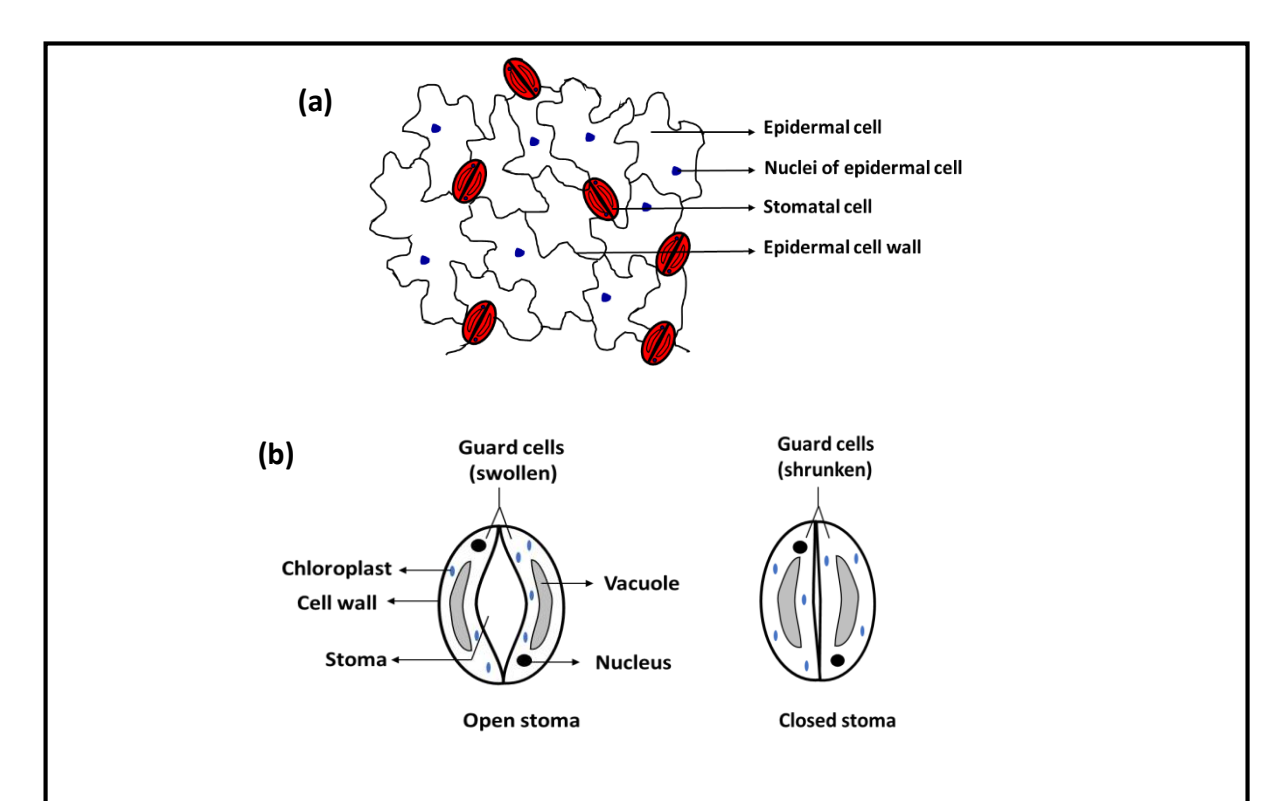


Figure 2.1. Pictorial representation of (a) lower epidermis of the plant leaves (b) open and closed stoma.

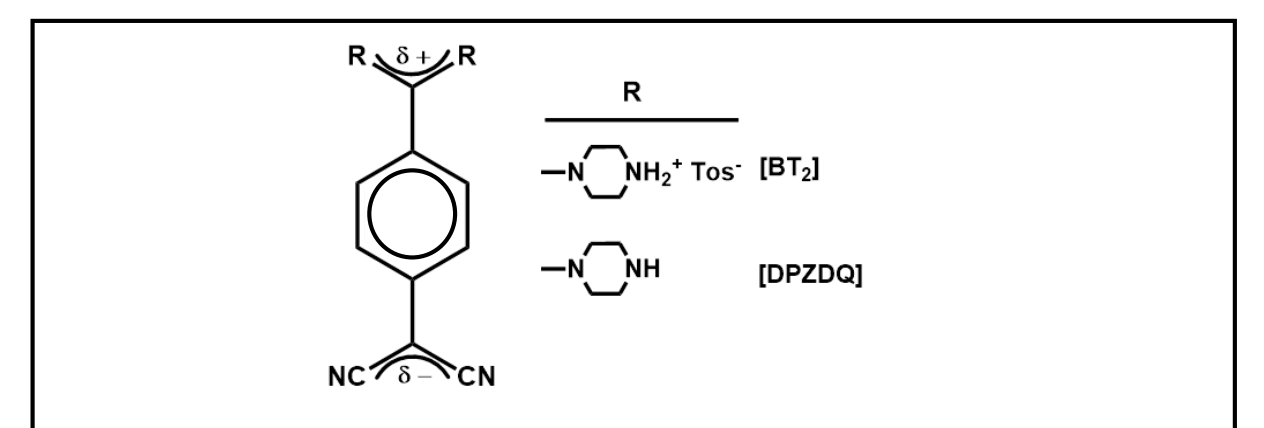


Figure 2.2. Molecular structure of the main DADQ derivatives discussed in this chapter, BT2 and DPZDO.

aggregated/solid states are uniquely relevant for imaging, as high concentrations of the dye can be used without self-quenching issues; even though a few aggregation-induced emission based luminogens have been developed as labels for organelles like membrane and mitochondria, <sup>29,30</sup> HeLa cells and MCF-7 breast cancer cells, <sup>31</sup> and extracellular calcium ions, <sup>32</sup> there are no examples of stomatal imaging using such dyes. In the following sections, we discuss the successful demonstration of high contrast, spatially well-resolved and selective imaging of stomatal and epidermal cell walls and nuclei in the epidermal layer of pea (Pisum sativum L. cv. Arkel) leaf, using the DADQ derivative, 7,7-bis(piperazinium)-8,8dicyanoquinodimethane bis(p-toluene sulfonate) (B<sup>2+</sup>[Tos<sup>-</sup>]<sup>2</sup> or simply BT<sub>2</sub>, Figure 2.2).<sup>33</sup> The general utility of DADQs is illustrated using the other derivative shown in Figure 2.2, 7,7-bis(piperazine)-8,8-dicyanoquinodimethane (DPZDQ).<sup>34</sup>

Choice of the DADQ derivatives, BT2 and DPZDQ allows an unambiguous illustration of the critical relevance of strong electrostatic and H-bonding interactions that could lead to strong binding with biological molecules; the consequent rigid environment and aggregation effects induce enhanced fluorescence emission in DADQs and facilitate effective imaging. The relatively low cost of the materials, small concentrations required for staining, solubility in aqueous and organic media, feasibility of quick and easy sample preparation in water or buffer media, and the high quality and selectivity of stomatal imaging achieved are highlighted; selective staining of specific cell structures by the choice of the medium as well as the solvent used to prepare the dye solution are significant. Calorimetry, microscopy and spectroscopy investigations, as well as control experiments with a range of DADQs, provide insight into the molecular level interactions that lead to the efficient and selective imaging. It is specifically demonstrated that binding with polygalacturonic acid and its salt are critical. Demethyl esterified pectin (calcium salt of polygalacturonic acid), the major component of the cell wall plays a dominant role in its dynamics; the calcium ions enhance the strength to handle the turgor pressure. Even though replacement of the calcium by ionic dye molecules during the staining can impair the cell viability, the concentrations of the DADQs that we employ do not affect the cells adversely as seen from some of the specific experiments we have carried out. Finally, we establish the relevance of DADQ based imaging in the context of the autofluorescence response of pea leaf epidermal cells, the general applicability of DADQs in fluorescence imaging of various other kinds of cells, and the stability and noncytotoxic nature of these novel imaging dyes which are of great practical importance.

#### 2.2. **Synthesis and characterization**

DPZDQ and BT<sub>2</sub> were synthesized using reported procedure, by the reaction of tetracyanoquinodimethane (TCNQ) with piperazine followed by salt formation with ptoluene sulfonic acid;<sup>33,34</sup> they were purified by recrystallization and characterized. Details of the instruments used and characterization studies carried out are added in Appendix B.

## $BT_2(7,7-Bis(piperazinium)-8,8-dicyanoquinodimethane bis(p-toluene sulfonate))$

Yield= 75%, recrystallized from acetonitrile; m.p. 310°C (dec.); FTIR (KBr):  $\bar{\nu}/\text{cm}^{-1}$ = 2177.4, 2138.6, 1136.1; <sup>1</sup>H NMR (d<sub>6</sub>-DMSO):  $\delta/ppm = 9.0$  (s, 4H), 7.49 (d, 4H), 7.38 (d, 2H), 7.12 (d, 4H), 6.88 (d, 2H), 3.8 (m, 4H), 3.46 (m, 4H), 2.2 (s, 6H); <sup>13</sup>C NMR (d<sub>6</sub>-DMSO):  $\delta/ppm = 21, 36, 41, 43, 48, 113, 118, 123, 125, 128, 132, 138, 139, 145, 150, 171; elemental$ analysis (calcd., found for BT<sub>2</sub>.H<sub>2</sub>O i.e.  $C_{32}H_{40}N_6O_7S_2$ ): %C = (56.23, 56.14), %H = (5.82, 5.85), %N = (12.15, 12.28).  $\lambda_{max}^{abs}$ ; 415 nm,  $\lambda_{max}^{em}$ : 538 nm, Stokes shift: 123 nm, fluorescence quantum yield: 14.2 % (solid state), 0.05 % (solution state), fluorescence lifetime: 0.63 ns,  $\varepsilon$ : 10.912 M<sup>-1</sup>cm<sup>-1</sup>, brightness: 154.942 M<sup>-1</sup>cm<sup>-1</sup>.

## **DPZDQ** (7,7-Bis(piperazine)-8,8-dicyanoquinodimethane)

Yield= 80%, recrystallized from DMF-ether; m.p. 300°C (dec.); FTIR (KBr):  $\bar{\nu}/\text{cm}^{-1}$ =2171.6, 2130.3, 1593.1; <sup>1</sup>H NMR (d<sub>6</sub>-DMSO):  $\delta/ppm$ =7.3 (d, 2H), 6.8 (d, 2H), 3.5 (s, 2H), 3.3-3.1 (m, 8H), 2.8 (m, 8H);  ${}^{13}$ C NMR (d<sub>6</sub>-DMSO):  $\delta$ /ppm = 168, 149, 132, 123, 118, 114, 53, 46, 34; elemental analysis (calcd., found for DPZDQ i.e.  $C_{18}H_{22}N_6$ ): %C = (67.15, 67.8), %H = (6.81, 6.83), %N = (26.15, 26.08).  $\lambda_{max}^{abs}$ ; 391 nm,  $\lambda_{max}^{em}$ : 522 nm, Stokes shift: 131 nm, fluorescence quantum yield: 5.8 % (solid state), 0.07 % (solution state), fluorescence lifetime: 0.75 ns, ε: 17,871 M<sup>-1</sup>cm<sup>-1</sup>, brightness: 103.652 M<sup>-1</sup>cm<sup>-1</sup>.

#### 2.3. Stomatal cells imaging

#### 2.3.1. Specimen preparation and imaging

Epidermal strips were carefully peeled from the abaxial surface of the leaves of 2–3 weeks old pea plant grown in a greenhouse at 25 °C with supplementary lighting, washed with water and cut into  $\sim 4 \times 4 \text{ mm}^2$  pieces. The strips were placed on a microscope slide, stained directly with the appropriate dye solution, washed by brief dipping in water, protected with a coverslip, and imaged. Alternately, the strips were placed in the MES buffer in a 6well plate and maintained either in the dark or illuminated with a 100 W tungsten lamp with water jacket protection. The specimen was then transferred to a 24-well plate containing the MES buffer with the required dye solution, washed, placed on a microscope slide, protected with a cover plate and imaged. A Leica model ZEISS LSM 880 confocal laser scanning microscope (CLSM) was used for imaging, and an Ar/Ar-Kr laser as the excitation (488 nm) source; emission in the 500–650 nm range was detected. Images were obtained using 60× and 40× objective lens. Parameters like the detector gain and amplification offset/gain were adjusted to optimize the fluorescence intensity of the targets and the background. Under these experimental conditions the dyes are found to be quite photo-stable. Images were processed using the ZEN lite software (ZEISS ZEN 3.1).<sup>35</sup>

Preparation of 2-(N-morpholino)ethanesulfonic acid (MES) buffer: MES (Aldrich chemicals) was dissolved in high purity water (Millipore MilliQ, resistivity =  $18 \text{ M}\Omega$  cm), the pH was adjusted to 7.0 by adding potassium hydroxide, and potassium chloride was added to form the final solution (10 mM in MES-KOH and 50 mM in KCl). All experiments were carried out using high purity water.

#### 2.3.2. Imaging in buffer free state

Imaging experiments with no special precaution taken to maintain the specimen alive by keeping in a buffer, are still useful for various epidermal and stomatal studies such as stomatal indexing and guard cell size and aperture measurements. This has the advantage that undesirable interactions between the buffer medium and the cell components, if any, are avoided. Therefore we have first tested the utility of the DADQs in imaging, by direct treatment of the prepared epidermal layer in a buffer-free state, with the fluorophore solution. Very small quantities of BT<sub>2</sub> as aqueous solution (15  $\mu$ L of 0.05 or 1 mM) or as DMSO solution (15 µL of 1 mM) were spread directly on the epidermal layer of pea leaf placed on a microscope slide, kept for ~ 2 min, washed briefly to remove the excess dye, protected with a coverslip and imaged directly in CLSM; processes like incubation for extended time are not required, and the amount of dye used is extremely small, 0.75–15 nmol. Well resolved fluorescence images could be recorded (Figure 2.3; bright field images are also shown). When the lower concentration of BT<sub>2</sub> in water is used, only the inner wall of the guard cells is stained (Figure 2.3d-f); with the higher concentration, walls of the guard cell, as well as walls and nuclei of the epidermal cells are stained clearly (Figure 2.3g-i). Interestingly, BT<sub>2</sub> solution in DMSO on the other hand, enters the guard cell and stains its nucleus as well (Figure 2.3j–1); the 3-D view constructed using Z-stack images (Figure 2.4) shows clearly the staining of the nucleus. Interestingly, the staining by BT<sub>2</sub> is found to persist in samples which were washed rigorously and repeatedly, showing clearly its strong binding, a point explored in Sec. 2.3.4.

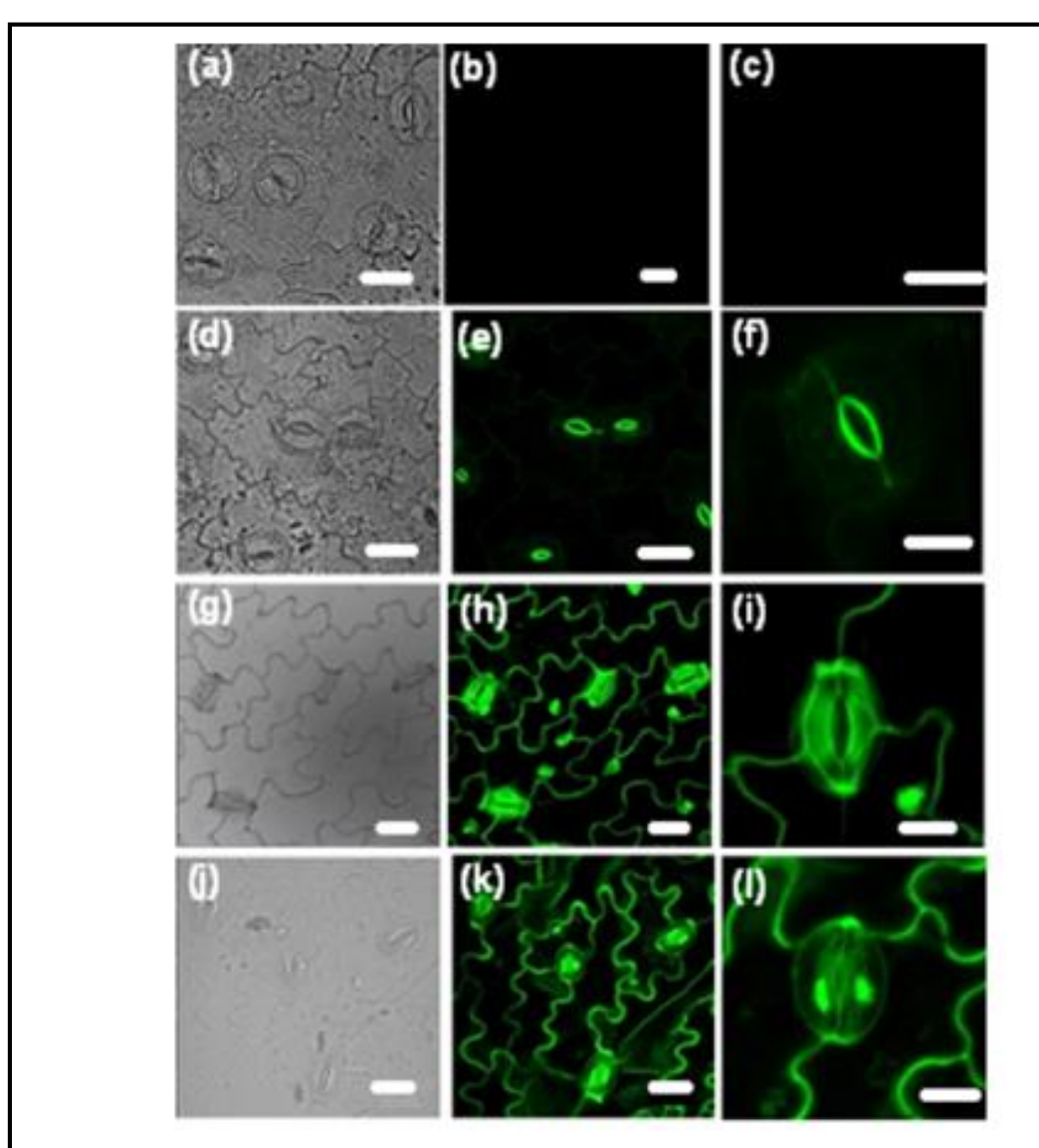


Figure 2.3. CLSM images of pea epidermis in buffer-free state: (a-c) control, and stained using, (d-f)  $BT_2$  solution in water (15  $\mu$ L of 0.05 mM), (g-i)  $BT_2$  solution in water (15  $\mu$ L of 1 mM), and (j-l)  $BT_2$  solution in DMSO (15  $\mu$ L of 1 mM); bright field images are shown in (a, d, g, j), and the fluorescence images at two magnifications in the remaining panels ( $\lambda_{exc}$ = 488 nm). Scale bar: 10  $\mu$ m in (c), (f), (i), (l); 20  $\mu$ m in all others.

#### 2.3.3. **Imaging in buffer medium**

Imaging experiments were also conducted on the epidermal layer kept in 500 µL of a buffer solution in which BT<sub>2</sub> solution in water (15 µL of 1 mM) has been added earlier; it may be noted that the effective concentration of BT<sub>2</sub> in this case is only 29 μM. After allowing the dye adsorption (for just 10 min), the sample was taken out, washed and placed on a microscope slide, protected with a coverslip and imaged in a CLSM. With the very low

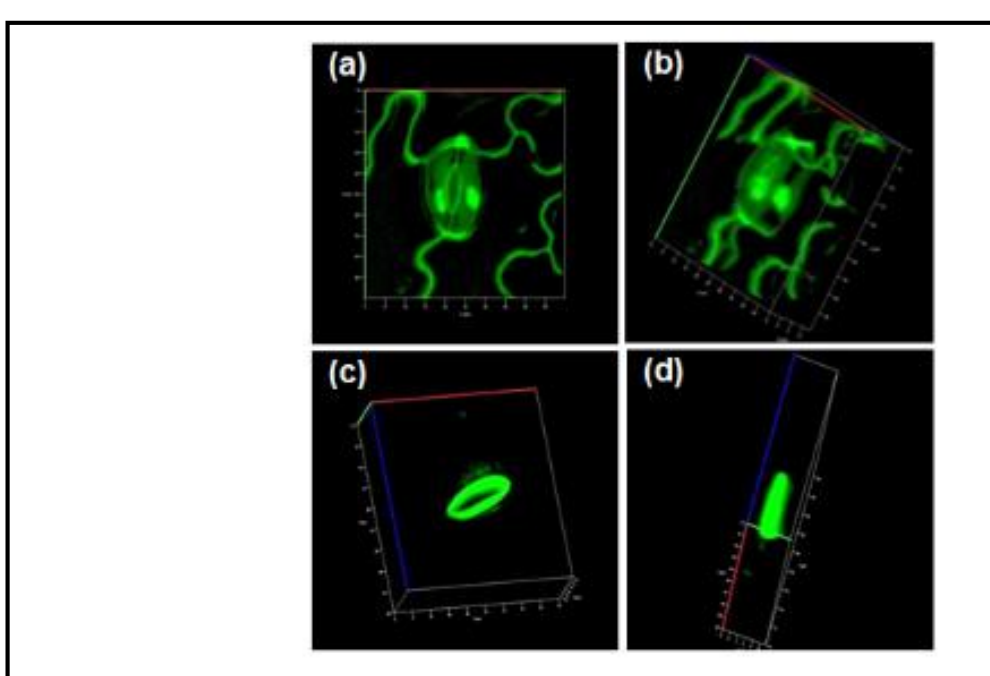


Figure 2.4. 3-D reconstructions (at different viewing angles) from CLSM Z-stack images of the pea epidermis stained using (a,b) DMSO solution of  $BT_2$  (15  $\mu L$  of 1 mM), in buffer-free state, and (c,d)aqueous solution of BT<sub>2</sub> (15  $\mu$ L of 1 mM) in buffer medium ( $\lambda_{exc}$ = 488 nm).

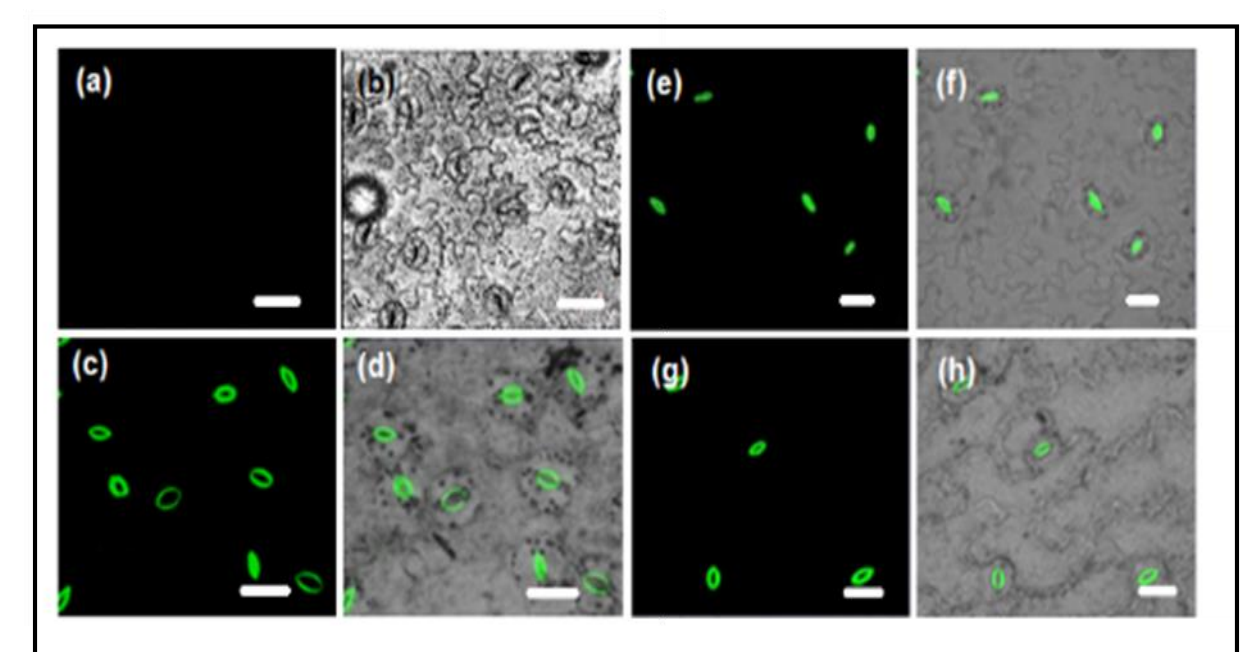


Figure 2.5. CLSM images of (fluorescence and overlay of fluorescence with bright field) of pea epidermis kept in buffer medium (500  $\mu$ L): (a,b) control, and stained using BT<sub>2</sub> solution in water (15  $\mu$ L of 1 mM) under different conditions: (c,d) irradiated for 3 h and stained, (e,f) kept in the dark for 3 h and stained, (g,h) stained and irradiated for 3 h ( $\lambda_{exc}$ = 488 nm). Scale bar: 20  $\mu$ m.

dye concentration used, only the inner guard cell wall is stained. Images obtained using BT2 in water, of the samples maintained under different conditions are shown in Figure 2.5; the guard cells are closed in the samples kept in the dark and stained (Figure 2.5e,f), but open in samples photo-irradiated and stained (Figure 2.5c,d), as well as those that were photoirradiated in presence of the dye (Figure 2.5g,h). The latter images clearly prove that the staining process did not affect the stomatal opening; the related question of cytotoxicity is addressed in Sec. 2.7. Figure 2.4c,d shows the 3-D view of the open inner guard cell wall. It is clear that the staining process does not affect the stomatal opening. BT<sub>2</sub> solution in DMSO gives very similar results (Figure 2.6). As the buffer helps to keep the cells alive, staining with BT<sub>2</sub> is of potential interest in live-cell studies that target the dynamics of the cell wall or related phenomena. A comparison with dyes such as aniline blue, 2',7'-dichlorofluorescein diacetate (DAF-2DA), 2',7'-bis(2-carboxyethyl)-5(6)-carboxyfluorescein acetoxymethyl ester (BCECF-AM), 4,5-diaminofluorescein diacetate (H2DCF-DA), propidium iodide (PI) and safranin, commonly used for stomatal imaging shows that BT<sub>2</sub> is advantageous in terms of the concentrations and time required for staining, as well as the solvent selections ( Table 2.1); in view of toxicity and environmental impact considerations, the possibility of using aqueous solutions is of major practical advantage, as noted earlier. Further, BT<sub>2</sub> has the unique capability of selective staining of the walls and nuclei of the guard cells and epidermal cells by suitable variation of the medium and solvent.

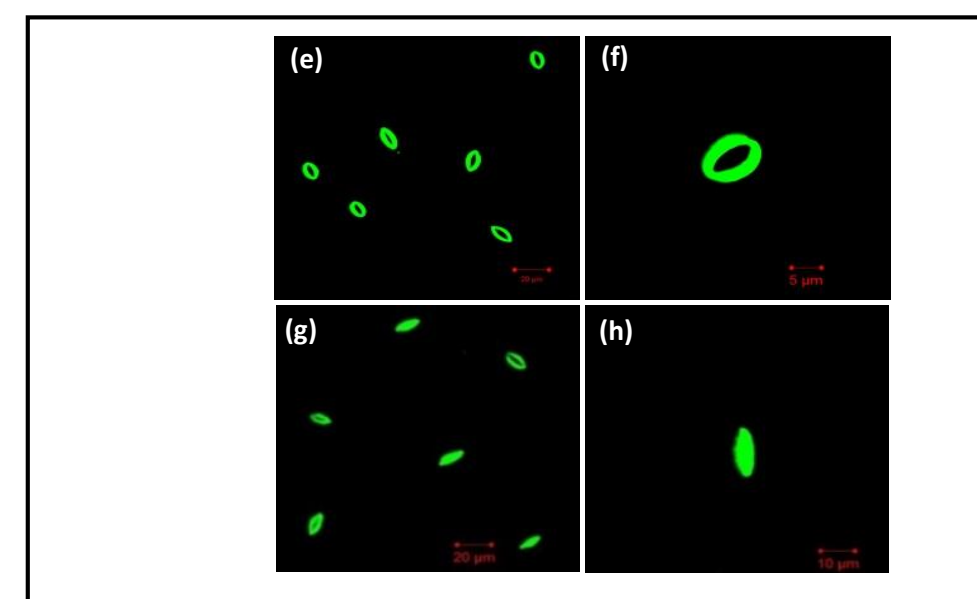


Figure 2.6. CLSM fluorescence images (at different magnifications) of pea epidermis kept in buffer medium (500  $\mu$ L) and stained with BT<sub>2</sub> solution in DMSO (15  $\mu$ L of 1 mM) under different conditions: (a, b) irradiated for 3 h and stained, (c, d) kept in the dark for 3 h and stained.

**Table 2.1.** Comparison of commercial dyes used for stomatal imaging with  $BT_2$  in terms of conditions and selectivity of staining.

Dye	Solvent	Concen tration (mM)	Staining time (min)	Part stained	Ref.	
Sample in buffer						
Aniline Blue	Water	0.67	-	Cell wall	36	
Aniline Blue	Water	0.67	-	Cell wall	37	
DAF-2DA	DMSO	0.02	30	Full cell	38, 39	
DAF-2DA*	DMSO	0.01	30	Full cell	40	
BCECF-AM*	DMSO	0.005	30	Full cell	40, 38	
H2DCF-DA*	Ethanol	0.03	30	Full cell	40	
$BT_2$	Water, DMSO	0.029	10	Inner cell walls	This work	
	Sample in buffer-free state					
PI	Water	1.5	2	Epidermis cell wall	41	
PI	Water	0.03	1-5	Cell wall	42	
PI	Water	0.02	5	Cell wall of viable cells	18	
Safranin	Ethanol-water	28.5	-	Cell wall	43	
Safranin	Water	28.5	-	Cell wall	44	
Safranin	Ethanol-water	28.5	-	Cell wall	45	
Safranin	Water	28.5	4 - 8	Cell wall	46	
BT <sub>2</sub>	Water, DMSO	1.0	2	Cell walls / nucleus	This work	

<sup>\*</sup>Dark state required.

## 2.3.4. Imaging experiments with different DADQs

Imaging experiments were conducted also with DPZDQ (Figure 2.2) to explore the general utility of DADQs in imaging. Even though DPZDQ has limited solubility in water, good quality images could be obtained using aqueous as well as DMSO solutions (Figure 2.7). With the DMSO solution, it was noticed that the washed samples displayed reduced staining compared to the unwashed ones, suggesting partial removal of the dye. We have found that other DADQ derivatives with amine groups as in DPZDQ (Figure 2.7) are also efficient for stomatal imaging; this should allow expanding the portfolio of DADQs for bioimaging applications.

$$R = -N NH_{2}^{+} Tos^{-} BT_{2}$$

$$-N NH DPZDQ$$

$$-N N-CH_{3} BMPDQ$$

$$-N O BMDQ$$

$$BPDQ$$

Dire	In water		In DMSO		
Dye	No wash	With wash	No wash	With wash	
BT <sub>2</sub>					
DPZDQ		• •		0 0 30 m	
BMPDQ		81 20 pm			
BMDQ	Insoluble	Insoluble	2010	20 yrs	
BPDQ	Insoluble	Insoluble	2 m	* + 20 jm	

Figure 2.7. Comparison of CLSM images of pea epidermis in buffer-free state, stained using 15  $\mu$ L of 1.75 mM solutions of different DADQ derivatives (structures shown) in water and DMSO for 2 min, with and without washing. Images recorded for control samples without the dye under identical microscope settings are also shown.

#### 2.4. **Molecular level interactions**

In order to gain insight into the molecular level interactions that facilitate the staining process, we have carried out control experiments with a few more selected DADQ derivatives. As seen in Figure 2.7, BT<sub>2</sub> (with the ionic piperazinium groups) and DPZDQ (with the H-bonding piperazine groups) stain the stomata; the stronger binding in the case of the former, suggested by the experiments on the washed samples, can be attributed to the electrostatic nature of the interactions. Experiments with DADQ derivatives bereft of both functionalities showed no effective staining (Figure 2.7).

## **2.4.1.** Isothermal titration calorimetry

The dominant biomacromolecule in the cell wall, namely polygalacturonic acid (PGA), in neutral (carboxylic acid) as well as anionic (calcium salt of carboxylate) states, is likely to be a major target for molecular level interactions for BT<sub>2</sub> and DPZDQ. In an effort to probe this point, isothermal titration calorimetry (ITC) experiments were carried out with 125 μM solution of BT<sub>2</sub> and 2 μM solution of DPZDQ in aqueous medium, <sup>47</sup> titrated against the 4 mM and 75 µM solution of sodium salt of PGA (PGA<sup>-</sup>Na<sup>+</sup>) respectively, also dissolved in water (concentration based on the assay of PGA<sup>-</sup>Na<sup>+</sup> (75%) was used in the analysis) at 298 K. The thermograms recorded are shown in Figure 2.8; data analysis of BT<sub>2</sub> vs PGA<sup>-</sup>Na<sup>+</sup> titration shows that the heat changes follow a simple binding model with an equilibrium constant of  $1.33 \times 10^6 \text{ dm}^3 \text{ mol}^{-1}$  and enthalpy and entropy changes of  $-5.97 \text{ kJ mol}^{-1}$  and 97.1 J mol<sup>-1</sup> K<sup>-1</sup> respectively (Table 2.2). These are indicative of strong binding, effected through enthalpic and entropic contributions. The molar ratio for binding is found to be 1.75, close to that expected for the two piperazinium sites of BT<sub>2</sub> locking with the negatively charged carboxylate sites on the PGA polyanion. ITC experiments with DPZDQ and PGA<sup>-</sup>Na<sup>+</sup> (Table 2.2, Figure 2.8c,d), on the other hand, indicated no meaningful binding; this may be attributed to the absence of any significant electrostatic interactions between the two. Due to problems of solubility in water, PGA in the fully neutral form could not be studied; organic media were not attempted, as it would be inappropriate for model studies relevant to processes in the biological system.

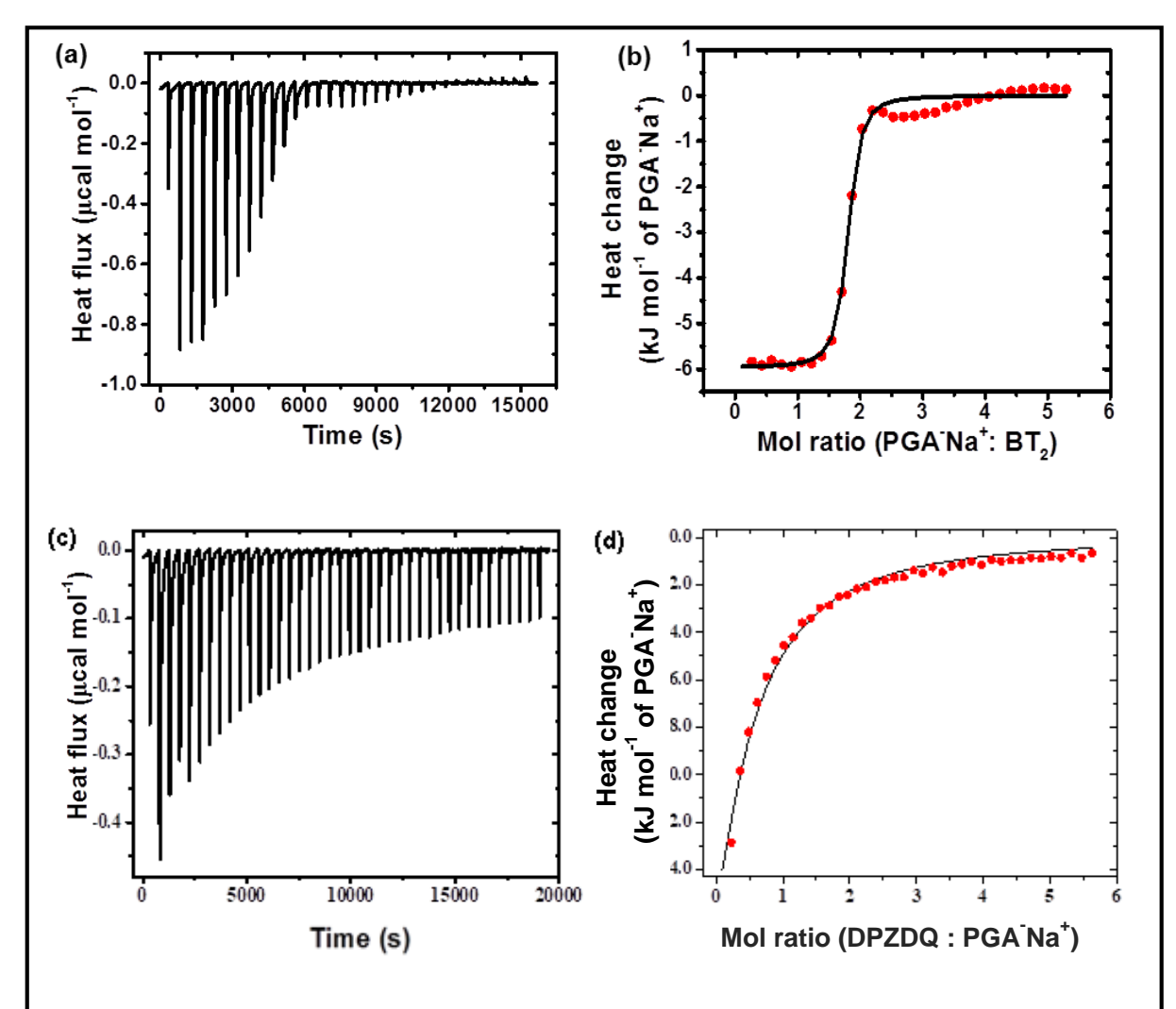


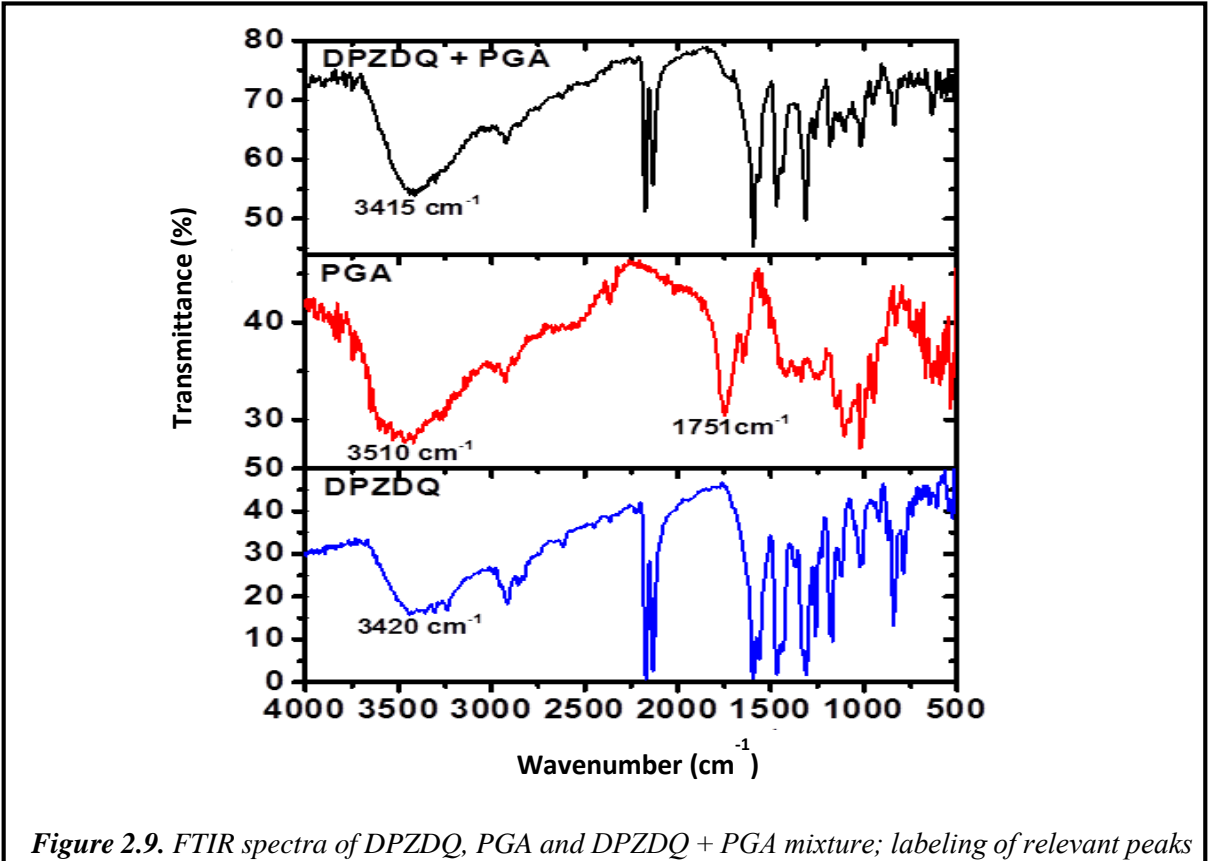
Figure 2.8. (a, c) Raw and (b, d) integrated thermograms from the isothermal titration of (a, b) PGA<sup>-</sup>Na<sup>+</sup> into BT<sub>2</sub> and (c, d) DPZDQ into PGA<sup>-</sup>Na<sup>+</sup> in aqueous solution. Fitting of the integrated thermogram is shown in (b, d).

Table 2.2. Binding and thermodynamic parameters from the ITC experiments on BT2 and DPZDQ with  $PGA^-Na^+$ ; errors are shown in parenthesis. N: stoichiometry, K: binding affinity,  $\Delta H^0$ : enthalpy change,  $\Delta G^{\circ}$ : free energy change,  $\Delta S^{\circ}$ : entropy change.

Parameter	Value (error)			
Tarameter	PGA <sup>-</sup> Na <sup>+</sup> : BT <sub>2</sub>	DPZDQ : PGA <sup>-</sup> Na <sup>+</sup>		
N	$1.74 (\pm 0.012)$	0.117 (± 0.15)		
K (10 <sup>5</sup> dm <sup>3</sup> mol <sup>-1</sup> )	13.3 (± 2.9)	0.116 (± 0.016)		
ΔH <sup>o</sup> (kJ mol <sup>-1</sup> )	-5.970 ( ± 0.0741)	-161.5 (± 217.2)		
ΔG° (kJ mol <sup>-1</sup> )	-34.9	-23.2		
$\Delta S^{o}(J \text{ mol}^{-1} K^{-1})$	97.1	-464		

## 2.4.2. Fourier transform infra-red (FTIR) spectroscopy

Since ITC experiment does not clearly demonstrate any molecular level binding of DPZDQ, in order to probe the possible interactions that could facilitates its staining, we have recorded the FTIR spectra of DPZDQ, PGA and the mixture of the two prepared by grinding the solids together (Figure 2.9). The prominent peak due to the carbonyl stretch vibration in PGA at ~1751 cm<sup>-1</sup> is found to diminish significantly in the mixture; this is likely to be a consequence of the H- bonding interaction with the piperazine moieties in DPZDQ. It is noticed also that the broad peaks due to N-H stretch vibration in DPZDQ centered around 3420 cm<sup>-1</sup> and O-H stretch vibration in PGA around 3510 cm<sup>-1</sup>, transform to a relatively narrower peak at 3415 cm<sup>-1</sup> in the mixture, which again is suggestive of a well-defined Hbonding situation.



is indicated

# 2.4.3. Field emission scanning electron microscopy (FESEM) and energy dispersive Xray (EDX) spectroscopy

PGA in the leaf cell walls has both ionic (carboxylate) and neutral (carboxylic acid) sites. The well-known 'egg box model' envisions Ca2+ ions stitching the PGA chains together through the carboxylate groups.  $^{48}$  The strong binding between  $PGA^{-}Na^{+}$  and  $BT_{2}$ demonstrated by the ITC experiment, is enabled by the interaction of the dicationic moiety,  $B^{2+}$  with the ionic sites of PGA $^-$ . This would involve displacement of the  $Ca^{2+}$  ions as

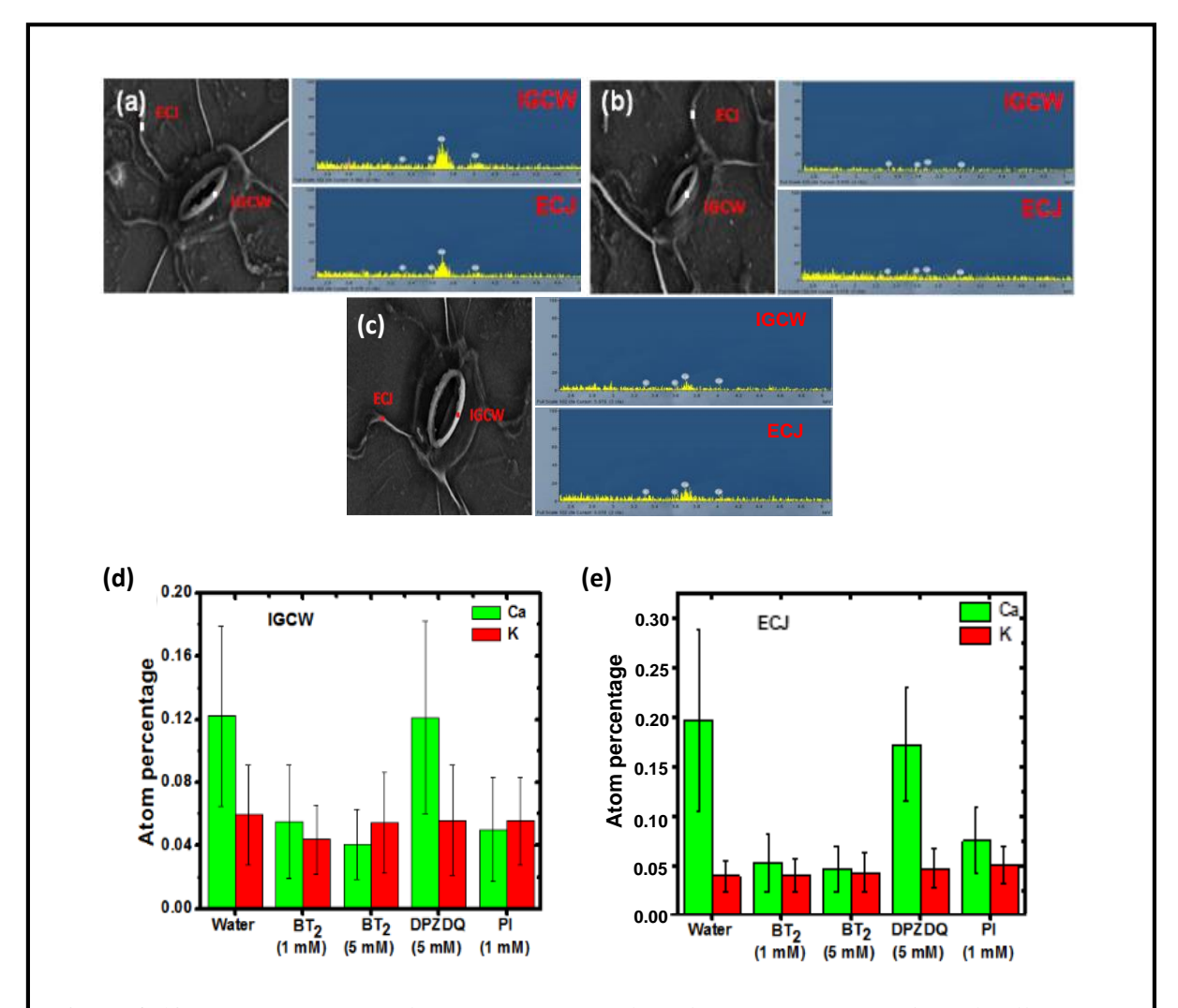


Figure 2.10. FESEM image and EDX spectra of selected regions (ECJ: epidermal cell junction; IGCW: inner guard cell wall) shown in the image, of pea epidermis (a) placed in pure water, and (b) stained using BT<sub>2</sub> solution in water (0.5 mL of 5 mM) for 2 min. (c) stained using DPZDQ solution in water (0.5 mL of 5 mM) for 2 min. Average Ca and K content in the (d) IGCW (e) ECJ region of the pea epidermis under different conditions.

reported with propidium iodide using fluorescence imaging;<sup>49</sup> this possibility is further supported by the distance of 7.7 Å between the ammonium N atoms in the piperazinium moieties of BT<sub>2</sub>,<sup>33</sup> which fits well with the inter-chain distance of 6–8 Å in calcium pectate.<sup>50</sup> We visualized that a precise analysis of the local elemental composition, specifically in terms of the Ca content in the guard cell wall and regions such as the epidermal cell junctions could provide direct and critical insight into this; the composition of other ions like K<sup>+</sup> which are not involved in the binding of the dye with the biomacromolecules would serve as useful control. The epidermal layer placed in pure water, as well as in aqueous solution of BT<sub>2</sub> and subsequently washed, were imaged in a FESEM, and EDX spectra recorded at several points

**Table 2.3.** Atom % of Ca and K (with standard deviations) on the inner guard cell wall (IGCW) and epidermal cell junction (ECJ) regions (Figure 2.10) of fresh (in water) and stained epidermis layer of pea plant leaf, determined using EDX spectroscopy with FESEM; dyes used are BT<sub>2</sub>, DPZDQ, PI.

Sample treatment	IGCW		ECJ	
Sample treatment	Ca	K	Ca	K
Water	0.122	0.0595	0.197	0.039
	(0.0568)	(0.0315)	(0.0917)	(0.0162)
BT <sub>2</sub> (1 mM in water)	0.0549	0.0438	0.0519	0.0400
212 (1 1111/1 111 // 4141)	(0.0358)	(0.0220)	(0.0290)	(0.016)
BT <sub>2</sub> (5 mM in water)	0.0406	0.0544	0.0466	0.0421
	(0.0222)	(0.032)	(0.0230)	(0.020)
DPZDQ (5 mM in water)	0.121	0.056	0.172	0.0467
	(0.0610)	(0.035)	(0.0567)	(0.0195)
PI (1 mM in water)	0.0500	0.0555	0.0744	0.0503
2 2 (2 mm/1 m water)	(0.0330)	(0.0277)	(0.0332)	(0.0180)

**Table 2.4.** Atom % of Ca and K (with standard deviations) on the inner guard cell wall (IGCW) and epidermal cell junction (ECJ) regions, of epidermis layer of pea plant leaf maintained in water, MES buffer and MES buffer containing BT<sub>2</sub>.

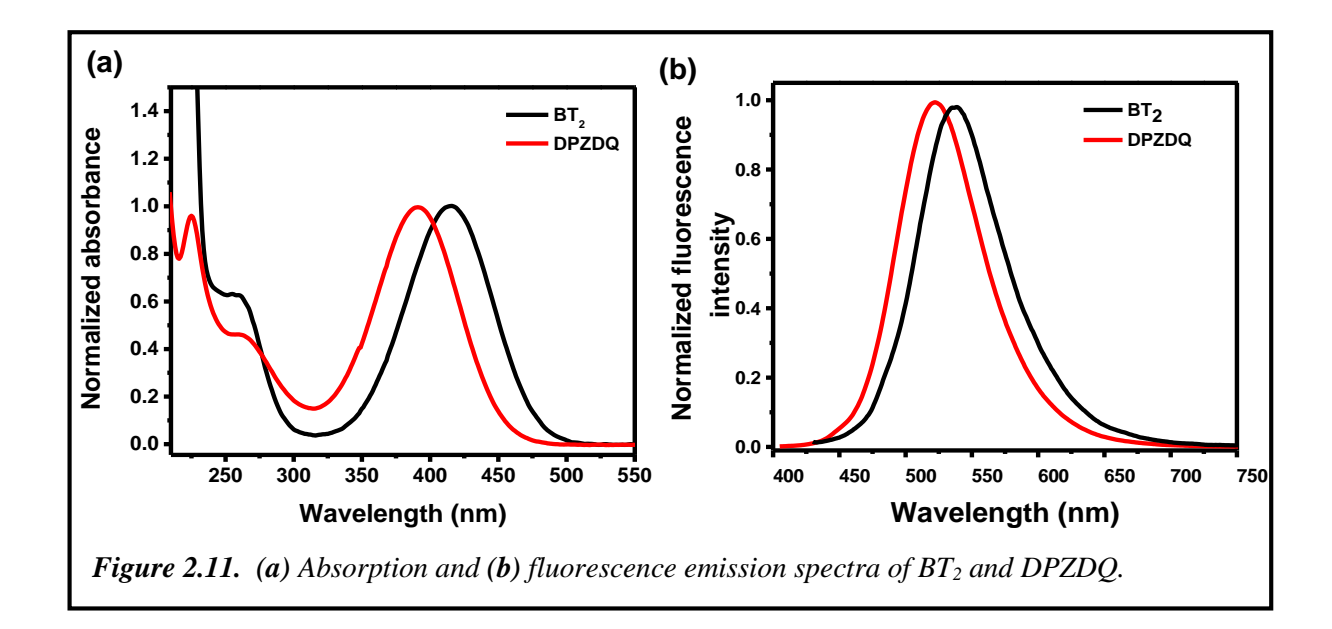
Cample treatment	IGCW		ECJ	
Sample treatment	Ca	K	Ca	K
Water	0.122	0.0537	0.197	0.0445
	(0.0568)	(0.0409)	(0.0917)	(0.0345)
MES buffer (pH=7.0)	0.0475	0.186	0.173	0.525
	(0.0378)	(0.111)	(0.118)	(0.173)
BT <sub>2</sub> (1 mM in water + MES buffer)	0.0180	0.219	0.093	0.731
	(0.00920)	(0.0708)	(0.0450)	(0.162)

in the relevant regions; the images and representative spectra are shown in Figure 2.10a,b. Average values of the atomic content of Ca and K in the inner guard cell wall region under different treatments of the epidermis including two concentrations of BT2, DPZDQ and propidium iodide are plotted in Figure 2.10d; the relevant values are collected in Table 2.3. A clear reduction in the Ca content is seen in the samples treated with BT<sub>2</sub>, with the effect being enhanced with higher concentration of the dye; changes in the K content are not significant. DPZDQ has practically no impact as expected (Figure 2.10d). Experiments with propidium iodide show effects similar to BT<sub>2</sub>. Parallel trends are seen in the epidermal cell junction as well (Figure. 2.10e). It is important to note that all these experiments used pure water medium for placing the samples; as expected, the buffer medium itself can disturb the composition of Ca and K ions as shown by the data presented in Table 2.4.

The various experiments presented above establish the binding of DADQs with PGA in different forms. The staining pattern of the guard cell walls (inner and outer) and epidermal cell wall (Figure 2.3) is a consequence of the dye concentration, and likely to be related to the PGA content in the different regions. With higher concentrations, the nuclei of the epidermal cells also get stained, as the epidermal cell walls are relatively thinner. The DMSO medium with a lower dielectric constant than water, allows easier passage of the BT<sub>2</sub> salt into the guard cell leading to the staining of the nucleus. In the case of the nuclei, B<sup>2+</sup> is likely to bind to the polyanions of the nucleic acids; in this context, it is notable that DPZDQ does not stain the nucleus.

#### 2.4.4. Fluorescence spectroscopy

Having gained an understanding of the molecular level interactions responsible for the dye binding with the cell wall or organelles, we have probed the basis for the strong fluorescence that facilitates the bright and high contrast imaging. As noted earlier, the DADQs show enhanced emission in the aggregated state due to the restriction of internal motions as well as the obstruction of intermolecular energy transfer pathways 11,16; the former would indeed be relevant in highly viscous and rigid environments.<sup>47</sup> The absorption and fluorescence emission spectra of BT<sub>2</sub> and DPZDQ are shown in Figure 2.11. In order to mimic the impact of the binding of BT<sub>2</sub> and DPZDQ in the cell wall, we have monitored its fluorescence response in aqueous medium, in presence of increasing amount of PGA<sup>-</sup>Na<sup>+</sup>. 0.5 mL of 0.2 mM aqueous solution of BT<sub>2</sub> was taken in a quartz cuvette and appropriate



volumes of a 10 mM solution of PGA<sup>-</sup>Na<sup>+</sup> were added to obtain varying mol ratios (polymer: BT<sub>2</sub>; calculated using the monomer molecular weight, taking into account the purity of the polymer). The solution was mixed thoroughly and made up to 3 ml in each case, ensuring identical concentration of BT<sub>2</sub> in all the experiments (Figures 2.12).

The absorbance remains nearly constant, as the  $BT_2$  concentration is kept the same. However as the polymer:  $BT_2$  mol ratio increases, the fluorescence intensity increases and begins to saturate above a ratio of ~200:1 (Figure. 2.13a); the  $\lambda_{max}$  remains nearly constant

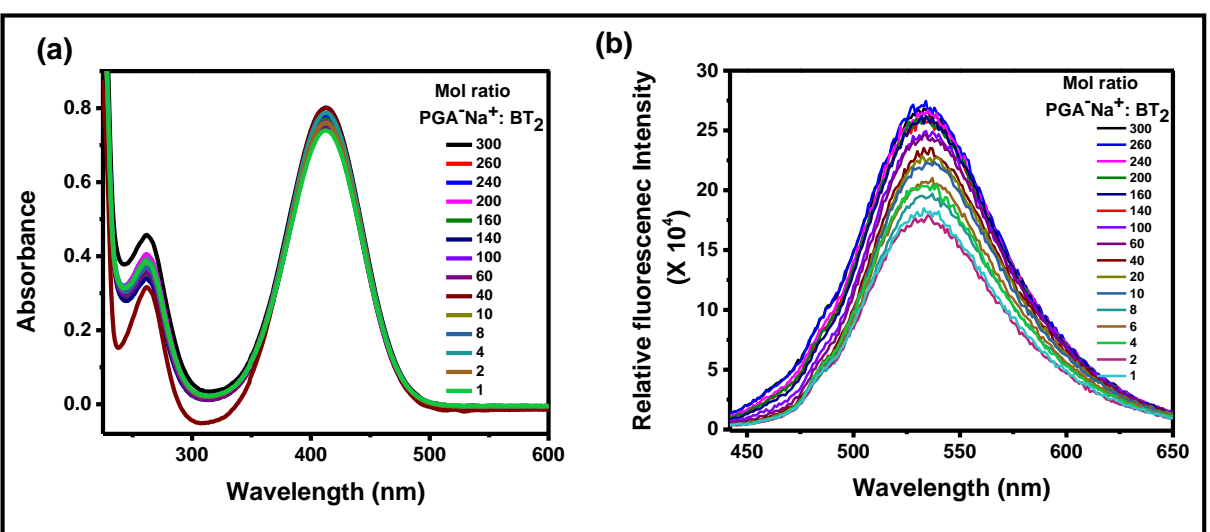


**Figure 2.12**. (a) Absorption and (b) fluorescence emission spectra of  $BT_2$ - $PGA^-Na^+$  from mole ratio 1:1 to 1:300.

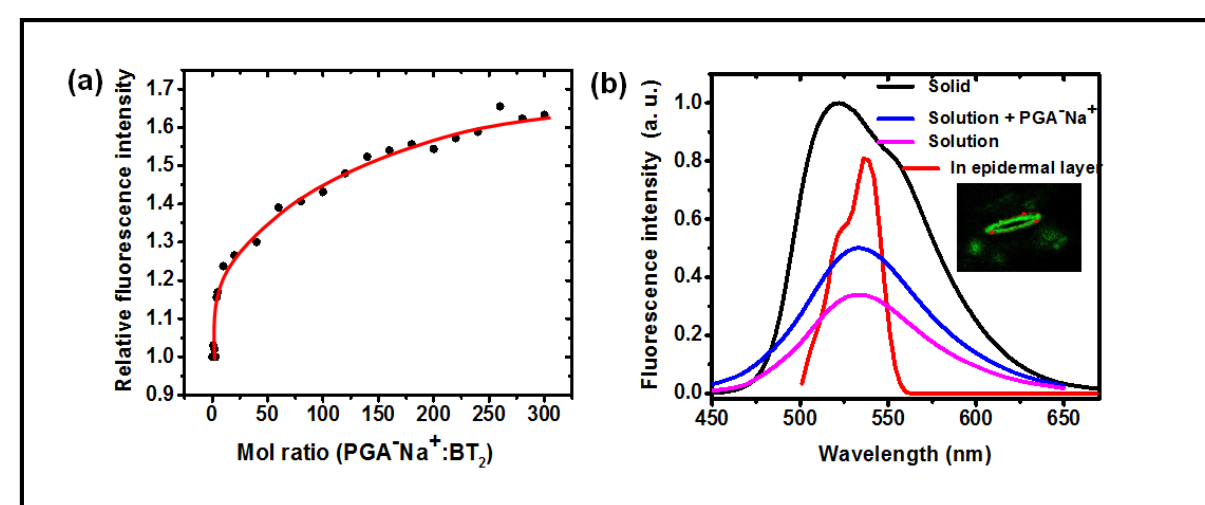


**Figure 2.13.** (a) Variation of the intensity of the fluorescence emission of  $BT_2$  on adding  $PGA^-Na^+$ in increasing mol ratios (the line is only a guide to the eye); (b) fluorescence emission spectra of  $BT_2$  in different forms: as microcrystalline solid, aqueous solution, aqueous solution with  $PGA^-Na^+$ (200:1 ratio) and stain in pea epidermal layer (recorded in CLSM at the red points shown in the image in the inset).

at ~535 nm as in the pure aqueous solution (Figure. 2.13b). These observations suggest that the interaction between the dye and the polymer and the local viscosity due to the polymer chains reduce the internal motions of the dye molecule, leading to fluorescence enhancement. The emission spectrum recorded on the CLSM corresponding to the fluorescence image of the stomatal guard cell stained with BT<sub>2</sub> (Figure. 2.13b) shows a  $\lambda_{max} \sim 537$  nm with a shoulder at ~525 nm. The blue shifted peak is indicative of the presence of neighboring zwitterionic BT<sub>2</sub> molecules, and their local field effects. <sup>15</sup> This is supported by the emission spectrum of BT<sub>2</sub> in the microcrystalline solid with a  $\lambda_{max}$  at ~522 nm (Figure. 2.13b); the broadening in this case arises due to well-known effects of different intermolecular interactions in the solid lattice. It should be noted that the emission intensity is enhanced significantly in the solid;<sup>11</sup> the spectrum in the figure is meant only to highlight the peak positions. The various observations suggest that the BT<sub>2</sub> molecules exist in isolated (as in solution, but in a rigid environment) as well as aggregated (as in the solid) states within the cell wall; similar situation is likely in the case of nucleus staining as well. The strong fluorescence emission of BT<sub>2</sub> bound within the confines of the cell can be attributed to the restriction of excited state geometry relaxations as well as local aggregation effects.

## 2.5. General utility of DADQs

In order to probe the general utility of BT<sub>2</sub>, imaging experiments were carried out with leaves of dicotyledon plants such as crape jasmine (*Tebernaemontana divaricate*), paper rose (*Bougainvillea glabra*), and thale cress (*Arabidopsis thaliana*) as well as a monocotyledon plant onion (*Allium cepa*). It showed that BT<sub>2</sub> is useful for a range of specimens (Figure. 2.14). In addition, we have carried out the fluorescence imaging experiments with live DU145 human prostate cell lines (live mammalian cells) and synechocystis pcc 6803 cells (cyanobacteria, fixed cells) using BT<sub>2</sub> (15 μl of 1 mM aqueous solution) and BBEDQ (7,7-bis(benzylamino)-8,8-dicyanoquinodimethane, 5 μl of 5 mM DMSO solution) respectively; the observations confirm that they are potentially useful for imaging different kinds of cells (Figure 2.15).

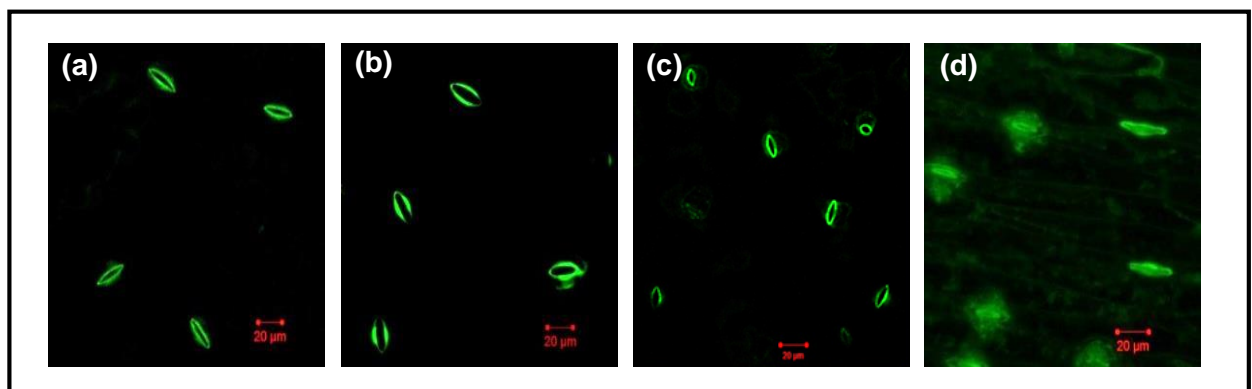


**Figure 2.14.** CLSM images of stomata in the leaves of dicotyledon plants, (a) crape jasmine (Tabernaemontana divaricate), (b) paper rose (Bougainvillea glabra), and (c) thate cress (Arabidopsis thaliana), as well as a monocotyledon plant, (d) onion (Allium cepa) maintained in 500  $\mu$ L buffer and stained using 15  $\mu$ L aqueous solution of BT<sub>2</sub> having concentrations, 5 mM (a-c) and 0.05 mM (d).

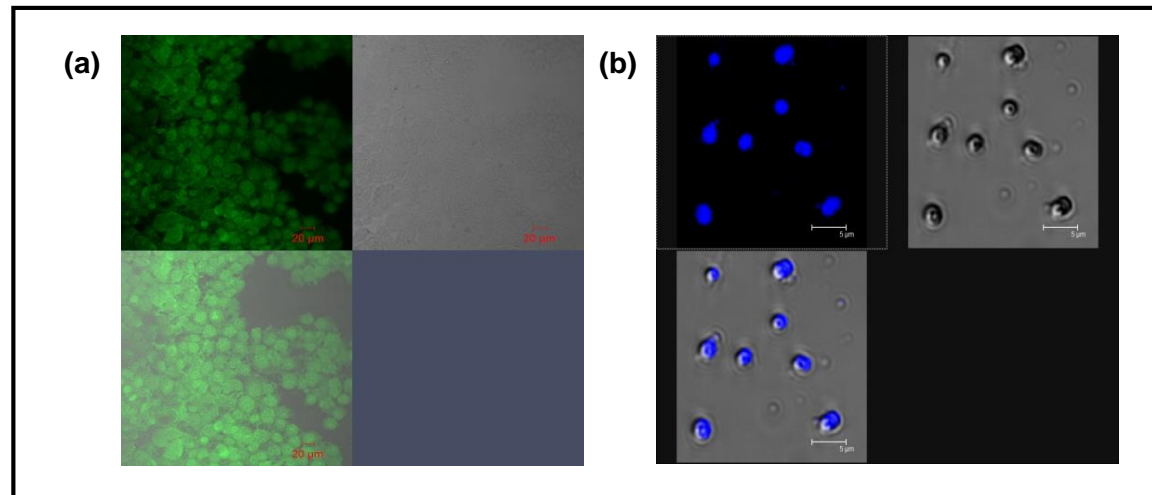
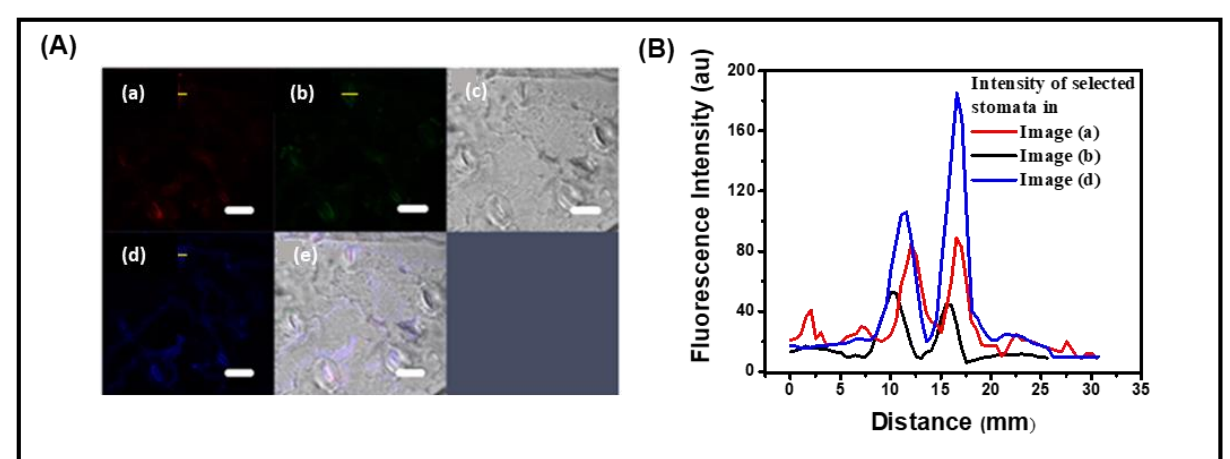


Figure 2.15. CLSM images (fluorescence and overlay of fluorescence with bright field) of the stained (a) DU145 cell lines using  $BT_2$  and (b) synechocystis pcc 6803 cells using BBEDQ.

#### **2.6. Autofluorescence analysis**

As various biological systems exhibit autofluorescence, it is pertinent to verify the relevance of BT<sub>2</sub> based imaging in the current context. Autofluorescence of the guard cell wall arises due to components such as ferulic acid, p-coumaric acid and cinnamic acid present; pattern, color and intensity vary with the species. Cell walls of the pea epidermis the layer are known to show relatively weak autofluorescence compared to other species.<sup>51,52</sup> We have recorded the autofluorescence response of the pea leaf epidermal cells in the CLSM



**Figure 2.16.** (A) CLSM images using autofluorescence of fresh epidermis layer: (a)  $\lambda_{exc} = 514$  nm,  $\lambda_{em} = 540\text{-}600 \text{ nm}$ , laser power: 100%, master gain: 1077 V, (b)  $\lambda_{exc} = 488 \text{ nm}$ ,  $\lambda_{em} = 490\text{-}570 \text{ nm}$ , laser power: 100%, master gain: 940 V, (c) bright field, (d)  $\lambda_{exc} = 405$  nm,  $\lambda_{em} = 410$ -470, laser power: 35%, master gain : 881 V, (e) overlay of fluorescence with bright field. Scale bar: 20 μm. (B) Fluorescence intensity profiles [along the yellow lines marked on the stomata in the images in (Aa, Ab, Ad)].

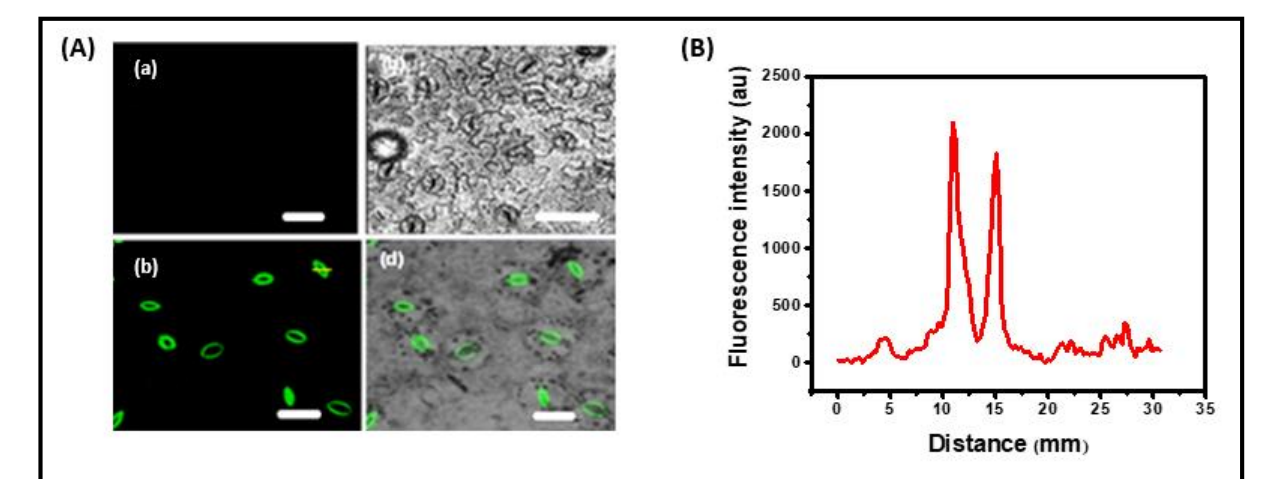


Figure 2.17. (A) CLSM Images (fluorescence and overlay of fluorescence with bright field) of pea epidermis kept in buffer medium (500 μL): (a, b) control, and (c, d) stained using BT<sub>2</sub> solution in water (15  $\mu$ L of 1 mM);  $\lambda_{exc} = 488$  nm,  $\lambda_{em} = 500-570$  nm, laser power: 5% and master gain: 700-800 V. Scale bar: 20 µm. (B) Fluorescence intensity profile [along the yellow line marked on the stomata in the image in (Ac)].

by exciting at different wavelengths: 514, 488 and 405 nm. The images obtained even with significantly higher laser power and gain (Figure 2.16A), are quite dull compared to those obtained with BT<sub>2</sub> based imaging (Figure 2.17A) highlighting the utility of the latter; the enhancement of brightness is quantified by the fluorescent intensity profiles shown clearly in Figures 2.16B, 2.17B.

#### 2.7. **Stability and Cytotoxicity**

We have examined several factors relevant to the practical use of BT<sub>2</sub> and DPZDQ. They have relatively high melting points and are stable for extended periods of time under ambient conditions requiring no specialized environment for storage; they also show very good photo-stability as shown by the fluorescence intensity as a function of irradiation time (Figure 2.18); BT<sub>2</sub> is particularly attractive in this context.

Another important issue related to the application of the new dye in bioimaging is its cytotoxicity that could be detrimental to the cells being imaged and also make the handling hazardous. MTT (3-(4,5-dimethylthiazol-2-yl)-2,5-diphenyltetrazolium bromide) assay experiments using L929 cell lines (normal cell) indicated that both BT<sub>2</sub> and DPZDQ are absolutely non-toxic (cell viability data are provided in Figure 2.19). Experiments using HeLa cell lines also showed that they have no cytotoxicity; the IC<sub>50</sub> values of BT<sub>2</sub> and DPZDQ are found to be  $1468 \pm 345.4 \,\mu\text{g/ml}$  and  $790.70 \pm 98.73 \,\mu\text{g/ml}$  respectively (Figure 2.20). All these factors highlight the practical utility as well as efficiency of BT<sub>2</sub> and other DADQs in bioimaging.

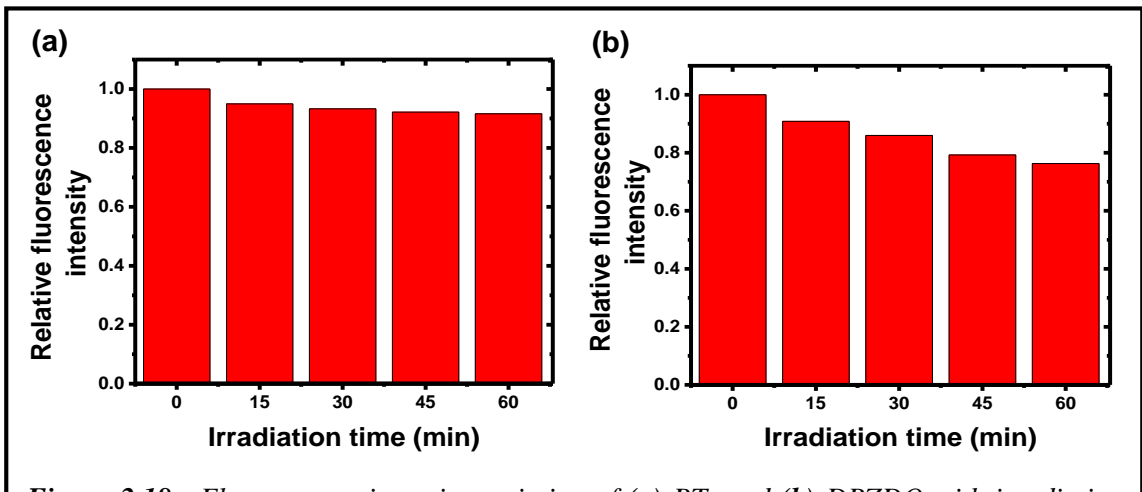


Figure 2.18. Fluorescence intensity variation of (a) BT<sub>2</sub> and (b) DPZDQ with irradiation time.

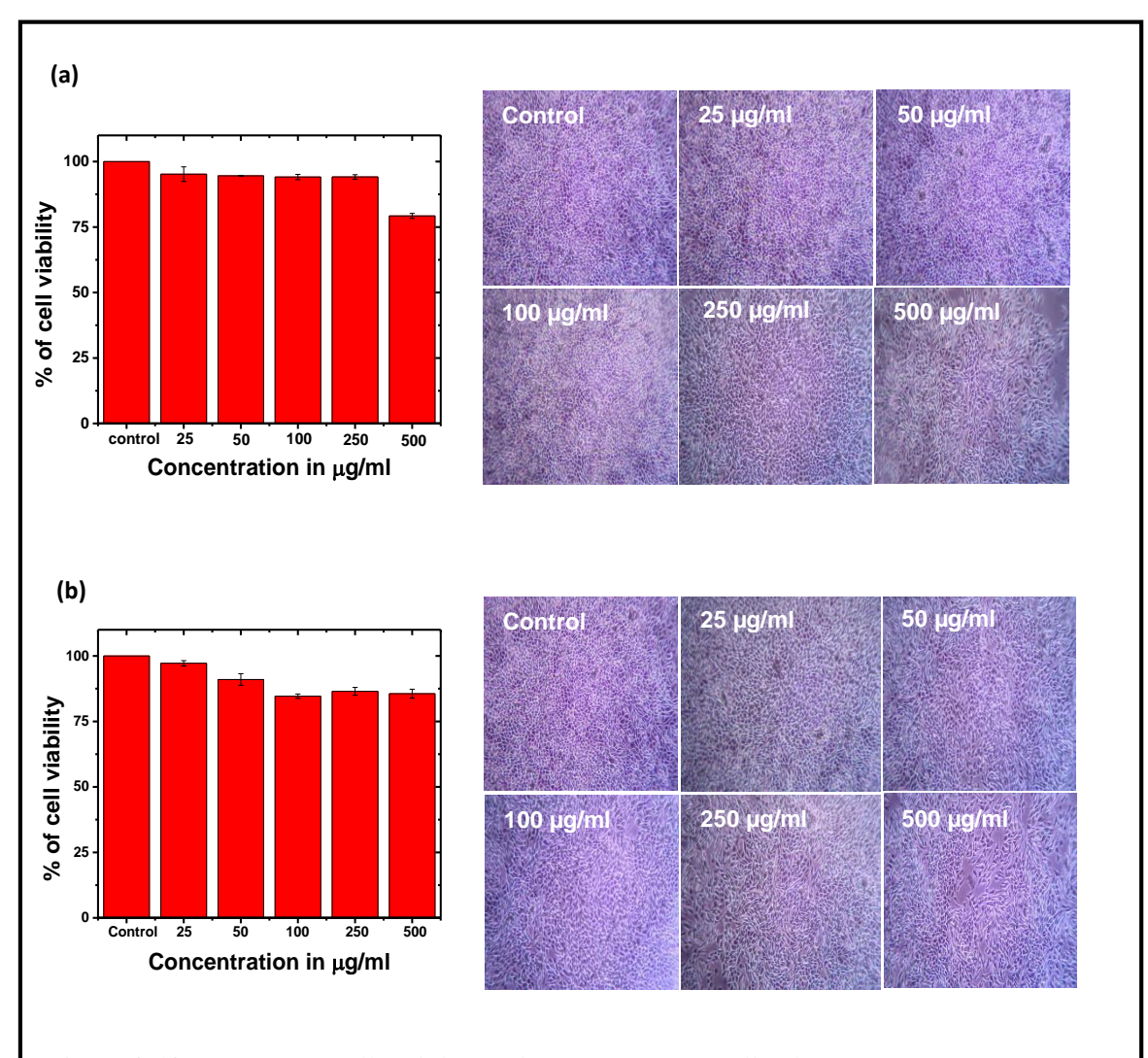


Figure 2.19. Percentage cell viability and impact on L929 cell colony formation in presence of different concentrations of (a)  $BT_2$  and (b) DPZDQ at 24 h.

#### 2.8. **Summary**

We have demonstrated the efficient use of DADQs with appropriate functionalities in fluorescence based stomatal imaging. Selective staining of cell walls alone or cell walls together with the nuclei could be achieved by tuning the staining conditions; the latter is particularly relevant in view of the fact that many of the traditionally used dyes are not selective, or stain only the cell wall. In addition to the bright and high contrast images that they provide, the simple and flexible molecular design and low cost of DADQs are important features. Calorimetry, microscopy and spectroscopy based investigations provide useful insight into the molecular level interactions involved in the binding of the dye molecules to the biological system and the basis for the enhanced fluorescence responses. DADQs are

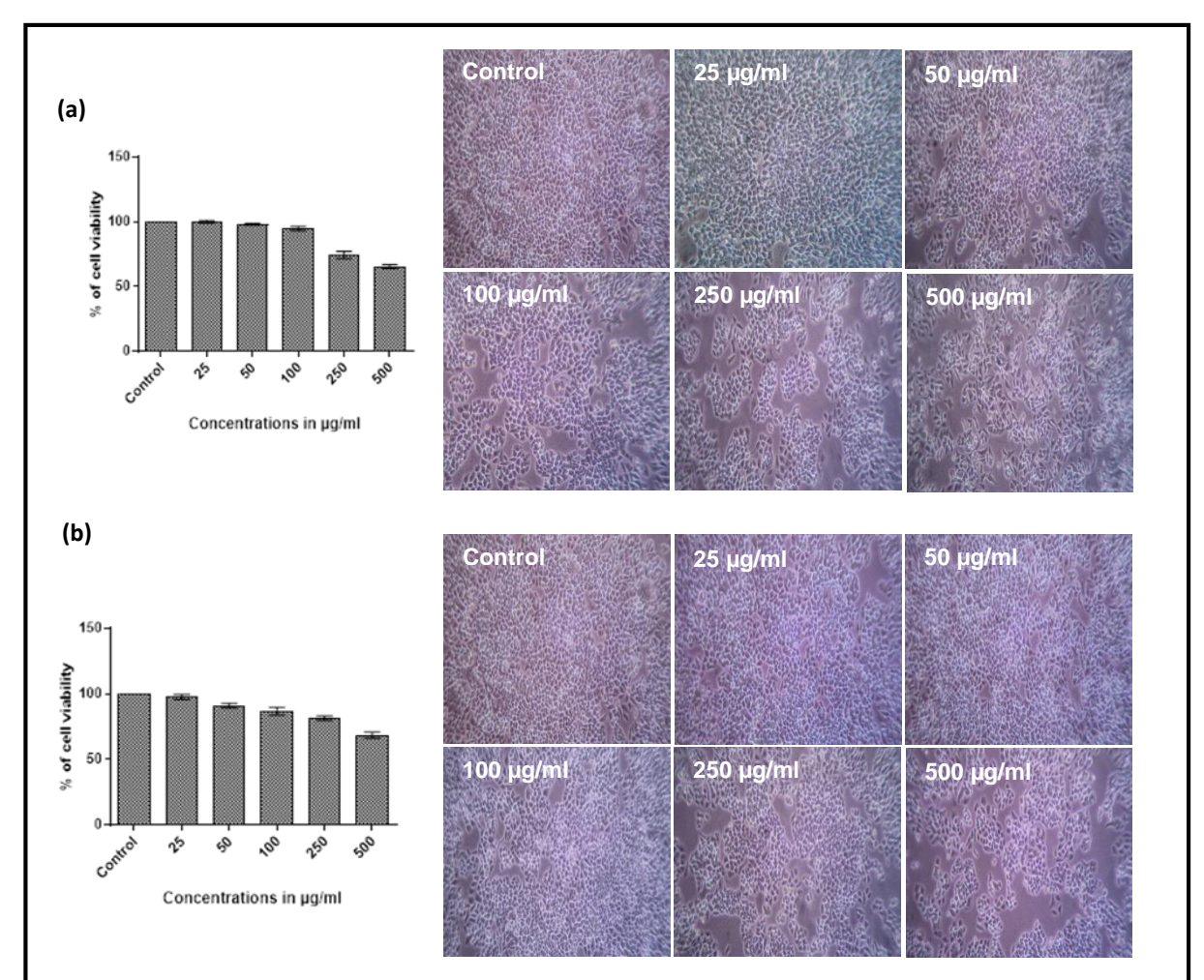


Figure 2.20. Percentage cell viability and impact on HeLa cell colony formation in presence of different concentrations of (a)  $BT_2$  and (b) DPZDQ at 24 h.

potentially efficient fluorescence labels that can be incorporated through non-covalent interactions for a variety of wider bioimaging applications. Their utility in imaging bacteria and their spores is the focus of the work in the following chapter.

#### References

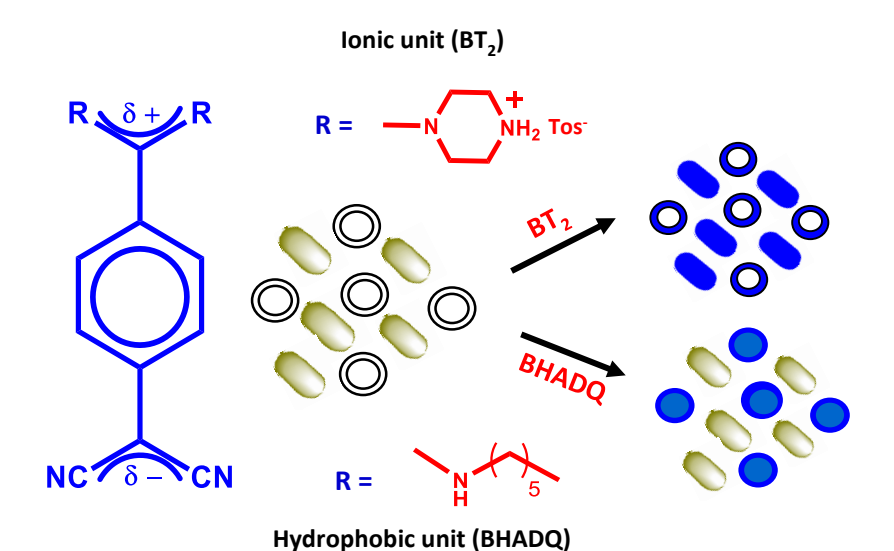
- 1. Z. Liu, L. D. Lavis and B. Betzig, *Mol. Cell*, 2015, **58**, 644-659.
- Z. Cai, Z. Ye, X. Yang, Y. Chang, H. Wang, Y. Liu and A. Cao, Nanoscale, 2011, 3, 2. 1974-1976.
- E. S. Swenson, J. G. Price, T. Brazelton and D. S. Krause, Stem. Cells, 2007, 25, 3. 2593-2600.
- 4. J. Wiedenmann, F. Oswald and G. U. Nienhaus, *Iubmb Life*, 2009, **61**, 029-1042.
- T. J. Morikawa, H. Fujita, A. Kitamura, T. Horio, J. Yamamoto, M. Kinjo, A. Sasaki, 5. H. Machiyama, K. Yoshizawa, T. Ichimura, K. Imada, T. Nagai and T. M. Watanabe, Sci. Rep., 2016, 6, 22342 (1-13).
- 6. Z. Li, J. Peng and H. L. Chen, J. Nanosci. Nanotechnol., 2011, 11, 7521-7536.
- 7. Z. Tao, G. Hong, C. Shinji, C. Chen, S. Diao, A. L. Antaris, B. Zhang, Y. Zou and H. Dai, Angew. Chem. Int. Ed., 2013, 52, 13002-13006.
- 8. Z. Zhao, J. W. Y. Lam, and B. Z. Tang, J. Mater. Chem., 2012, 22, 23726-23740.
- R. Davis, N. S. S. Kumar, S. Abraham, C. H. Suresh, N. P. Rath, N. Tamaoki and S. 9. Das, J. Phys. Chem. C, 2008, 112, 2137-2146.
- 10. Y. Hong, J. W. Y. Lam and B. Z. Tang, Chem. Commun., 2009, 29, 4332-4353.
- S. Jayanty and T. P. Radhakrishnan, Chem. Eur. J., 2004, 10, 791-797. 11.
- 12. A. Patra, N. Hebalkar, S. Sreedhar, M. Sarkar, A. Samanta and T. P. Radhakrishnan, Small, 2006, 2, 650-659.
- C. G. Chandaluri and T. P. Radhakrishnan, Angew. Chem. Int. Ed., 2012, 51, 11849-13. 11852.
- 14. P. Srujana and T. P. Radhakrishnan, Angew. Chem. Int. Ed., 2015, 54, 7270-7274.
- P. Srujana, T. Gera and T. P. Radhakrishnan, J. Mater. Chem. C., 2016, 4, 6510-6515. 15.
- 16. S. Gilroy, M. D. Fricker, N. D. Read and A. J. Trewavas, *The Plant Cell*, 1991, 3, 333-344.
- P. Apostolakos, P. Livanos and B. Galatis, Cell Motil. Cytoskel., 2009, 66, 342-349. 17.
- 18. R. Chitrakar and M. Melotto, J. Vis. Exp., 2010, 44, 2-5.
- M. G. Ajuru and B. E. Okoli, Int. J. Mod. Botony, 2012, 2, 115-119. 19.
- P. Apostolakos, P. Livanos, T. L. Nikolakopoulou and B. Galatis, Ann. Bot., 2009, 20. **104**, 1373-1387.

- 21. M. R. Puli and A. S. Raghavendra, *J. Exp. Bot.*, 2012, **63**, 1349-1356.
- 22. O. Keech, E. Pesquet, A. Ahad, A. Askne, D. Nordvall, S. M. Vodnala, H. Tuominen, V. Hurry, P. Dizengremel and P. Gardestrom, Plant Cell Environ., 2007, 30, 1523-1534.
- Z. Chen and D. Liu, Computer And Computing Technologies In Agriculture, Eds. C. 23. Zhao and D. Li, Springer, Berlin, 2009.
- M. Jolicoeur, S. Germette, M. Gaudette, M. Perrier and G. Becard, *Plant Physiol.*, 24. 1998, **116**, 1279-1288.
- D. K. Gardner and M. A. Lane, Laboratory Guide To The Mammalian Embryo, Eds. 25. D. K. Gardner, M. Lane and A. J. Watson, Oxford University Press, UK, pp. 42-61, 2003
- J. Hebling, L. Bianchi, F. G. Basso, D. L. Scheffel, D. G. Soares, M. R. O. Carrilho, 26. D. H. Pashley, L. Tjaderhane and C. A. De Souza Costa, Dent Mater., 2015, 31, 399-405.
- 27. M. Nakamura, A. Awaad, K. Hayashi, K. Ochiai and K. Ishimura, Chem. Mater., 2012, **24**, 3772-3779.
- 28. W. R. Hertler, H. D. Hartzler, D. S.Acker and R. E. Benson, J. Am. Chem. Soc., 1962, **84**, 3387-3393.
- Q. Hu, M. Gao, G. Feng, X. Chen and B. A. Liu, ACS Appl. Mater. Interfaces, 2015, 29. **7**, 4875-4882.
- 30. W. D. Chen, D. W. Zhang, W. T. Gong, Y. Lin and G. Ning, Spectrochim. Acta A, 2013, 110, 471-473.
- H. H. Lin, Y. C. Chan, J. W. Chen and C. C. Chang, J. Mater. Chem., 2011, 21, 3170-31. 3177.
- 32. F. Ishiwari, H. Hasbe, S. Matsumura, F. Hajjaj, N. H. Hayashi, M. Nishi, T. Someya and T. Fukushima, Sci. Rep., 2016, 6, 24275 (1-11).
- S. Jeyanthy and T. P. Radhakrishnan, *Chem. Mater.*, 2001, **13**, 2460-2462. 33.
- M. Ravi, S. Cohen, I. Agranat and T. P. Radhakrishnan, Struct. Chem., 1996, 7, 225-34. 232.
- 35. ZEISS ZEN 2.5 (blue edition), Carl Zeis microscopy Gmbh, Cologne, Germany,
- 36. P. Apostolakos, P. Livanos and B. Galatis, Cell Motil. Cytoskel., 2009, 66, 342–349.
- 37. P. Apostolakos, P. Livanos, T. L. Nikolakopoulou and B. Galatis, New Phytol., 2010, **186**, 623–635.

- 38. M. R. Puli, P. Rajsheel, V. Aswani, S. Agurla, K. Kuchitsu and A. S. Raghavendra, Planta, 2016, 244, 831–841.
- S. Agurla, G. Gayatri and A. S. Raghavendra, Plant Nitric Acid Methods and 39. Protocol, Eds. K. J. Gupta, Humana Press, USA, pp. 49-56, 2016.
- M. R. Puli and A. S. Raghavendra, J. Exp. Bot., 2012, 63, 1349–1356. 40.
- Z. Kong, T. Hotta, Y. R. J. Lee and T. Horio and B. Liu, *Plant Cell*, 2010, 22, 191– 41.
- C. Hachez, K. Ohashi-Ito, J. Dong and D. C. Bergmann, Plant Physiol., 2011, 155, 42. 1458–1472.
- S. Tripathi and A. K. Mondal, *Int. J. Sci. Nat.*, 2012, **3**, 788–798. 43.
- M. G. Ajuru, and B. E. Okoli, *Int. J. Mod. Botany*, 2012, 2, 115–119. 44.
- S. Tripathi and A. K. Mondal, Int. J. Life Sci. Biotechnol. Pharma Res., 2012, 1, 104-45. 113.
- S. Mitra, G. C. Maiti and D. Maity, Adansonia, 2015, 37, 139–147. 46.
- C. G. Chandaluri, A. Patra and T. P. Radhakrishnan, Chem. Eur. J., 2010, 16, 8699-47. 8706.
- G. T. Grant, E. R. Morris, D. A. Rees, P. J. C. Smith and D. Thom, FEBS Lett., 1973, 48. **32**, 195-198.
- C. M. Rounds, E. Lubeck, P. K. Helper and L. J. Winship, *Plant Physiol.*, 2011, 157, 49. 175-187.
- I. Braccini and S. Perez, *Biomacromolecules*, 2001, **2**, 1089-1096. 50.
- G. Z. Cerovic, G. Samson, F. Morales, N. Tremblay and I. Moya, Agronomie, 1999, 51. **19**, 543-578.
- R. Hartley and P. Harris, Syst. Ecol., 1981, 8, 189-203. 52.

## **CHAPTER 3**

# **Zwitterionic Small Molecule Based Fluorophores for Efficient and Selective Imaging of Bacterial Endospore**



Zwitterionic diaminodicyanoquinodimethanes with appropriate substituent groups are shown to be efficient fluorophores for imaging bacterial endospores selectively, and in their dormant state; the staining protocols are very simple and the dyes photostable and non-cytotoxic. Studies which provide insight into the intermolecular interactions that lead to effective staining and images, are presented.

## **Synopsis**

In the current scenario of increasing antibiotic resistance and pathogen transmission, the danger posed by bacterial endospores in important areas like food industry, health and medicine highlights the urgent need to develop efficient probes for their detection. The sturdy and impermeable multilayer coat of endospores makes desirable methods like fluorescence imaging extremely difficult. Selective imaging of endospores in the presence of the bacteria is even more challenging. Furthermore, it is preferable to maintain the dormant state of endospores through the imaging process, when extended monitoring is required; many of the available techniques involve lethal germination or destruction of the endospores, making such monitoring impossible. As has been highlighted in the previous chapter (Sec. 2.5), DADQs are potential fluorescence probes for imaging various biological cells. In this chapter, we show that simple zwitterionic diaminodicyanoquinodimethane (DADQ) molecules with selected functionalities are efficient dyes for fluorescence imaging of bacterial endospores due to their dipolar structure that facilitates the penetration into the endospore structure, and the enhanced fluorescence in the rigid/aggregated state. The facile structural tailorability allows DADQs with various appendage moieties to be synthesized; the derivative with ionic substituents ( $BT_2$ ), and another with optimally long alkyl chains and the resultant hydrophobic character (BHADQ) are shown to be excellent fluorescence probes for endospores. Nanomolar amounts of these dyes provide effective staining; while  $BT_2$  stains bacteria and endospores, most significantly, BHADO stains endospores selectively. To the best of our knowledge, this is the first example of selective fluorescence imaging of endospores in their dormant state. Spectroscopy, microscopy and calorimetry studies provide insight into the molecular level interactions that enable the efficient staining and bright images. BHADQ is shown to be photostable and non-cytotoxic; similar advantages of BT2 were already discussed in the previous chapter. The versatile structural tailorability of these dye molecules holds great promise for targeted imaging.

#### 3.1. Introduction

Endospore formation is an ingenious mechanism that allows bacteria to survive adverse environmental conditions, and transfer their genetic information to subsequent generations; a brief introduction to them has been provided in Sec. 1.3.3.2. Spore formation (sporulation) involves seven stages, illustrated in Figure 3.1. The dormant states are highly

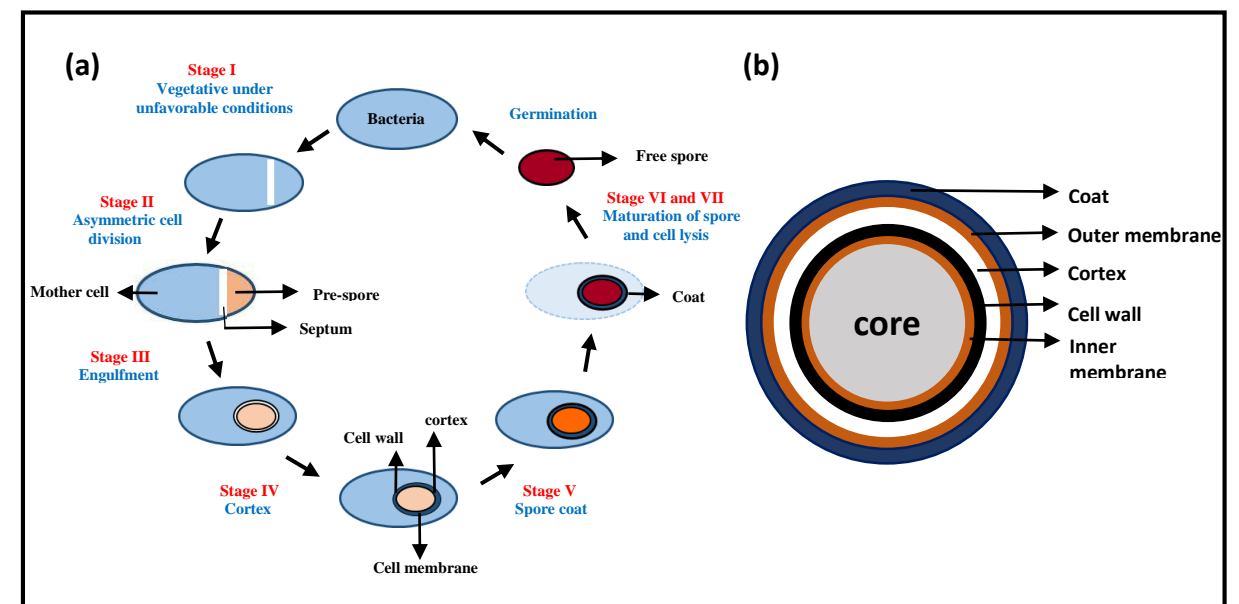


**Figure 3.1.** Schematic representation of (a) sporulation cycle, and (b) the structure of bacterial spore.

resistant to debilitating effects such as heat, dehydration, radiation and chemical treatment; the underlying factors for this robustness include the exosporium that provides adherence and biocide resistance, keratin based spore coat, cortex and spore wall made of peptidoglycan, and dipicolinate and the low water content in the core (Figure 3.1b).<sup>1</sup> The increasing susceptibility of humans and animals to infections arising from the bourgeoning antibiotic resistance of several bacterial strains has reached alarming levels. Since antibiotics and sterilization techniques are often ineffective against endospores, food and medical industries are at great risk;<sup>2-4</sup> endospores can also act as ominous biological weapons.<sup>5,6</sup> Development of efficient, cost-effective and facile methods for the detection of endospores, and assessment of their viability is an urgent and critical imperative.<sup>7-10</sup>

Even though optical absorption and fluorescence emission based imaging are desirable and facile techniques, the chemical resistance and permeability barriers due to the protective coats of endospores pose inherent challenges. The exosporium allows penetration of molecules with sizes typically < 150 kDa, whereas the coat/outer membrane allows only sizes < 8 kDa. For even smaller molecules such as water, the permeability of the coat including the inner membrane is very low, with the structure of the coat being critical. The non-fluorescence based imaging methods utilize staining protocols like Gram-stain, Ziehl-Neelsen, Dorner and Schaeffer-Fulton (Sec. 1.3.3.2). These generally require lengthy

specimen preparation involving extended heating in many cases and decolorisation using media such as acidified alcohol or acids. 12,13 Preferable alternatives based on flow cytometry and fluorescence microscopy require efficient fluorescence probes, even though the former could also utilize techniques like mass spectrometry. The common fluorescence probes such as DAPI, acridine orange, Hoechst 34580 and SYTO 9 are easy to use and suitable for clinical applications. However, they have crucial limitations like cell-impermeability and inefficiency in differentiating endospores from bacteria (discussed in Sec. 1.3.3).<sup>8,10,14</sup> Lethal germination induced by dodecylamine leads to core dehydration and spore destruction. 15 As dormant bacterial endospores are resistant towards staining, lethal germination which leads to the termination of dormancy is necessitated for the incorporation of the fluorescence dye. There are practically no effective dyes that can be used to selectively image bacterial endospores in their dormant state.

As discussed in Sec. 2.1, Several critical requirements need to be met for a probe molecule to be a practical and efficient agent for fluorescence imaging of endospores as well. The molecule must have appropriate functionalities to bind with the cell wall and nucleic acid of the endospores. While ionic or dipolar nature could facilitate staining Gram-stainpositive or negative bacteria and endospores, an optimal level of hydrophobicity might be needed for selective staining of the endospores. Finally, the staining protocol should be simple and quick, without the need for elaborate specimen preparation and multiple steps including chemical treatments. Diaminodicyanoquinodimethanes (DADQs) explored earlier in our laboratory for nonlinear optical<sup>16</sup> and fluorescence<sup>17</sup> applications (Sec. 1.1.3), is found to be ideally suited for selective imaging of bacterial endospores, especially maintaining their dormant state.

Fluorophores which exhibit enhanced light emission in their aggregated state (popularly called AIE system) 18,19 are of great interest in bioimaging;20 In the previous chapter, we have shown that specific DADQ derivatives are efficient probes for imaging stomatal cells.<sup>21</sup> In this chapter, we demonstrate the utility of the derivatives, 7,7bis(piperazinium)-8,8-dicyanoquinodimethane bis(p-toluene sulfonate) (BT<sub>2</sub>) and 7,7-bis(nhexylamino)-8,8-dicyanoquinodimethane (BHADQ) (Figure 3.2), in staining bacterial endospores. Significantly, the staining protocol is simple, requiring no prior heating or chemical treatment. Dormant endospores could be stained by the DADQ derivatives, and subsequently germinated in a nutrient medium demonstrating the non-destructive nature of the stains. Spectroscopy and calorimetry studies provide insight into the potential molecular level interactions that lead to the efficient staining of the endospores including their core.

#### **3.2.** Synthesis and characterization

Synthesis of BT<sub>2</sub> has been discussed in Sec. 2.2. Three other derivatives, BPADQ, BHADQ and BHPADQ presented in this chapter were synthesized using similar procedure, by the reaction of tetracyanoquinodimethane (TCNQ) with pentylamine, hexylamine and heptylamine respectively.<sup>22</sup> They were purified by recrystallization and characterized; details of instruments used and characterization studies carried out are added in Appendix B.

## BPADQ (7,7-*Bis*(*n*-pentylamino)-8,8-dicyanoquinodimethane)

Recrystallized from acetonitrile; m. p. = 244-246 °C (dec.); FTIR:  $\bar{\nu}/\text{cm}^{-1}$ = 3205, 2178.4, 2132.1; <sup>1</sup>H NMR (500 MHz) (d<sub>6</sub>-DMSO):  $\delta/ppm = 9.11$  (s, 1H), 8.54 (s, 1H), 7.20 (J = 8.5) Hz, d, 2H), 6.82 (J = 8.35 Hz, d, 2H), 3.26 (q, 4H), 1.61 (s, 2H), 1.49 (J = 6.5 Hz, t, 2H), 1.33 (s, 4H), 1.16 (s, 4H), 0.90 (s, 3H), 0.80 (J = 6.35 Hz, t, 3H);  $^{13}$ C NMR (d<sub>6</sub>-DMSO):  $\delta/ppm = 164.37, 147.8, 129.52, 124.35, 117.79, 115.4, 45.46, 42.71, 32.24, 29.48, 28.88,$ 28.34, 27.53, 22.19, 21.99, 14.29, 14.20.

#### BHADQ (7,7-Bis(n-hexylamino)-8,8-dicyanoquinodimethane)

Yield= 58%, Recrystallized from acetonitrile; m. p. = 218-220 °C (dec.); FTIR (KBr):  $\bar{\nu}/\text{cm}^ ^{1}$ = 3206, 2180, 2130;  $^{1}$ H NMR (400 MHz) (d<sub>6</sub>-DMSO):  $\delta/ppm = 9.20$  (s,1H), 8.56 (s, 1H), 7.19 (J = 8.4 Hz, d, 1H), 6.83 (J = 8.4 Hz, d, 1H), 3.27 (J = 7.6 Hz, q, 4H), 1.60 (J = 7.08)Hz, t, 2H), 1.48 (J = 6.56 Hz, t, 2H), 1.30 (b, 6H), 1.14 (b, 6H), 0.88 (J = 6.36 Hz, t, 3H), 0.81 (J = 9 Hz, t, 3H);  ${}^{13}$ C NMR (d<sub>6</sub>-DMSO):  $\delta/ppm = 164.35$ , 147.90, 129.53, 124.37, 117.79, 115.14, 45.41, 42.71, 32.24, 31.28, 31.04, 29.74, 27.79, 26.38, 25.81, 22.47, 22.38, 14.37, 14.27; elemental analysis (calcd., found for BHADQ i.e.  $C_{22}H_{32}N_4$ ): %C = (74.96, 74.85), %H = (9.15, 9.21), %N = (15.89, 15.76). Solution state:  $\lambda_{max}^{abs} = 380 \text{ nm}, \lambda_{max}^{em} = 490 \text{ nm}$ nm, Stokes shift = 110 nm; solid state:  $\lambda_{max}^{abs} = 368$  nm (broad),  $\lambda_{max}^{em} = 452$  nm, fluorescence quantum yield: 31 % (solid state), 0.18 % (solution state), fluorescence lifetime: 1.77 ns, ε: 29,920 M<sup>-1</sup>cm<sup>-1</sup>, brightness: 927.52 M<sup>-1</sup>cm<sup>-1</sup>.

Single crystal for X-ray diffraction analysis was grown from acetone solution of the compound synthesized by carrying out the reaction of *n*-hexyl amine and TCNQ in ethyl acetate.

#### BHPADQ (7,7-*Bis*(*n*-heptylamino)-8,8-dicyanoquinodimethane)

Recrystallized from acetonitrile; m. p. = 201-204 °C (dec.); FTIR:  $\bar{\nu}/\text{cm}^{-1}$ = 3204, 2176, 2132; <sup>1</sup>H NMR (500 MHz) (d<sub>6</sub>-DMSO):  $\delta/ppm = 9.18$  (s,1H), 8.54 (s, 1H), 7.18 ( J = 8.45 Hz, d, 2H), 6.83(J = 8.6 Hz, d, 2H), 3.27(J = 7.2 Hz, q, 4H), 1.60(J = 6.85 Hz, t, 2H), 1.48(s, 2H), 1.27 (b, 8H), 1.38 (b, 8H), 0.87 (J = 6.9 Hz, t, 3H), 0.83(J = 7.1 Hz, t, 3H);  ${}^{13}$ C NMR (d<sub>6</sub>-DMSO):  $\delta/ppm = 164.39, 147.99, 129.50, 124.32, 117.79, 115.20, 45.40, 42.69, 32.28, 32.62,$ 31.52, 29.74, 28.73, 28.49, 27.84, 26.67, 26.07, 22.49, 22.44, 14.37.

#### 3.3. Characteristic features of BT<sub>2</sub> and BHADQ

## 3.3.1. Crystallographic studies

DADQs are highly dipolar molecules with a zwitterionic structure arising from the push-pull character due to the presence of amino and cyano substituents (Figure 3.2). The molecular and crystal structures of BT<sub>2</sub> have been reported from our laboratory earlier.<sup>23</sup> Even though BHADO was synthesized earlier, 23 it was not structurally characterized; we have now carried out single crystal X-ray diffraction study of BHADQ (Table 3.1, Figure 3.3, 3.4). The R factor is relatively high, primarily because of the disorder in one of the hexyl chains in the molecule; the SQUEEZE option in PLATON was used to model it. Figure 3.3a shows the molecular structure with the disordered positions of the C atoms in that chain; the structure with only the atoms with higher occupancy in the disordered hexyl chain is shown in Figure 3.3.b. Figure 3.3c shows the unit cell, and Figure 3.4 shows the H-bonded assembly in the crystal; only those C atoms with higher occupancy in the disordered chain are shown for clarity. The molecular structure reveals an average torsion angle of ~44.9° between the diaminomethylene group and the aromatic ring moiety, the signature structural feature of DADQs.

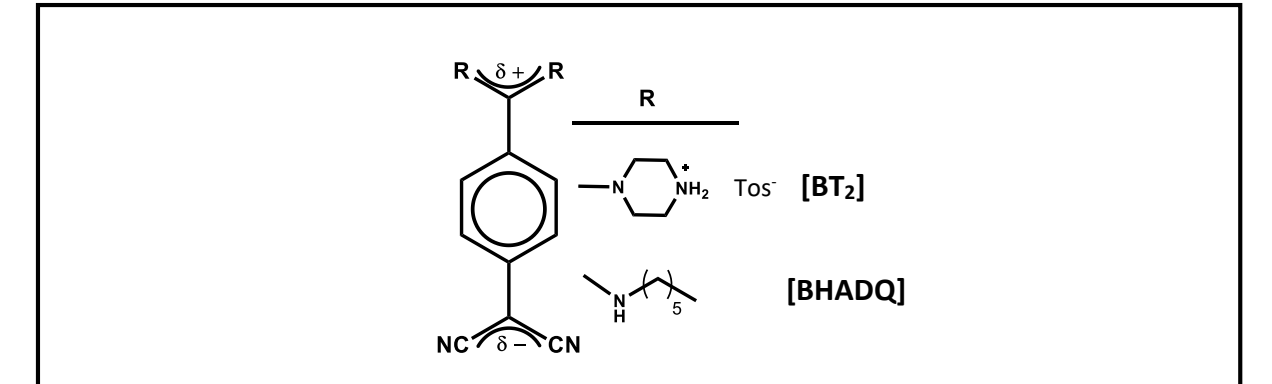


Figure 3.2. Molecular structures of the DADQ derivatives discussed in this chapter,  $BT_2$  and BHADQ.

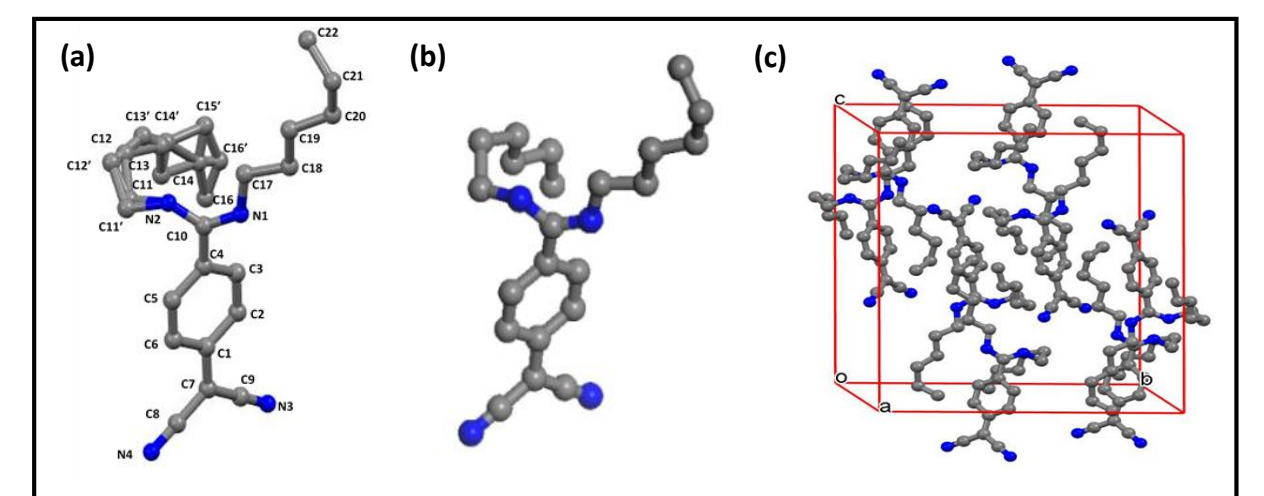


Figure 3.3. Molecular structure of BHADQ determined from single crystal X-ray analysis. (a) Showing the disordered positions of C11 - C16 and (b) The C atoms in position of higher occupancy in the disordered hexyl chain alone shown; (c) Unit cell of BHADQ (only higher occupancy C atoms in the hexyl chain shown). H atoms are omitted for clarity; N (blue) and C (grey) atoms are shown.

## **3.3.2.** Computational studies

Gaussian 09 (Revision C.01) program was used to compute the dipole moment of BT<sub>2</sub> and BHADQ molecules at the B3LYP/6-31G\* level. Molecular geometry from the respective crystal structures was used; only the DADQ part  $(B^{2+})$  was used in the case of  $BT_2$ . In BHADQ, in the disordered hexyl chain, only C atoms at the positions with higher occupancy were used, as the dipole moment is primarily determined by the DADQ unit alone; H atoms were added at optimal positions. The geometries used for the computations are shown in Figure 3.5; the computed dipole orientation is seen to be nearly parallel to the axis connecting the diaminomethylene and dicyanomethylene C atoms. The computed dipole moments of B<sup>2+</sup> and BHADQ are 34.1 and 21.9 D respectively.

Table 3.1. Basic crystallographic data of BHADQ.

	BHADQ
Empirical formula	$C_{22}H_{32}N_4$
Crystal system	Monoclinic
Space group	C2/c
a / Å	11.9834(4)
b / Å	18.5034(6)
c / Å	20.9250(7)
α / deg.	90.00
β/deg.	102.47
γ / deg.	90
V / Å <sup>3</sup>	4530.4(3)
Z	8
ρ <sub>calc.</sub> / g cm <sup>-3</sup>	1.034
μ / cm <sup>-1</sup>	0.62
Temperature / K	100 (2)
λ/Å	0.71073
No. of reflections	3965
No. of parameters	268
Max., Min. transmission	0.555, 1.000
GOF	1.036
R [for $I \ge 2\sigma_I$ ]	0.0878
wR <sup>2</sup>	0.2723
Largest difference peak and hole / eÅ-3	0.613/ -0.429
CCDC number	1950536

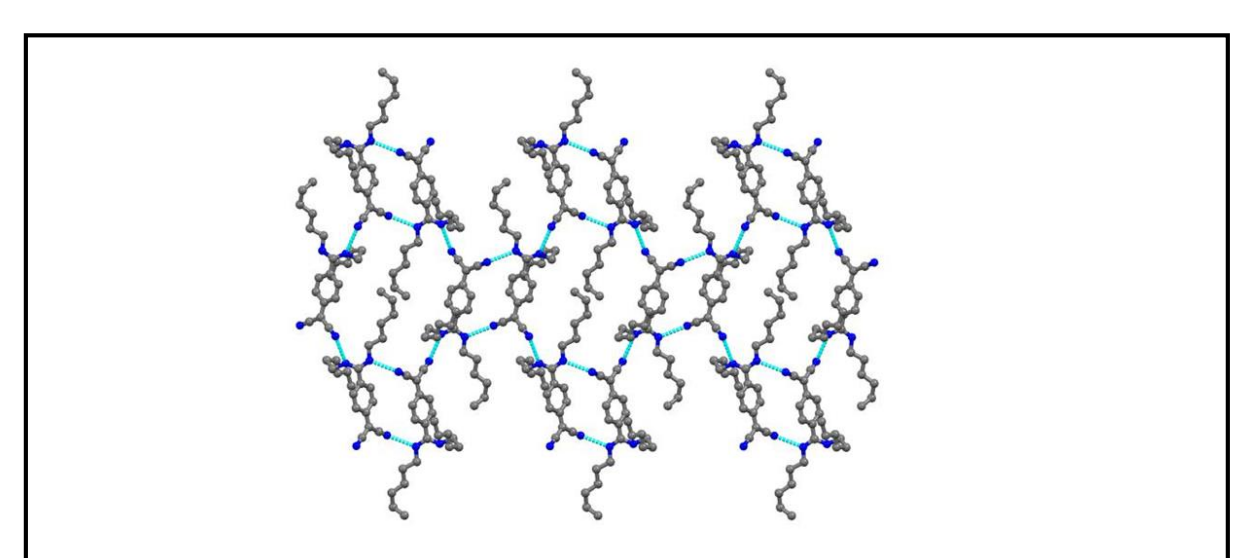


Figure 3.4. Supramolecular assembly in BHADQ crystal; intermolecular H bonds are indicated  $(cyan\ lines).\ H\ atoms\ are\ omitted\ for\ clarity;\ N\ (blue)\ and\ C\ (grey;\ in\ the\ hexyl\ chain\ with\ disorder,$ only the positions with higher occupancy) atoms are shown.

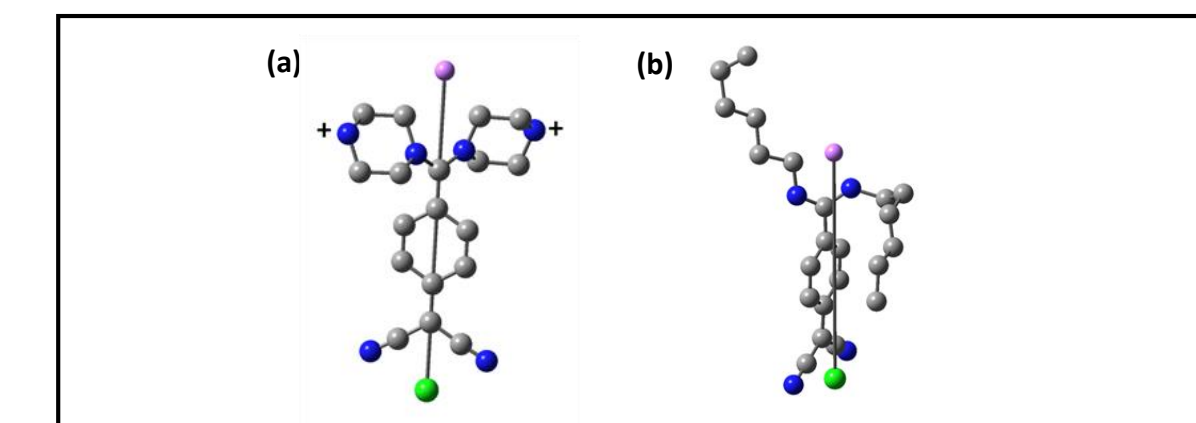
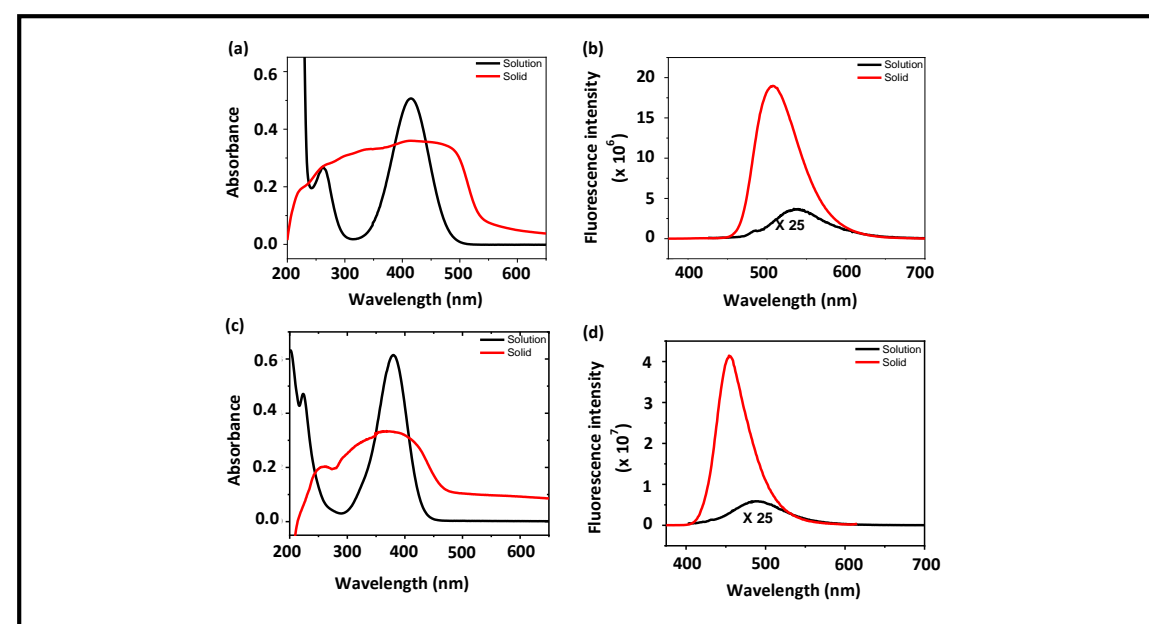


Figure 3.5. Molecular structure of (a) 7,7-bis(piperazinium)-8-8-dicyanoquinodimethane  $(B^{2+})$ and (b) 7,7-bis(n-hexylamino)-8,8-dicyanoquinodimethane (BHADQ) from their respective crystal structures, and the orientation of the computed (B3LYP/6-31G\*) dipole moment vector (line connecting the pink sphere (positive end) with the green sphere (negative end); H atoms are omitted for clarity, and N (blue) and C (grey; in the hexyl chain of BHADQ with disorder, only the positions with higher occupancy) atoms are shown.



**Figure 3.6.** (a) Electronic absorption and (b) fluorescence emission spectra of  $BT_2$  in the solid ( $\lambda_{exc}$ =365 nm) and aqueous solution ( $\lambda_{exc}$  =415 nm) states. (c) Electronic absorption and (d) fluorescence emission spectra of BHADQ in the solid ( $\lambda_{exc} = 368$  nm) and DMSO solution ( $\lambda_{exc} =$ 380 nm) states. Solution concentrations = 0.1 mM; fluorescence spectra were recorded on solution and solid samples with the same optical density.

## 3.3.3. Spectroscopic studies

The molecules show strong electronic absorption in the blue region due to the intramolecular charge transfer. The spectra of BT<sub>2</sub> and BHADQ in the solution and solid states are shown in Figure 3.6a,c; the broadening in the solid state occurs due to the intermolecular interactions. The fluorescence emission spectra (Figure 3.6b,d) show clearly the enhancement in the emission from the solution to the solid state (the spectra are recorded on samples with the same optical density). There is also a small blue shift in the solid state; this can be attributed to the effect of the local field due to the neighbouring dipolar molecules as demonstrated in earlier studies in our laboratory (Ref. 24). The fluorescence enhancement arises due to the inhibition of the excited state structure relaxation via the torsional motion of the diaminomethylene moiety, and curtailment of intermolecular energy transfer due to specific molecular orientations; detailed investigations of the factors have been reported from our laboratory earlier.<sup>17</sup> A significant feature of the DADQs is the ease of structural tuning through the facile single-step synthesis. This provides access to a wide range of substituents on the diaminomethylene group, while retaining the essential  $\pi$ -conjugated fluorophore moiety.

#### **3.4. Endospore preparation**

#### 3.4.1. **Bacterial culture**

Our studies have used mainly, bacillus and Halobacillus, two different genus belonging to the bacterial phylum Firmicutes; these are a group of rod-shaped, Gram-stainpositive, aerobic (or under some conditions anaerobic) bacteria that produce endospores. We have used also Escherichia coli (E. coli), a Gram-stain-negative bacterium that belongs to the class Gamaproteobacteria of the phylum Proteobacteria, not known to produce endospores. The bacteria were cultured on Petri plates containing the nutrient agar medium (HiMedia), and incubated overnight at 25°C for growth. The bacteria growing in the nutrient broth were harvested by centrifugation (10,000 rpm at 4°C for 5 min) and washed twice with MilliQ water, before the imaging experiment.

#### **3.4.2.** Spore formation

Bacillus sp. strain JC39 (according to 16S rRNA gene sequence similarity, strain JC39 is closely (98.9%) related to Bacillus cereus strain ATCC 14579<sup>T</sup>), JC1009 (99.5% similarity with Bacillus subtilis strain FW2<sup>T</sup>), JC1008 (99.3% similarity with Bacillus paralicheniformis strain KJ-16<sup>T</sup>), JC1005 (100% similarity with Bacillus tequilensis strain KCTC-13622<sup>T</sup>) and Halobacillus sp. strain JC554 (99.3% similarity with Halobacillus dabanensis strain D-8<sup>T</sup>), were grown in a conical flask containing the nutrient broth (HiMedia), and incubated at 25°C for 12 h. The cultures were further incubated at 4°C for 3 weeks to induce spore formation.

## 3.4.3. Isolation of spores

The endospores of the above mentioned bacterial strains were isolated from the vegetative cells following the earlier reported procedure<sup>25</sup> with some modifications. The spore induced cultures of bacterial strains were centrifuged at 6,000 rpm for 10 min. The pellets were washed thrice with the PBS buffer (pH = 7.8) and re-suspended in 50 ml of tris-EDTA buffer containing 1.2 mg ml<sup>-1</sup> lysozyme, and were incubated at 37 °C for 1 h with stirring. 10 ml of 10% sodium dodecyl sulfate (Sigma) was added to this solution and incubated further at 37 °C for 20 min. It was then centrifuged at 6,000 rpm for 10 min. The pellet obtained was washed twice with 0.1% Tween 20 (Himedia). It was then re-suspended in sterilized distilled water and stored at 4 °C. The yield of spores was ~ 90%.

#### 3.4.4. Staining and imaging

The endospore staining protocol that we have developed is extremely simple, consisting of the following general steps: (i)  $\sim 12-24$  nmols of the DADQ dye in aqueous or DMSO solution was mixed with the bacteria or spore sample taken in aqueous medium and incubated for  $\sim 5$  min under ambient conditions; (ii) the mixture was concentrated by centrifugation at low temperature, the deposited pellets re-suspended in water and a drop used for imaging. The detailed procedure is given below.

A suspension of the endospores (100  $\mu$ L) was taken in a 1.5 ml sterilized microcentrifuge tube; 6  $\mu$ L of 4 mM BHADQ (solution in DMSO) or 6  $\mu$ L of 2 mM BT<sub>2</sub>

(solutions in DMSO or water) was added and incubated at 28°C for 15 min with constant shaking. Samples were then centrifuged (10,000 rpm at 4°C for 5 min) and the deposited pellet was re-suspended in 30 µL of MilliQ water. One drop of the stained endospores or bacteria was cast on the microscope slide and protected with a coverslip. A Leica model ZEISS LSM 880 confocal laser scanning microscope (CLSM) was used for imaging. A 405 nm laser diode (Carl Zeiss) was used as the excitation source and emission in the 410 - 480 nm range was detected; these parameters were chosen as a uniform set for all imaging, since they are well-suited for BHADQ (selective imaging), and sufficiently sensitive for BT<sub>2</sub> in the aggregated/solid state. Images were obtained using 60× or 40× objective lens. Parameters such as the detector gain and amplification offset/gain were adjusted to optimize the fluorescence intensity of the targets and the background. ZEN lite software (Zeiss Zen 3.1)<sup>26</sup> was used for image processing. In addition to the normal 2-D images, their layered depth displays are also presented as 2.5-D (pseudo 3-D) images viewed from different angles; the fluorescence intensity values are converted into height plots in the 2.5-D images. It may be noted that, the strong fluorescence emission makes the elongation in the Z-direction slightly prominent in the 2.5-D images of the spores and bacterial cells, including some substrate surface roughness, but provides a magnified and clear view of the specimen.

## 3.4.5. Extraction of DNA from the *Halobacillus* sp. strain JC554 bacteria

Genomic DNA of Halobacillus sp. strain JC554 bacteria was extracted using nucleopore gDNA Fungal/Bacterial Mini Kit as per manufacturer's instructions and used in isothermal titration calorimetry and fluorescence experiments (Sec. 3.8). Quantification of the extracted DNA was done using a NANODROP 2000 Spectrophotometer.

#### 3.5. Imaging of bacterial cells and its endospore using BT<sub>2</sub>

In view of our earlier studies on the imaging of stomatal cells,<sup>21</sup> we carried out the initial investigations on endospore imaging using BT<sub>2</sub>. BT<sub>2</sub> was found to stain the endospores; however, it stains Gram-stain-positive and negative bacterial cells as well as seen from the following results. Figure 3.7 shows the CLSM images obtained for endospores of Halobacillus sp. strain JC554, and Figure 3.8, the images for the Halobacillus sp. strain JC554 (Gram-stain-positive) and Escherichia coli (Gram-stain-negative) bacteria. An

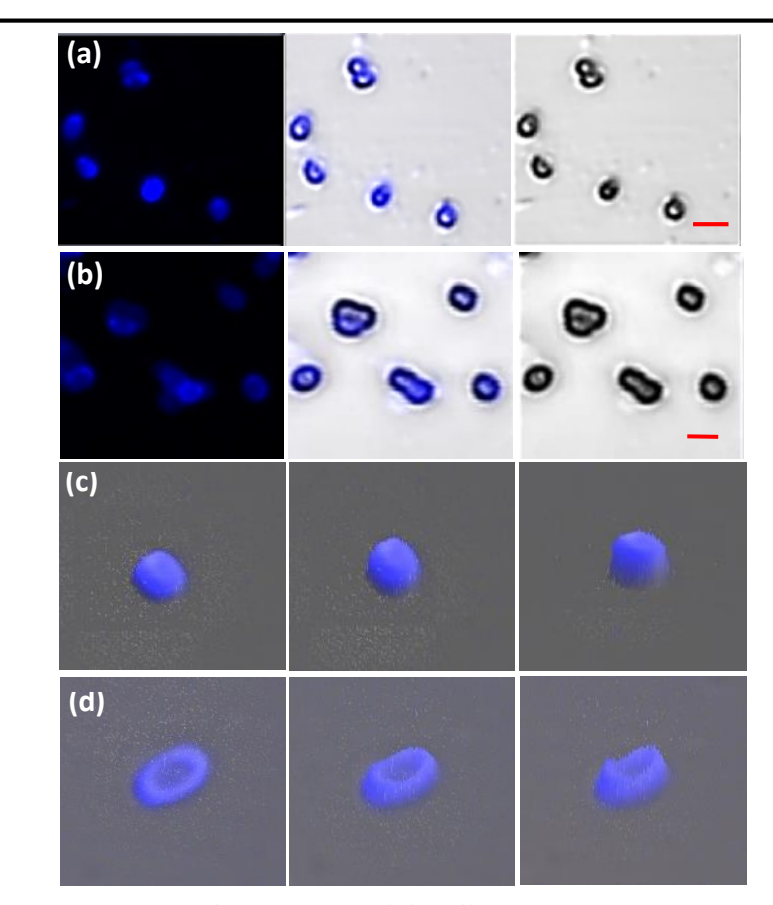


Figure 3.7. CLSM images of endospores of Halobacillus sp. strain JC554 stained using 0.11 mM solution of  $BT_2$  in (a) water and (b) DMSO (scale bar = 1.5  $\mu$ m; panels, left: fluorescence, right: bright field, middle: merged); 2.5-D images of single endospore of Bacillus sp. strain JC1005 stained by BT<sub>2</sub> in (c) water and (d) DMSO, viewed at different angles.  $\lambda_{exc} = 405$  nm,  $\lambda_{em} = 410-485$ nm.

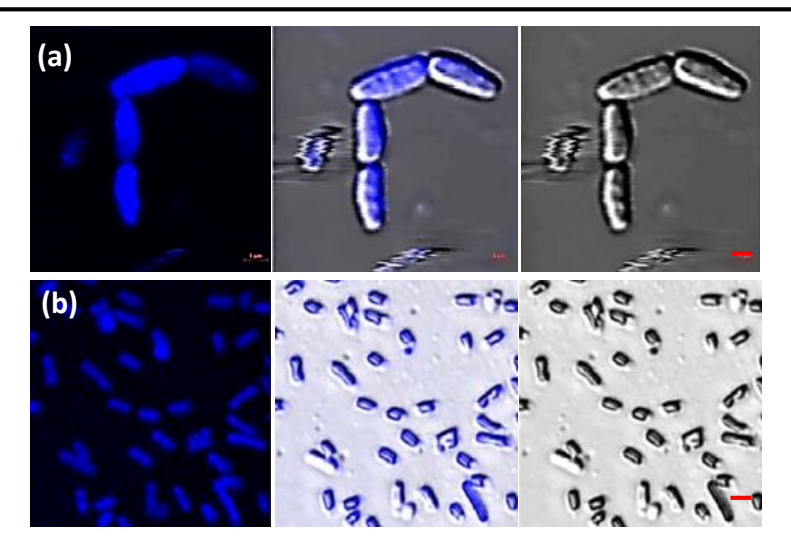


Figure 3.8. CLSM images of (a) Halobacillus sp. strain JC554 (Gram-stain-positive, scale bar = 1  $\mu$ m), and (b) E. coli (Gram-stain-negative, scale bar = 2  $\mu$ m) bacteria, stained using 0.11 mM solution of BT<sub>2</sub> in water (panels, left: fluorescence, right: bright field, middle: merged).  $\lambda_{exc} = 405$ nm,  $\lambda_{em} = 410-485 nm$ .

interesting observation in the case of the former (Figure 3.7) is that BT<sub>2</sub> taken as a DMSO solution stains only the cell wall of the spore, but when in aqueous solution, it penetrates into the endospores in some cases; this is seen clearly in the 2.5-D images in Figure 3.7c, d. The indiscriminate staining of bacteria and endospores (seen also clearly in Figure 3.9) is a limitation of the BT<sub>2</sub> dye. We ascribe it to the positive charges on the ammonium moieties, and the strong electrostatic interactions with the negative charges on the cell walls of the bacteria and the endospores, as discussed in Sec. 3.7.

#### **3.6.** Imaging of endospores using different DADQs; selective imaging with **BHADQ**

Based on the foregoing experiments, we inferred that an optimal hydrophobic character could induce different interaction with the peptidoglycan matrix forming the cortex, enabling selective staining of endospores. We therefore explored DADQs with a variety of substituents including cyclic aromatic and aliphatic groups, without and with H-bonding or basic functionality, as well as alkyl chains (Figure 3.10). The alkyl derivatives were found to be very useful. Butylamine and pentylamine derivatives were inefficient (Figure 3.11); this may be due to the shorter alkyl chain hydrophobic components not being sufficient to balance the dipolar character of the DADQ core.

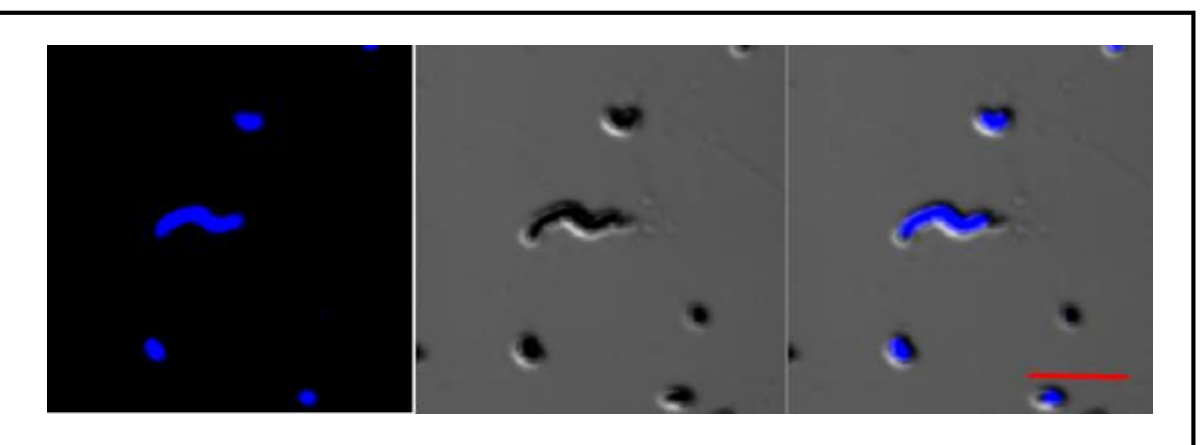


Figure 3.9. CLSM images of the Halobacillus sp. strain JC554 bacteria and endospores stained using 0.11 mM solution of BT<sub>2</sub> in water.  $\lambda_{exc} = 405$  nm,  $\lambda_{em} = 410-485$  nm. Scale = 5  $\mu$ m.

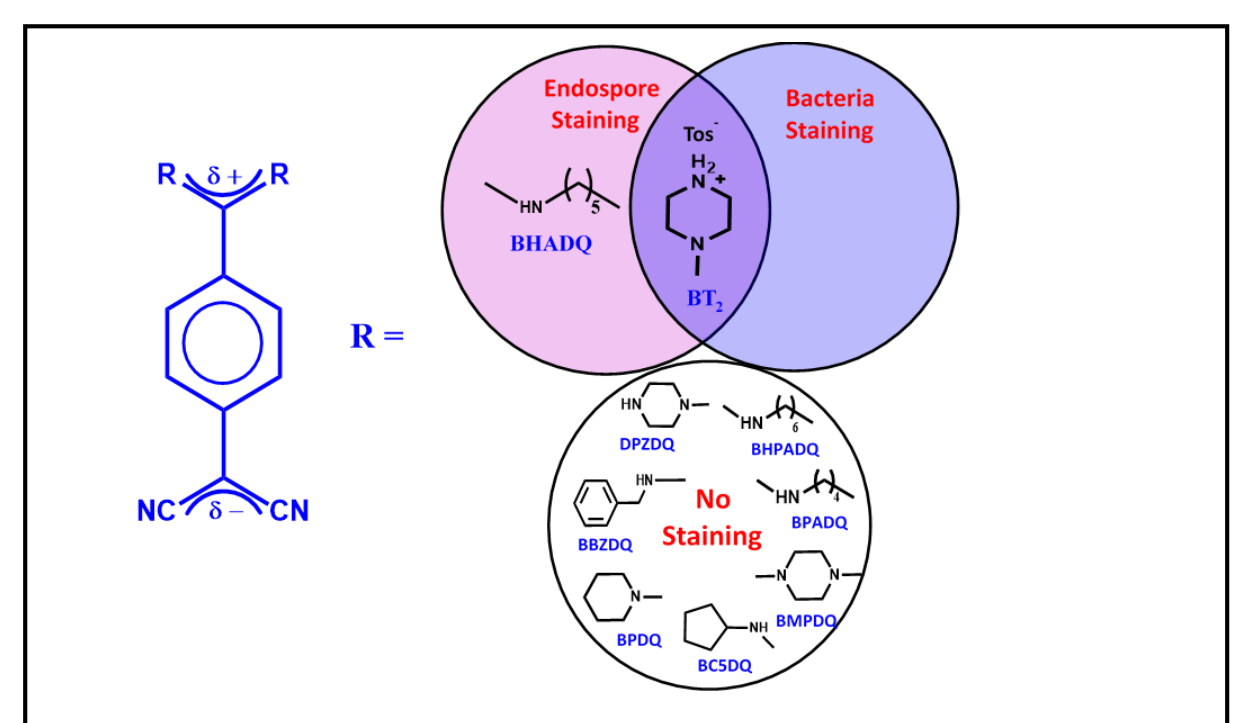


Figure 3.10. Pictorial representation of the results of staining experiments on Halobacillus sp. strain JC554 bacteria and their endospores, using different DADQ derivatives.

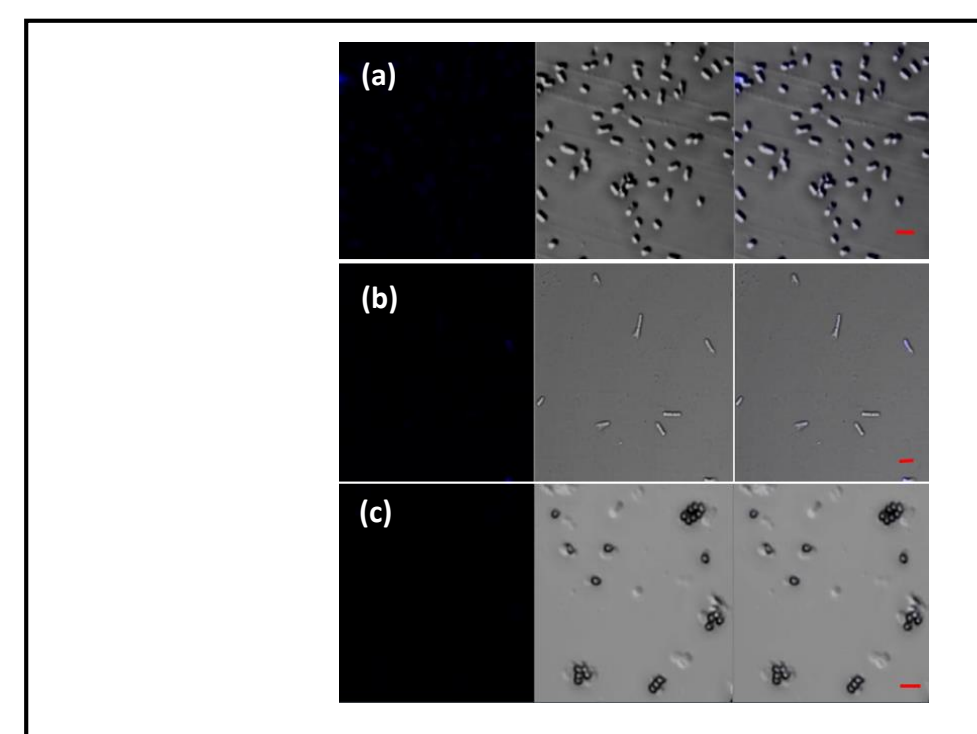


Figure 3.11. CLSM images of (a) E. coli (Gram-stain-negative) bacteria, (b) Halobacillus sp. strain JC554 (Gram-stain-positive) bacteria, and (c) Halobacillus sp. strain JC554 endospores treated with 0.22 mM solution of BPADQ in DMSO.  $\lambda_{exc} = 405$  nm,  $\lambda_{em} = 410-485$  nm. Scale = 5  $\mu$ m.

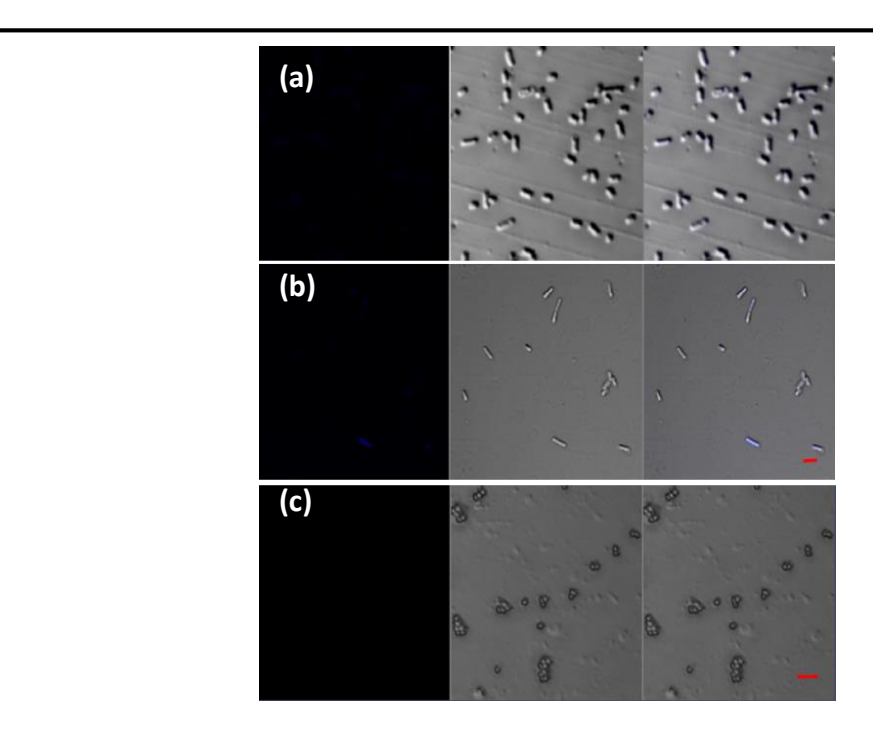


Figure 3.12. CLSM images of (a) E. coli (Gram-stain-negative) bacteria, (b) Halobacillus sp. strain JC554 (Gram-stain-positive) bacteria, and (c) Halobacillus sp. strain JC554 endospores treated with 0.22 mM solution of BHPADQ in DMSO.  $\lambda_{exc} = 405$  nm,  $\lambda_{em} = 410$ -485 nm. Scale = 5  $\mu$ m.

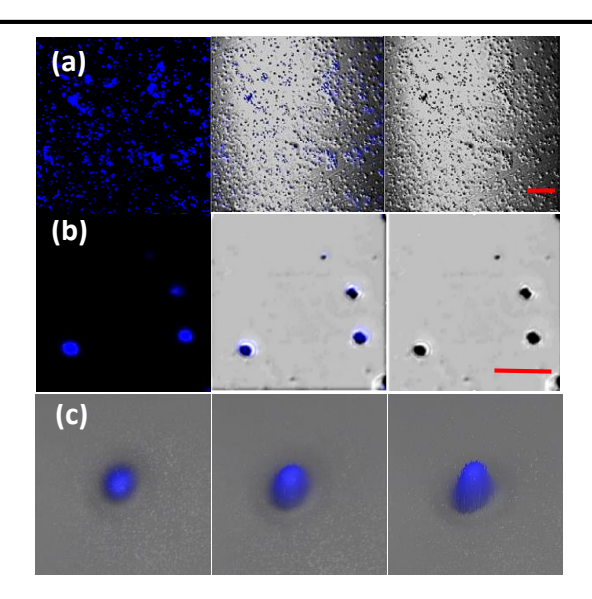


Figure 3.13. CLSM images of the endospores of Halobacillus sp. strain JC554 stained using 0.22 mM solution of BHADQ in DMSO: (a) scale bar = 40  $\mu$ m, (b) scale bar = 4  $\mu$ m (panels, left: fluorescence, right: bright field, middle: merged). (c) 2.5-D image of a single stained endospore viewed at different angles.  $\lambda_{exc} = 405$  nm,  $\lambda_{em} = 410-485$  nm.

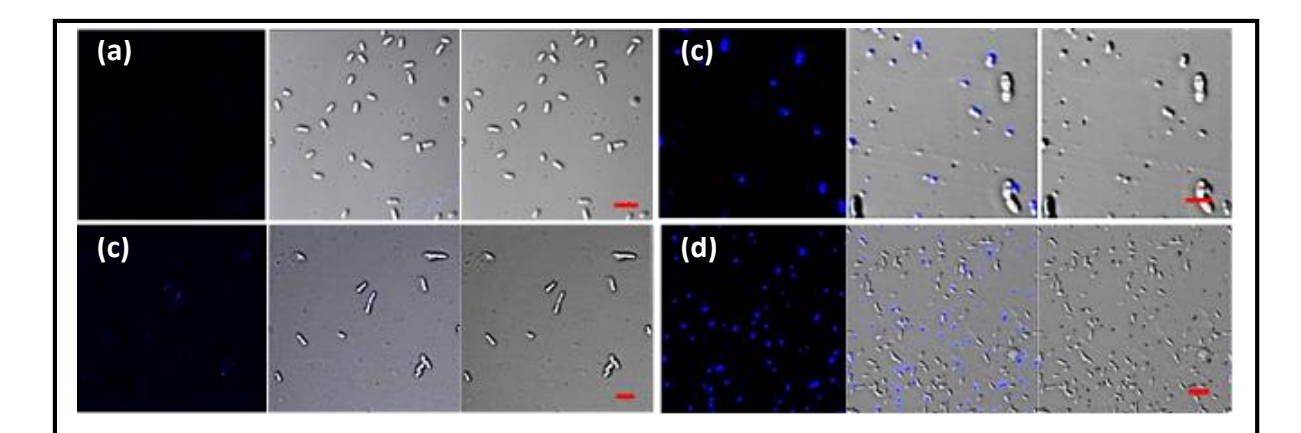


Figure 3.14. CLSM images of (a) E. coli (Gram-stain-negative) bacteria and (b) Halobacillus sp. strain JC554 (Gram-stain-positive) bacteria (scale bar = 5  $\mu$ m), and endospores together with bacteria of Halobacillus sp. strain JC554 (c) scale bar = 5  $\mu$ m and (d) scale bar = 20  $\mu$ m, treated with 0.22 mM solution of BHADQ in DMSO (panels, left: fluorescence, right: bright field, middle: merged).  $\lambda_{exc} = 405 \text{ nm}, \lambda_{em} = 410-485 \text{ nm}.$ 

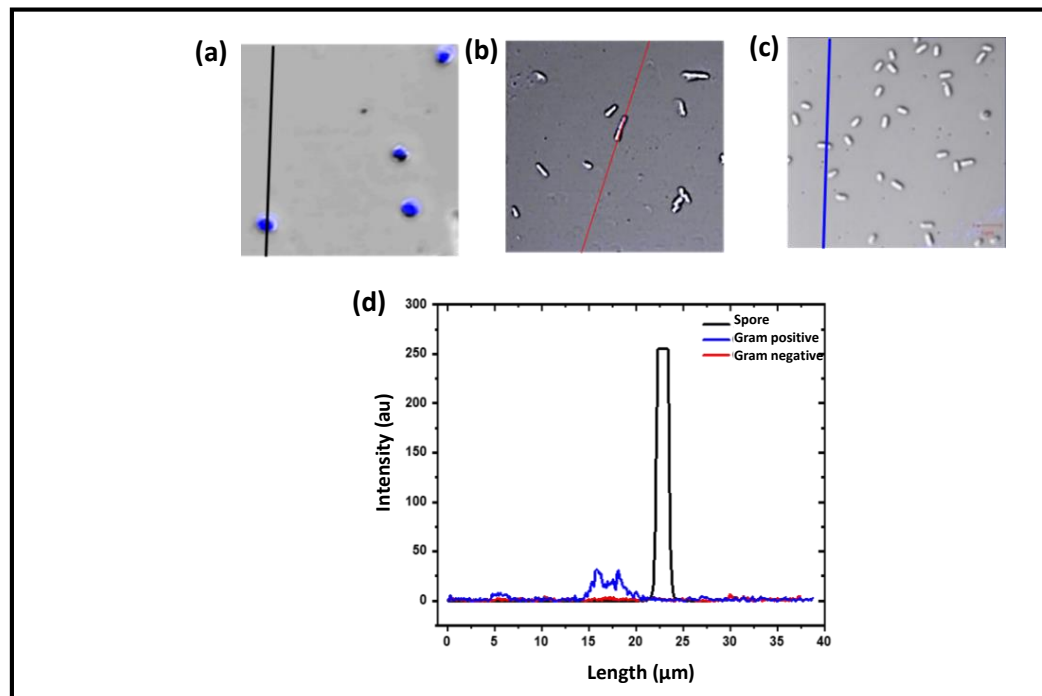


Figure 3.15. CLSM images of (a) Halobacillus sp. strain JC554 endospores, (b) Halobacillus sp. strain JC554 (Gram-stain-positive) bacteria, and (c) E. coli (Gram-stain-negative) bacteria treated with 0.22 mM solution of BHADQ in DMSO. (d) Fluorescence intensity plots along the lines indicated in the images (a - c).

Interestingly, the hexylamine derivative, BHADQ, showed selective staining of endospores; longer alkyl chain derivatives could not be used effectively because of their relatively poorer solubility (Figure 3.12). Figure 3.13 shows the images obtained for endospores of *Halobacillus* sp. strain JC554 stained with BHADQ; the images at different scales (Figure 3.13a,b) show that the staining is extensive and efficient. The 2.5-D images (Figure 3.13c) reveal the successful staining of the cell coat and the core of the endospores. Most significantly, BHADQ stains the endospores selectively, with no staining of Gramstain-negative bacteria, and very weak and rare staining of Gram-stain-positive bacteria A clear comparison of the staining selectivity is illustrated by the (Figure 3.14). corresponding intensity histogram (Figure 3.15). Figure 3.14c and d (especially the overlay images in the middle panels) show the selective staining of endospores when they are present together with the rod-like bacteria; the left-end panels reveal the staining of all the endospores.

# 3.7. Molecular level interactions of BT<sub>2</sub> and BHADQ with components of the endospore cell wall

Structurally, Gram-stain-positive bacteria have an inner plasma membrane and a peptidoglycan outer cover with a periplasmic space in between; Gram-stain-negative bacteria possess an additional outer membrane with a second periplasmic space separating it from the peptidoglycan coat. Endospores possess additional protection consisting of a cortex (with less cross-linked peptidoglycan) and an endospore coat (made of keratin protein, calcium etc.) as shown in Figure 3.1b. We believe that the strongly dipolar nature of the zwitterionic DADQs allows them to penetrate the multi-layered protection of the endospores. The ionic functionality (in BT<sub>2</sub>), and the optimally long alkyl chain (in BHADQ) that engenders efficient intermolecular dispersion effects enable different interactions, and hence stain the bacteria and/or endospores. We have probed the molecular level interaction of the DADQ dyes with peptidoglycan which forms a major component of the cell wall and cortex, as well as the DNA and calcium dipicolinate in the core, to gain insight into the staining of bacteria and endospores.

## 3.7.1. Fluorescence spectroscopy

Fluorescence emission of the DADQs is very sensitive to molecular aggregation and rigidification of the structure as noted in Sec. 3.3.3. Hence fluorescence spectroscopy experiment can provide very useful insight into the fate of the DADQ in the staining process. 0.2 mg of peptidoglycan (PGN) was taken in 1 ml of water and subjected to ultrasonication for 10 min to obtain a homogeneous suspension. Increasing volumes of the PGN suspension was added to a 30  $\mu$ l of a 1 mM solution of BT<sub>2</sub> in water, so that different weight ratios of the two are obtained in the mixture; the fluorescence emission spectra of the solutions were

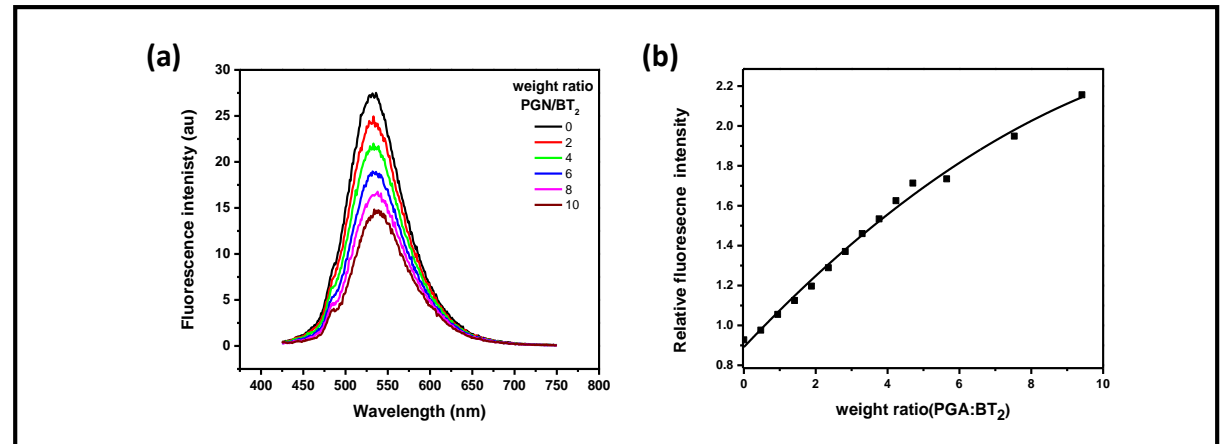


**Figure 3.16.** (a) Fluorescence emission spectra ( $\lambda_{exc}$  =415 nm) of mixtures of PGN and BT<sub>2</sub> in different weight ratios, PGN/BT<sub>2</sub> in water. (b) Plot of the fluorescence emission intensity with respect to the weight ratios (the line is only a guide to the eye).

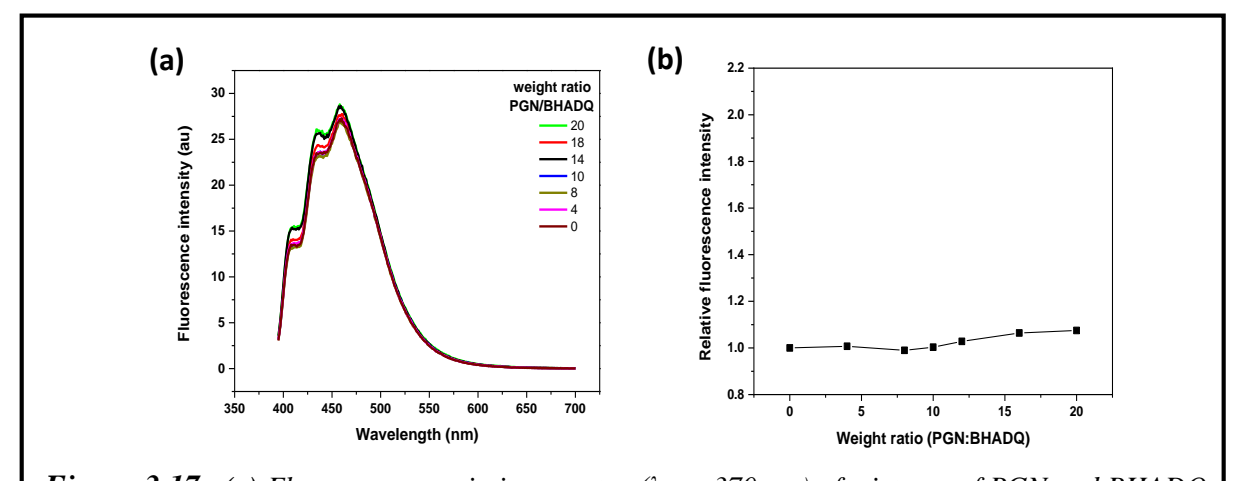
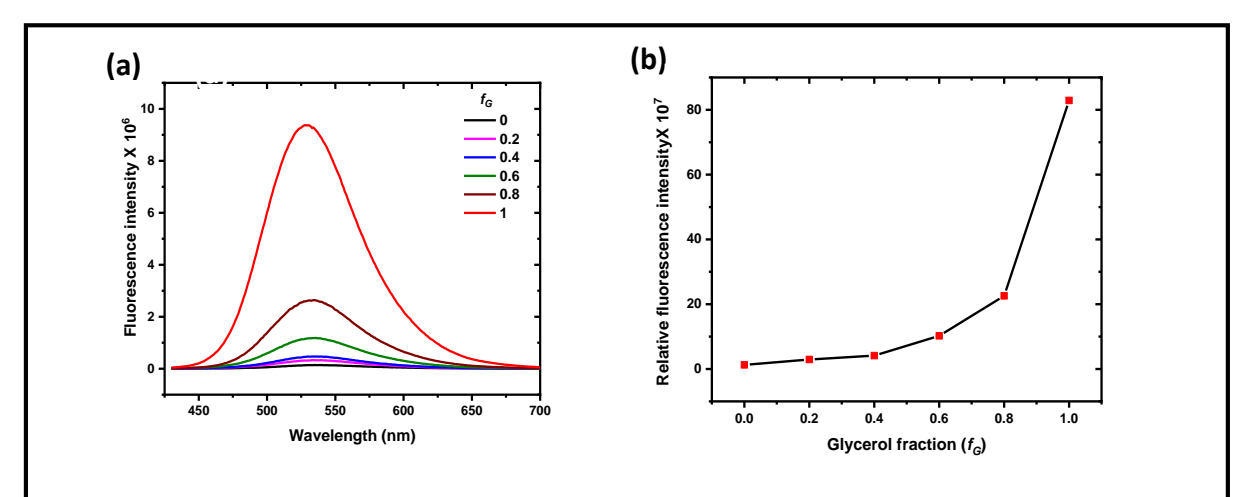


Figure 3.17. (a) Fluorescence emission spectra ( $\lambda_{exc} = 370 \text{ nm}$ ) of mixtures of PGN and BHADQ in different weight ratios, PGN/BHADQ in ethanol. (b) Plot of the fluorescence emission intensity with respect to the weight ratios. Y axis scale is same as in figure 3.16 (b) to enable comparison.



**Figure 3.18.** (a) Fluorescence emission spectra ( $\lambda_{exc}$ = 415 nm) of BT<sub>2</sub> in glycerol-water mixtures with different volume fraction of glycerol  $(f_G)$ ; (b) the corresponding fluorescence intensity plot.

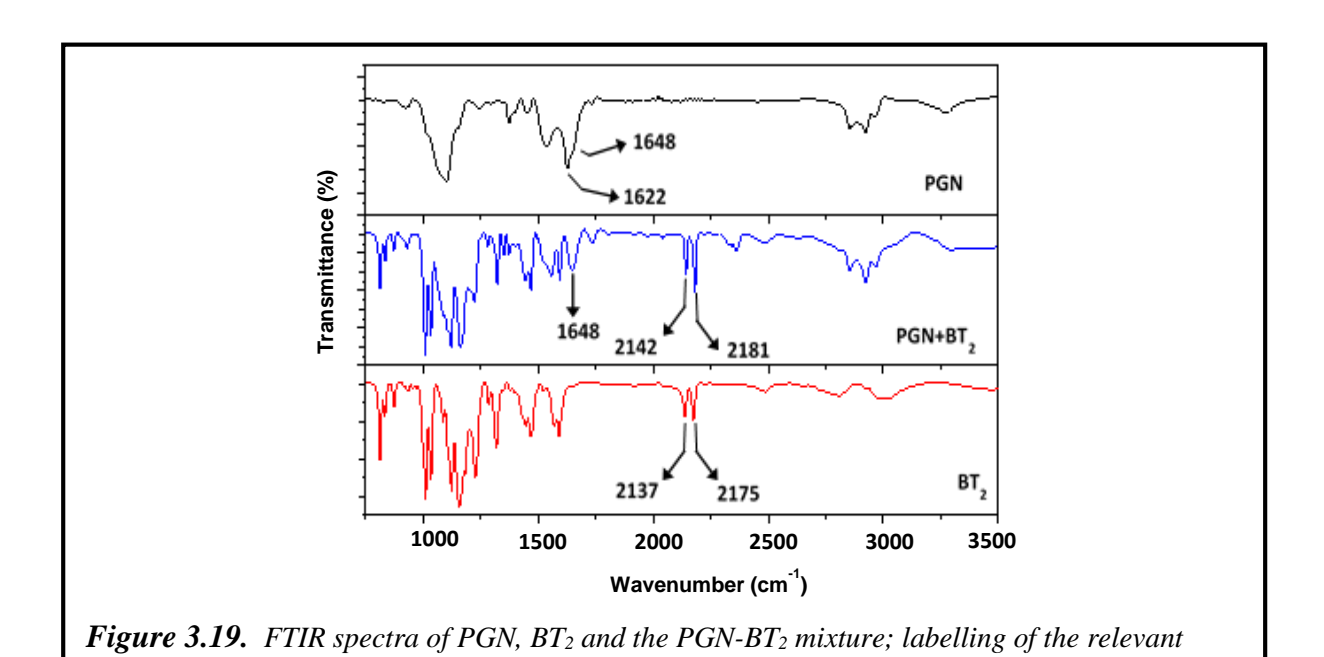
recorded. When increasing proportions of peptidoglycan are added to a fixed concentration of BT<sub>2</sub>, the fluorescence intensity increases (Figure 3.16) indicating that the polymer tends to increasingly restrict the non-radiative excited state relaxation of the fluorophore. Parallel fluorescence experiments with BHADQ (1 mM, DMSO) in place of BT<sub>2</sub> showed no marked variation in the fluorescence intensity (Figure 3.17). This seems to suggest relatively weaker interactions between BHADQ and PGN. Consequence of this is discussed below.

The fluorescence enhancement in the case of BT<sub>2</sub> can be due to local viscosity effect and/or binding interactions with PGN. The following experiment indicates the strong impact of local viscosity on the fluorescence emission of BT<sub>2</sub>. 25 µL of a 2 mM solution of BT<sub>2</sub> in water was added into 1 ml of glycerol-water mixture with varying glycerol volume fraction  $(f_G)$  from 0.0 - 1.0 and the fluorescence emission spectra of the solutions were recorded. Figure 3.18 shows that the fluorescence increases with increasing glycerol content, demonstrating the impact of local viscosity on the emission of BT2; it may be noted that the  $\lambda_{max}$  does not shift, discounting the possibility of molecular aggregation. experiment carried out without BT<sub>2</sub> ensured that there is practically no overlap of the weak emission of the glycerol with that of BT<sub>2</sub>, so that the emission intensities plotted are genuinely that of BT<sub>2</sub>. The overall observation indicates the impact of the matrix effects, similar to that reported with other DADQ derivatives.<sup>27</sup>

## 3.7.2. FTIR spectroscopy

peaks is indicated.

We have also probed the existence of possible binding interactions through FTIR spectral studies. FTIR spectra of PGN, BT<sub>2</sub> and their ground mixtures (weight ratio, 1:1) were recorded. Figure 3.19 shows the amide carbonyl stretch vibration at ~1622 cm<sup>-1</sup> with a shoulder at 1644 cm<sup>-1</sup>; the lower wavenumber peak is likely to arise from the intramolecular H-bonding with the hydroxy groups in the polymer. Disappearance of this peak in the spectrum of the ground mixture with BT<sub>2</sub> points to the break-up of these H-bonds. Interestingly, the cyano stretch vibrations in BT<sub>2</sub> shift to slightly higher wavenumbers in the spectrum of the mixture (2137, 2175 cm<sup>-1</sup> to 2142, 2181 cm<sup>-1</sup>); this is consistent with the replacement of the strong H-bonds involving water molecules of crystallization in BT<sub>2</sub>, <sup>22</sup> by the relatively weaker H-bond interactions involving the hydroxy groups of peptidoglycan. Thus the overall picture is that the H-bonds of the hydroxy groups with the carbonyl groups within the peptidoglycan are replaced by the H-bonds with the cyano groups of BT<sub>2</sub> in the mixture. Electrostatic interaction between the negatively charged polymer and the positively charged dye possibly contributes further to their binding. Parallel experiments with BHADQ in place of BT<sub>2</sub> indicated very little interaction with peptidoglycan at a molecular level (Figure 3.20), consistent with the fluorescence experiments.



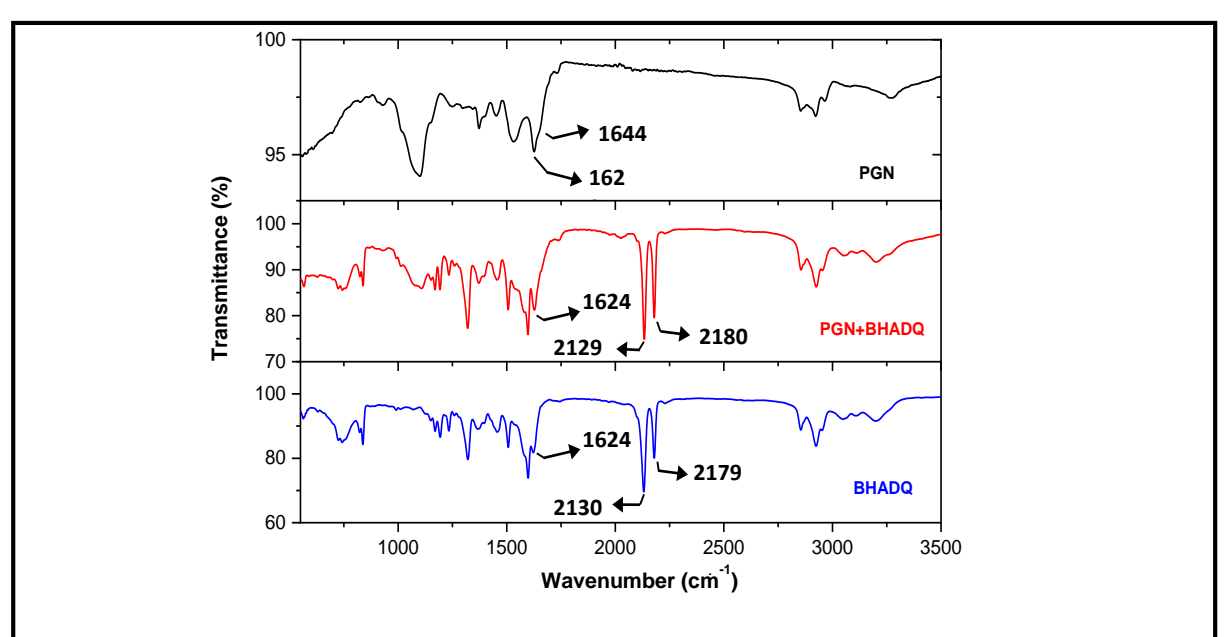


Figure 3.20. FTIR spectra of PGN, BHADQ and the PGN-BHADQ mixture; labelling of the relevant peaks is indicated.

The fact that BT<sub>2</sub> stains bacteria efficiently, whereas BHADQ gets washed away and hence does not stain them, is consistent with these molecular level interactions. They also support our observation that BHADQ does enter into the core of the endospore, whereas BT<sub>2</sub> (in DMSO) is stopped at the outer layers, possibly at the peptidoglycan stage. With BHADQ, the strong fluorescence emanating from the endospore wall in addition to the core suggests that interaction of the hexyl groups of the dye with the specific supramolecular architecture of the peptidoglycan coats is important; critical relevance of the hexylamine chains in this context is reminiscent of the well-established adsorption of dodecylamine on the cortex polymeric matrix facilitated by the hydrophobic alkyl chain.<sup>28</sup>

## 3.8. Molecular level interaction of BHADQ with components of the endospore core

Since the experiments described above suggests relatively less interactions between BHADQ and the PGN component of the endospore coat at the molecular level, we have carried out three experiments to probe the fate of BHADQ in the core of the endospore, with focus on two major components of the core, the DNA and calcium dipicolinate. We have conducted the following experiments: (i) isothermal titration calorimetry (ITC) and (ii) fluorescence emission experiments to assess the binding of BHADQ to the DNA extracted from the bacteria (Sec. 3.4.5), and (iii) FTIR experiments on mixtures of BHADQ with sodium dipicolinate, again a major component of the core. We have also carried out DLS and fluorescence lifetime experiments to probe the role of BHADQ in the endospore staining process.

#### **3.8.1.** Isothermal titration calorimetry

Isothermal titration calorimetry experiments were carried out with aliquots (1.5 µl) of 1 mM of BHADQ solution injected at time intervals of 150 s into 30 µM of DNA taken in the cell having a volume of 240 µl at 298 K. Choice of the solvent for this experiment posed significant problems; after several trial experiments, a water-ethanol mixture with 55 vol% of ethanol was found to be the best choice. Blank experiments were carried out by titrating the BHADQ solution into the pure solvent mixture taken in the cell. Data fitting indicated that enthalpic contributions are likely to be more relevant (Figure 3.21, Table 3.2).

It may be noted that saturation of the heat flux could not be realized due to the experimental limitations dictated by the low solubility of the components, as well as the relatively weak binding interactions. Even though saturation levels could not be reached, a weak and cooperative binding of the dye to the DNA could be identified; A single-site binding model was used to fit the integrated thermogram. The association constant is of the order of  $\sim 3\times 10^3$  M<sup>-1</sup>. The large value of N obtained is not uncommon in DNA titrations;<sup>29</sup>

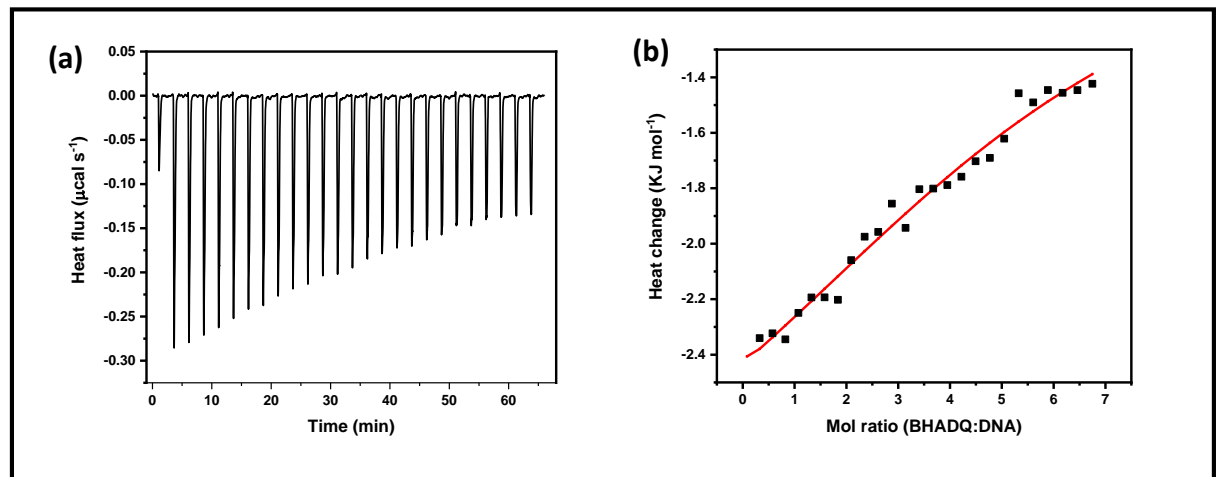


**Figure 3.21.** (a) Raw and (b) integrated thermograms from the isothermal titration of BHADQ-DNA; fitting of the integrated thermogram is shown in (b).

Table 3.2. Binding and thermodynamic parameters for the BHADQ-DNA system estimated from the isothermal calorimetry; errors are shown in parenthesis. N: stoichiometry,  $K_D$ : dissociation constant,  $\Delta H$ : enthalpy change,  $\Delta G$ : free energy change,  $\Delta S$ : entropy change.

Parameters	Value (error)
N (Sites)	10.4 (±0.572)
K <sub>D</sub> (10 <sup>-6</sup> M)	330 (± 238)
ΔH (kcal mol <sup>-1</sup> )	-4.99 (± 1.96)
ΔG (kcal mol <sup>-1</sup> )	-4.75
ΔS (cal mol <sup>-1</sup> K <sup>-1</sup> )	-0.788

in the present case, it could also arise due to aggregation of BHADQ which might occur concomitantly with the binding. Such a picture is also consistent with the fact that the binding is driven by the enthalpic rather than entropic factor (the latter is dominant if the dye binds strongly to multiple sites on the DNA).

#### 3.8.2. Fluorescence spectroscopy

Increasing aliquots of DNA dissolved in ethanol was added into a 0.05 µM solution of BHADQ in ethanol, maintaining the total volume of the mixture constant and the fluorescence emission spectra were recorded. An interaction between the BHADQ and DNA could be confirmed by the observation of a steadily increasing fluorescence intensity, when increasing proportions of DNA are added to a fixed concentration of BHADQ in ethanol solution (Figure 3.22).

In order to probe the fate of BHADQ in the core of the endospore, the fluorescence emission spectra of BHADQ in DMSO-water mixtures with increasing fraction of water were recorded; DMSO is a solvent and water a non-solvent for BHADQ. Figure 3.23 clearly shows that the fluorescence emission of the BHADQ rises abruptly when the water fraction in the solvent mixture exceeds 60% indicating the onset of molecular aggregation. The clear blue shift of the  $\lambda_{max}$  is indication of molecular aggregation.<sup>30</sup> This is the characteristic experiment used to demonstrate aggregation induced emission. 19,20

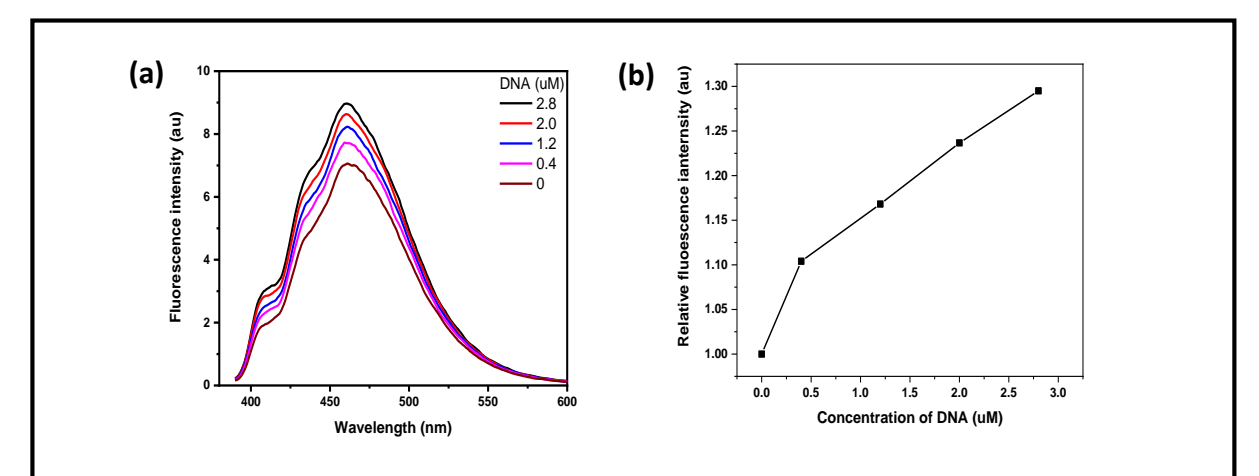


**Figure 3.22.** (a) Fluorescence emission spectra ( $\lambda_{exc}$ = 370 nm) of BHADQ with different concentration of DNA added, and (b) plot of the corresponding fluorescence emission intensity variation.

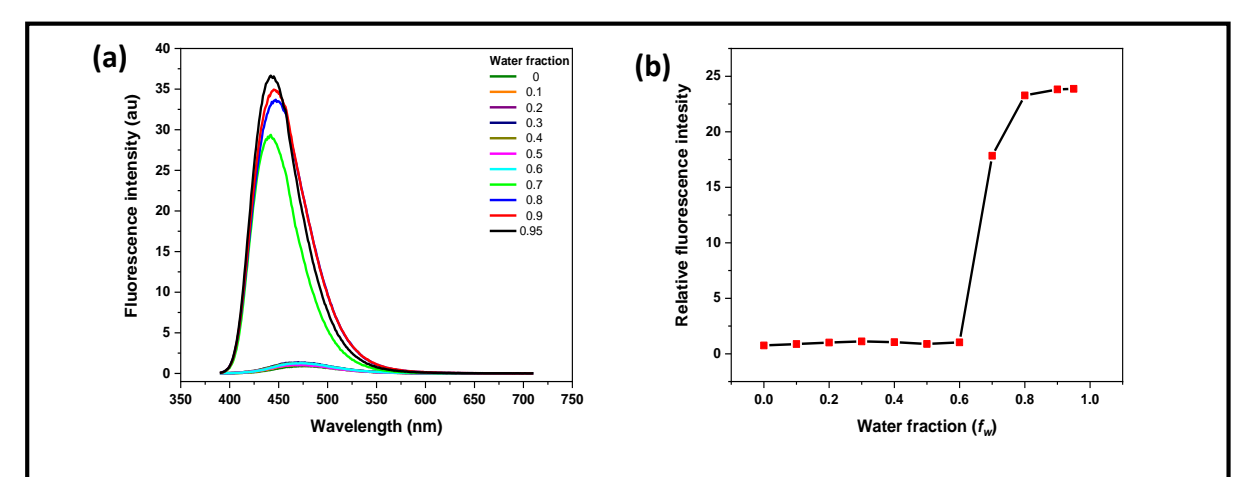


**Figure 3.23.** (a) Fluorescence emission spectra ( $\lambda_{exc}$ = 370 nm) of BHADQ in DMSO-water mixture with different volume fractions of water. (b) Plot of the fluorescence intensity with respect to the water fraction in the solution mixture.

## **3.8.3.** FTIR spectroscopy

FTIR spectra of sodium dipicolinate, BHADQ and their ground mixture (1:1) revealed no strong intermolecular interactions. However a notable effect upon mixing is the slight blue shift of the CH wagging vibration of the dipicolinate (Figure 3.24); this possibly arises from weak  $\pi$ - $\pi$  interactions with the aromatic ring in BHADQ.

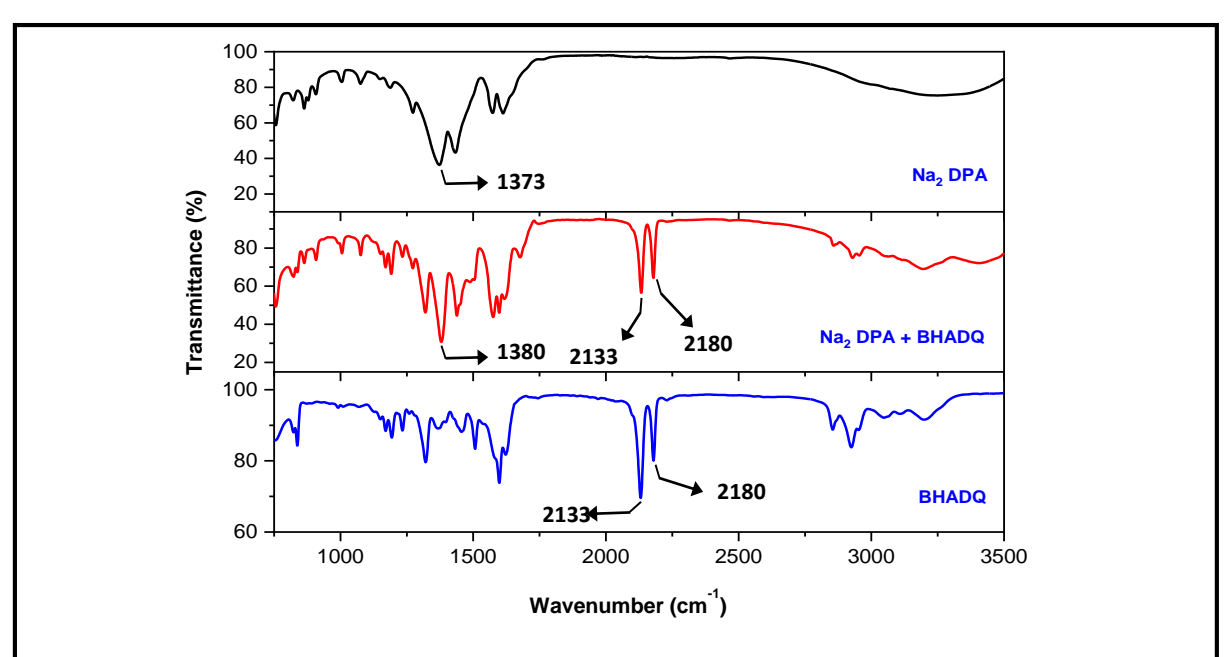


Figure 3.24. FTIR spectra of Na<sub>2</sub>DPA, BHADQ and Na<sub>2</sub>DPA-BHADQ (1:1) mixture; the relevant peaks are labelled.

# 3.8.4. Dynamic light scattering (DLS) experiment

Both molecular aggregation and local polarity difference can influence the enhancement of the fluorescence emission of BHADQ in the core of stained endospores. In order to probe the extent of aggregation of BHADQ in an aqueous medium, DLS experiments were carried out to assess the size of any aggregates that may be formed. 50 µL of a 4 mM solution of BHADQ in DMSO was injected into 3 ml of MilliQ water and the particle size analysed; DLS data presented in Figure 3.25 show a monodisperse distribution of particles with an average size of  $140 \pm 20$  nm. This observation together with the experiments described earlier, leads to the conclusion that the efficient staining of the endospore core by BHADQ is enabled by the weak binding with the core components that rigidifies the dye molecule, as well as molecular aggregation in the aqueous environment of the core.

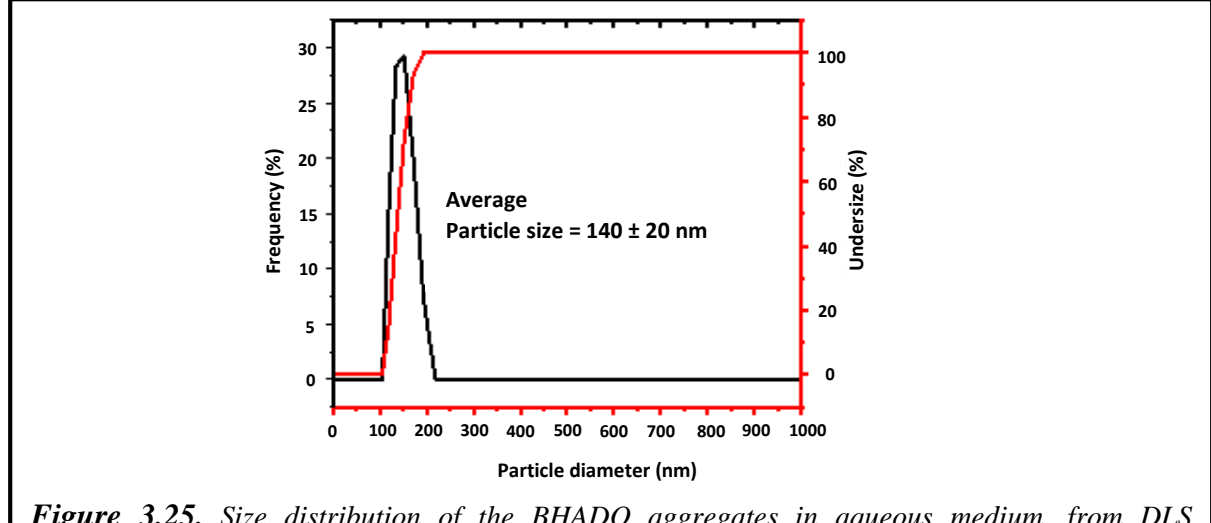


Figure 3.25. Size distribution of the BHADQ aggregates in aqueous medium, from DLS experiment.

#### 3.8.5. Fluorescence lifetime imaging studies

Fluorescence lifetime imaging of *Halobacillus* sp. strain JC554 endospores (5  $\mu$ L) stained using BT<sub>2</sub> (0.11 mM solution in water) shows clearly bright outer rings, whereas the whole structure is bright with 0.22 mM solution of BHADQ. In the case of BT<sub>2</sub>, the lifetime could be estimated only for the outer coat (1.2 ns); with BHADQ, comparable values (1.57 and 1.73 ns) were obtained for both the outer coat and the inner core as shown by the data presented in Table 3.3 (Figure 3.26). In all cases, the excited state lifetimes are comparable to that of the pure dyes (~1.40 – 1.80 ns), suggesting that the increased local population of the fluorophores is responsible for the bright fluorescence. It is notable that the experiments with the unstained endospores required significantly higher excitation power to elicit the auto-fluorescence, which is observed only from the outer coat containing the emissive functionalities. Together, these observations prove that the fluorescence emission from the stained samples arises exclusively from the fluorophore dyes, and that BT<sub>2</sub> binds only to the outer coat and cortex of the spore, whereas BHADQ enters into the core as well.

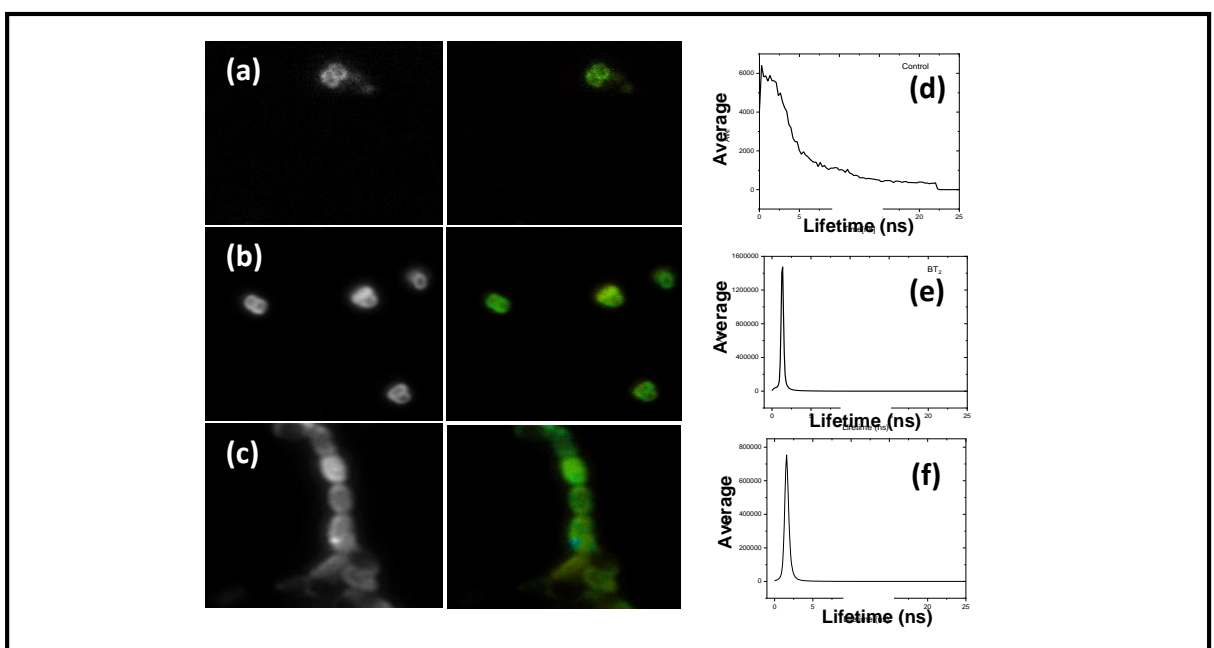


Figure 3.26. Fluorescence lifetime images of (a) untreated Halobacillus sp. strain JC554 endospores, and the endospores stained with (b)  $BT_2$  (0.11 mM solution in water) and (c) BHADQ(0.22 mM solution in DMSO) together with (**d-f**) the respective lifetime histograms. Scale = 2  $\mu$ m.

**Table 3.3.** Excited state lifetime of the pure DADQ materials, the dyes staining Halobacillus sp. strain JC554 endospores, and the unstained endospores, estimated from fluorescence lifetime imaging experiments (the excitation power used in 1 - 4 was 0.15  $\mu$ W and in 5, 0.74  $\mu$ W).

Sl. No.	Dye		Lifetime (ns)
1	BT <sub>2</sub>		1.40
2	BHADQ		1.81
	Dye + Spores	Core	Outer Coat
3	Endospore	-	3.03
4	BT <sub>2</sub> + endospore	-	1.20
5	BHADQ+ endospore	1.57	1.73

#### 3.9. Plausible staining mechanism

The different spectroscopy and calorimetry experiments involving the dyes and the endospore components described in the previous sections lead to the following several conclusions. BT2 binds efficiently with peptidoglycan so that it is able to stain bacteria as well as the endospore, with stronger interaction with the coat in the latter case; the BT<sub>2</sub> bound in the rigid environment shows strong fluorescence. BHADQ on the other hand shows negligible binding with peptidoglycan, so that it does not stain bacteria. With endospores, it passes into the core, but also gets trapped partially in the supramolecular structure of the coat, so that the whole system is stained efficiently. The enhanced fluorescence arises due to the rigidification of BHADQ in the coat environment and the bound state with the DNA in the core, as well as possible molecular aggregation within the aqueous environment in the core.

## 3.10. Effect of staining on endospores

#### 3.10.1. Dormancy of endospores

We carried out Raman spectral studies<sup>31,32</sup> to detect the dormancy of the stained endospores. An aliquot (5  $\mu$ L) of endospores taken in aqueous medium and stained with a 4 mM solution of BHADQ in DMSO, was drop cast on the microscope glass slide and protected with a coverslip; Raman spectra were recorded (Figure 3.27).

Figure 3.27 shows that the crucial peak due to the symmetric ring breathing mode of calcium dipicolinate at 1018 cm<sup>-1</sup> is retained in the sample treated with BHADQ; if dead or germinated, loss of calcium dipicolinate would cause this peak to diminish or disappear (the former is shown in the bottom panels of Figure 3.27). Raman spectral studies thus indicate that the staining process does not alter the chemical structure of the endospore coat in any definitive way.

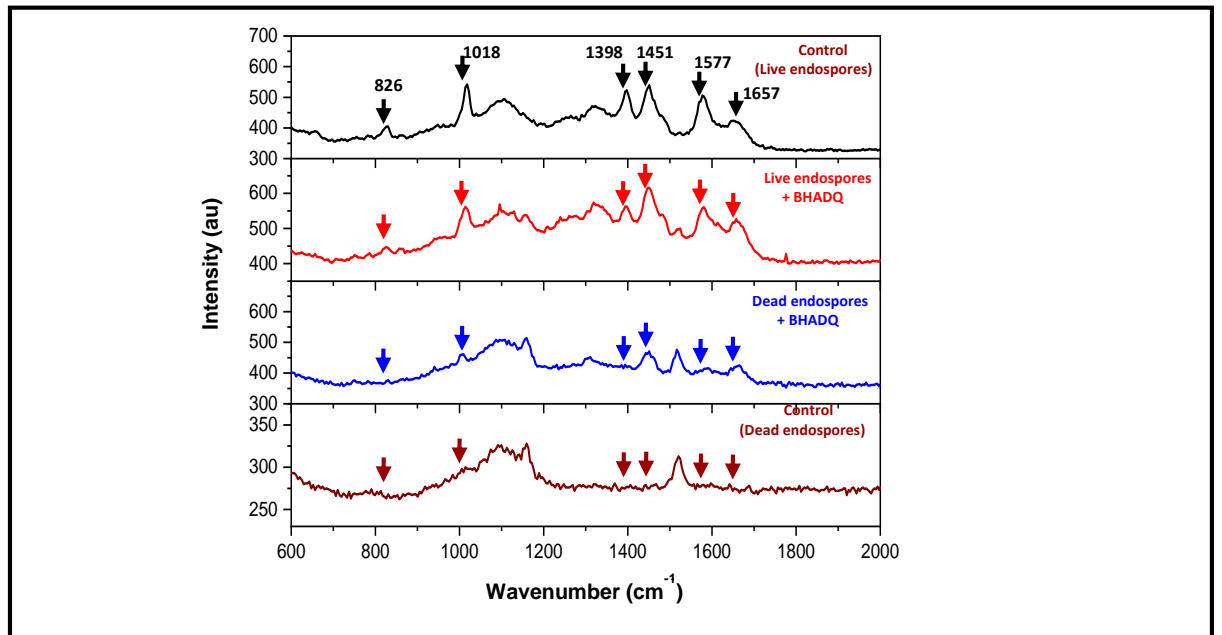


Figure 3.27. Raman spectra of live and dead endospores of Halobacillus sp. strain JC554, untreated (control) and treated with 0.22 mM solution of BHADQ in DMSO (stained).

#### 3.10.2. Lethal germination of endospores

#### (a) Phase contrast microscopy

Phase contrast microscopy<sup>33</sup> of the *Halobacillus* sp. strain JC554 endospores under different conditions was also carried out in order to assess the possibility of lethal germination in the presence of BHADQ and BT<sub>2</sub>. An aliquot (5 µL) of endospores stained using BT<sub>2</sub> (2 mM) and BHADQ (4 mM) in aqueous medium was drop cast on a microscope glass slide and covered with coverslips; their phase contrast images are shown in Figure 3.28. The bright images obtained in all cases show that the endospores are not germinated in presence of the dyes.

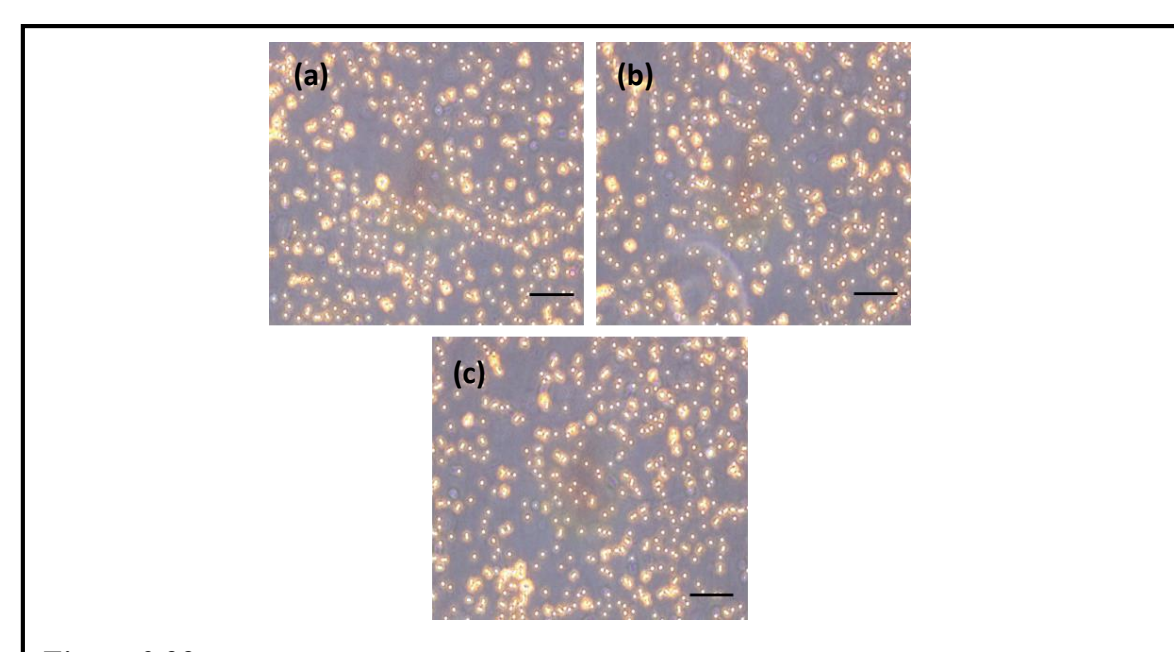


Figure 3.28. Phase contrast microscopy images of the Halobacillus sp. strain JC554 endospores, (a) unstained, and stained using (b)  $BT_2$  and (c) BHADQ.  $Scale = 10 \ \mu m$ .

#### (b) Germination assay

Germination assay experiment was also carried out in order to assess the possibility of lethal germination of *Halobacillus* sp. strain JC554 endospores in the presence of BHADQ and BT<sub>2</sub>. 60 µL of different concentrations of BHADQ (in DMSO) and BT<sub>2</sub> (in water and DMSO) were taken in a 1 ml quartz cuvette containing 700 µL of the endospore in aqueous medium. Homogeneity of the mixture was ensured by thorough mixing. The optical density at 600 nm was measured at 5 min intervals up to 1 h. It is seen from Figure 3.29 that no significant endospore germination occurs even after 60 min. We have specially verified that germination does occur in a nutrient medium. These experiments demonstrate unambiguously that the DADQ dyes do not damage the endospores; the endospores can be imaged in the dormant state, and possibly monitored through their germination under favorable conditions.

#### 3.10.3. Permeability assessment of endospores

Endospores were prepared for staining as described in Sec. 3.4. The washed endospores were separated into several portions. Three portions were individually treated with DMSO, 4 mM solution of BHADQ in DMSO, and 2 mM solution of BT<sub>2</sub> in water, at  $28^{\circ}$ C for 15 min. The fourth portion of endospores was treated with ethanol at  $70^{\circ}$ C for 1 h, in order to kill the endospores. Samples were washed thrice with MilliQ water and centrifuged (10,000 rpm at  $4^{\circ}$ C for 5 min). The washed endospores were incubated with 15  $\mu$ L of 83  $\mu$ M propidium iodide (PI) for 15 min and again washed twice; it may be enabled that PI stains any dead cells (Figure 3.30). The stained endospores were imaged in a CLSM using a 543 nm laser with emission collected in the 550 - 735 nm range. Protoplast of the permeabilized endospores was displayed red in the confocal images. Figure 3.30 shows that PI stains only those endospores which were treated with ethanol, confirming that the treatment with the DADQ dyes do not enhance the endospore

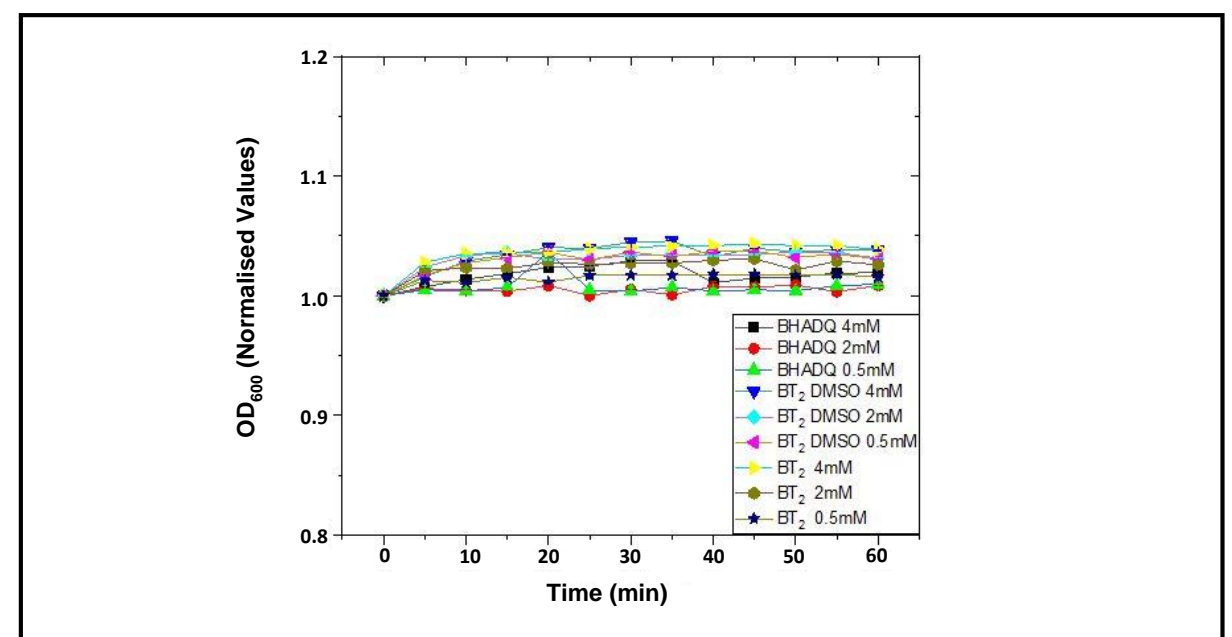


**Figure 3.29.** Time variation of the absorption at 600 nm  $(OD_{600})$  of the Halobacillus sp. strain JC554 endospores treated under different conditions.

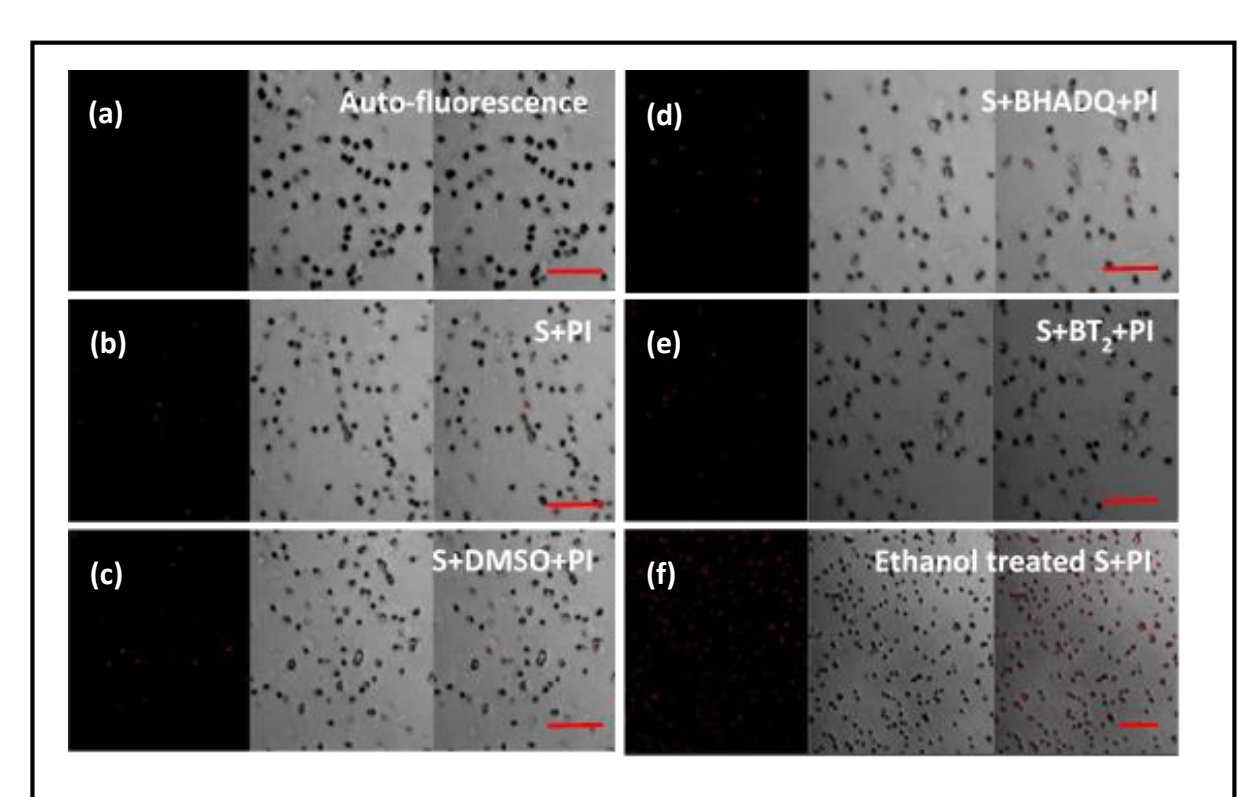
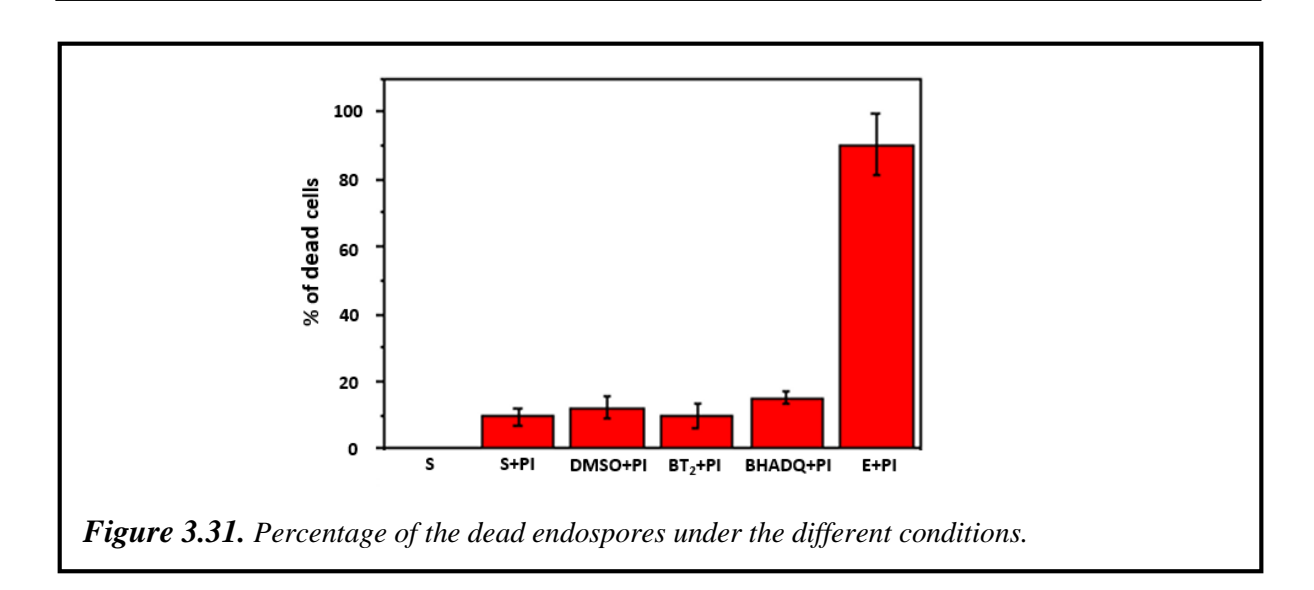


Figure 3.30. CLSM images of the (a) untreated endospores, and endospores (S) treated with (b) only PI, (c) DMSO followed by PI, (d) DMSO solution of BHADQ followed by PI, (e) aqueous solution of  $BT_2$  followed by PI, and (f) ethanol followed by PI. Scale = 10  $\mu$ m.



permeability. Dead endospores were counted using ImageJ<sup>34</sup> software in the different cases; the data in Figure 3.31 also confirms the above observation. The legends can be read as: S: Endospores only, S+PI: Endospores stained directly with PI, DMSO+PI: Endospores treated with DMSO followed by PI, BT<sub>2</sub>+PI: Endospores stained with BT<sub>2</sub> (in water) followed by PI, BHADQ+PI = Endospores stained with BHADQ (DMSO) followed by PI, E+PI = Endospores heated in 70 % ethanol for 1 h and incubated with PI. This series of experiments clearly rule out the possibility of BT<sub>2</sub> or BHADQ destroying the spore cell coats or inducing lethal germination of the endospores.

#### 3.10.4. Viability assay

 $BT_2$  and BHADQ solutions were filtered and sterilized using a syringe filter (0.2  $\mu$ m) to remove the bacteria in the solvents. The sterilized dyes were used for the staining experiments (Sec. 3.4). The stained endospores were washed twice with MilliQ water to remove the unbound dye molecules on the surface. The washed endospores were streaked on the nutrient agar medium containing plates. They were incubated for 12 h; bacteria germinated from the stained endospores were observed on the plates. It clearly indicated that both fluorescence dyes do not kill the endospores in the staining process.

## 3.11. General utility of BHADQ

Imaging experiments with other bacterial endospores such as those of *Bacillus* sp. strain JC1009, *Bacillus* sp. strain JC39 and *Bacillus* sp. strain JC1008 indicate that BHADQ is an efficient dye for imaging them as well (Figure 3.32). In the case of *Bacillus* sp. strain JC1009, the bacteria were present along with the endospores, and the latter are selectively stained (Figure 3.33). This demonstrates the potential utility of BHADQ for selective imaging of endospores. Further work with BHADQ has shown that it selectively stain endospores, leaving out polyhydroxybutyrate (PHB) granules.<sup>35</sup>

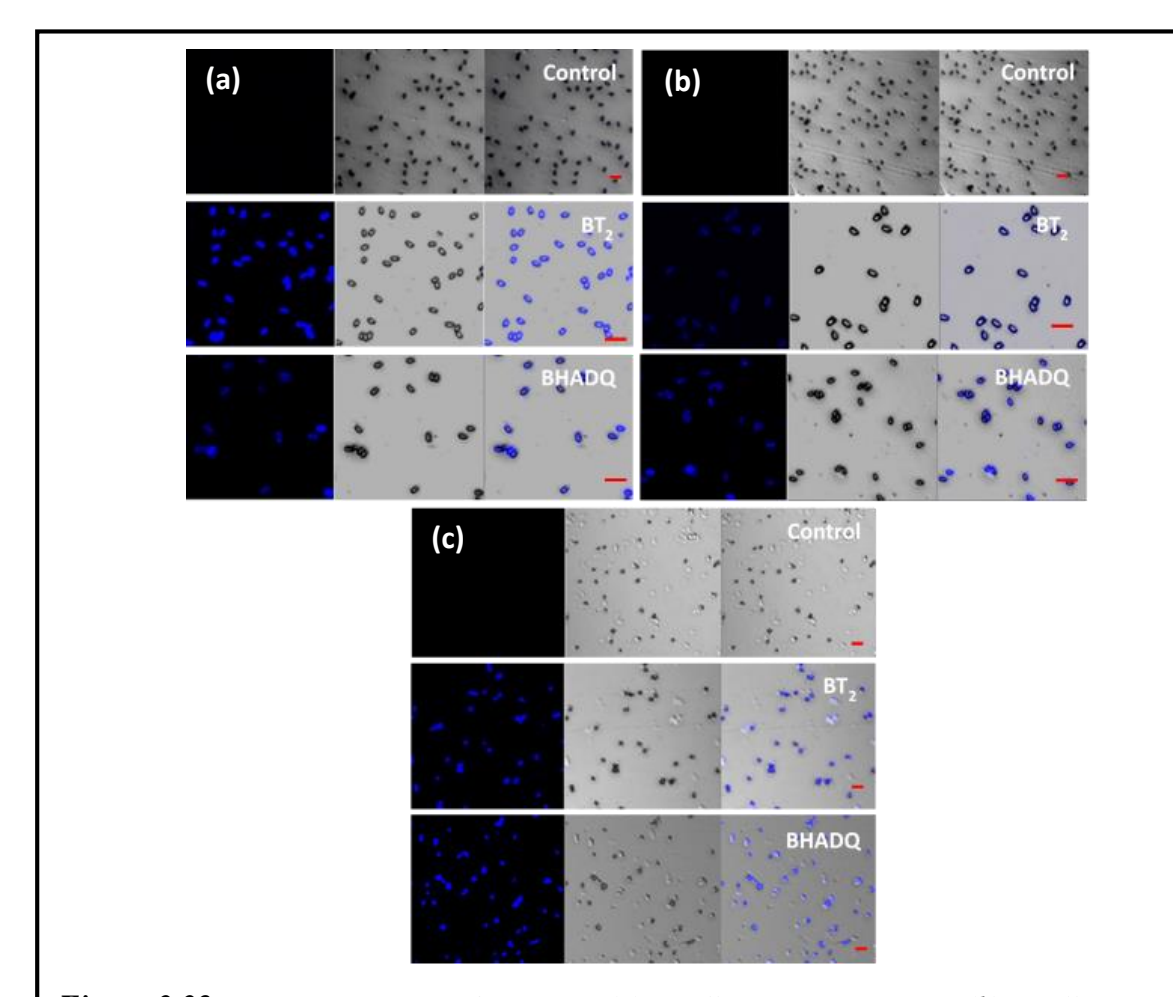


Figure 3.32. CLSM images of endospores of (a) Bacillus sp. strain JC1009 (b) Bacillus sp. strain JC39 and (c) Bacillus sp. strain JC1008 stained using 0.11 and 0.22 mM solution of BT2 and BHADQ in DMSO respectively.  $\lambda_{exc} = 405$  nm,  $\lambda_{em} = 410-485$  nm. Scale = 5  $\mu$ m.

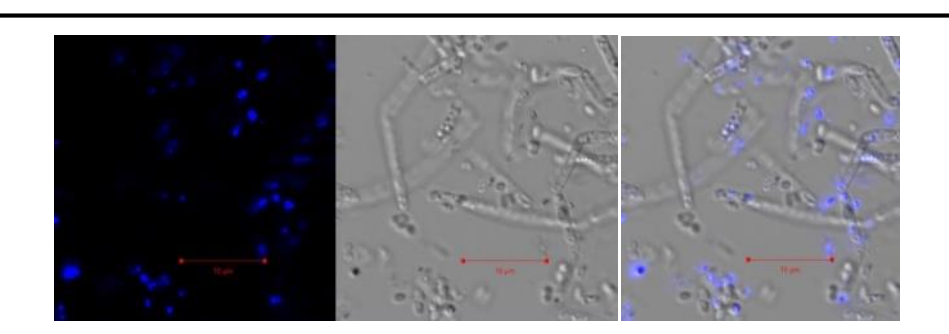


Figure 3.33. CLSM images of Bacillus sp. strain JC1009 bacteria and its endospores stained using 0.22 mM solution of BHADQ in DMSO.  $\lambda_{exc} = 405$  nm,  $\lambda_{em} = 410$ -485 nm. Scale = 10  $\mu$ m

#### 3.12. Supporting experiments

#### 3.12.1. Auto-fluorescence analysis

In order to select for our imaging experiments, those endospores which do not show auto-fluorescence, we had initially carried out the fluorescence imaging with various untreated endospores with different excitation wavelengths; the salient observations are added in Figure 3.34. *Halobacillus* sp. strain JC554 was chosen for our detailed imaging experiments discussed in this chapter as it does not show any auto-fluorescence under the imaging conditions employed in our experiments.

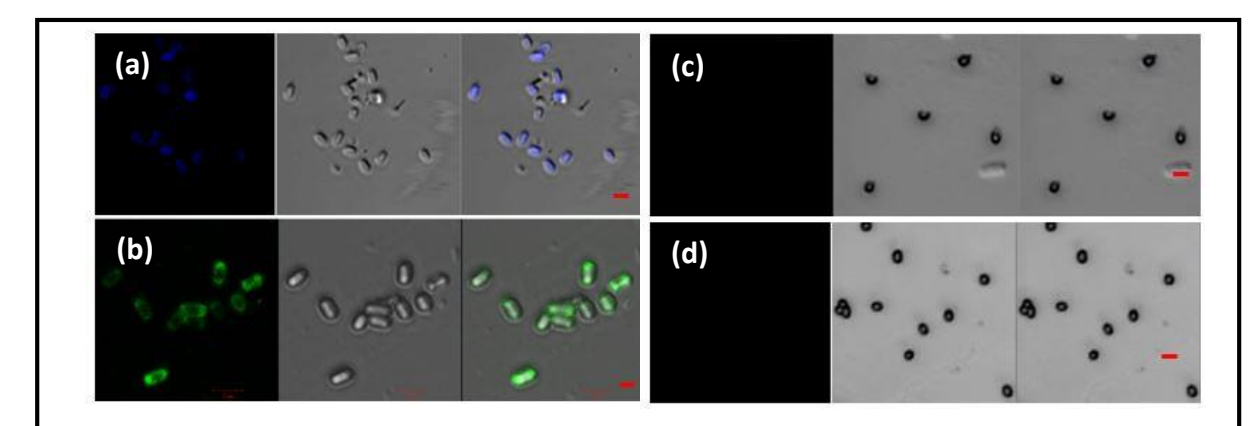


Figure 3.34. CLSM images of unstained endospores of Bacillus sp. strain JC1005 (a)  $\lambda_{exc} = 405$  nm,  $\lambda_{em} = 410$ -485 nm, (b)  $\lambda_{exc} = 488$  nm,  $\lambda_{em} = 500$ -585 nm, and Halobacillus sp. strain JC554 (c)  $\lambda_{exc} = 405$  nm,  $\lambda_{em} = 410$ -485 n,. (d)  $\lambda_{exc} = 488$  nm,  $\lambda_{em} = 500$ -585 nm. Scale = 2  $\mu$ m.

#### 3.12.1. Photostability and cytotoxicity

The photostability and absence of cytotoxicity are of critical importance to ensure the practical utility and safe handling of fluorescent dyes for imaging applications. Monitoring the fluorescence emission under continuous excitation shows that the DADQ molecules are stable for extended periods of time (Figure 3.35). Cytotoxicity studies using L929 and HeLa cell lines showed that the IC<sub>50</sub> value for both BT<sub>2</sub> and BHADQ are  $> 500 \mu g ml^{-1}$ , as the viability remained > 65% even at this concentration (Figure 3.36, 3.37). It is thus clear that, the concentrations used in our imaging experiments, 73 and 77  $\mu g ml^{-1}$  of BT<sub>2</sub> and BHADQ respectively, are well within the safety limits.

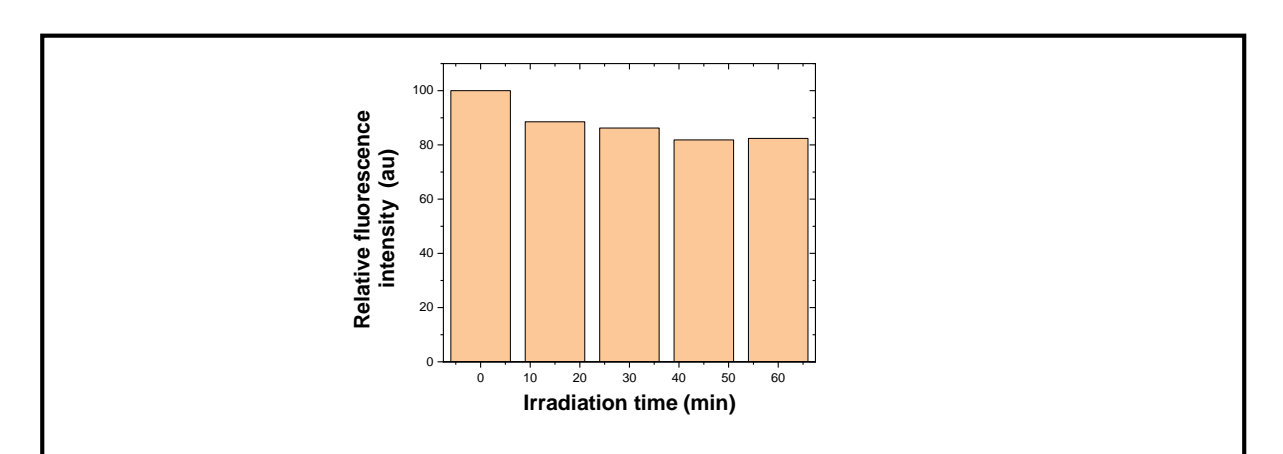


Figure 3.35. Intensity of the fluorescence emission of BHADQ in solution, as a function of the time period for which the excitation is carried out.

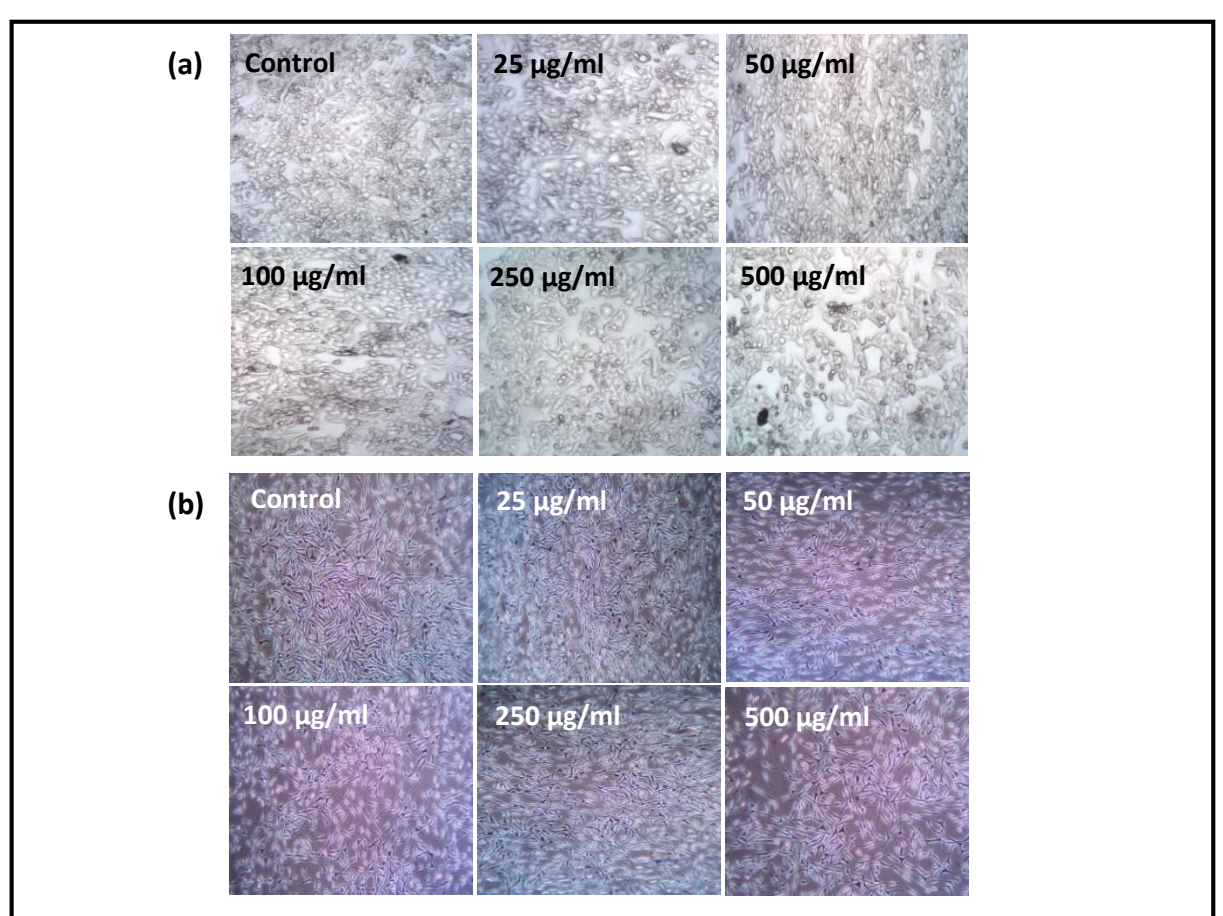
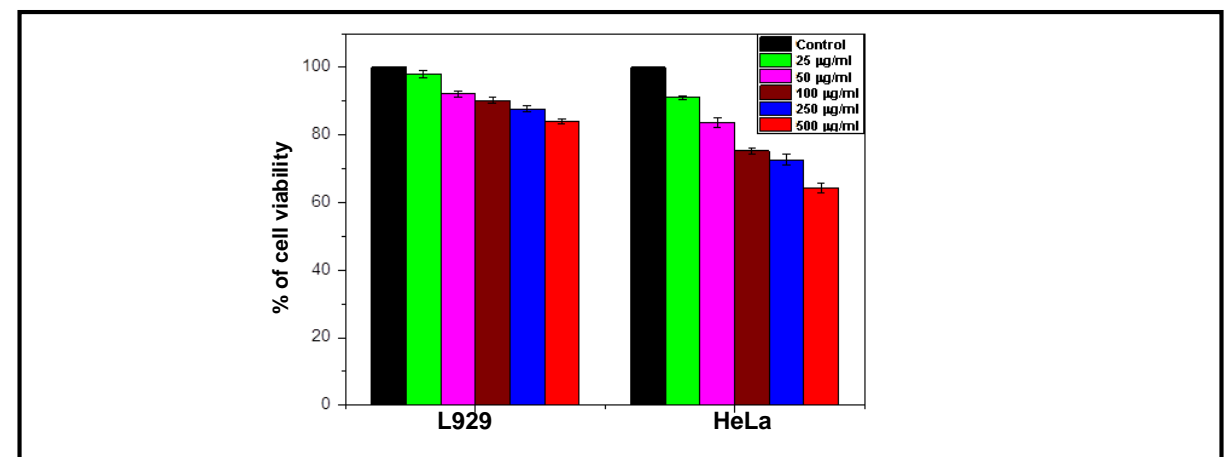


Figure 3.36. Inhibition of (a) HeLa and (b) L929 cell colony formation in presence of different concentrations of BHADQ at 24 h.



**Figure 3.37.** Cell viability of the L929 and HeLa cells in the presence of different concentrations of BHADQ (in  $\mu$ g/ml) at 24 h.

#### **3.13. Summary**

Selected DADQ derivatives are shown to be efficient dyes for bright fluorescence imaging of bacteria and their endospores; the staining protocols are extremely simple with no chemical or significant thermal treatments involved. Specific derivatives are shown to be selective for endospores; significantly, the staining does not destroy their dormant state. Several support and control experiments provided significant insight into the molecular/supramolecular level interactions that enable the incorporation of selected DADQ fluorophores inside the endospores; this is particularly relevant, such endospores are known to resist most of the conventional dyes, making their fluorescence based imaging extremely challenging. DADQs with their easily tailored molecular structure, zwitterionic framework, and strongly emissive character in the rigid/aggregated state are promising candidates to develop novel and efficient dyes for fluorescence based imaging of bacteria and their spores.

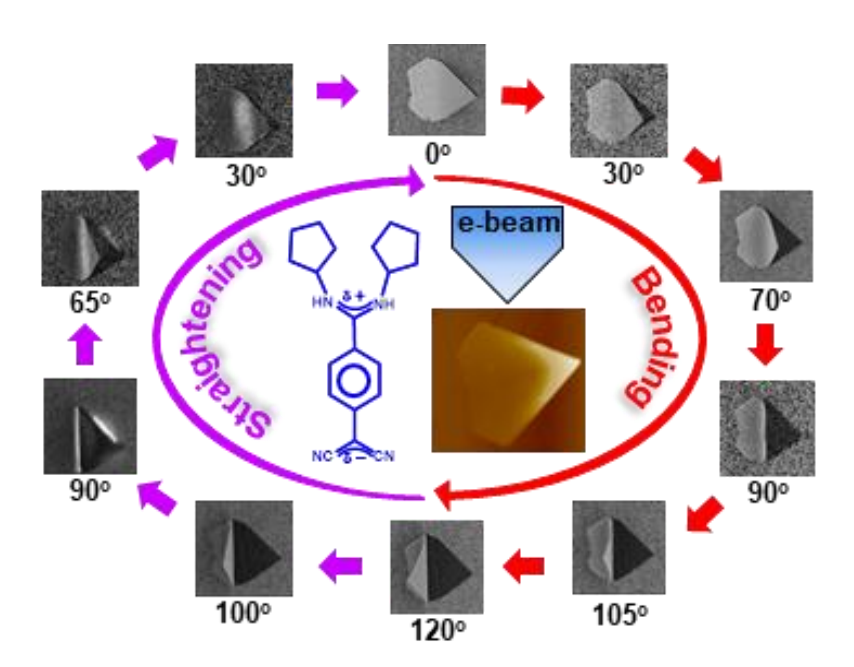
#### References

- 1. P. Setlow, Microbiol. Spectrum., 2014, 2, 1-14.
- 2. U. Ronner and U. Husmark, Adhesion of bacillus cereus spores- A Hazard to the dairy industry: Biofilms-science and technology, ed. L. F. Melo, Springer, Netherlands, 1992, vol. 223, pp. 403-406.
- A. Soni, I. Oey, P. Silcock and P. Bremer, Compr. Rev. Food Sci. Food saf., 2016, 3. **15**, 1139-1148.
- T. Sandle, Am. Pharmaceut. Rev., 2014, 17, 1-5. 4.
- C. E. Binkley, S. Cinti, D. M. Simeone and L. M. Colletti, Ann. Surg., 2002, 236, 9-5. 16.
- D. G. Bouzianas, *Trends. Microbiol.*, 2009, 17, 522-528. 6.
- 7. X. S. Liang, C. Liu, Z. Long and X.H. Guo, AMB Expr., 2018, 8, 1-8.
- D. Schichnes, J. A. Nemson and S. E. Ruzin, *Microscope*, 2006, **54**, 91–93. 8.
- 9. D. K. Sharma and D. N. Prasad, Biotech. Histochem., 2015, 67, 27-30.
- 10. P. D'Incecco, L. Ong, S. Gras and L. Pellegrino, Micron, 2018, 110, 1–9.
- S. M. Knudsen, N. Cermak, F. F. Delgado, B. Setlow, P. Setlow and S. R. Manalis, 11. J. Bacteriol., 2016, 198, 168–177.
- W. Dorner, Le Lait, 1926, 6, 8-12. 12.
- 13. R. D. Lillie and H. J. Conn, H. J. Conn's Biological stains: a handbook on the nature and uses of the dyes employed in the biological laboratory, Williams & Wilkins, Baltimore, 1969, vol. 1, pp. 1-522.
- C. Laflamme, S. Lavigne, J. Ho and C. Duchaine, J. Appl. Microbiol., 2004, 96, 684-14. 692.
- L. J. Road and W. Foster, J. Bacteriol., 1961, 81, 768-779.
- 16. T. P. Radhakrishnan, Acc. Chem. Res., 2008, 41, 367-376.
- P. Srujana, P. Sudhakar and T. P. Radhakrishnan, J. Mater. Chem. C, 2018, 6, 9314-17. 9329.
- A. Qin and B. Z. Tang, Aggregation-Induced Emission: Fundamentals and 18. applications, ed.B. Z. Tang, John Wiley & Sons. Ltd, United Kingdom, 2013, vol.1, pp. 1-699.
- J. Mei, Y. Hong, J. W. Y. Lam, A. Qin, Y. Tang and B. Z. Tang, Adv. Mater., 2014, 19. **26**, 5429–5479.

- 20. H. Wang and G. Liu, J. Mater. Chem. B, 2018, 6, 4029-4042.
- 21. N. Senthilnathan and Ch. G. Chandaluri and T. P. Radhakrishnan, *Sci. Rep.*, 2017, **7**, 10583 (1-11).
- 22. P. Gangopadhyay, S. Sharma, A. J. Rao, D. N. Rao, S. Cohen, I. Agranat and T. P. Radhakrishnan, *Chem. Mater.*, 1999, **11**, 466-472.
- 23. S. Jayanty and T. P. Radhakrishnan, *Chem. Mater.*, 2001, **13**, 2460-2462.
- 24. P. Srujana and T. P. Radhakrishnan, *Angew. Chem. Int. Ed.*, 2015, **54**, 7270 –7274.
- 25. T. Bosak, R. M. Losick and A. Pearson, *PNAS*, 2008, **105**, 6725-6729.
- 26. ZEISS ZEN 3.1 (ZEN lite edition), Carl Zeis microscopy Gmbh, Cologne, Germany, 2018.
- 27. D. Bloor, Y. Kagawa, M. Szablewski, M. Ravi, S. J. Clark, G. H. Cross, L. O. Pålsson, A. Beeby, C. Parmer and G. Rumbles, *J. Mater. Chem.*, 2001, **11**, 3053-3062.
- 28. L. Mi, A. D. White, Q. Shao, P. Setlow, Y. Li and S. Jiang, *Chem. Sci.*, 2014, **5**, 3320–3324.
- 29. P. Paul and G. S. Kumar, *J. Fluoresc.*, 2012, **22**, 71-80.
- 30. CH. G. Chandaluri and T. P. Radhakrishnan, *Angew. Chem. Int. Ed.*, 2012, **51**, 11849 –11852.
- 31. L. Kong, P. Setlow and Y. Q. Li, *Analyst*, 2012, **137**, 3683-3689.
- 32. G. Wang, P. Zhang, P. Setlow and Y. Q. Li, *Appl. Environ. Microbiol.*, 2011, 77, 3368-3379.
- 33. L. Kong, P. Zhang, G. Wang, J. Yu, P. Setlow and Y. Q. Li, *Nat. Prot.*, 2011, **6**, 625-639.
- 34. Rasband, W. S. ImageJ, U. S. National Institutes of Health, Bethesda, Maryland, USA, https://imagej.nih.gov/ij/, 1997-2018.
- 35. A. Ali, K. Gaurav, N. Senthilnathan, T. P. Radhakrishnan, Ch. Sasikala and Ch. V. Ramana, J. Microbial. Methods, 2020, 177, 10609 (1-6).

# **CHAPTER 4**

# **Molecular Hopper Crystals and Electron Beam Triggered Action**



Upon simple reprecipitation and growth, a select class of strongly zwitterionic molecules forms microcrystals with a highly asymmetric 'hopper' morphology. They exhibit a smooth and prominent reversible actuation under optimal conditions of electron beam irradiation. A simple electrostatic model for the mechanical response is proposed, based on the crystal structure and morphology, supporting and control experiments, and simulation studies.

## **Synopsis**

Molecular crystals with unusual morphologies characteristic of "hopper crystals" have rarely been explored; such structures are potentially interesting to elicit specific responses triggered by external fields or stimuli. In this chapter, we demonstrate the fabrication of a new class of asymmetric hopper organic crystals from select members of a family of strongly zwitterionic diaminodicyanoquinodimethane (DADQ) molecules through simple reprecipitation method. Their mechanical response under electron beam irradiation is also highlighted. Assembly of the molecules into microcrystals is monitored by their characteristic fluorescence enhancement. X-ray diffraction, microscopy, and surface potential mapping provide insight into the development of the unique morphology. Under optimized conditions of electron beam irradiation in a scanning electron microscope, the prototype microcrystal is found to exhibit smooth, prominent, and reversible actuation. Even though electrically triggered macromolecular actuators as well as mechanically responsive and photo/ thermosalient molecular crystals are known, controlled bending/folding induced by electron beams are rare; such phenomenon has been demonstrated only in specially fabricated nanostructures. Our observations with a simple small-molecule-based hopper microcrystal are analyzed by a detailed examination of the crystal lattice structure and the asymmetric dipole distribution, together with simulations of the electron beam interactions with the microcrystal. We have developed an empirical model for the responses in the local electrostatic field, providing a mechanistic understanding of the actuation process.

#### 4.1. Introduction

Disparities in the growth rates at different locations on crystals, typically the edges and corners accumulating nutrients and growing faster than the faces, especially under supersaturation conditions, lead to the formation of 'hopper crystals'; the step-like features arise due to growth patterns that are intermediate between spiral, and dendritic or fractal.<sup>1</sup> They are known mostly in non-metallic inorganics; chains of miniatures of the original sodium chloride cube emerging during fast growth under supersaturation conditions (Figure 4.1a)<sup>2</sup>, and face-centered pits forming in calcium carbonate crystals grown in viscous media<sup>3</sup> (Figure 4.1b) are well-known examples. Rare cases are known in metals such as bismuth (Figure 4.1c). To the best of our knowledge, the only report of hopper structure in an organic crystal is of a highly hindered alcohol (Figure 4.1d);<sup>5</sup> there have been no investigations of

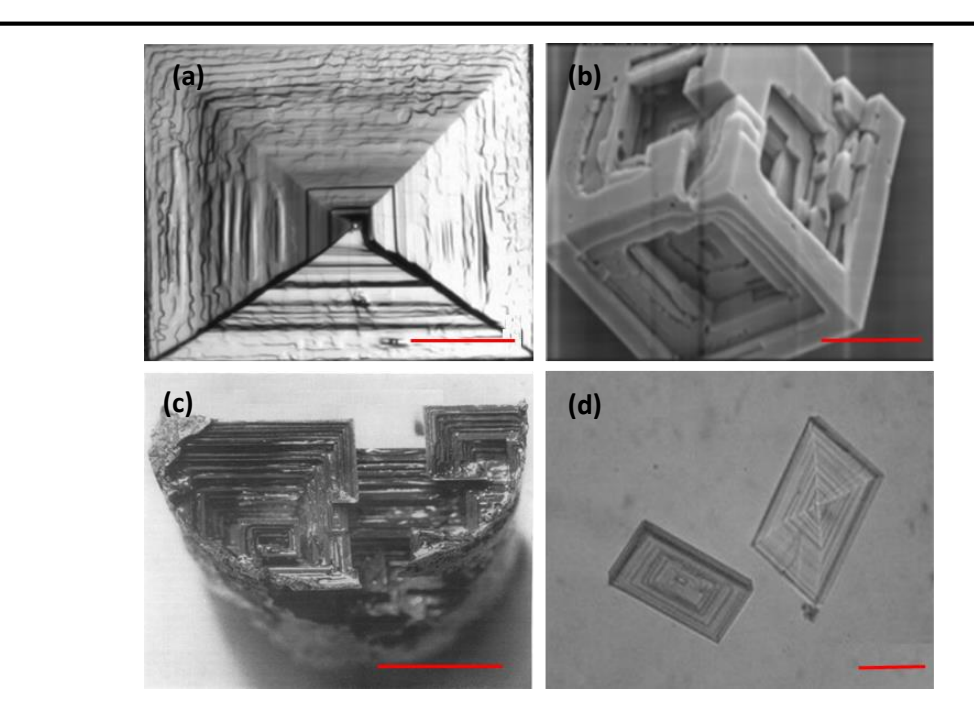


Figure 4.1. Hopper morphology of (a) sodium chloride (scale=  $100 \mu m$ ), (b) calcium carbonate (scale=  $100 \mu m$ ), (c) bismuth metal (scale=1 cm) and (d) phenol AO-60 (scale=  $75 \mu m$ ) crystals. Adapted with permission from ref. 2-5.

the materials relevance of the hopper morphology in molecular crystals. From a fundamental crystal growth perspective, it is interesting to explore potential small molecules and their assembly that can provide insight into the formation of hopper morphologies (Sec. 1.4.2). Diaminodicyanoquinodimethane (DADQ) molecules possessing a zwitterionic, dipolar structure have been investigated extensively, for their nonlinear optical and solid-state fluorescence responses as discussed in Sec. 1.1.3.<sup>6,7</sup> In the previous chapters, we have also demonstrated their utility in various bioimaging applications. Here we present our observations as select DADQs that form non-centrosymmetric crystal lattices, when grown as microcrystals through the simple, but controlled reprecipitation route, developing unusual and highly asymmetric, and yet perfectly reproducible morphologies. The hopper morphology of these crystals and its evolution can be controlled by optimization of the growth conditions. The local supersaturation and quick crystallization involved in the reprecipitation process, coupled with the dipolar structure at the molecular as well as materials level, appear to induce the unique morphologies. The asymmetric microcrystals

can potentially be exploited to elicit sensitive responses, including mechanical, under external stimuli.

Controlled mechanical responses of molecular and macromolecular materials are useful in actuators, sensors, and molecular machines and a brief introduction to this field was given in Sec. 1.4. Designs of active matter such as micro and nanoscale objects capable of chemical and photo-induced locomotion are mostly elaborate or complex.<sup>8-11</sup> Actuators useful in biomedical applications, 12 have been developed using polymers that respond to optical and electrical stimuli. 13,14 Among constitutionally and structurally simple systems, molecular crystals that bend, twist and coil under direct physical manipulation as well as show photo or thermosalient effects have been investigated. Some of them can serve as photo-actuators.<sup>17</sup> The emergence of adaptive crystals and their potential device applications have been highlighted recently.<sup>18</sup>

Distortion and motion of specimen, especially organic materials, are encountered as an inherent nuisance in electron microscopy; they are uncontrolled and often accompanied by sample damage. 19-21 There are very few examples of controlled mechanical responses of nano/microstructures under electron beam irradiation. Bending and bundling of gold-coated epoxy nanoposts and GaAs nanowires fabricated by molecular beam epitaxy, <sup>22-24</sup> and folding of gold nanoparticle based Janus-like membranes into tubes have been reported.<sup>25</sup> Sliding back of layers of perylenediimide microribbons deformed by light, is another rare example.<sup>26</sup> Eliciting controlled mechanical responses from small molecule based microcrystals (fabricated through simple colloidal routes) using electron beams, would be a significant development. The torque required for bending a body can commonly arise from either a differential thermal expansion of its parts, or an uneven charge distribution and related electrostatic forces in a local field; an asymmetric morphology is of potential interest in this The hopper microcrystal based on the novel DADQ molecule, 7,7context. bis(cyclopentylamino)-8,8-dicyanoquinodimethane (BCPADQ), is found to show a smooth and prominent bending, followed by straightening under an electron beam. The reversible, repeatable actuation appears to result from the response of the asymmetric morphology, dipole distribution, and transient charges induced on the microcrystal under the electron beam, to the local electrostatic fields. Support and control experiments, together with simulation and modelling studies, lead to an empirical model that provides mechanistic insight into these observations.

#### 4.2. Synthesis and characterization

NC CN 
$$\frac{\delta + \lambda}{1}$$
 Acetonitrile  $\frac{70 \text{ °C}, 3 \text{ h}}{-2 \text{HCN}}$   $\frac{\delta + \lambda}{1}$   $\frac{$ 

BCPADQ was synthesized following the general procedure reported in Ref. 27. 100 mg (0.49 mmol) of 7,7,8,8-tetracyanoquinodimethane was added to a solution of 193 μL (1.96 mmol) of cyclopentylamine in acetonitrile at 70 °C and stirred for 3 h (CAUTION: HCN is the byproduct). The general synthesis scheme is shown in scheme 4.1. The yellow precipitate formed was filtered out and recrystallized from acetonitrile; the recrystallization was repeated several times until nearly colorless hollow tube-shaped crystals were obtained. For parallel and control experiments, some more DADQ derivatives were prepared. 7,7-bis(propylamino)-8,8-dicyanoquinodimethane (BPADQ) and 7,7-bis(butylamino)-8,8-dicyanoquinodimethane (BCBADQ) and 7,7-bis(cyclohexylamino)-8,8-dicyanoquinodimethane (BCHADQ) were also synthesized following similar procedure as shown in Scheme 4.1. Details of instruments used and characterization studies carried out are added in Appendix B.

#### BCPADQ 7,7-Bis(cyclopentylamino)-8,8-dicyanoquinodimethane

Yield= 57%; recrystallized from acetonitrile; M.P. ( $^{\circ}$ C) = 278; FTIR (KBr):  $\bar{\nu}/\text{cm}^{-1}$  = 3135, 2186, 2135.  $^{1}$ H NMR (500 MHz) : 9.15 (J = 5.2 Hz, d,1H), 8.36 (J = 6.4 Hz, d, 1H), 7.17 (J = 6.8 Hz, d, 2H), 6.8 (J = 6.84 Hz, d, 2H), 4.10 (J = 4.76 Hz, t, 1H), 3.78 (J = 5.96 Hz, t, 1H), 2.01 (b, 2H), 1.89 (b, 2H), 1.63 (b, 10H), 1.45 (b, 2H);  $^{13}$ C NMR (125 MHz): 163.2, 147.83,

129.56, 124.42, 117.81, 115.57, 57.77, 53.93, 33.11, 32.05, 24.15, 23.99; elemental analysis (calcd., found for BCPADQ i.e.  $C_{20}H_{24}N_4$ ): %C = (75.00, 74.91), %H = (7.50, 7.41), %N = (17.50, 17.61). Solution state:  $\lambda_{max}^{abs} = 380$  nm,  $\lambda_{max}^{em} = 484$  nm, Stokes shift = 106 nm. Solid state:  $\lambda_{\text{max}}^{\text{abs}} = 375 \text{ nm}$  (broad),  $\lambda_{\text{max}}^{\text{em}} = 442 \text{ nm}$ , Stokes shift = 97 nm, fluorescence quantum yield = 26 % (solid state), 0.4 % (solution state, DMSO); fluorescence lifetime = 1.12 ns.

## BCBADQ 7,7-Bis(cyclobutylamino)-8,8-dicyanoquinodimethane

Recrystallized from acetonitrile; M.P. (°C) = 270; FTIR (KBr):  $\bar{\nu}/\text{cm}^{-1}$  = 3182, 2177, 2129; <sup>1</sup>H NMR (500 MHz): 9.45 (s, 1H), 8.5 (s, 1H), 7.14 (d, 2H), 6.84 (d, 2H), 4.24 (s, 1H), 3.92 (S, 1H), 2.38 (d, 2H), 2.17 (m, 6H), 1.65 (m, 4H); <sup>13</sup>C NMR (125 MHz): 161.66, 148.47, 129.78, 124.19, 117.77, 114.86, 50.77, 47.29, 32.71, 30.97, 29.48, 15.03, 14.14. Crystal system = Monoclinic, Space group =  $P2_1/n$ , a = 9.2278 Å, b = 18.643 Å, c = 19.314 Å,  $\alpha$  = 90°,  $\beta = 98.896$ °,  $\gamma = 90$ °.

#### BCHADQ 7,7-Bis(cyclohexylamino)-8,8-dicyanoquinodimethane

Recrystallized from acetonitrile; M.P. (°C) = 285; FTIR (KBr):  $\bar{\nu}/\text{cm}^{-1}$  = 3209, 2184, 2130; <sup>1</sup>H NMR (500 MHz): 9.01 (d, 1H), 8.33 (d, 1H), 7.17 (d, 2H), 6.84 (d, 2H), 3.7 (s, 1H), 3.24 (t, 1H), 1.89 (s, 2H), 1.75 (m, 6H), 1.56 (m, 4H), 1.33 (s, 4H), 1.08 (S, 4H); <sup>13</sup>C NMR (125 MHz): 162.60, 147.81, 129.34, 124.42, 117.85, 115.69, 55.72, 51.32, 33.17, 32.10, 31.69, 25.09, 24.77. Crystal system = Orthorhombic, Space group =  $Pna2_1$ , a = 10.867 Å, b = 19.61 Å, c = 9.327 Å,  $\alpha = 90^{\circ}$ ,  $\beta = 90^{\circ}$ ,  $\gamma = 90^{\circ}$ .

#### 4.3. **Characteristics of BCPADQ**

#### 4.3.1. **Crystallographic studies**

Crystal structures of the three new DADQ derivatives, BCPADQ, BCBADQ and BCHADQ were determined. We discuss in detail, the case of BCPADQ that is the main focus of the work presented in this chapter. Needle-shaped single crystals of BCPADQ grown by slow evaporation of an acetonitrile solution and its basic crystallographic data are collected

**Table 4.1.** Basic crystallographic data of BCPADQ.

	BCPADQ
Empirical formula	$C_{20}H_{24}N_4$
Crystal system	Orthorhombic
Space group	$Pna2_1$
a / Å	11.4335 (14)
b/Å	17.368 (2)
c / Å	9.2392 (11)
α / deg.	90.00
β/deg.	90.00
γ / deg.	90.00
V / Å <sup>3</sup>	1834.7 (4)
Z	4
ρ <sub>calc.</sub> / g cm <sup>-3</sup>	1.160
μ / cm <sup>-1</sup>	0.71
Temperature / K	100 (2)
λ/Å	0.71073
No. of reflections	3209
No. of parameters	233
Max., Min. transmission	0.865, 0.995
GOF	1.061
R [for $I \ge 2\sigma_I$ ]	0.0358
wR <sup>2</sup>	0.0895
Largest difference peak and hole / eÅ-3	0.280/ -0.203
CCDC deposition number	1957115

in Table 4.1; the crystal system belongs to the orthorhombic space group,  $Pna2_1$ . The molecular structure and unit cell of the BCPADQ determined from X-ray diffraction analysis are shown in Figure 4.2a and b respectively. H-bonded supramolecular assembly and extensive H-bonding interactions between the amino H and cyano N atoms lead to intertwined triple helical supramolecular motifs in the crystal; there are shown in Figure 4.2c and d respectively.

BCPADQ microcrystals obtained by reprecipitation and grown for  $\sim 6$  h (details are given in Sec. 4.4), were also studied by X-ray diffraction analysis. The basic crystallographic data are collected in Table 4.2; it is fully consistent with the structure of the single crystal shown in Table 4.1.

Table 4.2. Basic crystallographic data of BCPADQ microcrystal.

	BCPADQ
Empirical formula	$C_{20}H_{24}N_4$
Crystal system	Orthorhombic
Space group	Pna2 <sub>1</sub>
a / Å	11.5990 (11)
b/Å	17.953 (2)
c / Å	9.2168 (11)
$\alpha$ / deg.	90.00
$\beta$ / deg.	90.00
γ / deg.	90.00
V / Å <sup>3</sup>	1919.3 (4)
Z	4
$\rho_{\text{calc.}} / \text{g cm}^{-3}$	1.109
μ / cm <sup>-1</sup>	0.067
Temperature / K	296 (2)
λ/Å	0.71073
No. of reflections	3376
No. of parameters	233
Max., Min. transmission	0.995, 0.992
GOF	0.994
R [for $I \ge 2\sigma_I$ ]	0.0800
wR <sup>2</sup>	0.2427
Largest difference peak and hole / eÅ-3	0.203 / -0.182

# 4.3.2. Computational studies

Gaussian 09 (Revision C.01) program was used to compute the dipole moment of the BCPADQ molecule at the B3LYP/6-31G\* level. Molecular geometry from the crystal structure was used; the computed dipole orientation is seen to be nearly parallel to the axis connecting the diaminomethylene and dicyanomethylene C atoms (Figure 4.3). The computed dipole moment is 23.0 D.

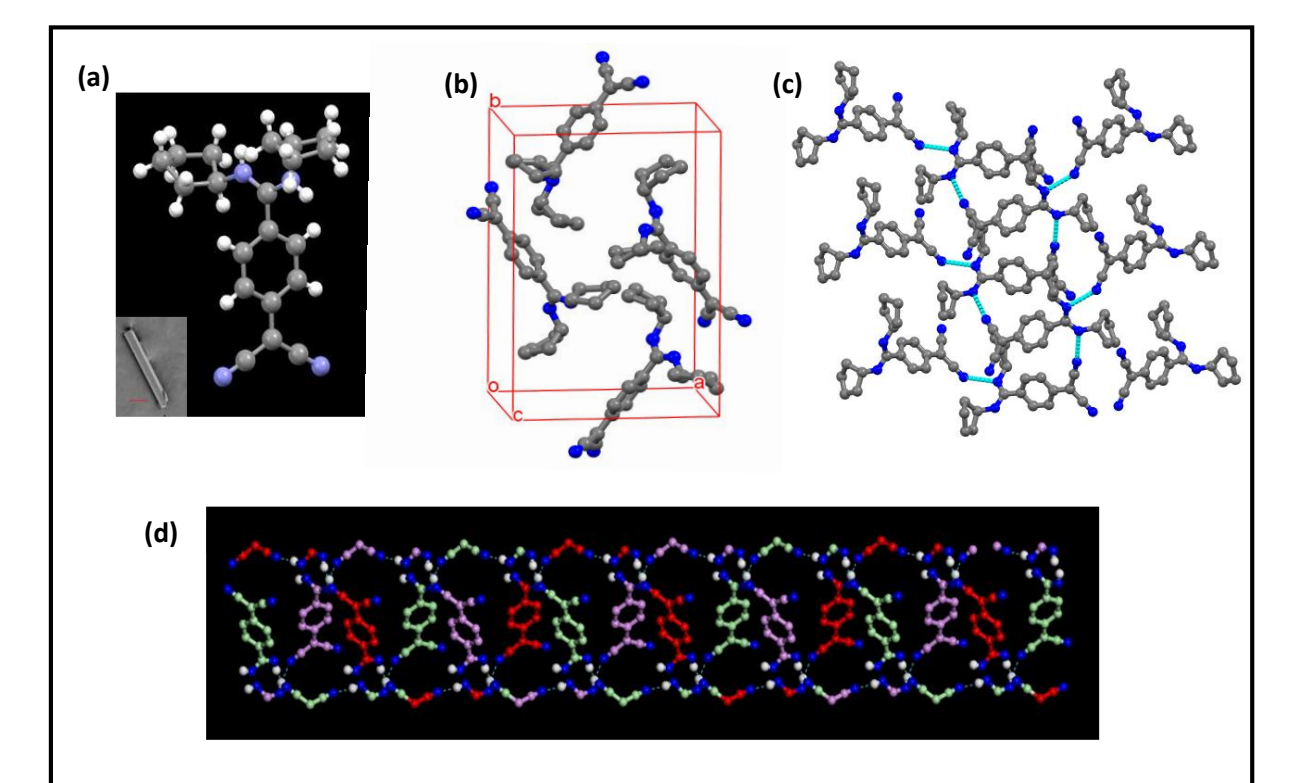
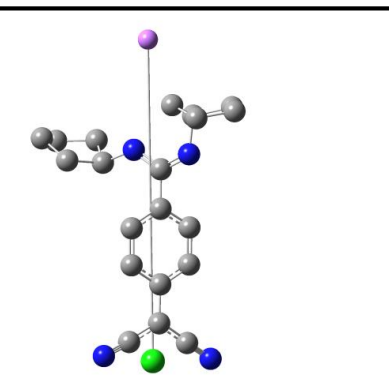
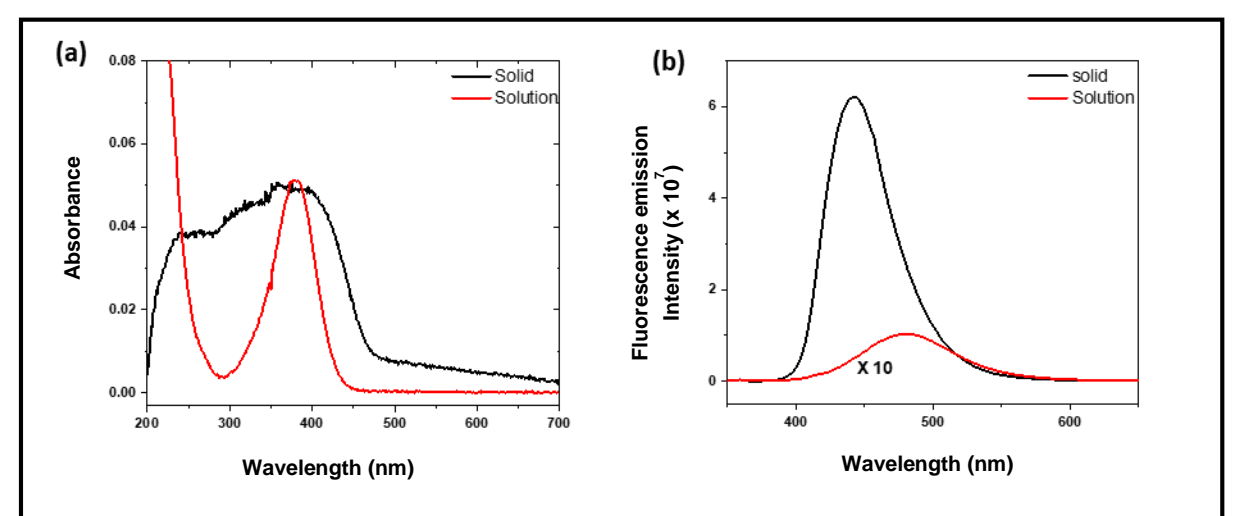


Figure 4.2. (a) Molecular structure of BCPADQ determined from the single crystal X-ray diffraction analysis (inset: FESEM image of a single crystal; scale =  $100 \mu m$ ). (b) Unit cell and (c) supramolecular assembly in BCPADQ crystal; H atoms are omitted for clarity; C (grey) and N (blue) atoms are shown and intermolecular H bonds are indicated (cyan lines), (d) The H-bonded triple helical supramolecular assembly in BCPADQ crystal; C (green, red and purple for the molecules belonging to the three helices), N (blue) and H atoms involved in the H-bond (white), and only the dicyanomethylene group of the linking molecules are shown for ease of visualization.



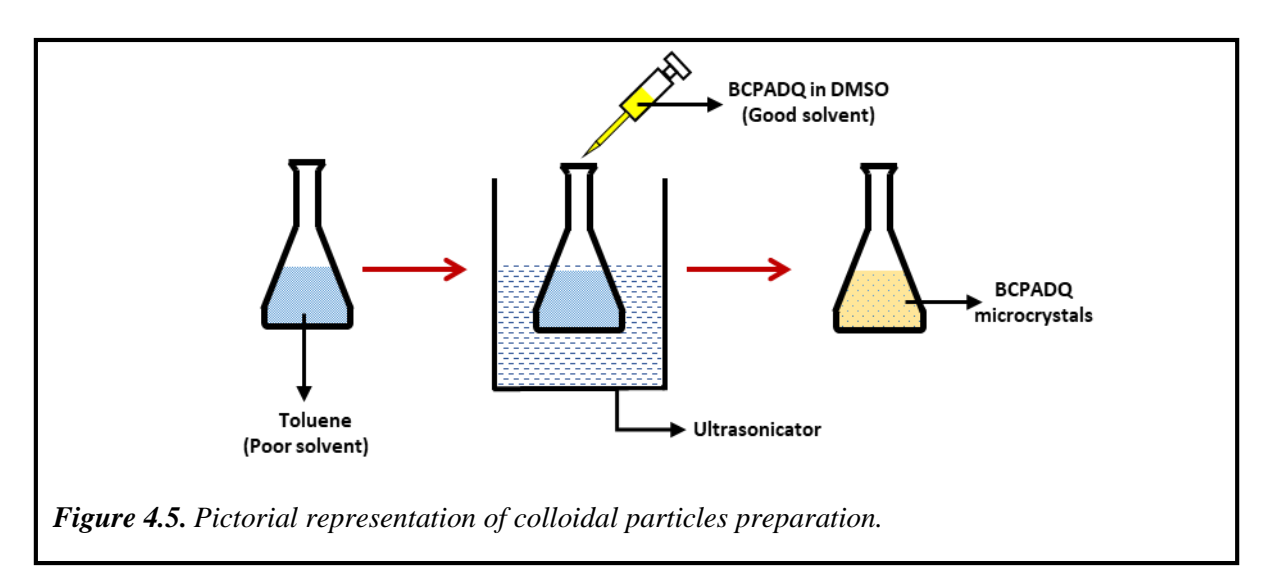
**Figure 4.3.** Molecular structure of BCPADQ from single crystal X-ray diffraction study, and the orientation of the computed  $(B3LYP/6-31G^*)$  dipole moment vector (line connecting the green sphere (negative end) to the pink sphere (positive end); H atoms are omitted for clarity, and C (grey) and N (blue) atoms are shown.



**Figure 4.4.** (a) Electronic absorption, and (b) fluorescence emission ( $\lambda_{exc} = 375$  nm) spectra of BCPADQ in the solution and solid states.

#### 4.3.3. Spectroscopic studies

Absorption and fluorescence emission spectra of BCPADQ recorded in the solid and solution state are shown in Figure 4.4. Solid BCPADQ has a broad electronic absorption with  $\lambda_{max} \sim 375$  nm, and exhibits strong fluorescence emission with  $\lambda_{max} \sim 442$  nm, blueshifted with respect to the solution. The fluorescence emission quantum yield is 26%, significantly higher than that of the solution (0.4 % in DMSO) as discussed in earlier chapters; this is characteristic of the DADQs, attributed to the inhibition of excited state structural relaxations, and the impact of specific relative molecular orientations in the aggregated state.<sup>7</sup>



#### 4.4. Hopper microcrystals

#### 4.4.1. Preparation of microcrystals of BCPADQ

A schematic representation of the colloidal particles preparation method is illustrated in Figure 4.5. 30  $\mu$ L of a 2 mM solution of BCPADQ in DMSO (good solvent) was injected into 4.97 ml of toluene (poor solvent) in the presence or absence of ultrasonication. The ultrasonication can promote extreme nucleation and uniform assembly. The mixture was maintained at ambient temperature (25 °C) for the growth of the particles formed, which were filtered out after different time intervals on a nylon membrane (pore size  $\sim 0.1~\mu$ m); a stainless steel syringe filter holder (13 mm dia.) and glass syringe (5 ml) were used for the filtration. Asymmetric morphology of the BCPADQ microcrystals fabricated are shown in Figure 4.6a, b.

#### 4.4.2. Microcrystals of other DADQ derivatives

Under similar colloid fabrication conditions, equally interesting asymmetric morphologies were obtained with the cyclohexylamino and n-butylamino derivatives (BCHADQ and BBADQ respectively) as well (Figure 4.6c – e). Notably, these compounds could also be grown as normal single crystals by slow evaporation of solutions, and the structures determined by X-ray diffraction; interestingly, they are also found to belong to the non-centrosymmetric space group,  $Pna2_1$ , as BCPADQ. The closely related cyclobutylamino and n-propylamino derivatives (BCBADQ and BPADQ, respectively) form centrosymmetric crystals (space groups  $P2_1/c$  and C2/c, respectively). Notably, they produced only normal polyhedral or plate-like microcrystals under the similar colloid fabrication conditions (Figure 4.6f, g).

Even though it is tempting to propose that the non-centrosymmetric crystallographic space group is the key determinant for the realization of the asymmetric morphologies, more examples are required to prove it decisively. A recent report of the formation of triangular habit single crystals, resulting from the polar lattice structure and differences in solvent-surface interactions, <sup>28</sup> is of interest in this context; however, no hopper morphology was found in those crystals. Our observations suggest that the non-centrosymmetric assembly of the dipolar molecules induces significant charge asymmetry in the microcrystals, and the nonequilibrium conditions and local supersaturation during reprecipitation lead to the hopper

structures, exacerbating the uneven dipole distribution. We focus on the prototypical case, BCPADQ, to probe deeper into the molecular assembly characteristics and microcrystal growth.

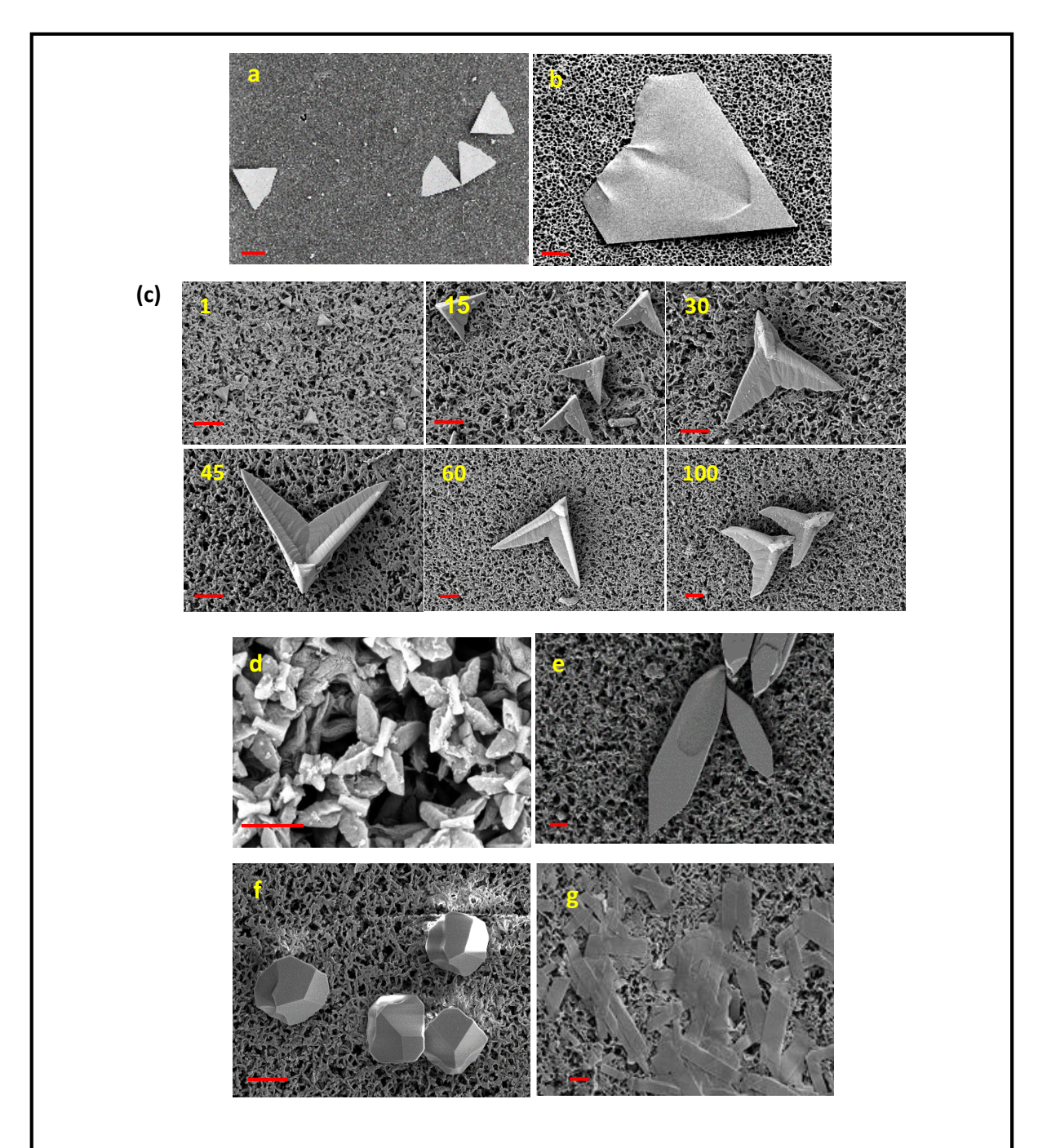


Figure 4.6. FESEM images of microcrystals: BCPADQ grown from DMSO-toluene for (a) 30 min (scale = 10  $\mu$ m) and (b) 120 min (scale = 5  $\mu$ m), BCHADQ grown (c) from DMSO-toluene for different time periods in minutes (scale = 5  $\mu$ m) (d) from acetonitrile-toluene for 60 min (scale = 1  $\mu$ m), (e) BBADQ grown from acetonitrile-toluene for 60 min (scale = 2  $\mu$ m). (f) BCBADQ grown from DMSO-toluene for ~1 h (scale = 5  $\mu$ m) and (g) BPADQ microcrystals grown from DMSOtoluene for  $\sim 1 h$  (scale = 2  $\mu m$ ).

#### 4.4.3. Fluorescence spectroscopy of BCPADQ colloids

Colloids of BCPADQ were prepared by the simple reprecipitation method as described above. In order to monitor the molecular aggregation process, the experiment was conducted by rapidly injects 30  $\mu$ L of a 10 mM solution in DMSO into 4.97 ml of DMSO-toluene mixtures with the toluene volume percentage varying from 98 – 99 under ultrasonication for 2 – 3 min. The colloid was then aged for different time periods to allow growth. The formation and growth of the microcrystals were conveniently monitored by the enhancement of the fluorescence emission in the aggregated/solid-state; Figure 4.7a, b show the sharp change when the volume% of toluene exceeds 98.9. Starting from the injection, fluorescence emission spectra were recorded for the colloid solutions after different time intervals up to at least an hour (Figure 4.7c-h). The spectra were deconvoluted to estimate the intensities of the emission arising from the aggregate/solid ( $\lambda_{max} \sim 440$  nm) and solution ( $\lambda_{max} \sim 490$  nm) states of BCPADQ; the relevant intensities are plotted in Figure 4.7i, j, for the different solvent mixtures. It is seen that the aggregate dominates soon after injection in mixtures with  $\geq$  98.9 volume % of toluene.

## 4.4.4. Growth of the BCPADQ microcrystals

A graphic view of the growth is provided by the FESEM images (Figure 4.8a) of the microcrystals maintained in the colloid for different time intervals at 25 °C, and filtered out on a nanoporous nylon membrane with pore size  $\sim 0.1~\mu m$ . Even though the microcrystals eventually acquire a symmetric parallelepiped plate morphology, those formed early possess a triangular or truncated parallelepiped, wedge-like morphology. They also have an unusual, asymmetric thickness profile, as revealed by the AFM images of single particles (Figure 4.8b). The microcrystal formed in  $\sim 1$  h has a roughly isosceles triangular shape with the base (*b*) and altitude (*l*) being  $\sim 40$  and  $\sim 35~\mu m$  respectively; thickness at the base end is  $\sim 30~nm$  and at the tip (*h*)  $\sim 1.5~\mu m$ . The description as a 'hopper crystal' is based on the crater-like structure; enhanced growth from the edges that form the tip of the isosceles triangle morphology is clearly visible. The growth of the microcrystals is depicted by the evolution of the line profile along *l* (Figure 4.8). Figure 4.9 provides the phase images recorded in AFM and 3-D topography views of the growing microcrystals. The hopper morphology is less evident in the microcrystals formed without ultrasonication; growth of the crystals was relatively slower and less uniform as seen from the AFM images in Figure 4.10.

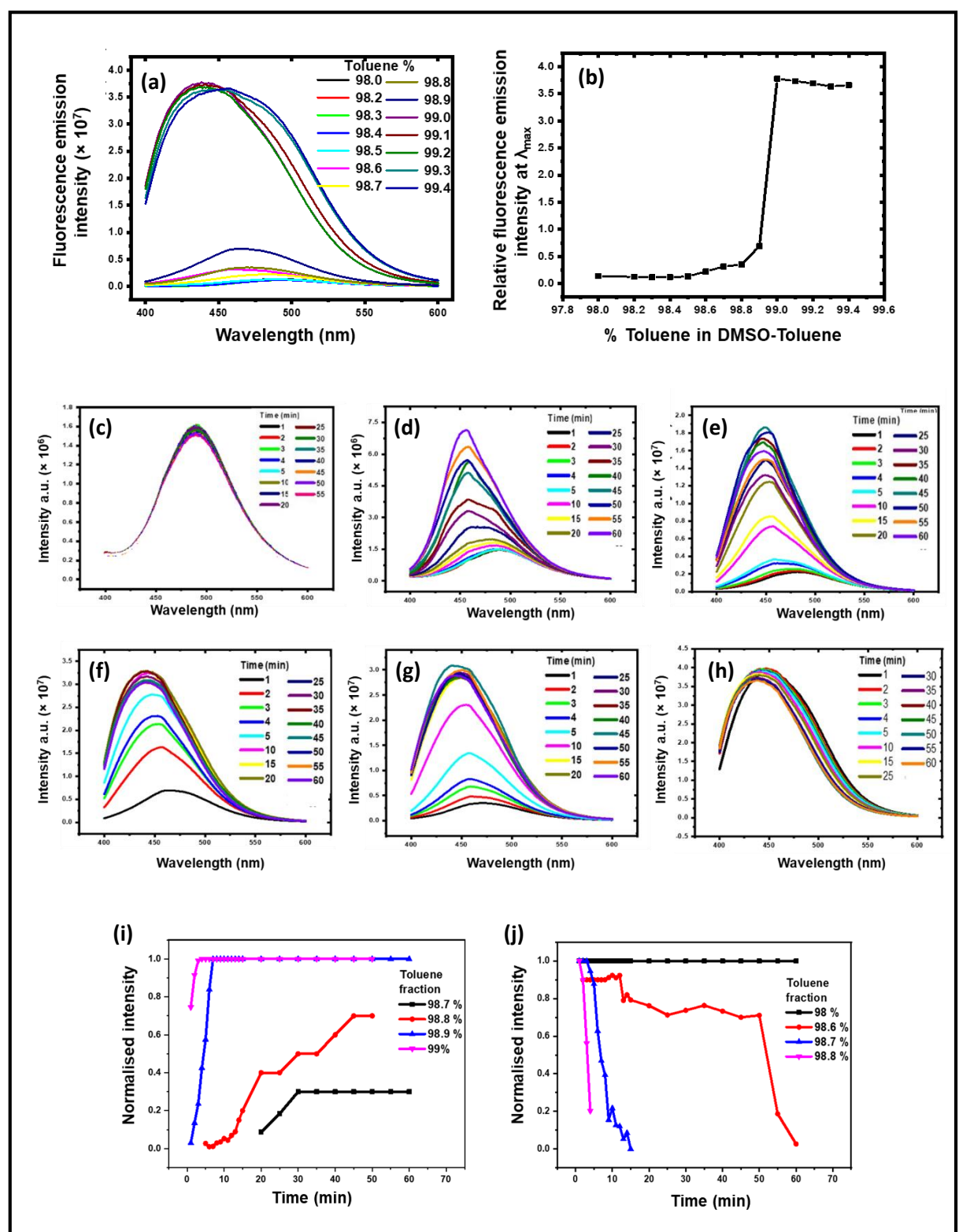


Figure 4.7. Fluorescence emission spectra of BCPADQ in DMSO-toluene mixtures: (a) Variation of the fluorescence intensity with different volume percentage of toluene and aged for 60 min (in the case of the colloids);  $\lambda_{exc} \sim 375$  nm, (b) Plot of the relative intensity at  $\lambda_{max}$ . Variation of the fluorescence intensity with different volume percentage of toluene, (c) 98.0, (d) 98.6, (e) 98.7, (f) 98.8, (g) 98.9 and (h) 99.0, at different times after injection. Note that the y-axis limit increases from c) to h). Variation of the fluorescence intensity of the peaks due to the, (i) aggregate/solid  $(\lambda_{max} \sim 425 \text{ nm})$ , and  $(\mathbf{j})$  solution  $(\lambda_{max} \sim 520 \text{ nm})$  states.

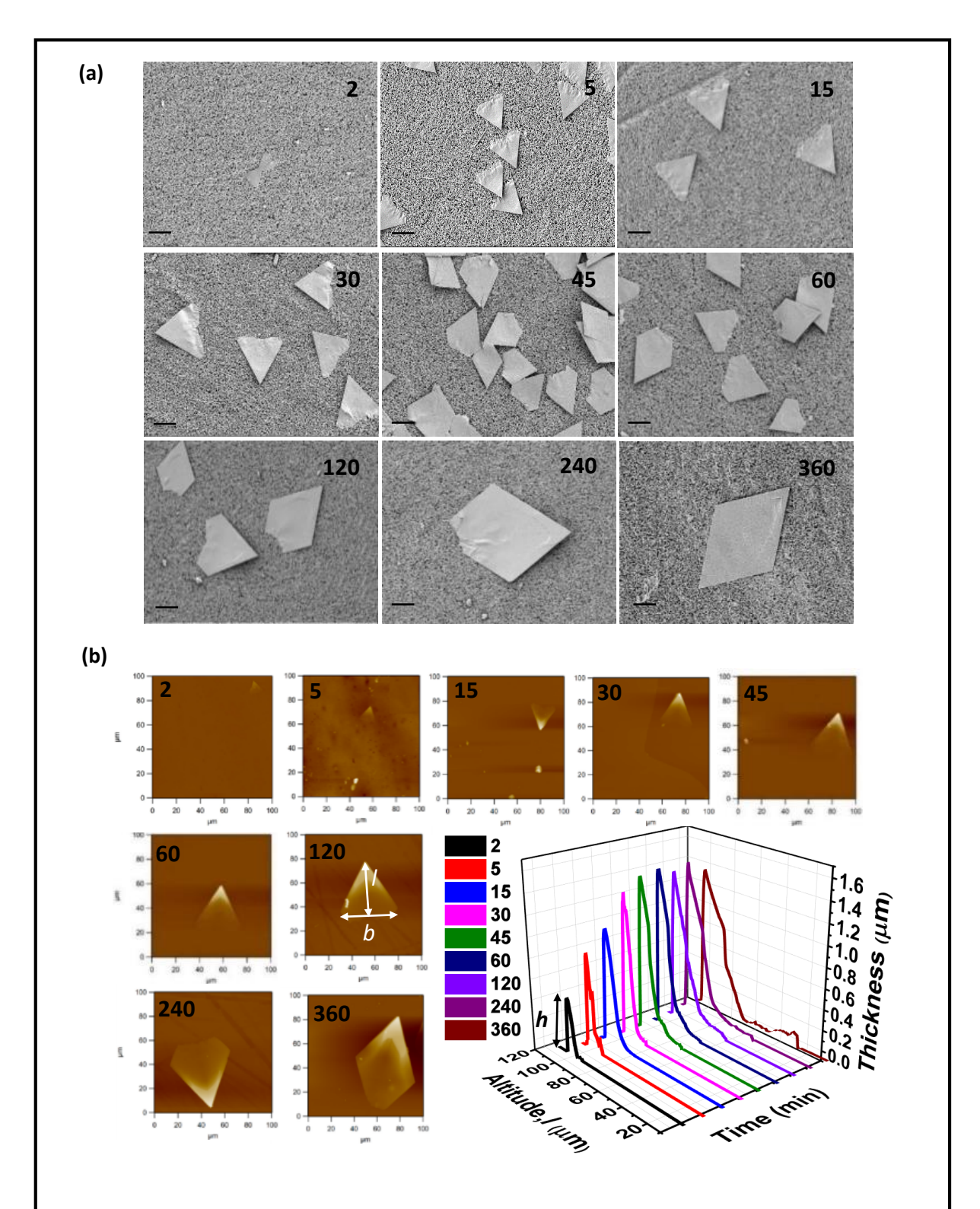


Figure 4.8. (a) FESEM images of collections of BCPADQ microcrystals (scale =  $20 \mu m$ ) grown over different time periods (minutes) and (b) AFM image ( $100 \mu m \times 100 \mu m$ ) of a single microcrystal [the altitude (l) and base (b) dimensions are indicated in the  $120 \mu m$  minutes], along with a plot of the evolution of the line profile along the altitude direction [the thickness (h) is indicated], as a function of time (minutes).

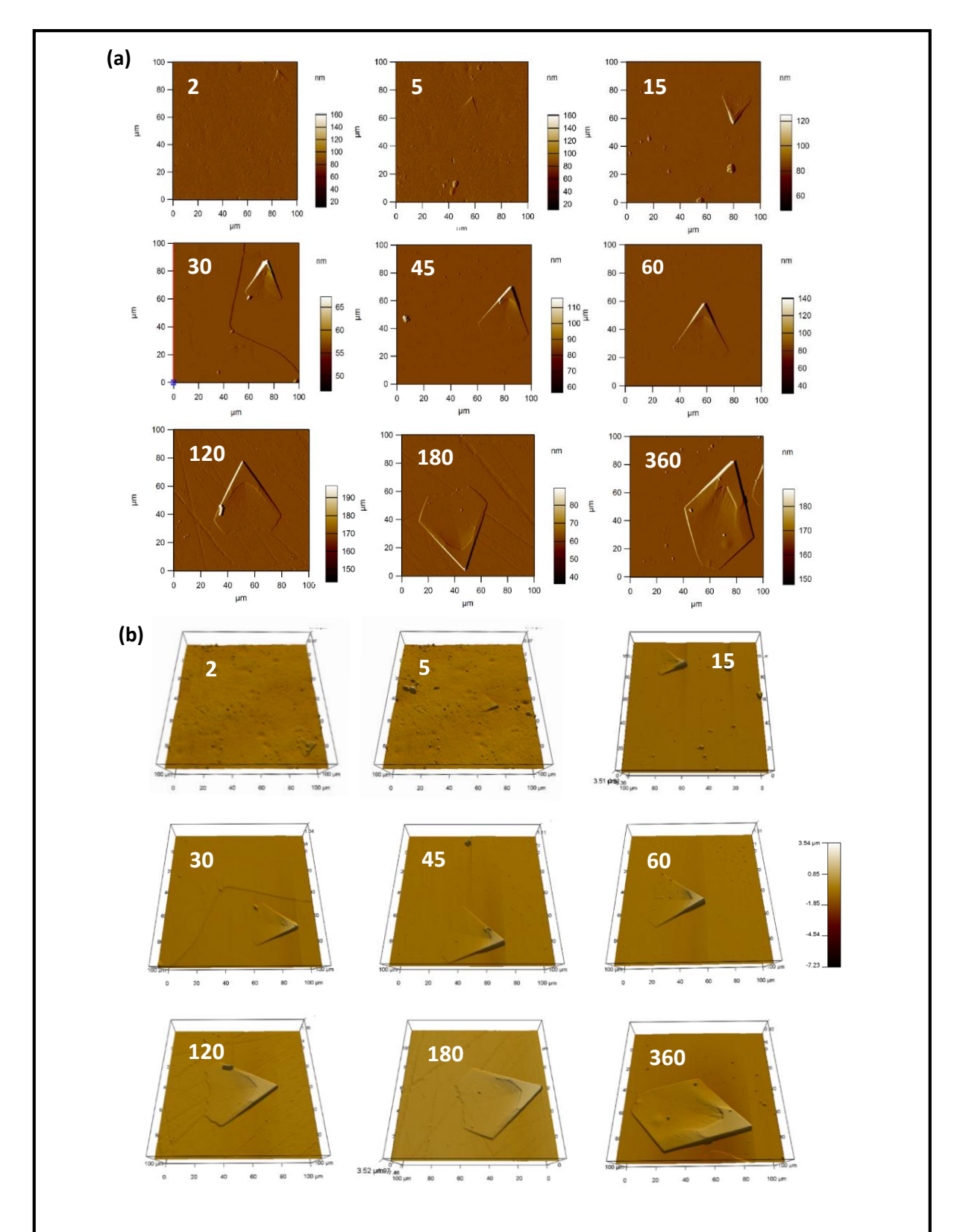
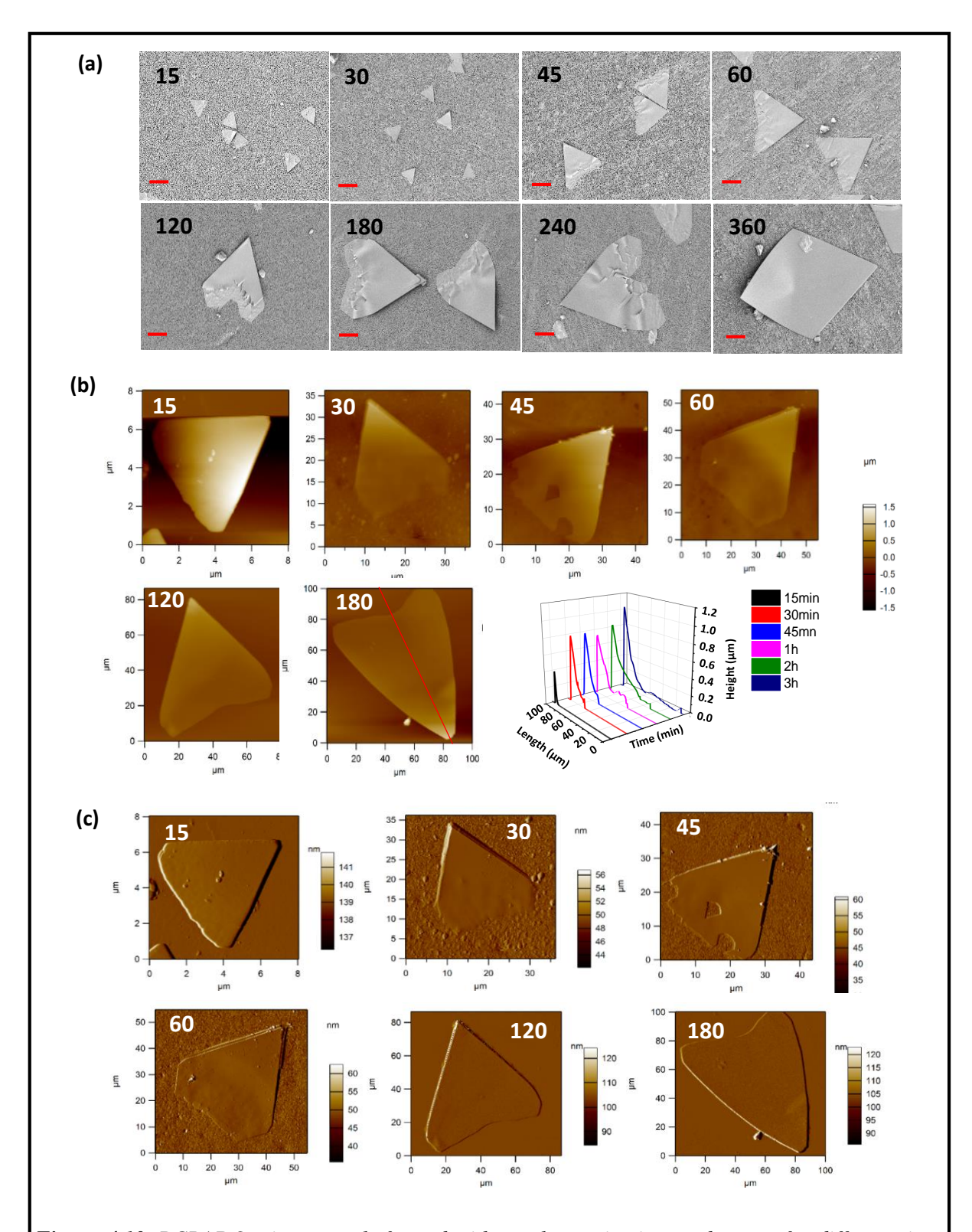


Figure 4.9. AFM (a) phase and (b) 3D topography images of BCPADQ microcrystals grown for different time intervals in minutes.



**Figure 4.10.** BCPADQ microcrystals formed without ultrasonication, and grown for different time periods in minutes: (a) FESEM images (Scale =  $40 \mu m$ ); (b) AFM tophography images, and corresponding line profiles along the line indicated in the last image, and (c) AFM phase images; note that the scales are different in the different images in (b) and (c).

# 4.4.5. Face indexing

Examination of a relatively large, asymmetric microcrystal (formed with ultrasonication and grown for ~ 6 h, Sec. 4.4.1) on an X-ray diffractometer showed that it is indeed a single crystal; face indexing of the microcrystal was done using OLEX-2 software<sup>29</sup> and shown in Figure 4.11a. An important feature deciphered is that the basal plane is (0 0 1). The molecular dipole orientations in the unit cell (Figure 4.11b) and their direction cosines  $(\alpha, \beta, \gamma)$  along the unit cell axes (a, b, c) respectively) shown in Figure 4.11c; prove that a net dipole component exists only along the c direction.

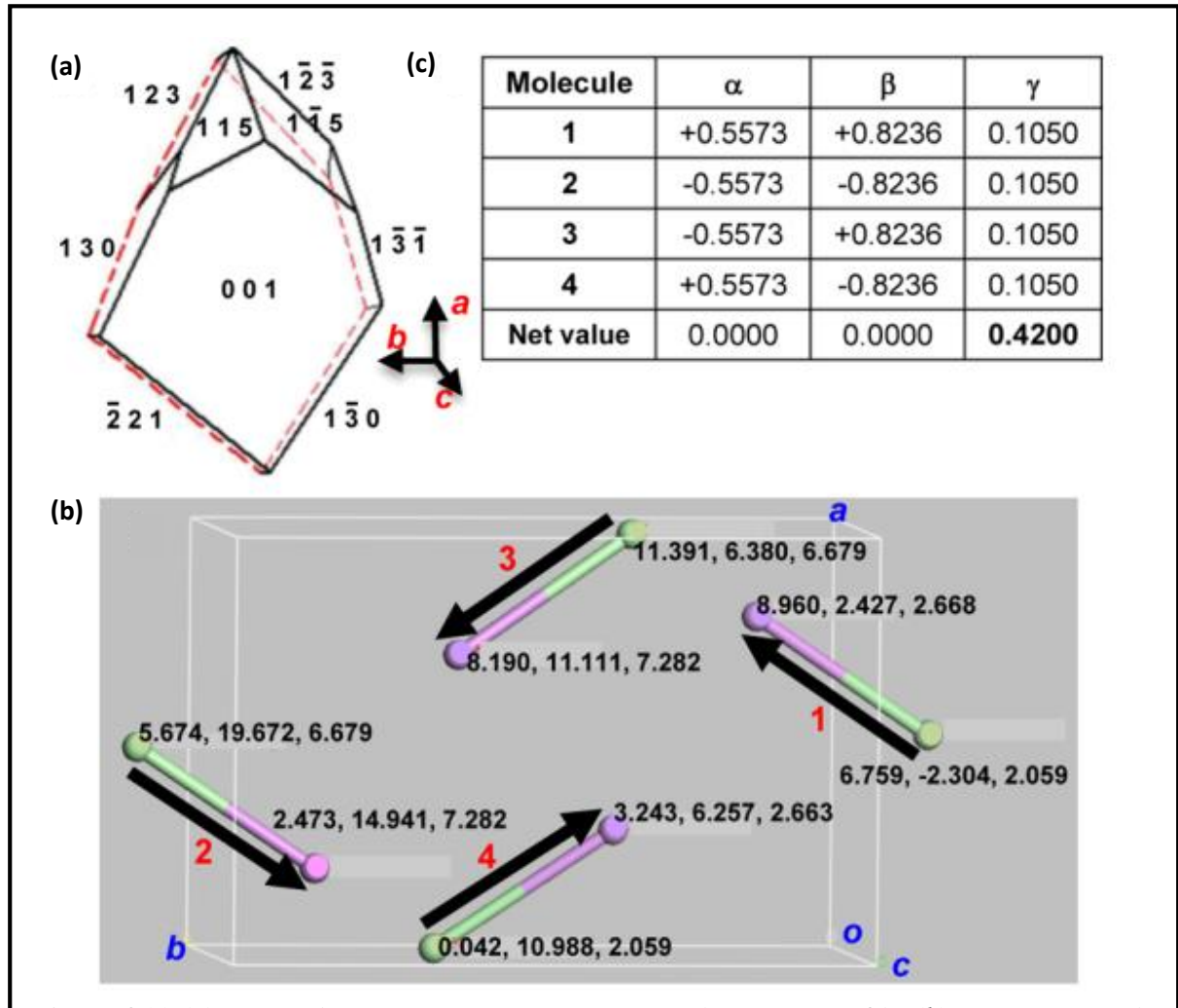


**Figure 4.11.** (a) Face indexing of a BCPADQ microcrystal grown for  $\sim 6$  h. (b) Orientation of the molecular dipoles (represented by a rod connecting the dicyanomethylene (green) diaminomethylene (pink) C atoms, with their coordinates indicated) of the four molecules in the unit cell of BCPADQ; direction of the dipoles is indicated by arrows. (c) Direction cosines  $(\alpha, \beta, \gamma)$  of the dipole vector of the molecules, 1-4 along the unit cell axes, a, b, c respectively.

# 4.4.6. Scanning Kelvin probe microscopy

Scanning Kelvin probe microscopy analysis revealed the surface potential distribution over the microcrystal (Figure 4.12), consistent with the dipole orientation, the enhanced moment at the thick end and the work functions relative to the metal tip.<sup>30</sup> Molecular packing along the shortest unit cell axis, and the pronounced growth due to the local dipole fields at the apex appear to promote the hopper morphology.

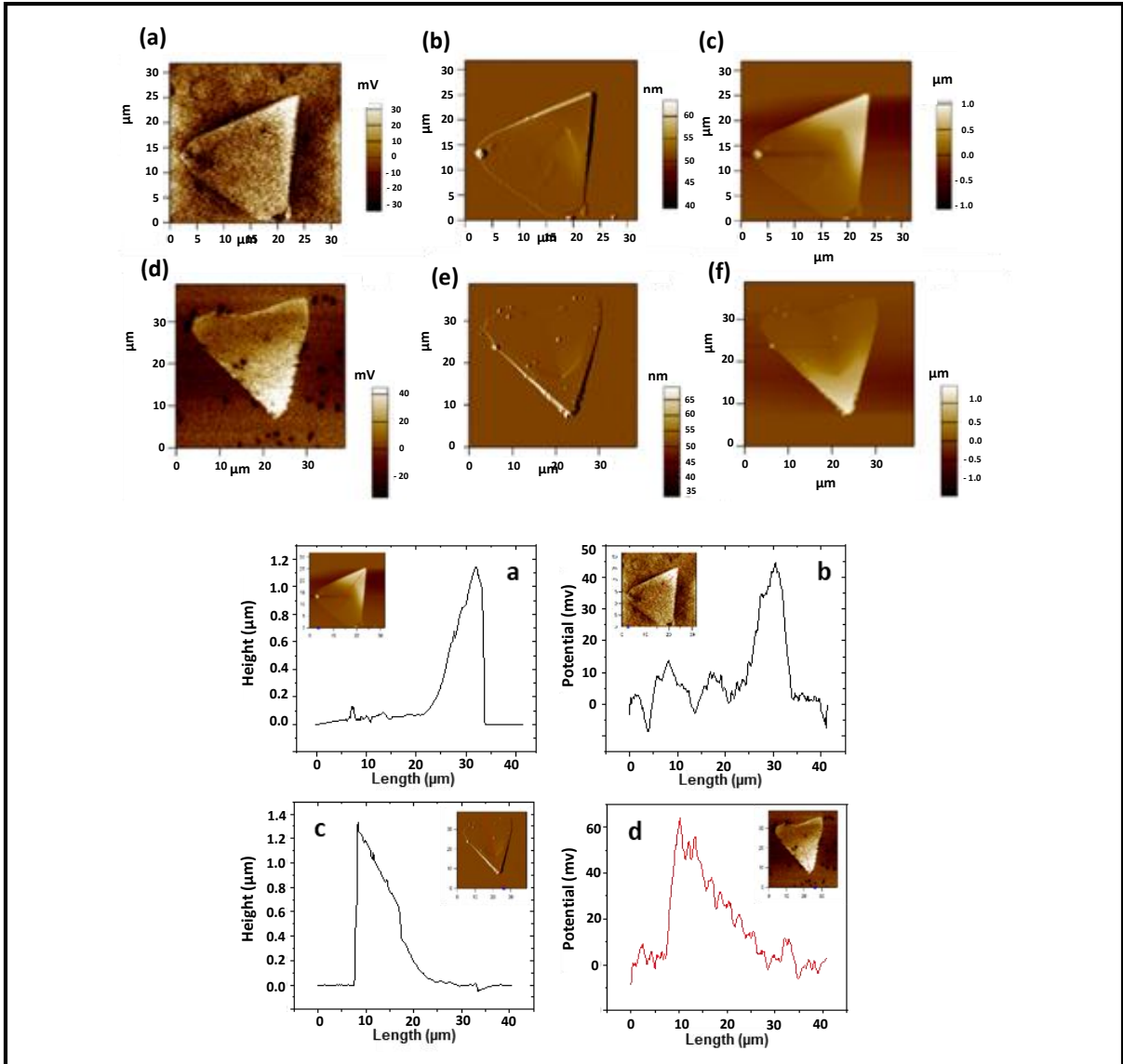


Figure 4.12. (a, d) Surface potential, (b, e) phase and (c, f) topography images of BCPADQ microcrystals grown for different time periods, 30 min (a-c) and 60 min (d-f). The (g, i) topography and (h, j) surface potential line profiles for the two microcrystals, grown for 30 min (g, h) and 60 min (e,d); the line is shown in the insets.

#### 4.5. **Actuation of the microcrystals**

During the FESEM examination, we observed a clean actuation involving smooth bending of the gold coated microcrystals under a 2 kV electron beam. The primary observations are collected in Figure 4.13, which shows a series of images of a microcrystal with  $l \sim 60 \mu m$  (grown for  $\sim 3 h$ ) at different time intervals under the electron beam; the prominent bending occurs close to halfway along the altitude. We define the bending angle,  $\theta$  as  $0^{\circ}$  in the flat position (determination of bending angle ( $\theta$ ) is discussed in Sec. 4.5.1). After reaching the maximum,  $\theta > 90^{\circ}$ , if the electron beam irradiation is stopped, the crystal remains bent indefinitely; if the 2 kV irradiation is continued, the bending angle reduces slightly, but stays in that state subsequently. It was observed that gold coating on the microcrystals is important for the bending of the microcrystals (details are given in Sec. 4.5.2). If irradiated with an enhanced voltage beam (starting with 3 kV and then, 5 - 6 kV), the bent crystal straightens out, returning nearly to the original state.

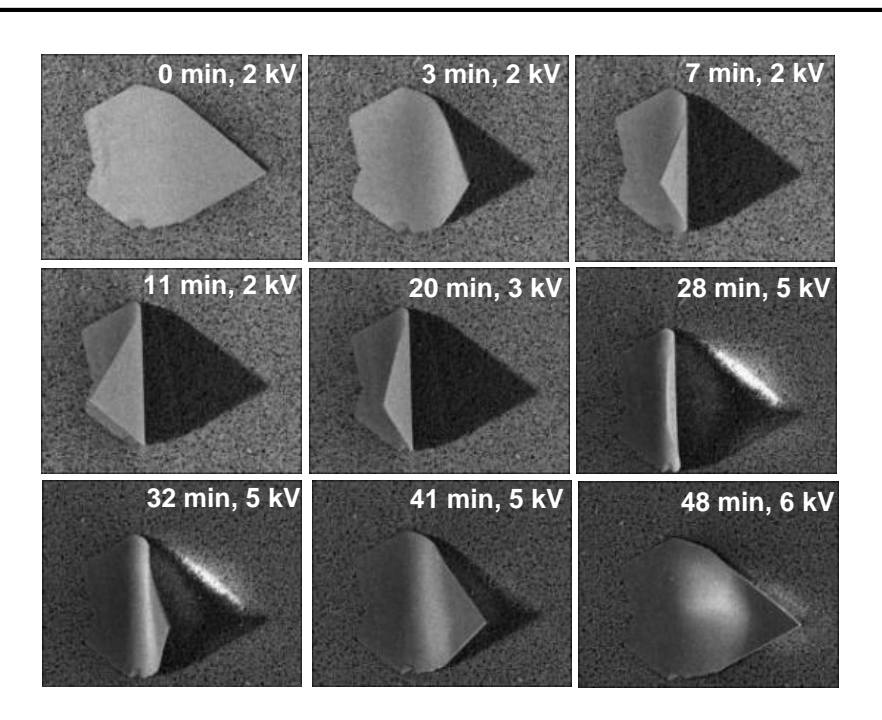
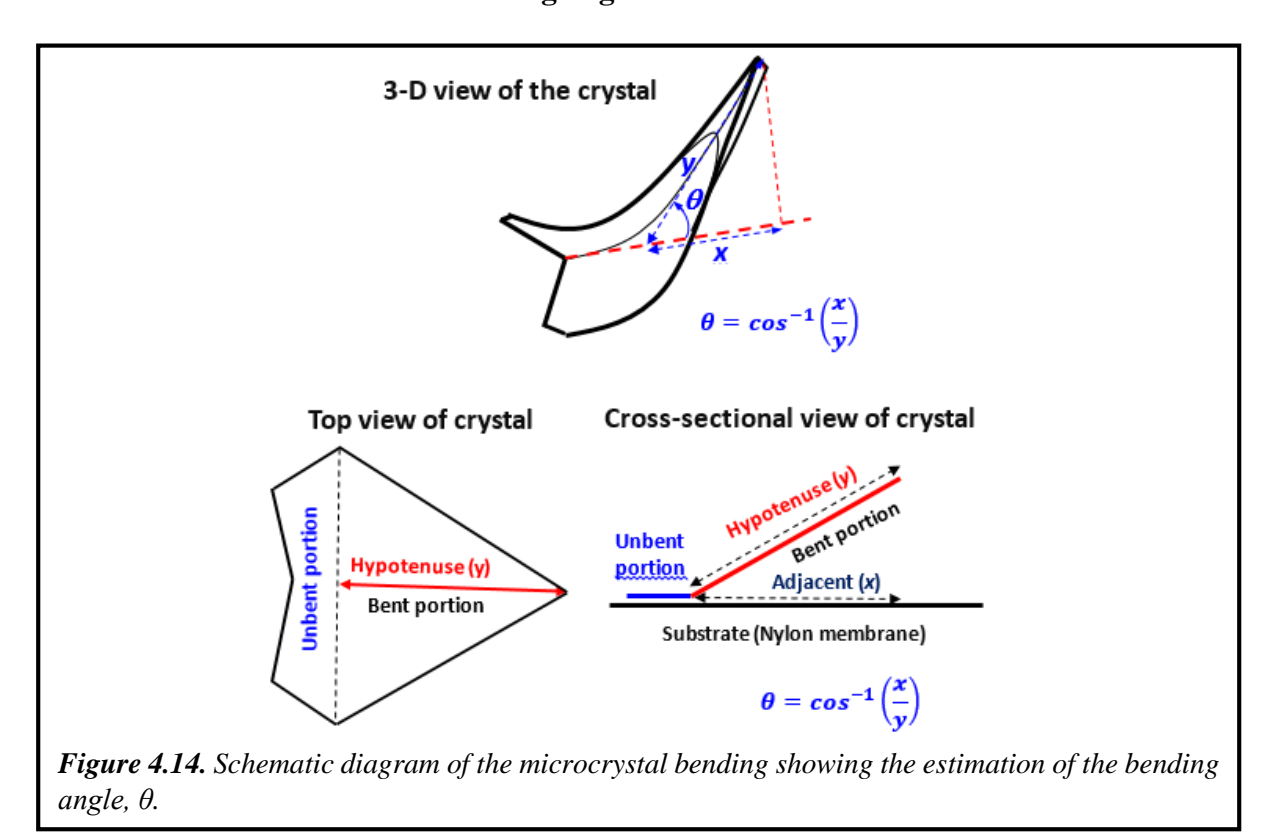


Figure 4.13. FESEM images of a BCPADQ microcrystal (grown for ~ 3 h) on a nylon membrane, under electron beam irradiation at different times (the beam voltages and time of imaging are indicated).

# 4.5.1. Determination of the bending angle



Bending angle of the microcrystal was estimated using ImageJ software Version 1.46r,  $^{31}$  by measuring the lengths corresponding to the hypotenuse (y) and side adjacent (x) to the bending angle  $(\theta)$ . Calculation of the angle is shown in Figure 4.14; by carrying out repeated measurements, we have estimated the percentage standard deviation in the angles estimated, to be in the range, 0 - 6%.

# 4.5.2. Factors influencing the bending and straightening of the microcrystal

Several experiments were carried out to determine the conditions under which the actuation occurs, and the controlling factors. Initial experiments showed that the microcrystal size, the electron beam accelerating voltage (V) and the working distance (WD), nature of the substrate, and the extent of sputter coating of gold are relevant. The mechanical responses can be visualized by the variation of  $\theta$  with time. The detailed observations are plotted in Figure 4.15, and individual cases discussed below.

Preparation condition	Growth time (h)	<i>l</i> (μm)	<i>b</i> (μm)	<i>h</i> (μm)	θ (°)	t (min)
With ultrasonication	0.5	21	18	1.2	42	2
	1	36	31	1.8	88	5
	3	75	61	2.3	113	7
	6	110	78	2.3	124	12
Without	3	104	96	1.8	129	19

Table 4.3. Influence of the size of the BCPADQ microcrystals on their bending under electron beam irradiation. 1: altitude; b: base; h: thickness of tip;  $\theta$ : bending angle; t: time taken for bending.

Relevance of the microcrystal size, tuned by the growth time (Table 4.3), was examined first. Figure 4.15a shows that the maximum bending attained is higher for larger crystals, the crystal with  $l \sim 60 \mu m$  reaching up to  $\sim 110^{\circ}$  with V = 2 kV. Impact of V on the rate of bending and straightening is shown for the crystal with  $l \sim 60 \mu m$  in Figure 4.15 b and c respectively; notably, the bending does not occur at V < 1 kV and > 5 kV. The bending is most prominent at  $V \sim 2 \text{ kV}$ , the speed decreasing with increasing V. The requirement of an optimal voltage is similar to that reported for gold-coated epoxy nanoposts bending under electron beam irradiation.<sup>22</sup> The straightening (decrease of  $\theta$ ) is slow and partial at V ~ 2 kV, but accelerated and nearly complete, when V is increased to 6 kV. Working distance between the samples and the objective lens also influences the rate of bending and straightening of the microcrystals. Figure 4.15 d shows that the maximum extent of bending decreases with increasing WD; considering the convergence angle of the beam, a WD of 7.7 mm was taken as optimal for further work.

Relevance of the gold coat on the bending was also investigated. In order to estimate the thickness of coating, gold thin films were sputtered on mica sheets for different time periods. A line was scratched on the coating using a syringe needle, to create a fine groove. Examination using an AFM provided the thickness of the sputtered films. The AFM topography images and line profiles are collected in Figure 4.16, and the thickness inferred, in Table 4.4. Figure 4.15 e shows that the bending does not occur when there is little or no coating. The crystal bending is fastest at an optimal coating of ~ 9 nm (corresponding to 60 s coating time); it decreases again with thicker coating, possibly due to the adverse changes in the mechanical properties of the surface.

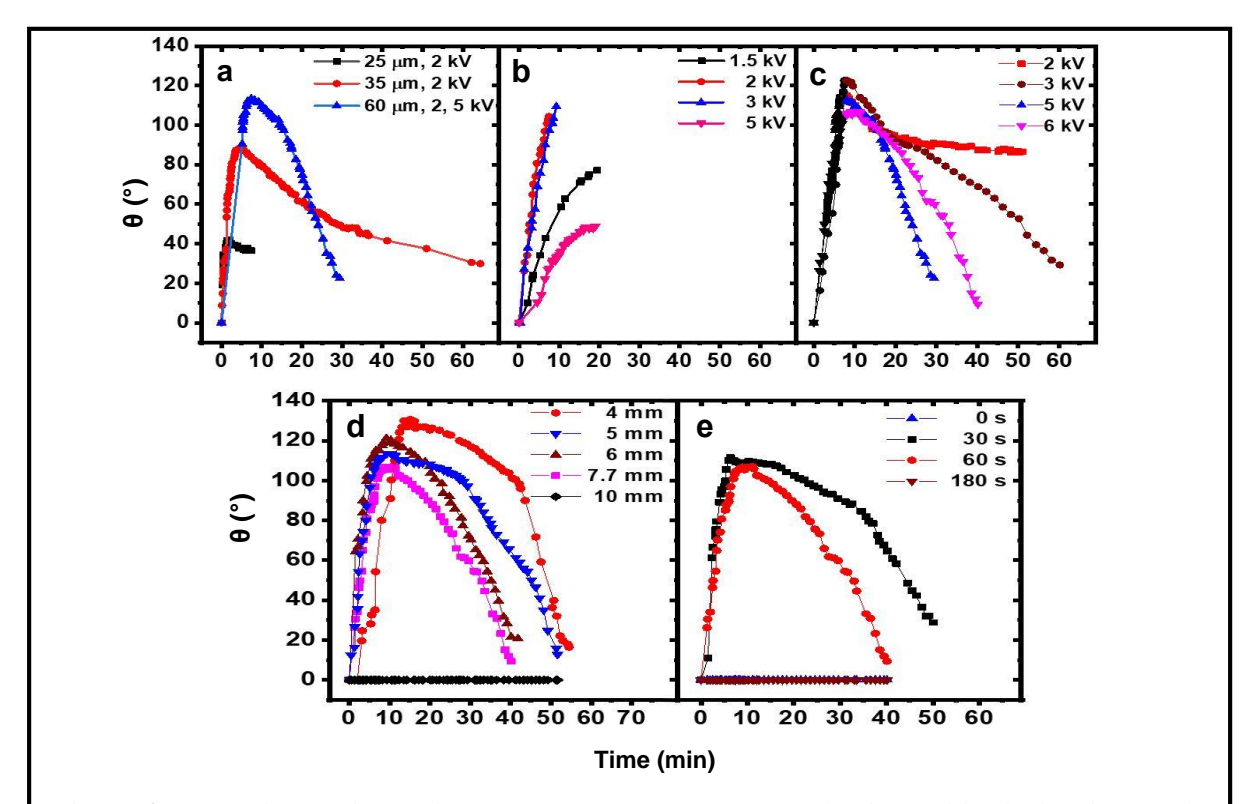
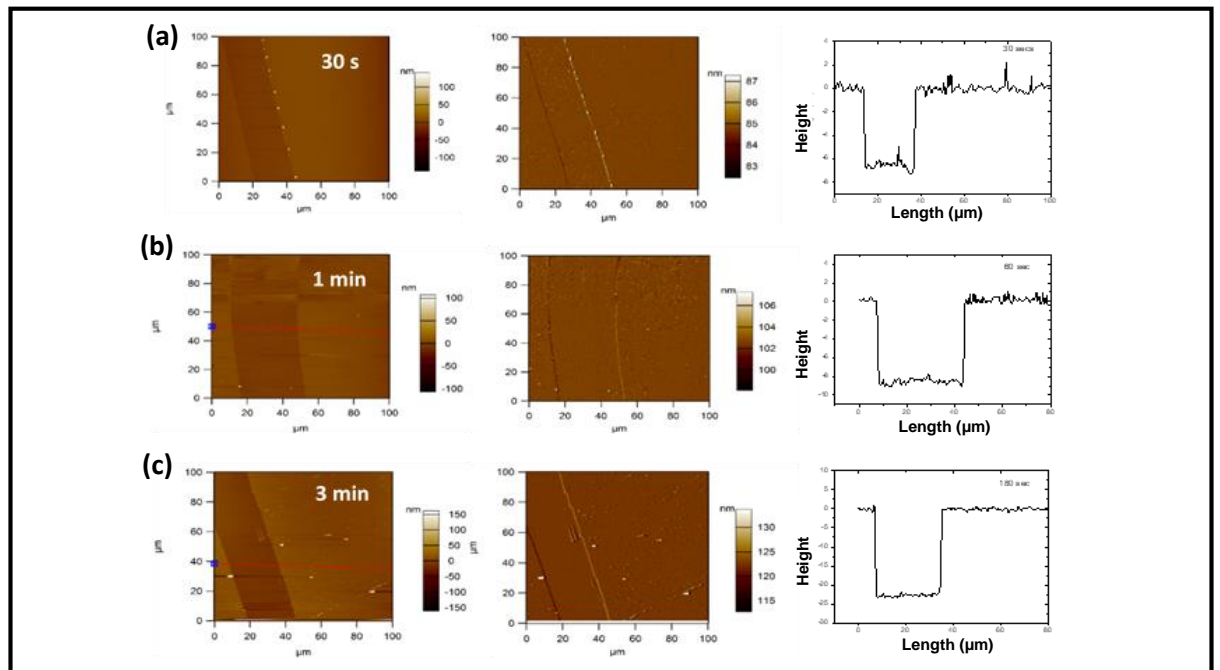


Figure 4.15. Bending and straightening of BCPADQ microcrystals (denoted by the bending angle,  $\theta$ ) as a function of time of electron beam irradiation: (a) microcrystals with different sizes (l) [WD = 7.7 mm, V = 2 kV and 5 kV for straightening of the largest crystal]; (b) bending under different  $V[l = 60 \mu m, WD = 7.7 mm]$ ; (c) straightening under different  $V[l = 60 \mu m, WD = 7.7 mm]$ ; all bending under 2 kV]; (d) at different  $V[l = 60 \mu m, V = 2 kV (bending), 6 kV (straightening)]$ ; (e) microcrystals with gold coat sputtered for different times  $[l = 60 \mu m, V = 2 kV (bending), 6 kV (straightening), WD = 7.7 mm]$ . In a - d, the gold coat sputtering is done for  $1 min (\sim 9 mm)$ .



**Figure 4.16.** AFM images of gold films sputtered on mica sheet for different time periods (a) 30 s, (b) 1 min, (c) 3 min and a groove scratched on it, together with the corresponding line profiles.

Sputtering time (s)	Thickness of gold film (nm)
10	$3.8 \pm 0.5$
30	$7.2 \pm 0.7$
60	$8.9 \pm 1.9$
180	$21.7 \pm 1.0$

Table 4.4. Thickness of gold films sputtered on mica sheet for different time periods, inferred from the AFM images.

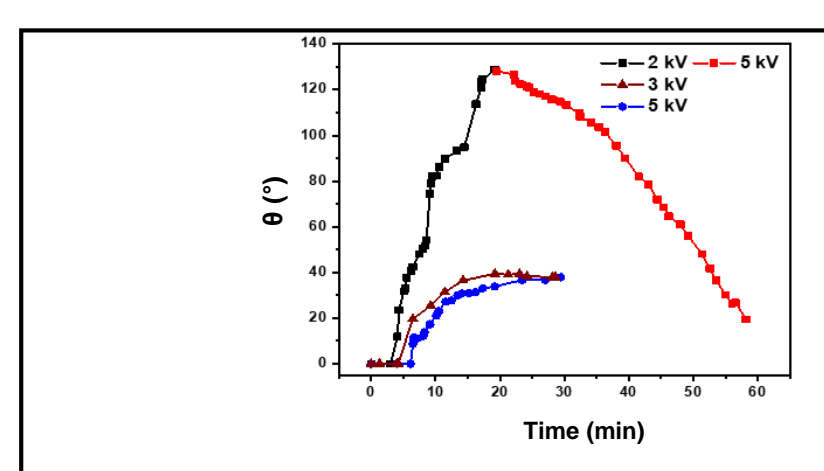


Figure 4.17. Variation of the bending and straightening angle of BCPADQ microcrystals formed without ultrasonication with time, for different accelerating voltage of the electron beam.

Finally we note that the microcrystals formed without ultrasonication and hence less distinct hopper morphology, showed significantly slower bending (Figure 4.17). It indicates that hopper morphology an important factor influencing the rate of actuation.

# 4.5.3. BCPADQ microcrystal on different substrates under AFM cantilever

The substrate (filter membrane) on which the microcrystals are collected, is important, while examining the actuation process. Relevance of the substrate was examined using microcrystals filtered out on different nanoporous membranes: alumina, mixed cellulose ester, cellulose nitrate, teflon, nylon, and nylon with a very thin gold coating; silicon wafer and carbon-coated copper (TEM) grid were also studied. The bending observed on nylon membrane occurs also on the gold-coated nylon membrane, indicating that an electrically insulating substrate is not essential. The bending was not observed on any of the other substrates. A simple experiment in the AFM showed that this was due to the adhesion

between the microcrystals and the substrate, as pushing using the tip failed to move the microcrystals. Significantly, we found that, on nylon membrane, the crystals could be slid easily by pushing with the AFM tip.

# 4.5.4. Repeat cycles of BCPADQ microcrystal actuation

We have investigated the important issue of reversibility and repeatability of the actuation. The FESEM experiments described in Sec. 4.5.2 were all conducted at the default speed of 4 s/scan; the bending at 2 kV and straightening at 6 kV took ~ 10 min and ~ 30 min respectively (Figure 4.15a,b). Under these conditions, the bending-straightening sequence could not be repeated. We envisioned that this was due to the relatively less effective beam penetration in each fast scan necessitating longer exposure overall, and the consequent damages in the microcrystal, especially under the higher voltage beam used for straightening. Therefore we carried out a careful optimization of the scan speed (SS) to explore the possibility of repeating the actuation.

A general protocol involving bending (V = 2 kV, SS = 4 s/scan) followed by straightening (V = 7 kV, SS = 26 s/scan) turned out to be successful. Four cycles of bending-straightening of a microcrystal are shown in Figure 4.18. In the first cycle, the crystal bent up to  $\theta \sim 110^{\circ}$  in about 10 min as seen in Sec. 4.5.2. In order to effect the straightening,

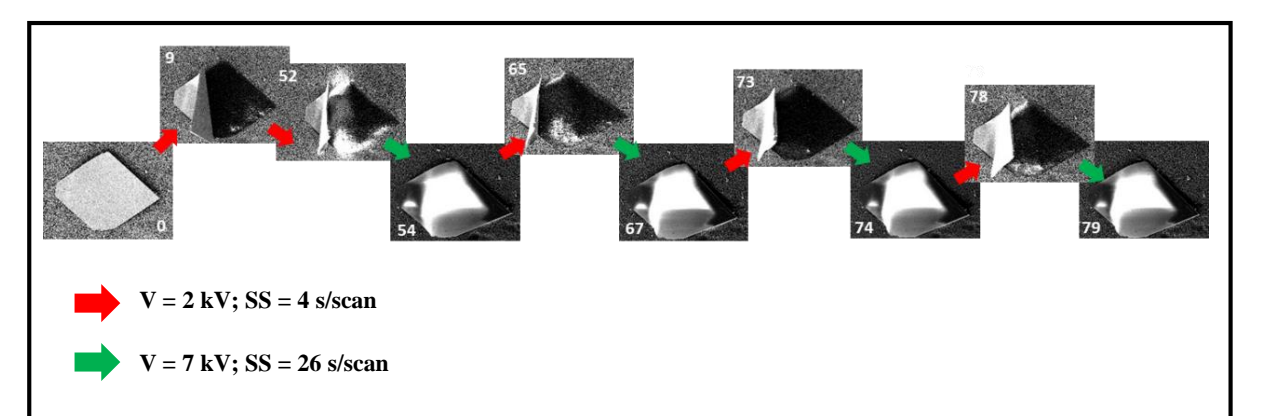


Figure 4.18. FESEM images of a single microcrystal through four cycles of reversible actuation; the time in minutes is indicated on the images and the electron beam voltage and scanning speed employed indicated by the respective colored arrows. The extent of bending is schematically (not to scale) represented by the vertical positioning of the images. In the first cycle, the bending angle fluctuated before settling at the position at 52 min.

it is preferable to have  $\theta \sim 90^{\circ}$ ; on continued irradiation with the 2 kV beam, the bending fluctuated a little and settled slowly near the vertical position. With the 7 kV electron beam and slow scanning, the straightening step took < 2 min; the quick straightening is the critical step needed to ensure repeatability of the process. In the subsequent cycles, the bending was smoother and generally occurred up to  $\sim 90^{\circ}$  in 5 – 10 min; the straightening in 1 – 2 min could be carried out thereafter. This experiment clearly demonstrated the reversibility and repeatability of the actuation process.

# 4.5.5. Stability of the microcrystals

It is important to probe whether the microcrystals remain stable through the actuation process, since it is well established that DADQs show strong fluorescence in the crystalline solid state, which is sensitive to even amorphization of the solid, 32 we have examined the fluorescence responses of the microcrystals. Careful imaging of the BCPADQ microcrystals before and after the bending-straightening, using confocal laser scanning fluorescence microscopy, ascertained the maintenance of their integrity (Figure 4.19). Further, we have examined the Raman spectra of fresh and irradiated microcrystals (V= 2 kV, time= 60 min, WD= 7.7 mm; Figure 4.20); identical spectra observed in the pristine and irradiated crystals rule out any obvious chemical change in the material. It is however possible that some changes in the molecular assembly occur locally, in the part of the crystal that gets stretched during the bending, similar to the morpho-structural effects demonstrated during the plastic deformation of hexachlorobenzene;<sup>33</sup> this could be the reason for the crystal remaining bent, if not straightened by a higher energy electron beam.

#### 4.6. An empirical model for the actuation

Even though a complete molecular level picture of the electron beam triggered actuation phenomenon is not clear at the moment, we have developed a mechanistic model using the experimental observations and crystal characterizations, simulation of the electron beam interactions, and analysis of the relevant electrostatic forces. The microcrystal with an asymmetric thickness profile and specific dipole orientation possesses an uneven potential

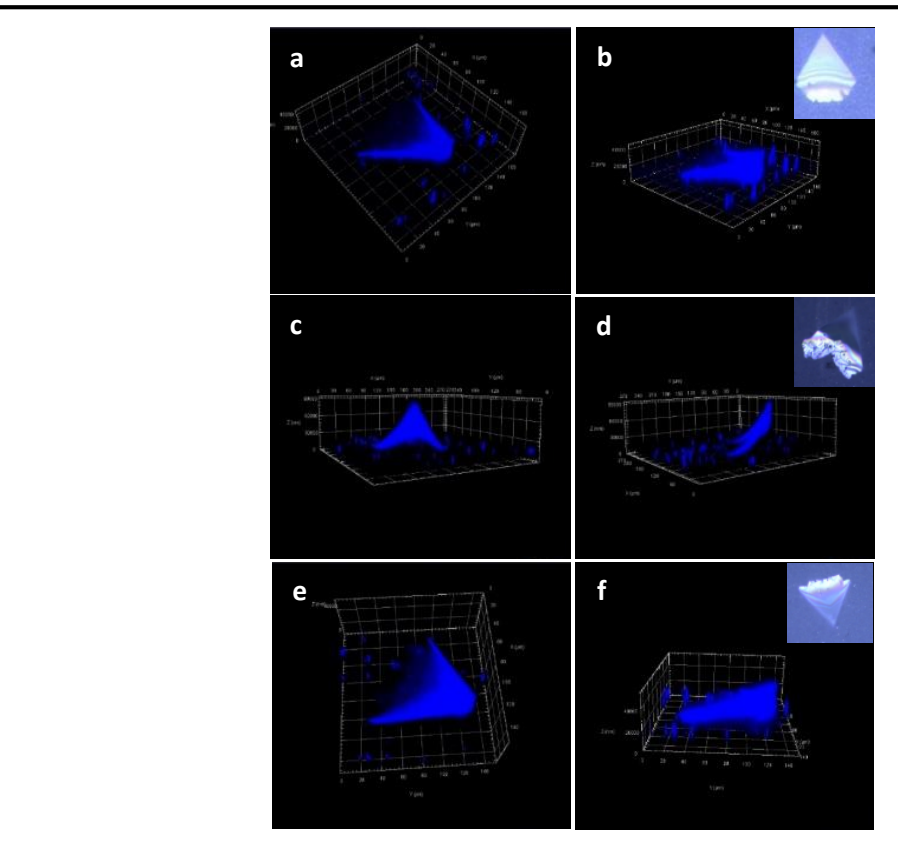


**Figure 4.19.** 3-D CLSM fluorescence images viewed from two different angles, of a BCPADQ microcrystal: (**a**, **b**) before subjecting to electron beam irradiation, (**c**, **d**) bent upon irradiation by a 2 kV beam for 10 min, and (**e**, **f**) subsequently straightened upon irradiation by a 6 kV beam for 20 min. Inset in each case shows the corresponding optical image. ( $\lambda_{exc} = 405$  nm,  $\lambda_{em} = 415-480$  nm)

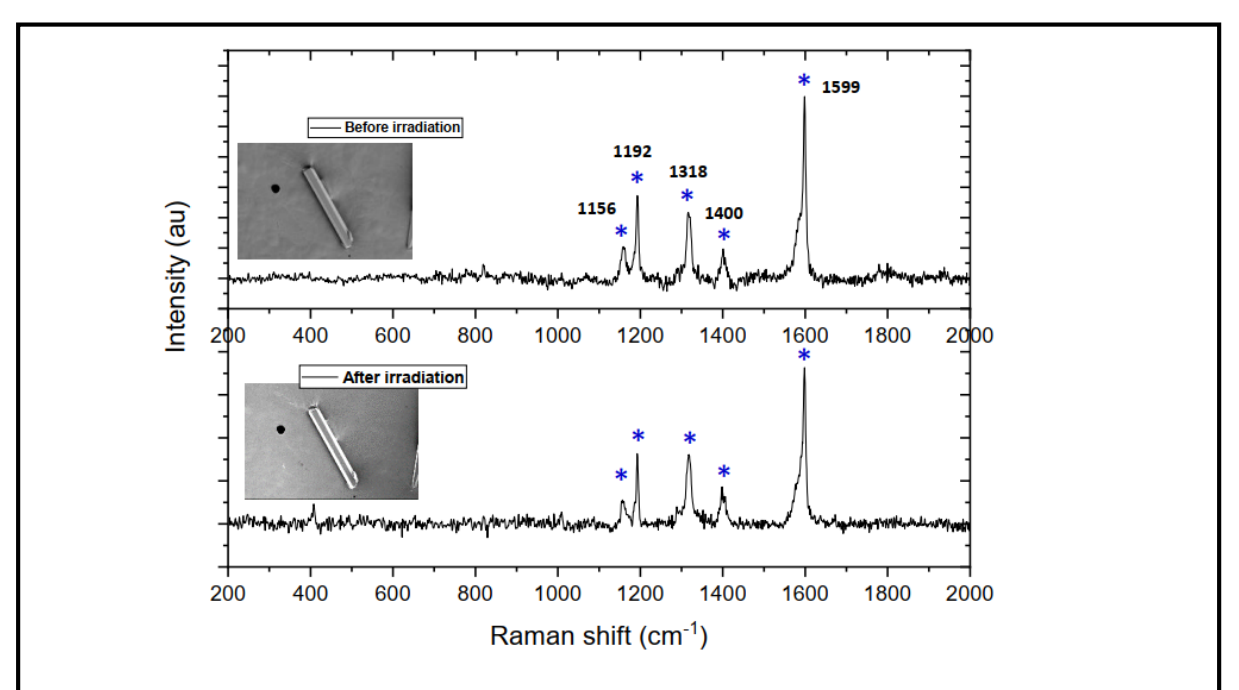


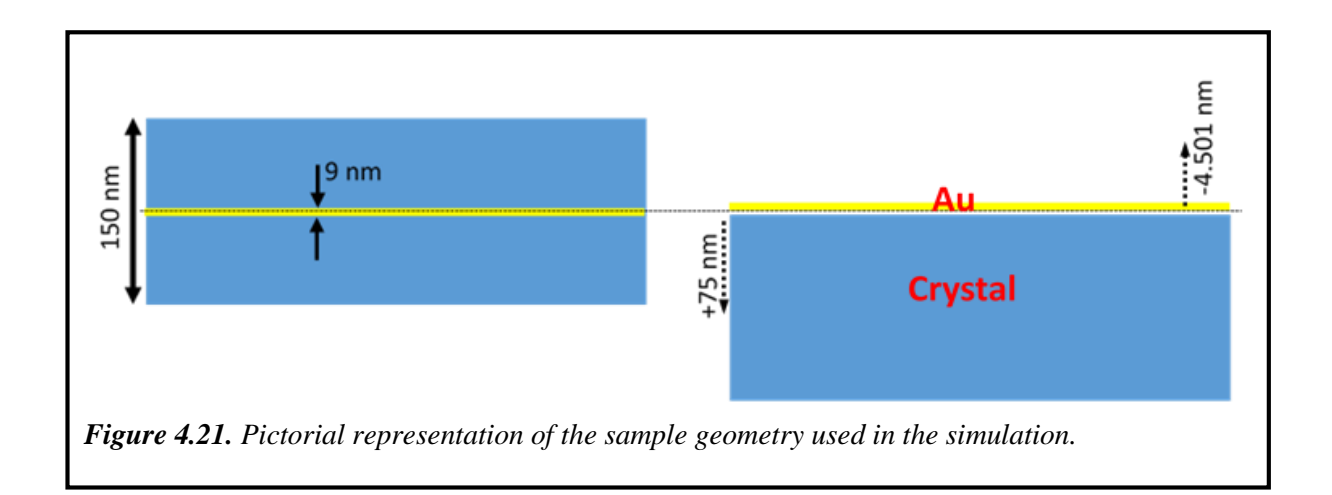
**Figure 4.20.** Raman spectra ( $\lambda_{exc} = 532$  nm) of BCPADQ crystals before and after irradiation by the electron beam (inset: image of an irradiated microcrystal).

distribution as noted in Sec. 4.4.6. The optimal gold coating on the microcrystal prevents beam deflection and facilitates imaging in the FESEM. Depending on its energy, the electron beam passing through the coat and penetrating into the microcrystal, can induce a net charge.<sup>34</sup> It is well known that the ratio of inelastic to elastic scattering of electron beam scales as  $\sim 20/Z$  (Z = atomic number);<sup>21</sup> and hence it is expected to be appreciable for the organic crystal. With negligible charge evacuation to the ground, a relatively low energy beam can induce positive charging on an insulating sample surface, whereas a higher energy beam can create negative charge accumulation deeper inside the sample.<sup>35</sup>

# 4.6.1. Simulation of electron beam trajectories

In order to visualize the electron beam trajectories in the crystal, we carried out simulations using the CASINO (version 3.3.0.4) Monte Carlo software;<sup>36</sup> details of the sample geometry, and conditions used to run the simulation are provided in Box 4.1 and the sample geometry depicted in Figure 4.21.

Samples with three thickness values, 30 nm, 150 nm and 1.5 µm, modelling the thin end, middle region (close to where the bending occurs) and the thick end of the microcrystal respectively, with a gold coat (~ 9 nm), under electron beam voltages of 2 and 6 kV were considered. Graphical representation of the simulated trajectories and plots of the maximum depth of electron in the three cases are shown in Figure 4.22, 4.23 and 4.24 respectively, and representative summary of the simulation graphics are presented in Figure 4.25. The incident, transmitting, backscattered, and secondary electron emission tracks are shown in the figure. It is clearly seen that, the 2 kV beam penetrates the thin sample fully; the 6 kV beam



penetrates the thin and mid-size samples fully, but only to some depth in the thick one (the distribution of maximum depth of electrons are shown in Figure 4.22-4.24). With the 2 kV beam, significant secondary electron emission occurs in all cases; the magnified image in Figure 4.25d, and the estimated backscattering coefficients and secondary electron yields (Table 4.5) show this clearly.

# Box 4.1- Details of the sample geometry used for the simulations

# Mid-size sample

Box0: Crystal, Size = 5000×5000×150 nm³; Translation = 75 nm (in order to ensure that the top surface of the box is at the horizontal level; Figure 4.21)
 Molecular formula C<sub>20</sub>H<sub>24</sub>N<sub>4</sub>, Density = 1.16 (from crystal structure analysis)
 Plasmon energy = 8 eV; Work-function energy = 8 eV (based on computed ionization energy)

2. **Box1:** Au, Size =  $5000 \times 5000 \times 9 \text{ nm}^3$ ; Translation = -4.501 nm (in order to ensure that the bottom surface of the box is at the horizontal level, with a very tiny gap as per the simulation program requirement; Figure 4.21)

# Thin sample

- 1. **Box0:** Crystal, Size =  $5000 \times 5000 \times 30 \text{ nm}^3$ ; Translation = 15 nm
- 2. **Box1:** Au, Size =  $5000 \times 5000 \times 9 \text{ nm}^3$ ; Translation = -4.5001 nm

# Thick sample

- 1. **Box0:** Crystal, Size =  $5000 \times 5000 \times 1500 \text{ nm}^3$ ; Translation = 750 nm
- 2. **Box1:** Au, Size =  $5000 \times 5000 \times 9 \text{ nm}^3$ ; Translation = -4.5001 nm

# **Simulation settings**

Generate SE electron: Yes; Beam diameter: 10 nm; Maximum order of SE generated: 10; Default physical models

Table 4.5. Back scattering (BS) coefficients and secondary electron (SE) yields computed from CASINO (3.0.0.4) simulation, for the three different samples under electron beams of two different energy; the number of simulated electrons was kept 10000, in order to obtain improved precision for the SE yield and BSE coefficients. The mean and standard deviation are estimated from ten simulation runs.

Cwystal	Beam volta	ige = 2 kV	Beam voltage = 6 kV			
Crystal thickness (nm)	BS coefficient [std. dev.]	SE yield [std. dev.]	BS coefficient [std. dev.]	SE yield [std. dev.]		
30	0.487 [0.005]	0.645 [0.014]	0.213 [0.004]	0.117 [0.008]		
150	0.487 [0.005]	0.644 [0.011]	0.235 [0.004]	0.123 [0.005]		
1500	0.488 [0.006]	0.651 [0.015]	0.245 [0.003]	0.127 [0.008]		
150*	0.078 [0.003]	0.016 [0.001]	0.036 [0.002]	0.005 [0.001]		

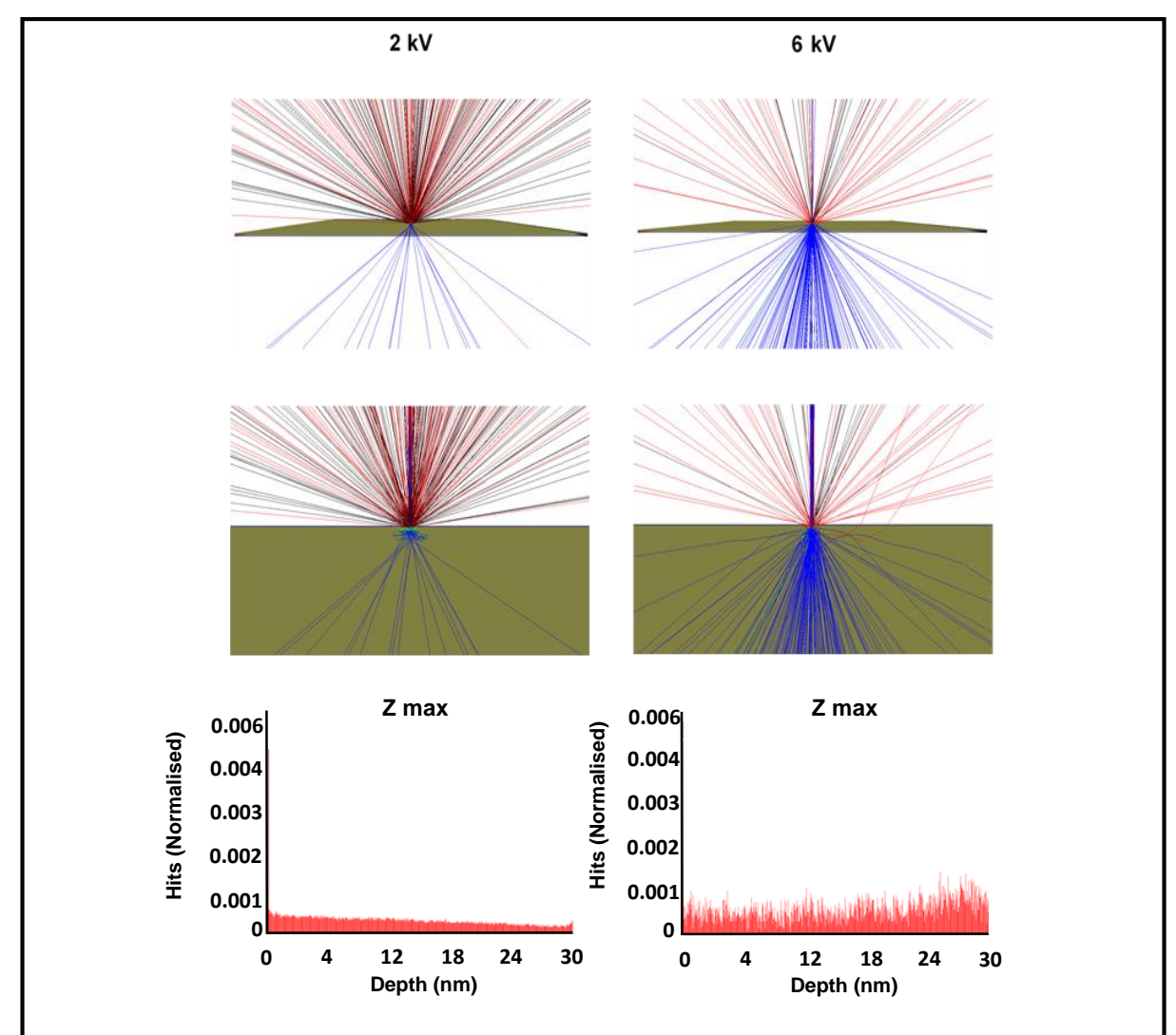
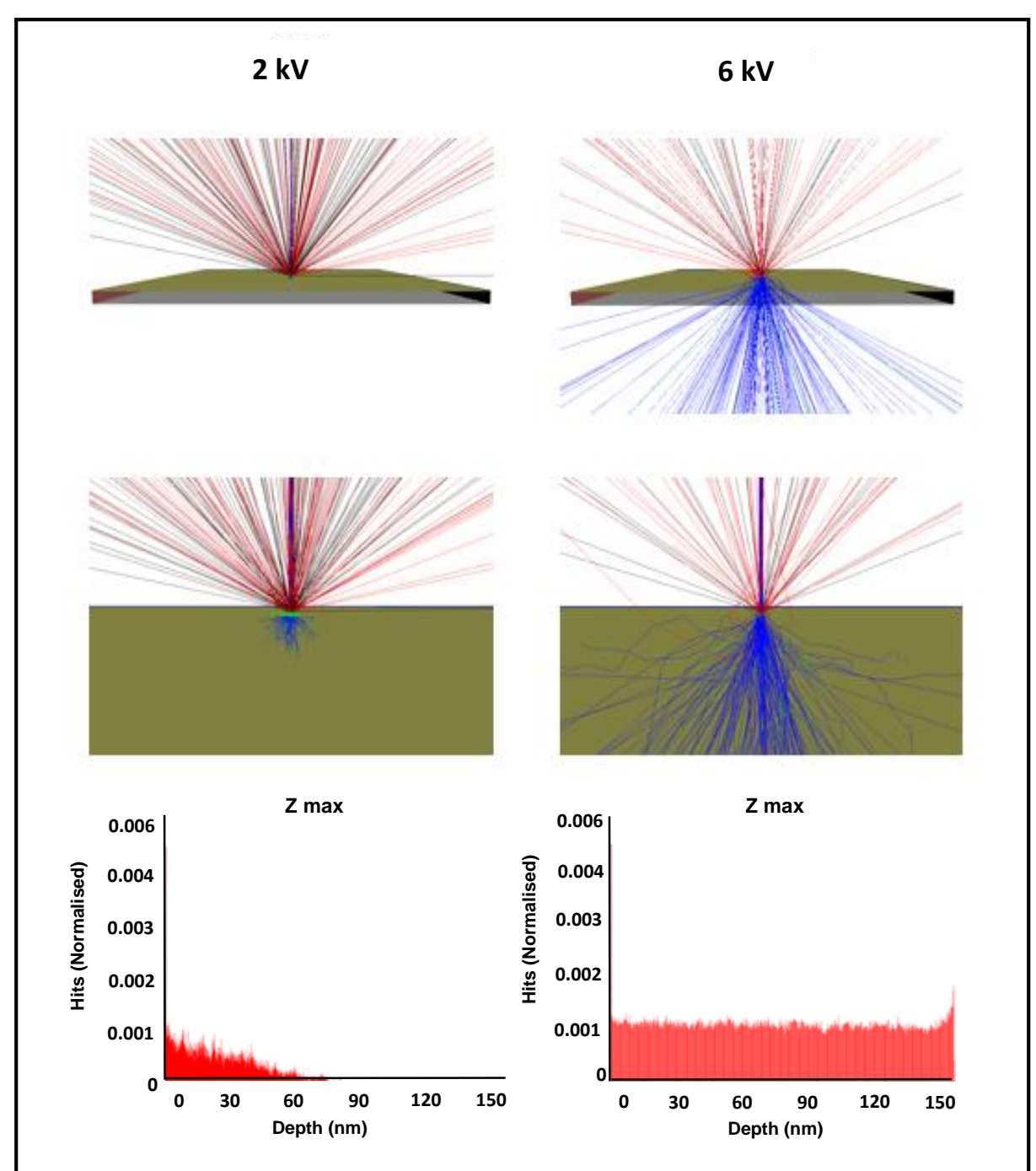


Figure 4.22. Electron beam trajectories (blue: incident and transmitting; red: back scattered; green/black: secondary electron emission) together with a magnified view, and distribution of the maximum depth of electrons in the thin end of the microcrystal (30 nm), at beam voltages of 2 kV (left) and 6 kV (right).



**Figure 4.23.** Electron beam trajectories (blue: incident and transmitting; red: back scattered; green/black: secondary electron emission) together with a magnified view, and distribution of the maximum depth of electrons in the middle part of the microcrystal (150 nm), at beam voltages of 2 kV (left) and 6 kV (right).

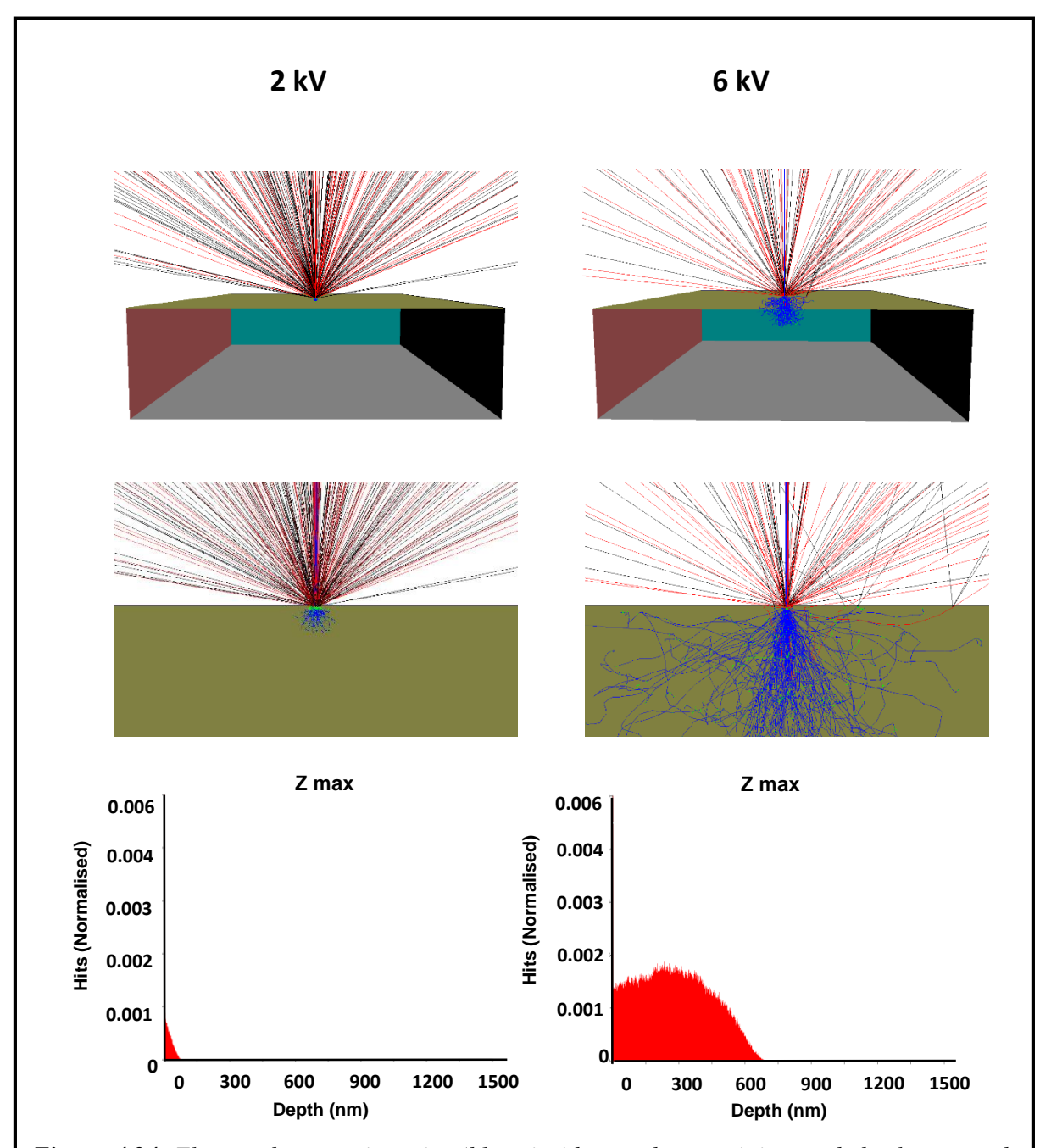
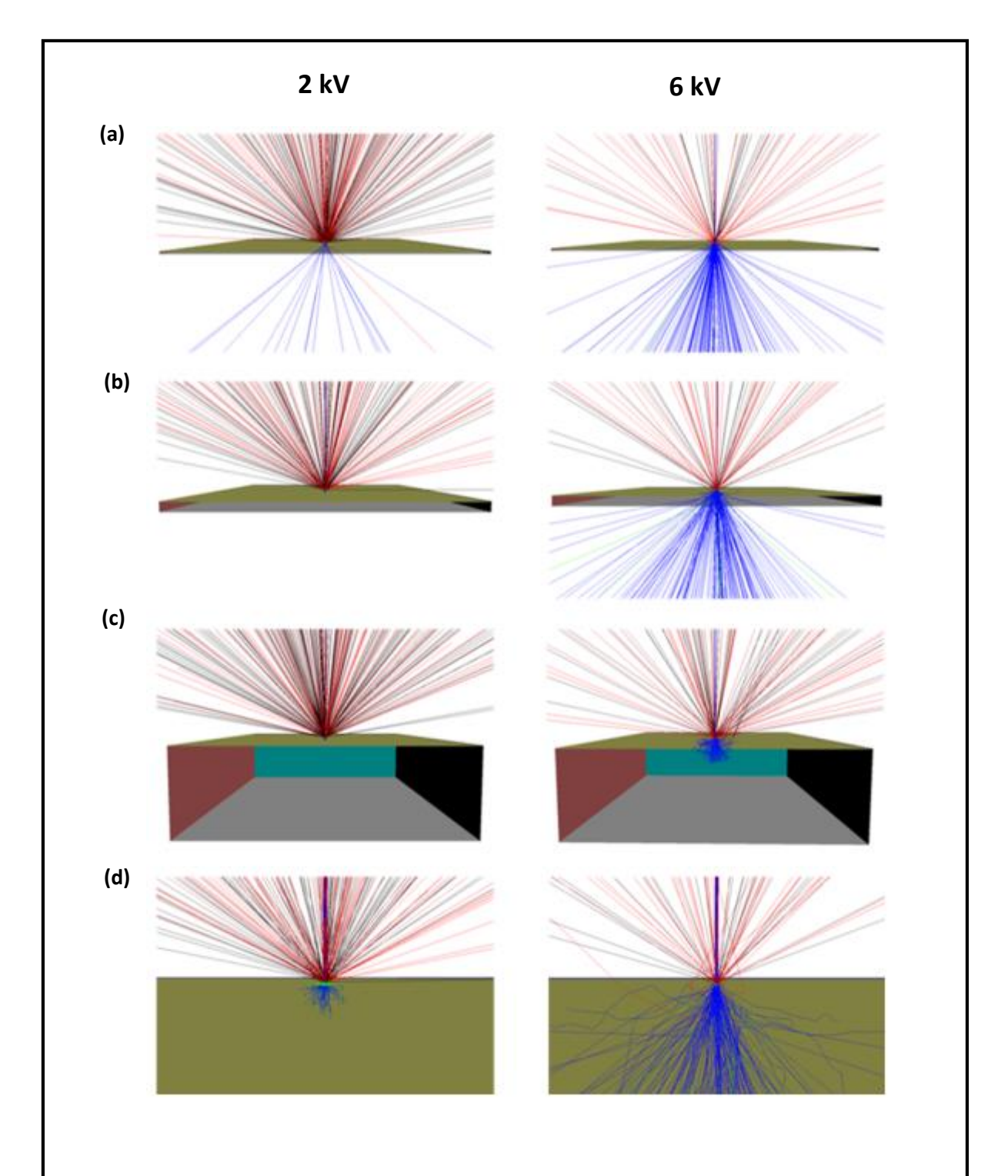


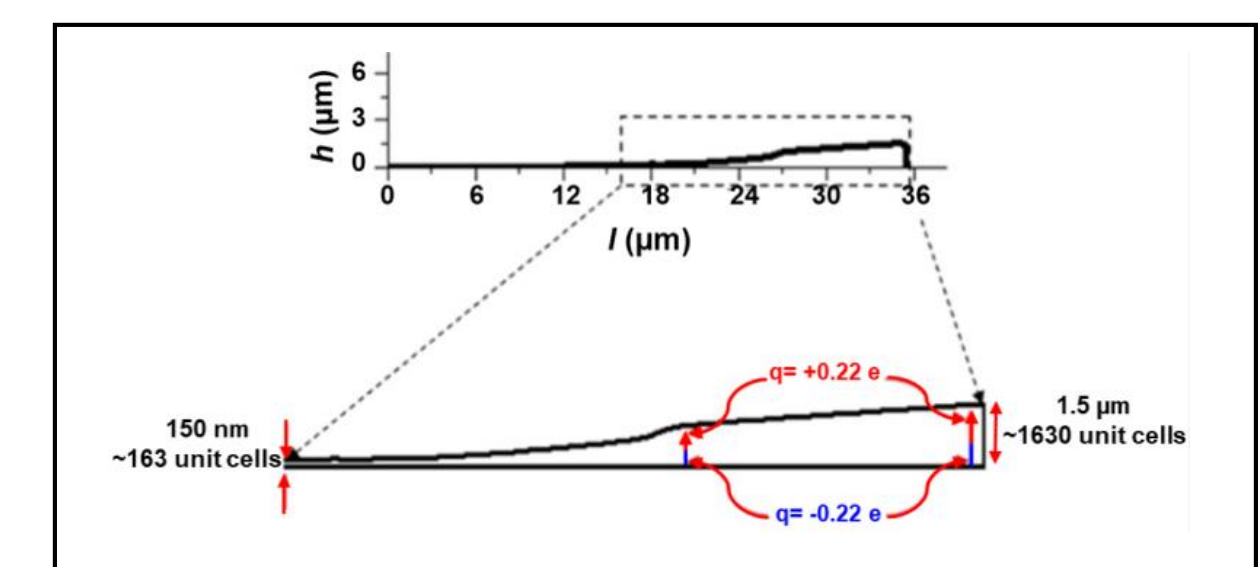
Figure 4.24. Electron beam trajectories (blue: incident and transmitting; red: back scattered; green/black: secondary electron emission) together with a magnified view, and distribution of the maximum depth of electrons in the thick end of the microcrystal (1500 nm), at beam voltages of 2 kV (left) and 6 kV (right).



**Figure 4.25.** Electron beam trajectories (blue: incident and transmitting; red: back scattered; green/black: secondary electron emission), with beam voltages of 2 kV (left) and 6 kV (right) for the microcrystal with thickness, (a) 30 nm, (b) 150 nm, (c) 1500 nm, and (d) 150 nm (magnified view).

# 4.6.2. Impact of slope surfaces

Since the hopper microcrystal has slope surfaces (Figure 4.8) and secondary electron emission is sensitive to the angle of incidence of the electron beam, <sup>37</sup> simulation studies were carried out to examine this factor as well. It is well-known that the secondary electron (SE) generation is enhanced when the electron beam is incident on a slope surface of the specimen, since the oblique incidence increases the effective emission area.<sup>37</sup> In order to assess the impact of the beam incidence on the sloping parts of the microcrystal, we have carried out modelling using the CASINO (ver. 3.3.0.4) software. The maximum slope as the crystal gets thicker towards the triangle apex part of the hopper crystal is ~17° (Figure 4.26). We used the 'Truncated Pyramid' option in the CASINO software to prepare the crystal sample with different slopes,  $\beta$  ranging from 5 to 30°; typical dimensions for the case of  $\beta = 15^{\circ}$  are shown in Figure 4.27 (the step on the top is exaggerated).



Computed dipole moment of the molecule = 23 D (Sec. 4.3.2.)

Projection on the crystal c axis (per molecule) = 0.105 (Figure 4.11c)

Projection on the crystal c axis (4 molecules in the unit cell) = 0.42

Dipole component along the c axis =  $23.0 \times 0.42 = 9.66 \text{ D}$ ; unit cell length (c) = 0.92 nm

Charge (q) = 0.22 e [Note: 1 D = 0.0208 e.nm]

Figure 4.26. Profile of the BCPADQ microcrystal along l (defined in Figure 4.8), and a magnified view of the thick end indicating the unit cell counts and dipole charges. Estimation of the dipole charges in the microcrystal is shown.

The gold coating was modeled using the 'Box' option as before, with 9 nm thickness. The box was appropriately translated and rotated to ensure precise placement on the crystal surface with a very tiny gap of 0.001 nm as before (Box 4.1); the geometry details are collected in Table 4.6. The simulations were run with 2 kV electron beam energy (Figure 4.28a); number of simulated electrons was kept 10000, in order to obtain improved precision for the SE yield and BSE coefficients. The mean values from 10 simulation runs along with the estimated standard deviations are plotted in Figure 4.28b. It is seen that the SE yield increases with increasing tilt angle. Figure 4.28 and Table 4.6 demonstrate the increase of secondary electron emission with the surface slope.

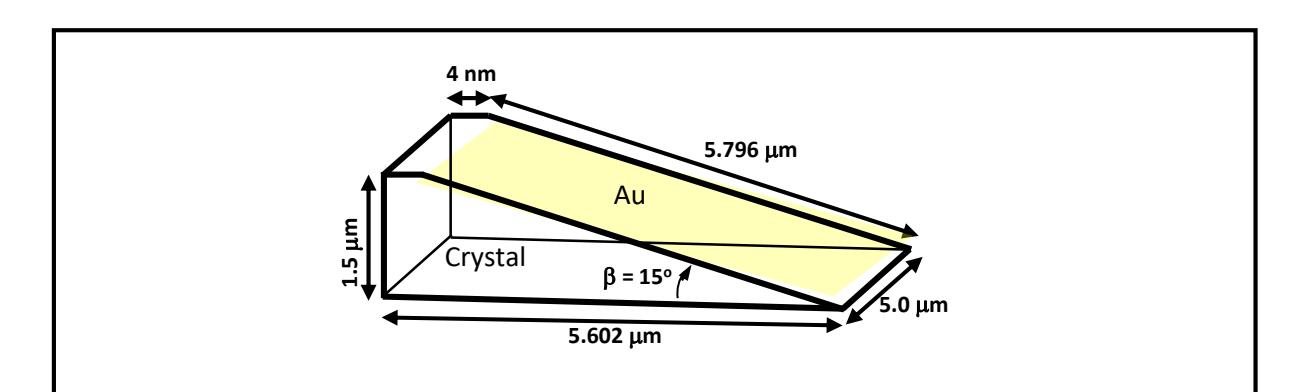


**Figure 4.27.** Pictorial illustration of the 'Truncated Pyramid' geometry used in the CASINO (ver. 3.3.0.4) stimulation study.

**Table 4.6.** Parameters used for sample geometry in the CASINO simulation runs for slope surfaces.

β (°)	Crystal (Truncated Pyramid) Angle: Ang <sub>A</sub> = 90°, Ang <sub>B</sub> = 90°, Ang <sub>C</sub> = 90°			Au (Box) Rotation: Rot $_{\rm Y}=0^{\rm o}$ , Rot $_{\rm Z}=0^{\rm o}$ Translation: $_{\rm X}=0$ , $_{\rm Y}=0$ , $_{\rm Z}=-754.501$ nm				
	X (nm)	Y (nm)	Z (nm)	Ang <sub>D</sub> (°)	X (nm)	Y (nm)	Z (nm)	Rot <sub>X</sub> (°)
5	5000	17149	1500	5	5000	17210	9	-5
10	5000	8511	1500	10	5000	8638	9	-10
15	5000	5602	1500	15	5000	5796	9	-15
20	5000	4125	1500	20	5000	4386	9	-20
25	5000	3221	1500	25	5000	3549	9	-25
30	5000	2602	1500	30	5000	3000	9	-30

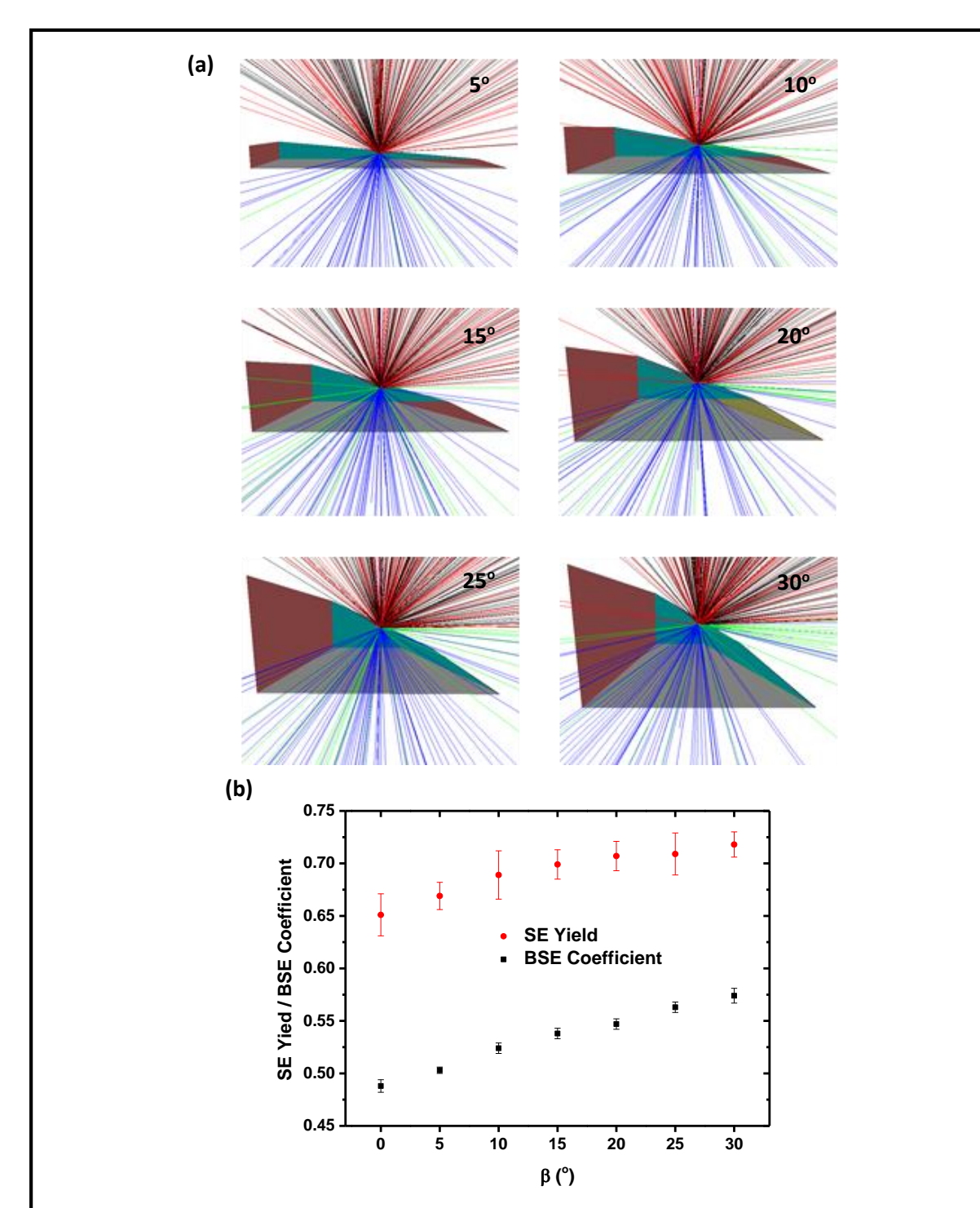


Figure 4.28. (a) Electron beam trajectories (blue: incident and transmitting; red: back scattered; green/black: SE emission) for incidence on sample surfaces with different slopes, with a beam voltage of 2 kV, and (b) variation of the estimated SE yield and BSE coefficient with the slope (the 0° case is based on the sample preparation described in Figure 4.21 and Box 4.1 with a thickness of 750 nm, corresponding to the mid-point in the slope surface samples).

The electron beam interactions can cause transient charging of the specimen depending on factors such as its electrical conductivity and the imaging scan speed; as discussed in Sec. 4.5.4, our experiments have shown the impact of scan speed on the reversibility of the actuation. In the insulating organic microcrystal, the secondary electron emission could induce positive charges at the surface which would vary with the morphology; with the higher voltage beam that penetrates deep, and the relatively less backscattering and secondary electrons (Table 4.5), a dominant negative charging is likely. Uncompensated charges on insulating specimen are known to cause their mechanical movement under electrostatic forces due to local fields.<sup>21</sup>

# 4.6.3. Model for the microcrystal bending/straightening

A schematic of the crystal profile along l (defined in Figure 4.8) and a magnified view of the thick end (Figure 4.26) illustrate the growing dipole resulting from the increasing number of unit cells (based on the crystal c parameter); the dipole charge is estimated to be  $\sim 0.22$  e (Figure 4.26). Based on the simulation studies and discussions presented in the previous section, it is clear that, depending on the electron beam voltage, the morphological details, the microcrystal would get uncompensated charges in it. The permanent dipoles and charges on the crystal will be effectively acted upon by any external electric field.

We assume the following simple model for the electrostatic forces between the molecular dipole ( $\mu$ ) or any uncompensated charge ( $\epsilon$ ) created on the microcrystal, and the electrostatic lens on the objective lens of the FESEM (Gemini column design<sup>38,39</sup>), present at the working distance (WD) (Figure 4.29a). The outer electrode of the electrostatic lens that is closest to the sample has the negative bias, and the inner electrode above has the positive bias, of the booster voltage (typically  $\sim$  8 kV) that decelerates the primary electron beam before landing and also helps to collimate and accelerate the secondary electrons (SE) towards the in-lens detector. The field is likely to decrease exponentially away from the lens. The effective field (E) at the sample (direction determined by the electrostatic lines of force) due to the electrostatic lens field ( $E^*$ ) will exert an attractive force on the ( $\mu$ ) dipole pointing upwards or any residual positive charge ( $\epsilon$ ) on the surface of the microcrystal and the attractive force would vary along the altitude profile, increasing significantly towards the thick end; the force will be repulsive if the residual charge is negative (Figure 4.29b).

The upward electrostatic force on the dipole is proportional to the dipole moment and the local field. It can be expressed as:

$$F_{dipole} = \mu . \frac{dE}{dx} \hat{\imath}$$

where î denotes the unit vector along the dipole moment. Based on the exponential decay of E\* (Figure 4.29b), the field at the microcrystal decreases downwards as:

$$E^{\circ} \sim E^* e^{-WD/x_0}$$

where WD is the working distance and  $x_0$  is the decay constant. Therefore the field variation along the dipole (upwards) can be written as

$$E \sim E^{o} e^{x/x_0}$$
  $\Longrightarrow \left[ \frac{dE}{dx} = \frac{E^{o}}{x_o} e^{x/x_0} = \frac{E}{x_o} \right]$ 

$$F_{dipole} = \mu \cdot \frac{E}{x_o} \hat{\imath}$$

As the thickness of the microcrystal (h) increases along the altitude (l),  $\mu$  will also increase since the number of unit cells increases (Figure 4.26). If we approximate the field as that present at the midpoint of the dipole,

$$E \sim E^{\circ} e^{h/2x_0}$$

$$|F_{dipole}| \propto he^h$$

In the case of residual charge,

$$F_{charge} = \varepsilon E$$

The estimates of relative forces on the dipoles along the microcrystal altitude profile (l) are shown in Figure 4.29 c.

With all the other parameters such as the electrical conductivity of the crystal and scanning rate remaining the same, the extent of positive charge created on the surface due to the SE emission at the low electron beam voltage (2 kV) can be considered to be proportional to the SE yield. Using the data in Figure 4.28b and its interpolation, the correspondence between charge and slope can be determined; using the slope at each point along the profile (Figure 4.9, 4.26), the correspondence between the charge and the position along the altitude can be determined. As the local electric field also depends on the height at each point along the altitude profile, one can arrive at the relative variation of  $F_{charge}$  plotted in Figure 4.29c. As the value of E is expected to be very small, we believe that the forces on the dipoles  $(F_{dipole})$  may be weak, those on the uncompensated charges  $(F_{charge})$  could be significant, as borne out by the fact that the actuation is triggered by the electron beam.

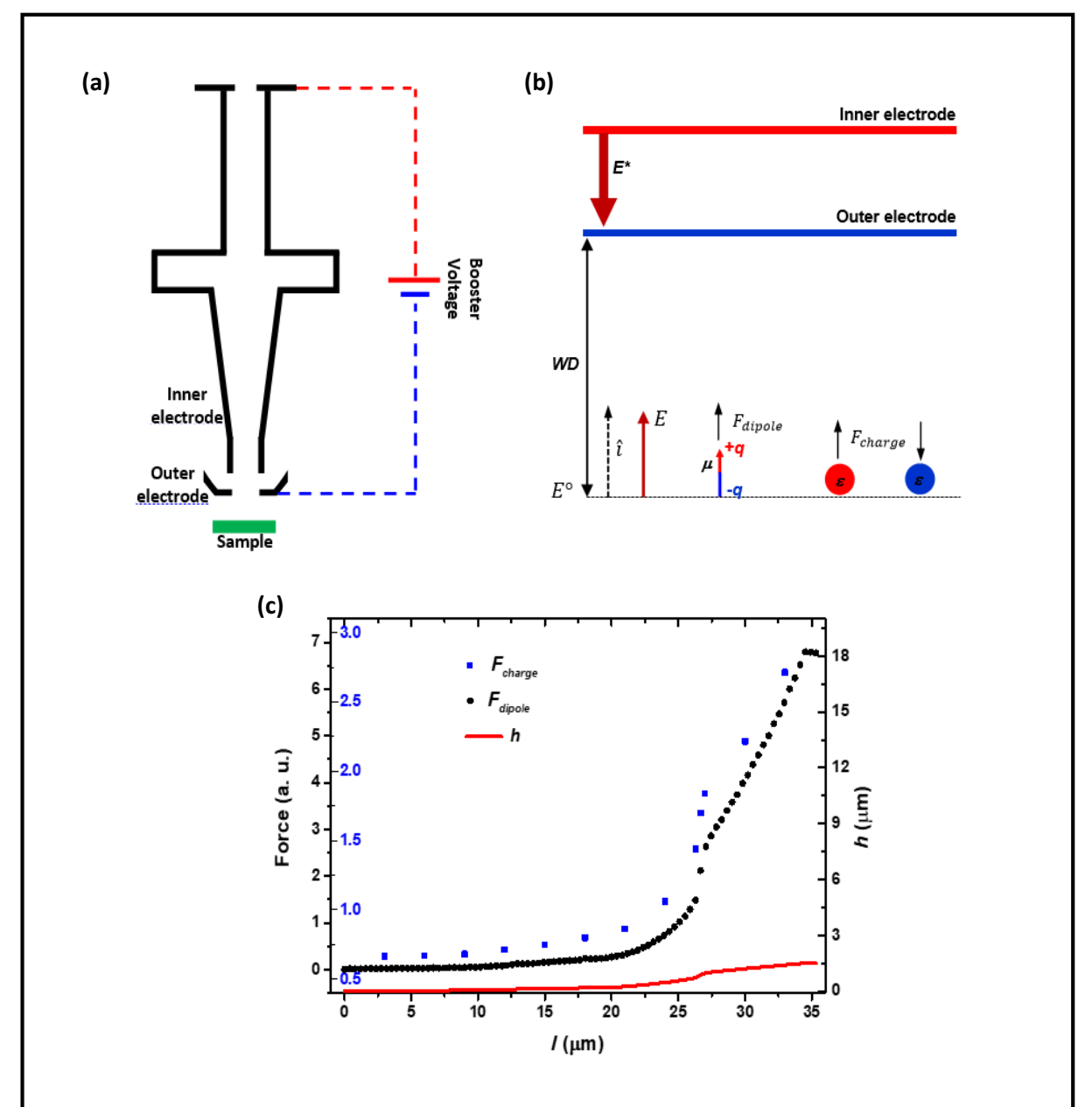


Figure 4.29. (a) Schematic diagram of the electrostatic lens. (b) Schematic diagram showing the forces due to the electrostatic lens field, on the dipoles or charges on the surface of the microcrystal. (c) Plot of the relative force variation along the length of the microcrystal due to the interaction of the field with the dipoles and charges.

### 4.6.4. Plausible mechanism of actuation

Based on the earlier discussions about the electron beam penetration into the different thickness regimes, it can be assumed that at low (~ 2 kV) beam voltages, the thin end of the microcrystal fully swamped by the electron beam would get some negative charging, whereas the thicker regions would be charged positive, with significant effects where the surface slopes are high (Figure 4.26 and 4.28b). The electrostatic forces due to the FESEM lens (Figure 4.29a) and the resulting torque would effectively bend the crystal (Figure 4.30). The strongly asymmetric thickness profile of the microcrystal is clearly, key to the actuation. It is notable also that this picture is consistent with the observed bending of the crystal close to the region where the thickness starts increasing markedly (Figure 4.13). If the beam voltage is very low (< 2 kV), the holes generated recombine with the electrons in the gold coating,<sup>34</sup> whereas a much higher (>> 2 kV) beam voltage would induce less positive or even negative charging, making the bending inefficient as observed. Once the crystal is bent, the effective surface exposure is reduced leading to less charge accumulation. Subsequently, when the beam voltage is increased to ~ 6 kV, negative charging occurs in the bulk of the whole microcrystal, or even on its lower surface, causing repulsive electrostatic forces that cause straightening (Figure 4.30). Elasticity of the microcrystals is obviously favorable for these mechanical deformations to occur reversibly.

Persistent charging or longer time irradiation with the higher voltage electron beam can cause irreversible fatigue in the microcrystal. As described in Sec. 4.5.4, this can be avoided and the actuation repeated, with low scan speed and quickened straightening subjecting the crystal to less high voltage beam exposure. The model described in Sec. 4.6.2 justifies the need for a gold coating (leading to enhanced secondary electron emission (Table 4.5)), and an optimal accelerating voltage to induce the microcrystal bending; very high operating voltage leads to negative charging of the microcrystal, or the beam penetrating it completely, smearing out effects of the asymmetric crystal profile. Increase of the extent of bending with decreasing working distance is consistent with the increasing local fields due to the electrostatic lens. Observation of the microcrystal bending on a gold-coated nylon membrane suggests that substrate charging is not important; strong adhesive interactions with the substrate are clearly detrimental.

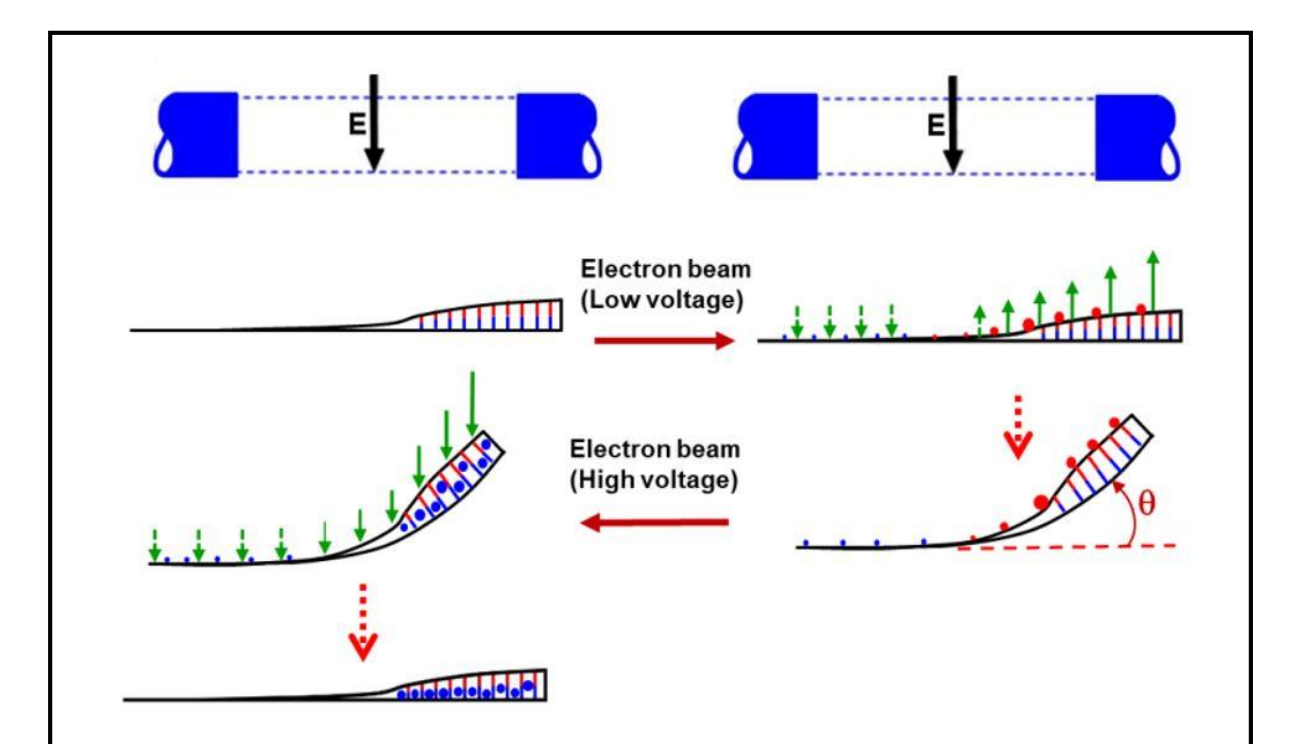


Figure 4.30. Model for bending (through angle,  $\theta$ ) and straightening of BCPADQ microcrystal under the impact of the electron beam with different voltages, and the local field (E) of the electrostatic lens (the negative outer electrode is indicated). Blue and red indicate negative and positive charges (dots) as well as the respective dipole ends (arrows/lines); radii and lengths indicate the magnitudes schematically. The green arrows indicate the forces, the intensity represented schematically by the length and type (full/broken) of lines.

#### 4.6.5. Consideration of alternate mechanisms for actuation

Other models can also be considered to explain the crystal bending. Differential thermal expansion across the asymmetric crystal is a possibility. A careful thermal imaging of the microcrystal under an electron beam with sufficient spatial resolution would be required to explore such a mechanism. However, this model appears to be less probable in view of the quick actuation observed with the slow scan experiments and the facile repeatability; thermal gradient formation and erasure would be slower. Further, direct heating in an oven and under infra-red light irradiation did not induce any noticeable actuation. A preliminary test using quick heating revealed no clear signature of thermosalient responses in these microcrystals; however, more careful experiments in this direction may be useful.

In view of the crystal space group of BCPADQ (Pna2<sub>1</sub>), another possibility could be based on a piezoelectric response. A field generated by the electron beam across the crystal with the asymmetric morphology, can lead to differential expansion and hence bending. A detailed investigation of the piezoelectric characteristics of the material and the induced fields is needed to probe such a scenario.

#### 4.7. Summary

This Chapter projects two significant findings, molecular hopper crystals and their electron beam triggered actuation. A novel instance of molecular hopper crystal formation is demonstrated, delineating the special molecular structural and assembly features as well as crystallization conditions that enable it. The insights gained through our study would be useful in exploring designed approaches to molecular hopper crystals. The asymmetric microcrystals grown in a controlled and tunable manner, show smooth, prominent and repeatable actuation responses under optimal electron beam irradiation; this adds a new dimension to the emerging field of dynamic crystals. The various experiments presented, not only provide critical guidance for effecting and manipulating the actuation, but also to formulate an empirical model to understand the mechanical process. Further explorations and theoretical investigations could provide deeper insight into the fundamental aspects of the phenomenon. This chapter provides new directions for the design of unusual molecular crystal morphologies, as well as novel micro electro-mechanical applications that can be derived from them.

# References

- 1. I. Sunagawa, Forma, 1999, 14, 147-166.
- 2. J. Desarnaud, H. Derluyn, J. Carameliet, D. Bonn and N. Shahidzadeh, *J. Phys. Chem. Lett.*, 2018, **9**, 2961-2966.
- 3. S. R. Dickinson and K. M. Mcgrath, *J. Mater. Chem.*, 2003, **13**, 928-933.
- 4. K. A. Jackson, D. R. Uhlmann and J. D. Hunt, *J. Cryst. Growth*, 1967, **1**, 1–14.
- 5. Y. Cao, S. Wang, H. Mou, H. Xu and C. Wu, J. Cryst. Growth, 2010, 312, 1747-1750.
- 6. T. P. Radhakrishnan, Acc. Chem. Res., 2008, 41, 367-376.
- 7. P. Srujana, P. Sudhakar and T. P. Radhakrishnan, *J. Mater. Chem. C.*, 2018, **6**, 9314-9329.
- 8. W. F. Paxton, S. Sundararajan, T. E. Mallouk and A. Sen, *Angew. Chem. Int. Ed.*, 2006, **45**, 5420-5429.
- 9. J. D. Posner, J. L. Moran, J. Wang and P. Wheat, *Funct. Nanosci.*, 2010, **1**, 21-39.
- 10. E. Uchida, R. Azumi and Y. Norikane, *Nature Commun.*, 2015, **6**, 7310 (1-7).
- 11. C. Chen, F. Mou, L. Xu, S. Wang, J. Guan, Z. Feng, Q. Wang, L. Kong, W. Li, J. Wang and Q. Zhang, *Adv. Mater.*, 2017, **29**, 1603374 (1-8).
- 12. E. Smela, Adv. Mater., 2003, 15, 481-494.
- 13. K. Kaneto, J. Phys. Conf. Ser., 2016, 704, 1-10.
- 14. Q. M. Zhang and M. J. Serpe, *Chemphyschem.*, 2017, **18**, 1451-1465.
- 15. P. Naumov, S. Chizhik. M. K. Panda, N. K. Nath and E. Boldyreva, *Chem. Rev.*, 2015, **115**, 12440-12490.
- R. Samanta, S. Ghosh, R. Devarapalli and C. M. Reddy, *Chem. Mater.*, 2018, 30, 577-581.
- 17. X. Dong, F. Tong, K. M. Hanson, R. O. Al-Kaysi, D. Kitagawa, S. Kobatake and C. J. Bardeen, *Chem. Mater.*, 2019, **31**, 1016-1022.
- 18. P. Naumov, D. P. Karothu, E. Ahmed, L. Catalano, P. Commins, J. M. Halabi, M. B. Al-Handawi and L. Li, *J. Am. Chem. Soc.*, 2020, **142**, 13256-13272.
- 19. D. T. Grubb, *J. Mater. Sci.*, 1974, **9**, 1715-1736.
- 20. A. F. Brilot, J. Z. Chen, A. Cheng, J. Pan, S. C. Harrison and C. S. Potter, *J. Struct. Biol.*, 2012, **177**, 630-637.
- 21. R. M. Glaeser, Specimen Behavior in the Electron Beam. In *Methods in Enzymology*, Eds. R. A. Crowther, Elsevier, pp. 19-39, Netherlands, **2016**.

- A. Seminara, B. Pokroy, S. H. Hang, M. P. Brenner and J. Aizenberg, Phys. Rev. B., 22. 2011, **83**, 235438 (1-6).
- 23. S. Carapezzi, G. Priante, V. Grillo, L. Montes, S. Rubini and A. Cavallini, *Acs Nano.*, 2014, 8, 8932-8941.
- 24. L. A. Bitzer, C. Speich, D. Schafer, D. Erni, W. Prost, F. J. Tegude, N. Benson and R. Schmechel, J. Appl. Phys., 2016, 119, 145101 (1-6).
- J. Jiang, J. He, S. A. Deshmukh, P. Kanjanaboos, G. Kamath, Y. Wang, S. K. R. S. 25. Sankaranarayanan, J. Wang, J. H. M. Jaeger and X. Lin, Nature Mater., 2015, 14, 912-918.
- Y. Zhang, C. Peng, Z. Zhou, R. Duan, H. Ji, Y. Che and J. Zhao, Adv. Mater., 2015, 26. **27**, 320-325.
- L. R. Hertler, H. D. Hartzler, D. S. Acker and R. E. Benson, J. Am. Chem. Soc., 1962, 27. **84**, 3387-3393.
- J. Xu, S. Huang and T. Cai, Cryst. Growth Des., 2020, 20, 2527-2534. 28.
- 29. O. V. Dolomanov, L. J. Bourhis, R. J. Gildea, J. A. K. Howard and H. Puschmann, J. Appl. Cryst., 2009, 42, 339-341.
- 30. W. Melitz, J. Shen, A. C. Kummer and S. Lee, Surf. Sci. Rep., 2011, 66, 1-27.
- 31. W. S. Rasband, ImageJ, U. S. National Institutes Of Health, Bethesda, Maryland, USA, Https://Imagej.Nih.Gov/Ij/, 1997-2018.
- P. Srujana and T. P. Radhakrishnan, *Angew. Chem. Int. Ed.*., 2015, **54**, 7270-7274. 32.
- 33. M. K. Panda, S. Ghosh, N. Yasuda, T. Moriwaki, G. D. Mukherjee, C. M. Reddy and P. Naumov, *Nature Chem.*, 2015, **7**, 65-72.
- J. B. Park, Y. J. Kim, S. M. Kim, J. M. Yoo, Y. Kim, R. Gorbachev, I. I. Barbolina, 34. S. J. Kim, S. Kang, M. H. Yoon, S. P. Cho, K. S. Novoselov and B. H. Hong, 2D Mater., 2016, 3, 045004 (1-8).
- 35. J. Cazaux, Scanning, 2004, 26, 181-203.
- H. Demers, N. P. Demers, A. R. Couture, D. Joly, M. Guilmain, N. De Jonge and D. 36. Drouin, Scanning, 2011, 33, 135-146.
- 37. J. I. Goldstein, D. E. Newbury, J. R. Michael, N. W. M. Ritchie, J. H. Scott and D. C. Joy, Scanning Electron Microscopy and X-Ray Microanalysis, Springer, Germany, 2018.
- https://www.zeiss.com/microscopy/int/products/scanning-electron-38. microscopes/geminisem.html
- M. A. Al-Khashab and N. S. Hujazie, *Dirasat, Pure Sciences*, 2011, **38**, 52-60. 39.

# **CHAPTER 5**

Overview of the present work and future prospects

# 5.1. Overview of the present work

Molecular materials exhibiting strong fluorescence emission in aggregated or solidstate are of immense interest due to their extensive applications in various fields. *Inter alia*, small molecule based fluorophores are gaining significant attention in terms of applications because of their tunable optical and electrical properties. Previous reports from our research group have demonstrated the strong fluorescence emission of various diaminodicyanoquinodimethane (DADQ) derivatives in the form of crystals, nanocrystals, amorphous particles and thin films compared to their solution state (Sec. 1.1.3). In this thesis, we have demonstrated the utility of DADQs in staining stomatal cells (Chapter 2) of pea leaves and bacterial endospores (Chapter 3).<sup>1,2</sup> Fluorescence-based bioimaging is an important tool to visualize live or fixed cells without disturbing their integrity and function by the fluorescence probes. However, understanding the interactions between the fluorescence probes and the chemical component of the biological cells is critical for designing and improving the efficiency of bioimaging. This is an aspect that we have specially focused on. We have also explored the fabrication of novel DADQ based microcrystals with a unique hopper morphology, and their actuation responses (Chapter 4).<sup>3</sup> The asymmetry of the particles can generate critical responses to external stimuli. The fabrication of organic-based actuators and their controlled mechanical actions under electron beam are rare. Controlling the growth of the asymmetric organic hopper crystals in a simple reprecipitation method is an interesting challenge. A schematic representation of the various domains of work presented in this thesis is provided in Figure 5.1.

Several advantages of the DADQ derivatives, such as structural tailorability, ease of synthesis, stability under light and heat and non-cytotoxic nature, make them potential candidates for bioimaging applications; further, unlike many well-known dyes, they require no special storage conditions. We have found a wide range of DADQ derivatives with suitable functional groups that can efficiently stain the stomatal and epidermal cells of the pea leaves as well as spores of the bacterial cells. We have developed single staining protocol and explored the molecular-level interactions that enable the efficient imaging. Staining of the epidermis layer of the pea leaves was achieved using piperazine (DPZDQ) or piperazinium (BT<sub>2</sub>) substituted DADQs under two conditions (i) buffer and (ii) buffer-free state. In the former case, selective staining of the cell walls was observed. In the latter case, selective staining of the cell wall with nuclei was achieved by simple and direct treatment of

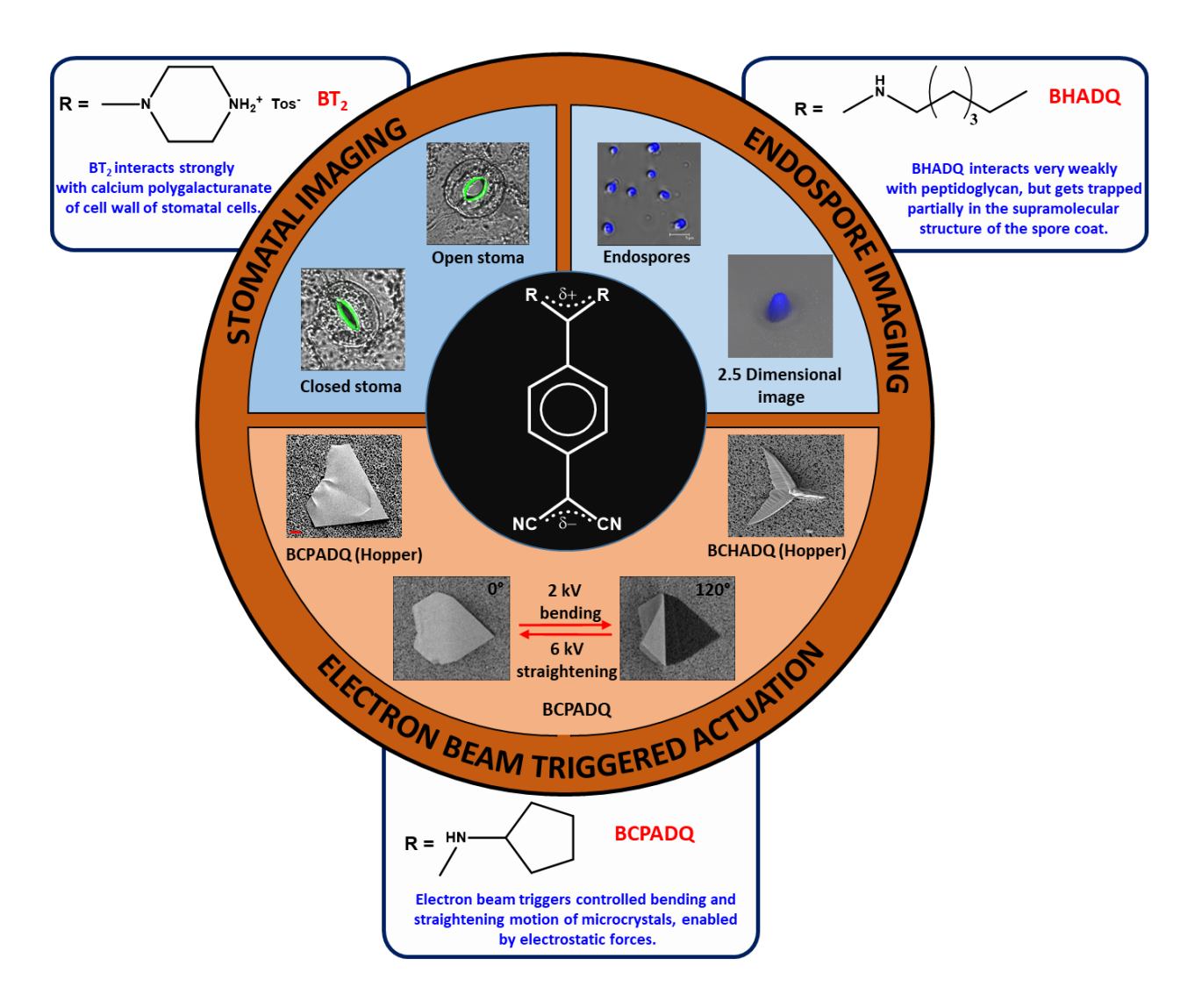


Figure 5.1. Schematic representation of the work presented in this thesis.

the epidermis layer with fluorophores. The quick staining protocol enhances the ease and efficiency of the imaging by avoiding undesirable interactions between the buffer medium and the cell component. The ionic functionalities are ideal for cell wall imaging due to the electrostatic properties of the cell wall. The ionic DADQ derivative, BT<sub>2</sub> was used to selectively stain the cell wall of the guard cells. Concentration of the fluorophores and solvents used in the staining procedure also play a critical role in the efficient imaging. The aqueous solution of BT<sub>2</sub> stains the inner and outer cell wall of the guard cells. On the other hand, BT<sub>2</sub> in DMSO solution penetrates into the guard cells and stains the cell wall with nuclei. Isothermal calorimetry, infra-red spectroscopy, and microscopy with energydispersive X-ray spectroscopic analysis enabled us to draw a clear picture of the molecular

level interactions involved in the staining. It is proposed that DADQs with ionic or hydrogen bonding functionalities bind to the polygalacturonate present in the cell wall of the guard cells, and epidermal cells. Various fluorescence experiments suggested that the bound BT<sub>2</sub> molecules exist in isolated as well as aggregated states within the cell wall; the latter enables bright fluorescence imaging.

In our investigations on the bacterial cells and endospores, it was found that BT<sub>2</sub> stains the endospores as well as both gram-positive and negative bacterial cells. Role of solvents was once again critical; DMSO solution of BT<sub>2</sub> stains only the cell wall of the spore, but aqueous solution enter deeper inside the endospores, in some cases. Spectroscopy and microscopy studies allowed us to identify two types of interactions between BT<sub>2</sub> and the major chemical component of the cell wall, peptidoglycan leading to the efficient staining; (i) hydrogen bonds between the hydroxyl groups of the peptidoglycans, replaced by the hydrogen bonds with the cyano groups of BT<sub>2</sub>, and (ii) electrostatic interactions between the positively charged fluorophore with the negatively charged peptidoglycan. Based on the control experiments, we have concluded that the optimal hydrophobic character of the hexylamine substituted DADQ derivative (BHADQ) is critical to selectively stain the endospores even in admixtures with the bacterial cells. The staining protocol that we have developed is extremely simple, with no chemical or significant thermal treatments involved. Germination and viability assay experiments showed that the staining does not affect dormant state of the endospores. The various imaging experiments, together with spectroscopy and microscopy investigations of the interactions between BHADQ and the major chemical component of the cell wall (peptidoglycan) and core (DNA and calcium dipicolinate) of the spores, show the basis for BHADO staining the endospores selectively in their dormant state, with no staining of bacteria. To best of our knowledge, BHADQ is the first fluorescence dye reported for selective imaging of endospores in their dormant state. In this thesis, we have addressed various issues related to the stability, toxicity, selectivity and specificity of the dyes, and possible interactions between the dyes and chemical components of the cell; these findings are useful to design new classes of efficient fluorescence dyes for various bioimaging applications.

We have also explored the novel avenue of molecular hopper crystals. The important role of molecular organization in the crystal and the microcrystal formation and growth are identified. The growth of the unique morphology and uneven dipole distribution of the microcrystals was monitored by microscopy investigations and surface potential mapping analysis. The interesting case of mechanical bending followed by straightening of the hopper crystals under an electron beam was observed; various factors such as voltage of the electron beam, working distance, size of the particles etc. that control the actuation responses were explored; this adds a new direction to the emerging field of dynamic crystals. We have addressed several issues related to the stability of the microcrystals under electron beam irradiation that is critical for their reversible actuation. Detailed examination of the crystal lattice structure and asymmetric dipole distribution, together with simulations of the electron beam interactions, provided insight into the mechanism involved in the microcrystals actuation triggered by electron beams. The observation and elucidation of these findings suggest new directions to devise asymmetric molecular crystal morphologies; moreover, it can spawn novel approaches to micro electro-mechanical applications.

#### **5.2. Future directions**

We have probed the general utility of DADQ derivatives as fluorescence probes for bioimaging mammalian and cyanobacterial cells in Chapters 2 and 3 (Sec. 2.5 and 3.11). The preliminary experiments and advantages of the DADQ derivatives have shown that the bioimaging applications of the DADQ derivatives with appropriate functionalities can be extended to visualize the wide range of biological samples. *In vivo* small animal imaging is an important tool in preclinical research. Recently, two-photon absorption dyes and near infra-red fluorescence probes are gaining interest in the in vivo bioimaging due to their advantages such as high spatial resolution and deep tissue penetration.<sup>4,5</sup> Introducing highly conjugated moieties in the DADQ framework could shift their emission into the near infrared region. Synthesis of DADQs with high two-photon absorption cross-sections is an important challenge. It would be interesting to reveal the biological process of living organisms by studying the interactions between the fluorophore and the bio component; DADQs and similar probes are ideally suited for such explorations.

Imaging multi organelle or molecular components of the cell, simultaneously in a single imaging experiment is the most appropriate technique to understand complex biological events.<sup>6</sup> Multi-target imaging in a single experiment using multifunctional quantum dots is well known. However, toxicity of the QDs limits their wider applications. Commercial dyes also have been used to achieve multi-target imaging.<sup>6</sup> In most cases, staining the cells with a mixture of two or more dyes at the same time has several disadvantages like spectral overlap, interactions between the dyes, and solubility issues of dyes. In such cases, biological cells are treated with dyes consecutively; it prolongs the experiments. With extended exposure to dyes and organic solvents, cells and their biological functions might be altered. However, the synthesis of multi functionalised single fluorescence probe is also complicated. Synthesis of a series of DADO derivatives with suitable functional groups without spectral overlap and negligible interactions would be a promising approach; it could also be applied in the multi organelle imaging technique.

In general, all bacterial cells do not produce spores; only selective classes of grampositive and negative bacterial cells produce spores. Bacterial cells, unknown to produce spores, can be easily identified using BHADQ. PHA (polyhydroxyalkanoate) granules are the subcellular organelle present inside the bacterial cells with spores. It is very difficult to differentiate the PHA granules from the spores using normal microscopy techniques due to their structural similarities. Based on the chemical composition of the PHA granules, DADQ based fluorescent probes with suitable functionalities can be developed to stain them selectively. It would be a challenging task to stain the spores and PHA granules in bacterial cells simultaneously using a mixture of BHADQ and PHA-selective dye in a single imaging experiment.

Studies presented in this thesis on the fabrication and actuation of the asymmetric hopper crystals have opened up a new path to device asymmetric organic hopper micro/nanocrystals. It can potentially be exploited to elicit sensitive mechanical responses under different external stimuli. Thanks to the asymmetric potential distribution along with the altitude, BCPADQ microcrystals could possibly be employed as micromotors under AC or DC electric field; their controlled propulsion in isotropic (water) and anisotropic (liquid crystals) environments can generate promising and interesting research problems. Study of the externally driven dynamics of asymmetric particles is an active research field. Like the electron beam responsive microcrystals, photoresponsive DADQ microcrystals can be fabricated and their mechanical motion under light might be another interesting problem to be explored. The new findings presented in this thesis can potentially evolve into major research ventures in the fields of imaging as well as active matter.

### References

- 1. N. Senthilnathan, Ch. G. Chandaluri and T. P. Radhakrishnan, *Sci. Rep.*, 2017, **7**, 10583 (1-11).
- 2. N. Senthilnathan, Kumar Gaurav, Ch. Venkata Ramana and T. P. Radhakrishnan, *J. Mater. Chem. B*, 2020, **8**, 4601-608.
- 3. N. Senthilnathan and T. P. Radhakrishnan, Chem. Mater., 2020, 32, 8567-8575.
- 4. H. Wang, Q. Zhang, J. Zhang, L. Li, Q. Zhang, S. Li, S. Zhang, J. Wu and Y. Tian, *Dyes Pigm.*, 2014, **102**, 263-272
- 5. J. Cao, B. Zhu, Zheng, S. He, L. Meng, J. Song and H. Yang, *Front. Bioeng. Biotechnol.*, 2020, **7**, 1-21.
- 6. P. Gao, W. Pan, N. Li and B. Tang, Chem. Sci., 2019, 10, 6035-6071.
- 7. P. Zrazhevskiy, M. Senaw and X. Gao, Chem. Soc. Rev., 2019, 39, 4326-4354.

## Appendix

Appendix A	Materials and Methods	171
Appendix B	Instrumentation	172
	Charecterization studies	174

### **APPENDIX A**

### **Materials and methods**

7,7,8,8-tetracyanoquinodimethane TCI Chemicals

Piperazine Sigma-Aldrich

Polygalacturonic (pectic) acid Sigma-Aldrich

Sodium Polygalacturonate Sigma-Aldrich

2-(*N*-morpholino)ethanesulfonic acid Sigma-Aldrich

*n*-hexylamine TCI Chemicals

Peptidoglycan from Bacillus subtilis Sigma-Aldrich

Sodium dipicolinate Sigma-Aldrich

Nutrient agar media HiMedia

Cyclopentylamine TCI Chemicals

Toluene (HPLC) Finar

DMSO (HPLC) Finar

Nylon membrane (0.1 µm pore size) Axiva Sichem Biotech

AFM probes Asylum Research Company

Ultrapure water Millipore MilliQ (resistivity =  $18 \text{ M}\Omega \text{ cm}$ )

7,7,8,8-tetracyanoquinodimethane (TCNQ) was recrystallized from acetonitrile prior to use, remaining chemicals were used as supplied.

### **APPENDIX B**

### **Instrumentations**

### Melting point

Melting temperatures of solids were determined using Labindia model MR-VIS visual melting range apparatus.

### Nuclear Magnetic Resonance Spectroscopy

 $^1\mathrm{H}$  and  $^{13}\mathrm{C}$  NMR spectra were recorded on a Bruker 400 and 500 MHz NMR spectrometer.

### Electronic absorption Spectroscopy

Absorption spectra were recorded on a Varian model Cary 100 UV-Vis spectrometer. Absorption spectra of solution samples were recorded in transmission mode and solid samples in diffuse reflectance mode.

### Fluorescence Spectroscopy

Steady state fluorescence emission and excitation spectra were recorded on a Horiba Jobin Yvon model FL3-22 Fluorolog spectrofluorimeter, in right angle geometry. Quantum yield of solid samples were determined using an integrating sphere and the PLQY Calculator v.3 software (Jobin Yvon).

### Fourier-transform infra-red Spectroscopy

FTIR spectra were recorded on a Thermo Fisher Nicolet IS5 Fourier-transform infra-red spectrometer.

### Single Crystal X-ray Diffraction

Single crystal X-ray diffraction studies were carried out on a Bruker SMART APEX CCD area detector system equipped with a graphite monochromator and a MoK $_{\alpha}$  fine-focus sealed tube ( $\lambda$  = 0.71073 Å) operated at 1200 W (40 kV, 30 mA) or Rigaku Oxford XtaLAB Pro-Pilatus3 R 200K-A detector system equipped with a CuK $_{\alpha}$  ( $\lambda$  = 1.54184 Å) MicroMax-003 microfocus sealed tube operated at 50 kV and 0.6 mA or a Bruker D8 Quest-Photon II detector system equipped with a MoK $_{\alpha}$  ( $\lambda$  = 0.71073 Å) microfocus sealed tube operated at 50 kV and 1 mA. Data was collected at 100 K (as

well as 298 K), and the reduction was performed using Bruker SAINT or CrysAlisPro software; the structure was solved and refined using the Bruker SHELXTL software.

### Confocal Raman Microscopy

WITec model Alpha300 R equipped with an AFM was used for recording the Raman spectra.

### Laser Scanning Confocal Microscopy

Carl Zeiss model LSM 710 NLO ConfoCor 3 microscope was used for confocal fluorescence microscopy studies. Second harmonic frequency of 780 nm laser was used for excitation.

### Fluorescence Lifetime Imaging Microscopy

Time-resolved confocal fluorescence microscope (MicroTime 200, PicoQuant) coupled to an Olympus IX71 microscope (PicoQuant) was used for fluorescence lifetime imaging studies. Excitation was carried out using a 405 nm pulsed-laser diode and the fluorescence observed through a 430 nm long-pass filter; the corresponding fwhm of pulse response function was 176 ps. Data acquisition was performed with a PicoHarp 300 TCSPC module using PicoHarp300 version 2.3 in a time-tagged timeresolved mode.

### Atomic force microscopy

AFM images were recorded on an NT-MDT Model Solver Pro-M atomic force microscope in semi-contact mode using a tip having a force constant of 12 Nm<sup>-1</sup>. Images were analyzed using the NOVA (version 1.0.26) software supplied by the microscope manufacturer.

### Field emission scanning electron microscopy

Field emission scanning electron microscope (FESEM) imaging with energy dispersive X-ray (EDX) spectroscopy was carried out on a Carl Zeiss model Merlin Compact equipped with an Oxford Instruments X-MaxN SDD (50 mm<sup>2</sup>) system and INCA analysis software, as well as an FEI Nova NanoSEM 450.

### Modelling Electron Beam Trajectories

CASINO (version 3.3.0.4) Monte Carlo software [Copyright 2016: D. Drouin, A. R. Couture, D. Joly, N. Poirier-Demers, H. Demers] was used.

### **Charecterization studies**

### Cytotoxicity assay

Cytotoxicity assay was carried out by Pondicherry Center for Biological Sciences, Pondicherry, India (http://http://pcbscience.webs.com/).  $2 - 4 \times 10^5$  HeLa cells were seeded in a 96-well cell culture plate with DMEM medium (Himedia) containing 1% anti-mycotic antibiotic (Himedia) and 10% FBS (Himedia), and incubated for 24 h in a CO<sub>2</sub> incubator at 37°C. The cells were treated initially with the test sample (DADQs) in different concentrations (25, 50, 100, 250 and 500 µg/mL) and incubated for 24 h. The medium was aspirated from the cells at the end of the treatment period. 0.5 mg/mL MTT and 1% PBS were added and incubated at 37°C for 4 h. After incubation, the medium containing MTT was discarded from the cells. The crystals formed were dissolved in 100 µL of DMSO; the absorbance at 570 nm was measured using a micro-plate reader to estimate the cell viability. IC<sub>50</sub> values were calculated using GraphPad Prism software.



### **PUBLICATIONS**

- 1. N. Senthilnathan, Ch. G. Chandaluri and T. P. Radhakrishnan, Efficient Bioimaging with Diaminodicyanoquinodimethanes: Epidermal and Stomatal Cell Staining and Insight into the Molecular Level Interactions, Sci. Rep., 2017, 7, 10583 (1-11).
- 2. N. Senthilnathan, Kumar Gauray, Ch. Venkata Ramana and T. P. Radhakrishnan, Zwitterionic Small Molecule Based Fluorophores for Efficient and Selective Imaging of Bacterial Endospores, J. Mater. Chem. B, 2020, 8, 4601-4608.
- 3. N. Senthilnathan and T. P. Radhakrishnan, Molecular Hopper Crystals and Electron Beam Triggered Actuation, Chem. Mater., 2020, 32, 8567-8575.
- **4. N. Senthilnathan** and T. P. Radhakrishnan, Diaminodicyanoquinodimethanes: Fluorescence Emission Enhancement in Aggregates and Solids, in *Handbook of* Aggregation-Induced Emission, Vol. 2: Typical AIEgens Design, Eds., B. Z. Tang and Y. Tang, Wiley and Sons. (in press)
- 5. A. Ali, K, Gauray, N. Senthilnathan, T. P. Radhakrishnan, Ch. Sasikala, Ch. V. Ramana, "Sporotan" a New Fluorescent Stain for Identifying Cryptic Spores of Rhodobacter johrii, *J. Microbiol. Methods*, 2020, **177**, 106019 (1-6).

### PATENT APPLICATIONS

- 1. N. Senthilnathan and T. P. Radhakrishnan, Diaminodicyanoquinodimethane Based Dyes for Bioimaging, Indian patent 201741017444 dated 18.05.2017.
- 2. N. Senthilnathan, Kumar Gaurav, Ch. Venkata Ramana and T. P. Radhakrishnan, Sporotan: A Spore Selective Fluorescent Dye for Identification of Cryptic Bacterial Spores, Indian patent 201941052617 dated 18.12.2019.

### **PRESENTATIONS**

1. Poster presentation: National Conference on Fluorescence and Raman Spectroscopy (FCS 2017), IIT Guwahati, Assam. December 17-21, 2017.

Efficient Bioimaging with Diaminodicyanoquinodimethanes: Selective Imaging of Epidermal and Stomatal Cells and Insight into the Molecular Level Interactions

**2. Poster presentation:** Symposium on Frontiers in Nanoscience and Technology, University of Hyderabad, Telangana.

April 06-07, 2018.

Efficient Bioimaging of Epidermal and Stomatal Cells with Diaminodicyanoquinodimethanes and Insight into the Molecular Level Interactions (**Best Poster Award**).

**3. Poster presentation:** International Conference on Recent Trends in Materials Science and Technology, (ICMST 2018), Vikram Sarabhai Space Centre, Thiruvananthapuram.

October 10-13, 2018.

Selective Bioimaging with Diaminodicyanoquinodimethanes: Insight into the Molecular Level Interactions.

**4. Poster presentation:** National Symposium on Convergence of Chemistry and Materials (CCM 2019), BITS-Pilani, Hyderabad campus.

December 17-18, 2019.

Mechanically Responsive Molecular Hopper Crystals: Electron Beam Triggered Action.

**5. Poster presentation:** National Workshop on Fluorescence and Raman Spectroscopy (FCS 2019), TIFR, Hyderabad.

December 19-21, 2019.

Selective bioimaging with Diaminodicyanoquinodimethanes: Insight into the molecular level interactions

**6. Oral presentation:** CHEM FEST 2020, University of Hyderabad, Hyderabad. February 27-28, 2020.

Diaminodicyanoquinodimethanes: Efficient Bioimaging and Mechanically Responsive Molecular Hopper Crystals

# Diaminodicyanoquinodimethanes: Bioimaging Applications and Mechanically Responsive Molecular Hopper Crystals

by N. Senthilnathan

# PhD Thesis

by N Senthilnathan

**Submission date:** 14-Dec-2020 12:41PM (UTC+0530)

**Submission ID: 1474464044** 

File name: N\_Senthilnathan\_PhD\_thesis\_TPR\_Lab\_SoC.pdf (11.55M)

Word count: 39703

Character count: 211409

PhD	Thesis			
ORIGINA	ALITY REPORT			
4 SIMILA	0% 27% INTERNET SOURCES	38% PUBLICATIONS	1% STUDENT F	PAPERS
PRIMAR	RY SOURCES		di	, when a
1	pubs.rsc.org Internet Source	0~		12%
2	N. Senthilnathan, T. P. R. "Molecular Hopper Crysta Triggered Reversible Acta Materials, 2020 Publication	als and Electro	on Beam-	11%
3	N. Senthilnathan, Ch. G. Radhakrishnan. "Efficient Diaminodicyanoquinodim Imaging of Epidermal and Insight into the Molecular Scientific Reports, 2017	Bioimaging wethanes: Sele	vith ctive lls and	5%
4	www.nature.com Internet Source	0	w publica	5%
5	mafiadoc.com Internet Source	Din	poblish	2%
6	www.ncbi.nlm.nih.gov Internet Source	0 ~	mbieste	1%

Prof. T.P. Radhakrishnan School of Chemistry University of Hyderabad Hyderabad-500 046, India

7	N. Senthilnathan, Kumar Gaurav, Ch. Venkata Ramana, T. P. Radhakrishnan. "Zwitterionic small molecule based fluorophores for efficient and selective imaging of bacterial endospores", Journal of Materials Chemistry B, 2020 Publication	<1%
8	Chandaluri, Ch.G "Zwitterionic diaminodicyanoquinodimethanes with enhanced blue-green emission in the solid state", Optical Materials, 201111 Publication	<1%
9	Ju Mei, Nelson L. C. Leung, Ryan T. K. Kwok, Jacky W. Y. Lam, Ben Zhong Tang. "Aggregation-Induced Emission: Together We Shine, United We Soar!", Chemical Reviews, 2015	<1%
10	S. Jayanty, T. P. Radhakrishnan. "Enhanced Fluorescence of Remote Functionalized Diaminodicyanoquinodimethanes in the Solid State and Fluorescence Switching in a Doped Polymer by Solvent Vapors", Chemistry - A European Journal, 2004	<1%
11	www.freepatentsonline.com Internet Source	<1%

12	idoc.pub Internet Source	<1%
13	Andrew C. Grimsdale, Khai Leok Chan, Rainer E. Martin, Pawel G. Jokisz, Andrew B. Holmes. "Synthesis of Light-Emitting Conjugated Polymers for Applications in Electroluminescent Devices", Chemical Reviews, 2009 Publication	<1%
14	Ch. G. Chandaluri, A. Patra, T. P. Radhakrishnan. "Polyelectrolyte-Assisted Formation of Molecular Nanoparticles Exhibiting Strongly Enhanced Fluorescence", Chemistry - A European Journal, 2010 Publication	<1%
15	link.springer.com Internet Source	<1%
16	archiv.ub.uni-marburg.de Internet Source	<1%
17	Submitted to University of Hyderabad, Hyderabad Student Paper	<1%
18	d-nb.info Internet Source	<1%
19	B. Balaswamy, Lasya Maganti, Sonika Sharma, T. P. Radhakrishnan. "Mechanical Control of	<1%

# Molecular Aggregation and Fluorescence Switching/Enhancement in an Ultrathin Film", Langmuir, 2012

Publication

20	hdl.handle.net Internet Source	<1%
21	Mengyao Hao, Weijie Chi, Chao Wang, Zhaochao Xu, Zesheng Li, Xiaogang Liu. "Molecular Origins of Photoinduced Backward Intramolecular Charge Transfer", The Journal of Physical Chemistry C, 2020 Publication	<1%
22	repository.hkbu.edu.hk Internet Source	<1%
23	Andres, Julien, and Anne-Sophie Chauvin. "Lanthanides: Luminescence", Encyclopedia of Inorganic and Bioinorganic Chemistry, 2012. Publication	<1%
24	www.faqs.org Internet Source	<1%
25	lib.uky.edu Internet Source	<1%
26	chemistry-europe.onlinelibrary.wiley.com Internet Source	<1%
27	Submitted to Higher Education Commission	<1%

28

P. Srujana, Pagidi Sudhakar, T. P. Radhakrishnan. "Enhancement of fluorescence efficiency from molecules to materials and the critical role of molecular assembly", Journal of Materials Chemistry C, 2018

<1%

Publication

29

Parvej Alam, Clàudia Climent, Gurpreet Kaur, David Casanova et al. "Exploring the Origin of "Aggregation Induced Emission" Activity and "Crystallization Induced Emission" in Organometallic Iridium(III) Cationic Complexes: Influence of Counterions", Crystal Growth & Design, 2016

<1%

Publication

30

Bhattacharjee, Subhadeep, and Rashmi Biswas. "A primogenius study on characterisation of c-Si solar cell", International Journal of Renewable Energy Technology, 2013.

<1%

Publication

31

McCalmont, W.F.. "Investigation into the structure-activity relationship of novel concentration dependent, dual action T-type calcium channel agonists/antagonists", Bioorganic & Medicinal Chemistry, 20050601

<1%

Publication

32	Inna Kalikhman, Vijeyakumar Kingston, Boris Gostevskii, Vadim Pestunovich, Dietmar Stalke, Bernhard Walfort, Daniel Kost. "Donor- Stabilized Silyl Cations. 5. Comparison between Mono- and Binuclear Siliconium Chelates ", Organometallics, 2002 Publication	<1%
33	dsc.duq.edu Internet Source	<1%
34	Sonika Sharma, T. P. Radhakrishnan. "Control of Crystal Packing in SHG Active 7,7-Bis(n-pentylamino)-8,8-dicyanoquinodimethane by Intermolecular H-bonds and Alkyl Chain Interactions", Molecular Crystals and Liquid Crystals Science and Technology. Section A. Molecular Crystals and Liquid Crystals, 2006 Publication	<1%
35	bioone.org Internet Source	<1%
36	www.ideals.illinois.edu Internet Source	<1%
37	Submitted to National University of Singapore Student Paper	<1%
38	D. Demus, J. Goodby, G. W. Gray, HW. Spiess, V. Vill. "Handbook of Liquid Crystals Set", Wiley, 1998	<1%

Esteban N. Lorenzón, Julia P. Piccoli, Eduardo <1% M. Cilli. "Interaction between the antimicrobial peptide Aurein 1.2 dimer and mannans", Amino Acids. 2014 Publication Melissa S. Egbertson, Charles T.-C. Chang, <1% 40 Mark E. Duggan, Robert J. Gould et al. "Non-Peptide Fibrinogen Receptor Antagonists. 2. Optimization of a Tyrosine Template as a Mimic for Arg-Gly-Asp", Journal of Medicinal Chemistry, 1994 Publication opac.ll.chiba-u.jp <1% 41 Internet Source umpir.ump.edu.my 42 Internet Source Submitted to University of Lancaster 43 Student Paper A. Turchanin. "Molecular Self-Assembly, 44 Chemical Lithography, and Biochemical Tweezers: A Path for the Fabrication of Functional Nanometer-Scale Protein Arrays", Advanced Materials, 02/04/2008 Publication

	with Coarse Grained Model", Chinese Journal of Chemical Physics, 2012.  Publication	
46	Submitted to University of British Columbia Student Paper	<1%
47	bmrservice.com Internet Source	<1%
48	Ch.G. Chandaluri, T.P. Radhakrishnan. "Zwitterionic diaminodicyanoquinodimethanes with enhanced blue—green emission in the solid state", Optical Materials, 2011 Publication	<1%
49	Submitted to University of Birmingham Student Paper	<1%
50	publications.lib.chalmers.se Internet Source	<1%
51	"Principles and Applications of Aggregation- Induced Emission", Springer Science and Business Media LLC, 2019 Publication	<1%
52	www.findlight.net Internet Source	<1%

Yan Ju. "Secondary Structure Analysis of Native

Cellulose by Molecular Dynamics Simulations

Exclude quotes Off Exclude matches < 12 words

Exclude bibliography Off